3-D DIRECT PRINTING OF SILICONE MENISCUS USING A NOVEL HEAT-CURING EXTRUSION BASED SILICONE PRINTER

GUNTUR ERIC LUIS ADIWATI

SCHOOL OF MECHANICAL AND AEROSPACE ENGINEERING

2019

3D DIRECT PRINTING OF SILICONE MENISCUS USING A NOVEL HEAT-CURING EXTRUSION BASED SILICONE PRINTER

GUNTUR ERIC LUIS ADIWATI

SCHOOL OF MECHANICAL AND AEROSPACE ENGINEERING

2019

A thesis submitted to the Nanyang Technological University in partial fulfilment of the requirement for the degree of

Doctor of Philosophy

2019

3D DIRECT PRINTING OF SILICONE MENISCUS USING A NOVEL HEAT-CURING EXTRUSION BASED SILICONE PRINTER

Statement of Originality

I hereby certify that the work embodied in this thesis is the result of original research done by me except where otherwise stated in this thesis. The thesis work has not been submitted for a degree or professional qualification to any other university or institution. I declare that this thesis is written by myself and is free of plagiarism and of sufficient grammatical clarity to be examined. I confirm that the investigations were conducted in accord with the ethics policies and integrity standards of Nanyang Technological University and that the research data are presented honestly and without prejudice.

15 MAR 2019
....
Date

....
Guntur Eric Luis Adiwati

Supervisor Declaration Statement

I have reviewed the content and presentation style of this thesis and declare it of sufficient grammatical clarity to be examined. To the best of my knowledge, the thesis is free of plagiarism and the research and writing are those of the candidate's except as acknowledged in the Author Attribution Statement. I confirm that the investigations were conducted in accord with the ethics policies and integrity standards of Nanyang Technological University and that the research data are presented honestly and without prejudice.

15 MAR 2019
Date

Assoc Prof Yeong Wai Yee

Authorship Attribution Statement

- This thesis contains material from one paper(s) published in the following peer-reviewed journal(s) / from papers accepted at conferences in which I am listed as an author.

1) content of Chapter 5 in thesis is published in E. Luis, H. M. Pan, A. Bastola, R. Bajpai, S. L. Sing, J. Song, W. Y. Yeong. Validation and Characterization of Post 3D-Printed Silicone Meniscus Implants. *3D Printing and Additive Manufacturing* **2019 (submitted)**
2) content of Chapter 3 in thesis is published in E. Luis, H. M. Pan, S. L. Sing, A. Bastola, G. D. Goh, G. L. Goh, H., K. J. Tan, R. Bajpai, J. Song, W. Y. Yeong. Silicone 3D-Printing: Process Optimization, Product Biocompatibility and Reliability of Silicone Meniscus Implants. *3D Printing and Additive Manufacturing* **2018 (undergoing review)**
3) content of Chapter 3 in thesis is published as E. Luis, H. M. Pan, R. Bajpai, S. Agarwala, J. Song, W. Y. Yeong. 3D Direct Printing of Silicone Meniscus Implant Using a Novel Heat-Cured Extrusion Based Printer. *3D Printing and Additive Manufacturing* **2019 (undergoing review)**
4) partial content of Chapter 2 in thesis is published in E. Luis, et al., **2018** A Review of Medical Silicone 3D-Printing Technologies and Clinical Applications. *Journal of Orthopedic Research and Therapy. JORT-1104 DOI*: 10.29011/2575-8241.001104
5) partial content of Chapter 6 in thesis published in "3D Printing of Medical Models from CT/MRI Images, 2016 " by Li Yihua and Eric Luis. Partridge Publication. ISBN Softcover 978-1-4828-9740-7. eBook 978-1-4828-7942-1

The contributions of the co-authors are as follows:

- Prof Yeong Wai Yee provided project direction. Prof Song assisted with materials, thermal analysis. Both assisted with manuscript editing.
- Dr Matthew Pan assisted with cell cultures experiments. Dr Sing SL assisted with statistical presentation. Dr Bajpai assisted with statistical Strata software.
- Mr Goh GD and Goh GL assisted with CT-X Ray.
- I designed all 3D printings and moldings of test specimens, prepared all specimens, standard and shape-memory specimens. I performed the rheological tests, performed the DOE characterization and mechanical tests of all specimens, analyzed the results and wrote the drafts of the manuscript.
- Mr Li YH provide technical input with segmentation software. Mr Liu Hang contributed to manuscript section, printer setup and experimental work.

15 MAR 2019 ....

Date Guntur Eric Luis Adiwati

ABSTRACT

Silicone implants have been widely used as treatment for osteoarthritis of the knee with meniscal pathologies. Silicone products have conventionally been manufactured by direct or indirect molding methods which are expensive and time-consuming. The geometrical precision and aesthetic parameters of the end-products are also highly operator-dependent. Silicone 3D printing provides immediate benefits of customization, time and cost savings for patients.

Typical non-printable meniscal substitutes lack the customizability of 3D printable implants and are mechanically weak for instantaneous weight bearing. Currently, 3D printed scaffolds, using hydrogels, suffer from the common major drawbacks of being mechanically weak and patients are unable to execute immediate post-surgical weight-bearing, ambulation and rehabilitation. To solve this problem, a 3D silicone meniscus implant which is 1) biocompatible, 2) mechanically similar to native meniscus and resistant to cyclic loading, and 3) directly 3D printable, has been developed.

The main objectives of this research are: 1)To design, manufacture and optimize a novel extrusion-based 3D silicone printer with unique heating processes. The optimization of various printing parameters and printing processes will be studied by conducting design of experiments (DOE). This silicone printer will be able to perform Liquid Additive Manufacturing with different ranges of medical and non-medical grade silicones. 2) To 3D print a customized meniscus which has comparable biomechanical properties as those of the native meniscus. In a future design to the 3D printed meniscus, micro-channels and reservoirs will be incorporated into the meniscus to provide slow release

mechanism for drugs, lubricants and growth factors. 3) To incorporate shape memory properties into currently commercially available liquid silicone rubber.

This work reports the first demonstration of direct extrusion of heat-cured silicone using a two-part Ecoflex silicone rubber. The results provide a better understanding on the fabrication and workings of a heat-cured extrusion-based printer in the direct 3D printing of a silicone meniscus. For subsequent experimental purposes, Ecoflex silicone rubbers are used for their costs and biocompatibility. Their rheological, mechanical and biological properties are first characterized and these form the basis for the design and fabrication of the silicone printer. All hardwares and softwares used are open-sourced materials. The printer developed contains a pre-mixing station to ensure homogenous mixing of silicone prior to dispensing. The printing volume is demonstrated with the printing of an 8 cm^3 cube. Secondly, printer parameters such as print velocities, nozzle diameters, nozzle-platform distance, flow-rates, nozzle temperatures and bed temperatures were selected for characterization and testing. The optimal processing window was established for each parameter. Overall, it was found that nozzle diameter and bed temperature were the major determinants on the accuracy and precision of printed dimensions in the x-y horizontal planes, while the bed temperature was the only significant determinant on construct.

Thirdly, the optimization of the selected printing parameters was performed through regression analysis using design of experiments (DOE) and analysis of variance (ANOVA) methods. Nozzle diameters, nozzle temperatures and bed temperatures were the critical parameters which determined the print quality of silicone samples. The resolution of printing was characterized using basic and complex shapes, ranging from struts, cylinders, T-bones, cubes, polyhedron and finally meniscus. Overall, the result shows that the dimensions of the printed structures were close to the design dimensions.

Fourthly, the printed silicone meniscus was compared with their molded counterparts through physical characterization (X Ray-CT, surface-profilometry, light-microscope, scanning electron microscopy, PBS absorption test), chemical characterization (FTIR, TGA/DSC, XRFS), mechanical characterization (compression tests, tensile, cyclic compression tests, failure tests) and biocompatibility characterization (proliferative and cell-viability assays). Results indicate that the silicone 3D Printing process does not alter the overall physical, biochemical, mechanical or biocompatible properties of the silicone meniscus implant printouts. Both the chemical and thermal stabilities of Ecoflex silicone rubber were demonstrated by FTIR and TGA/DSC, respectively. At all strain rates, Eco50 silicone meniscus implants and standard samples consistently showed higher stiffness and high modulus when compared to their Eco30 counterparts. Finally, cytotoxicity tests showed that both Eco30 and Eco50 silicone implants are safe for fibroblasts.

Finally, the prospects and challenges of this 3D Printed meniscus are explored. Challenges arising from MRI DICOM file conversion to CAD STL format, in particular during segmentation, are discussed. Further potential of 3D printed meniscus was explored in 2 designs, namely drug-delivery reservoir channel and shape memory. A safe way of incorporating micro-channels and reservoir using mixed molten sugar-honey sacrificial mold is also discussed. The proof-of-concept of shape-memory property incorporation using TPU, into the silicone meniscus is also demonstrated.

ACKNOWLEDGEMENTS

This work is dedicated to the memory of my grandparents.

First of all, I would like to thank my parents, my sister, my wife and my son for their everlasting love and encouragement in my pursuit of excellence.

I would like to express my heartfelt gratitude to Professor Chua Chee Kai for giving me this unique opportunity to pursue my research in Singapore Centre for 3D Printing, NTU. I am also indebted to my mentors Professor Low Yin-Peng at TTSH and Dr Daniel Tan at AH, who always have faith in me all these years.

I also acknowledge the research funding received from the SC3DP and the Singapore Prime Minister's office.

My deepest appreciation also goes to my supervisors Associate Professor Yeong Wai Yee and Assistant Professor Song Juha, for all their incredible support and guidance throughout the course of my research, and who have made my journey even more meaningful. I would also like to thank Associate Professor Chou Siaw Meng and Professor Ming C. Leu for being members of my Thesis Advisory Committee.

I am also very grateful to Dr. Matthew Pan, for his great help, friendship and dry humor and a continuous source of encouragement. I also would like to thank Mr Edmund Lim, Dr An Jia, Dr Sing Swee Leong, Dr Shweta, Mr Daniel Yeo, Mr Wong Hang Kit and all my friends, GuoDong, GuoLiang, Cher Fu, Joel, ZhengKai, Lewei, Daniel, Anil, Son, Yiling, Keith, all SC3DP staff and all the laboratory specialists from School of Mechanical and Aerospace Engineering, Nanyang Technological University, who have all helped to make this possible.

TABLE OF CONTENTS

LIST OF FIGURES

LIST OF TABLES

LIST OF SYMBOLS

a_i	Correction constant coefficient
a_j	Coefficient for linear effect
a_{ii}	Coefficient for quadratic effect
a_{ij}	Coefficient for interaction effect
G’	Storage modulus
G’’	Loss modulus
F	Test statistic
P	Probability
x_i	Independent variable
x_j	Independent variable
R^2	Data fit

LIST OF ABBREVIATIONS

3D	3 Dimensional
AM	Additive Manufacturing
ANOVA	Analysis of Variance
ASTM	American Society for Testing and Materials
CMI	Collagen Meniscus Implant
DICOM	Digital Imaging and Communications in Medicine
DSC	Dynamic Scanning Calorimetry
DTG	Derivative Thermogravimetric Graph
FTIR	Fourier Transform Infrared
GAG	Glycosaminoglycans
ISO	International Organization for Standardization
LSR	Liquid Silicone Resin
MCCS	Micro-channeled cellulose scaffold
MRI	Magnetic Resonance Imaging
NEMA	National Electrical Manufacturers Association
PBS	Phosphate Buffer Solution
PDMS	Polydimethylsiloxane
SEM	Scanning Electron Microscopy
SF	Silk Fibroin
SMP	Shape Memory Polymer
STL	Stereolithographic
TGA	Thermogravimetric Analysis
VAS	Visual Analogue Score
XRCT	X-Ray Computed Tomography
XRFS	X-Ray Energy Fluorescence Spectrometer

LIST OF PUBLICATIONS/PATENTS

1. Y. H. Li, E. Luis. 3D Printing of Medical Models from CT-MRI Images. *Partridge Publications* **2016**

2. E. Luis, H. M. Pan, A. Bastola, R. Bajpai, S. L. Sing, J. Song, W. Y. Yeong. Validation and Characterization of Post 3D-Printed Silicone Meniscus Implants. *3D Printing and Additive Manufacturing* **2019** (undergoing review)

3. E. Luis, H. M. Pan, S. L. Sing, A. Bastola, G. D. Goh, G. L. Goh, H., K. J. Tan, R. Bajpai, J. Song, W. Y. Yeong. Silicone 3D-Printing: Process Optimization, Product Biocompatibility and Reliability of Silicone Meniscus Implants. *3D Printing and Additive Manufacturing* **2018** (revision by author)

4. E. Luis, H. M. Pan, R. Bajpai, S. Agarwala, J. Song, W. Y. Yeong. 3D Direct Printing of Silicone Meniscus Implant Using a Novel Heat-Cured Extrusion Based Printer. *3D Printing and Additive Manufacturing* **2019** (undergoing review)

5. E. Luis, et al., **2018** A Review of Medical Silicone 3D-Printing Technologies and Clinical Applications. *Journal of Orthopedic Research and Therapy. JORT-1104 DOI*: 10.29011/2575-8241.001104

6. E. Luis, W. Y. Yeong, J. Song, H. M. Pan, S. L. Sing. Silicone Meniscus with Slow-Released Mechanism. *Provisional Patent No:* **2018-265-01-SG PRV**

7. E. Luis, H. M. Pan, S. L. Sing, H. K. J. Tan A., G. D. Goh, G. L. Goh, H., J. Song, W. Y. Yeong. Silicone 3D Printer. *Technology Disclosure No*: **NTU 2019-061**

8. E. Luis, H. M. Pan, J. Song, W. Y. Yeong
Shape-Memory (medical grade) Silicone Technology. *Technology Disclosure No*: **NTU 2019-065**

Chapter 1 – Introduction

This chapter provides the background, motivations, objectives and scope of the work. The background discusses the human meniscus, meniscus injuries and the challenges facing current treatment options. It highlights the capability of the current innovative extrusion based 3D printer to directly print silicone meniscus implant prototypes using medical grade silicones. The main objective and scope of this work are to characterize the medical grade silicone resin, develop and optimize this 3D silicone printer and directly print a silicone meniscus implant. The report organization gives an overview of the content of this thesis.

1.1 Background

The meniscus is one of the most important stabilizing and weight-bearing cushion within the knee. The meniscus is also most commonly torn as a result of knee injuries in the younger population and meniscal degeneration in the elderly. Its relative mobility within the knee joint predisposes it to trauma and injuries, making it the most frequently damaged structure within the knee. The surgical success rates of all previously tried techniques using sutures, fibrin glue and staples, were compromised by the sparse blood supply to the central meniscal region. Subsequently, the current gold standard of treatment for meniscal tear is partial meniscectomy, which partially removes the damaged meniscus, thus leaving behind the intact structure. This however has detrimental effect of tripling the force at the point of contact between the cartilaginous surfaces of both the femoral condyles and tibia plateau, thus predisposing the knee to premature osteoarthritis [1].

In the USA each year there are about one million cases of knee surgeries involving the meniscus. There is therefore a significant clinical demand for meniscal implant replacement, which can help retard the progression of osteoarthritis [2] and reduce the number of unnecessary knee replacement surgeries.

Current methods in tissue engineering, which have been tried for meniscal scaffold production include using Polycaprolactone (PCL), Poly (L-co-D,L lactic acid) PLDLA, hydrogels, 3D methacrylated gelatin (Gel MA), silk fibroin, bacterial cellulose and micro-channelled cellulose scaffold (MCCS). However these biological or synthetic scaffolds are marred by problems of inferior mechanical properties, poor cellular proliferation, slow extracellular matrix integration and scaffold dislodgement. All these problems preclude instantaneous weight bearing and rehabilitation. Partial and total meniscal implants have therefore been produced to overcome these challenges.

The two partial meniscal implants which are currently available commercially are Collagen Meniscus Implant-CMI (Menaflex) and Actifit. The former is a biological implant derived from Type I bovine Achilles' tendon while the latter is manufactured from 80% polycaprolactone and 20% stiff urethane. Presently the only total implant available worldwide is the NUSurface total meniscal implant, which is made from polycarbonate urethane reinforced circumferentially with high molecular weight polyethylene fibres. The two major drawbacks of these meniscal implants are their fixed geometrical dimensions with no option for customization and their sole application in

chronic meniscus injuries. Moreover, these partial implants have to be cut to be implanted. Until recently, there remains a huge obstacle to find a biocompatible and bio-implantable material which is directly 3D printable and demonstrate similar biomechanical properties to the native meniscus.

With the advancement of key-hole surgeries, almost all knee meniscal pathologies now can be managed arthroscopically and there is a resurgence of great interest in replacing the missing or defective meniscus. It is for this reason the direct 3D printing of a silicone meniscus implant which can replace the torn segment of the meniscus and which also permit immediate customised fitting, weight bearing and rehabilitation is pursued.

Since Lahey first used silicone drainage tubes in 1946, silicone still stands out as one of the best material for implants since it is versatile, biocompatible, hypoallergenic, ozone and UV safe and thermally stable. Currently liquid silicone rubbers have been used for the manufacture of silicone medical disposables items and silicone implants. Medical grade silicones have been chosen here for their bio-compatibility and bio-implantability. Medical grade silicones have the added advantages over other elastomers in that they are bioinert, resilient, capable of withstanding a wide range of sterilization methods and maintaining their mechanical properties at extreme temperature ranges.

Conventionally, silicone is manufactured by molding or indirect casting where a mold is 3D printed followed by conventional casting. Direct additive manufacturing (AM) of non-medical grade silicones was not possible until recently as described by Hinton, Fripps [3], ACEO, Liravi, Plott and Shih. However, direct 3D printing of medical grade silicone has not yet been explored. A few non-medical grade silicone AM technologies have been described in the last two years. For instance, Hinton described the Freeform Reversible Embedding Technique of Sylgard silicone, Fripps described the catalyst extrusion into a bath of silicone oil [24], ACEO described the drop-on-demand principle and UV-cured technology to print multi-material part silicones [4], Plott and Shih described the extrusion of moisture-cured silicone [5]. Liravi F and Toyserkani T described the use of UV curable silicone [6].

Extrusion method is chosen to allow for composite printing of different viscosities of silicone or combination of printing of different materials, ease of heating control at various stages of extrusion and therefore degree of gelation. Using a custom-built extrusion-based 3D printer, direct 3D printing of a human knee meniscus was carried out successfully for the first time, as a proof-of-concept, using heat-curable two-part silicone Ecoflex. The processes of rheological characterization of medical grade silicone resin, silicone printer hardware and software assembly, extruder and stepper drive calibration, Digital Imaging and Communications in Medicine (DICOM) file management and printing parameters setting, are described in later chapters.

The immense benefits of direct 3D printing of silicone medical implants or devices can be extended to neurosurgical, plastic and reconstructive, ENT, general surgical and other fields of medicine.

1.2 Motivation

A damaged meniscus, due to trauma, degeneration or surgery, grossly alters the biomechanics of the knee and predisposes the knee to developing premature osteoarthritis and necessitating total knee replacement surgeries. There is therefore unmet clinical and research need for an ideal implant replacement for the meniscus.

Being a biocompatible and bio-implantable material, the medical-grade silicone rubber still stands out as the best option for use in the production of meniscus implants, when compared to other elastomers.

Nevertheless, silicone medical disposables, implants and devices are currently still manufactured by the traditional processes of molding or indirect casting which are expensive and time-consuming. The geometrical precision and aesthetic parameters of the end-products are also highly operator-dependent.

Current advances in 3D silicone AM technologies, which will be discussed in detail in Section 2.3, have not been shown to be capable of directly 3D print medical grade silicones, all of which are heat-curable only.

1.3 Objectives

The main objectives of this research are:

1. To design, manufacture and optimize a novel extrusion-based 3D silicone printer with unique heating processes. The optimization of various printing parameters and printing processes will be studied by conducting design of experiments (DOE). This silicone printer will be able to perform Liquid Additive Manufacturing with different ranges of medical and non-medical grade silicones.

2. To 3D print a customized meniscus which has comparable biomechanical properties as those of the native meniscus. In a future design to the 3D printed meniscus, micro-channels and reservoirs will be incorporated into the meniscus to provide slow release mechanism for drugs, lubricants and growth factors.

3. To incorporate shape memory properties into currently commercially available liquid silicone rubber.

1.4 Scope

The scope of this research covers the following areas:

1. Rheological characterization of medical grade silicone resins, which are biocompatible and bio-implantable, using temperature sweep modes and frequency sweep modes, to understand the viscoelastic properties of the various silicone resins and to determine the optimal gelation times and curing temperatures for nozzle and printer bed heating.

2. Design, develop and manufacture of a functional 3D Silicone Printer and Nozzle which is able to directly 3D print medical-grade silicones. This involves using the rheological results obtained above, open source hardwares - RAMPS 1.4 and Arduino Mega and open source softwares - Repertier-Host and Marlin Firmware to design and manufacture a silicone printer prototype.

3. Optimize the 3D printing parameters (temperature, nozzle diameter, printing and extrusion speeds, extrusion height, flow rate) and heating processes for direct 3D printing of medical grade silicone, by the application of Design of Experiments (DOE) methods and statistical analysis. A full factorial design is used to investigate the single

and combined effects of the various printing parameters and to narrow down the ranges of values which can optimise the printing process.

5. Design, develop and 3D print meniscus implant prototype with channels and reservoirs to provide slow-release mechanism. Perform ASTM standard mechanical testings of silicone samples and silicone meniscus implants.

6. Design and incorporate shape-memory properties into the silicone meniscus implant.

1.5 Organization of the Report

This report consists of seven chapters.

Chapter 1 introduces the background, objectives and scope of this research.

Chapter 2 comprises literature review in three sections. The first section covers the most recent development in meniscus, meniscal scaffolds and meniscal implants. The second section covers the silicones, its chemistry, curing mechanisms, uses, its grade products and silicone implants. The final section presents the state-of-the-art silicone 3D printing technologies.

Chapter 3 presents the methods and materials used in the rheological characterization of the silicone resin and in the design followed by the development of the silicone 3D Printer. This is followed by a detailed description of the file conversion of MRI DICOM file to STL format and extrusion-based heat-cured printing processes. A preliminary selection of printing parameters is also presented. Finally, the mechanical characterization and determination of biocompatibility of the standard Ecoflex silicone samples, as prescribed by ASTM and ISO standards, are presented.

Chapter 4 presents the optimization of the printing parameters. The effects of critical printing parameters such as print speeds, nozzle diameters, nozzle temperatures and bed temperatures on printing, are analysed. The interaction of the above printing parameters are determined using Design of Experiment for Regression Analysis and Analysis of Variance of Printing Parameters.

Chapter 5 presents a detailed characterisation of 3D Printed silicone meniscus. Firstly, physical characterisation of the silicone meniscus are performed using X-ray-CT, surface profilometry, SEM and PBS absorption Test. Secondly, biochemical characterisation of the silicone meniscus are performed using FTIR, DSC, TGA, DTG and XRFS. Thirdly, mechanical characterisation is performed for Weibull failure analysis. Finally, the biocompatibility cytotoxicity test is performed via the Extraction Method (ISO 10993-12).

Chapter 6 presents the potentials and challenges in 3D printing of silicone meniscus. The first section presents a detailed preparation of the 3D printed meniscus STL file from Magnetic Resonance Imaging DICOM file, followed by the design of micro-reservoir and micro-channels within the silicone meniscus. The second section presents the incorporation of shape-memory properties within the silicone meniscus. The challenges of file preparation and shape-memory incorporation are discussed.

Finally, Chapter 7 presents the conclusion of the current work and future works to be done.

Chapter 2 - Literature Review

This chapter has three sections. The first section provides a comprehensive review of the human meniscus, the meniscus scaffolds and meniscus implants. The second section reviews the chemistry, crosslinking mechanisms and uses of silicone rubbers. The third section provides a detailed review on the state-of-the-art silicone printing technologies.

2.1 The Human Meniscus, Meniscal Scaffolds and Implants

2.1.1 Introduction

This section firstly discuss the anatomy, biochemical and mechanical properties of the meniscus and the effects of knee movements and meniscectomy (surgical removal of meniscus) on load transmissions across the knee joint. Secondly, absorbable and permanent scaffolds which have been experimented by different researchers to replace the injured meniscus, are discussed. Finally, commercially available partial and total meniscus implants are presented.

2.1.2 The Anatomy and Biomechanical Properties of Meniscus

(1) Meniscal Anatomy

The meniscus is a pair of fibrocartilaginous cushion which sits on the tibia plateau in the knee joint. They act as knee cushions which transmit body weight evenly across the knee joints, thus minimizing contact stresses between femur and tibia and damages to the articular surfaces [7]. Meniscal injuries and partial meniscectomy (partial removal of meniscus as the acceptable conventional treatment for meniscal tear) predispose the knees to developing premature osteoarthritis [8]. The anatomy of the meniscus is shown in **Figure 1**.

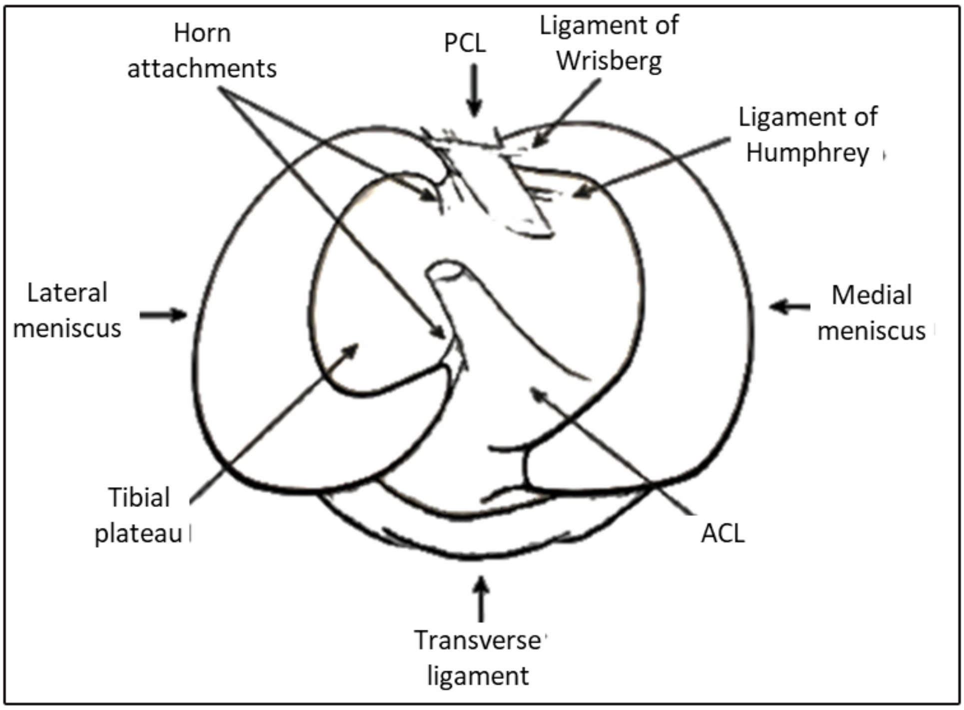

Figure 1 The meniscus anatomy [9]

The meniscus is divided into three zones, the outer red-red vascular zone, intermediate red-white zone and the inner white-white avascular zone. Spindle-shaped cells and chondrocyte-like cells occupy the outer and inner zones, respectively.

The meniscus obtains its limited blood supply from the peri-meniscal capillary plexus within the synovial and capsular tissues of knee. These plexus are branches of the medial and lateral geniculate arteries and extending for one to three millimeters over the articular surfaces of menisci. The blood supply to meniscus is age dependent. In adult, tears which occur at the most vascularized, peripheral 3 millimeters of the menisci (red-red region) are most amenable to repair and cellular regeneration, as opposed to the generally avascular tears, which usually occur in the white-white region, greater than 5 millimeters from the menisco-synovial junction, which are not reparable. For both the medial and lateral menisci, the vascular penetration is about 10-30 %. The regional variation in visualization is shown in Figure 2.

(2) Meniscal Composition and Cell Characteristics

The meniscus has a highly heterogeneous mix of extracellular matrix (ECM) and cellular distribution, as shown in **Figure 2**. The meniscal ECM is categorized by region. More than 80 % of the red-red region is composed of type I collagen by dry weight and the remaining 20 % comprises collagen of other types. In the white-white region, total collagen comprises 70 % of dry weight, with collagen types II and Types I accounting for 60 % and 40 %, respectively [1].

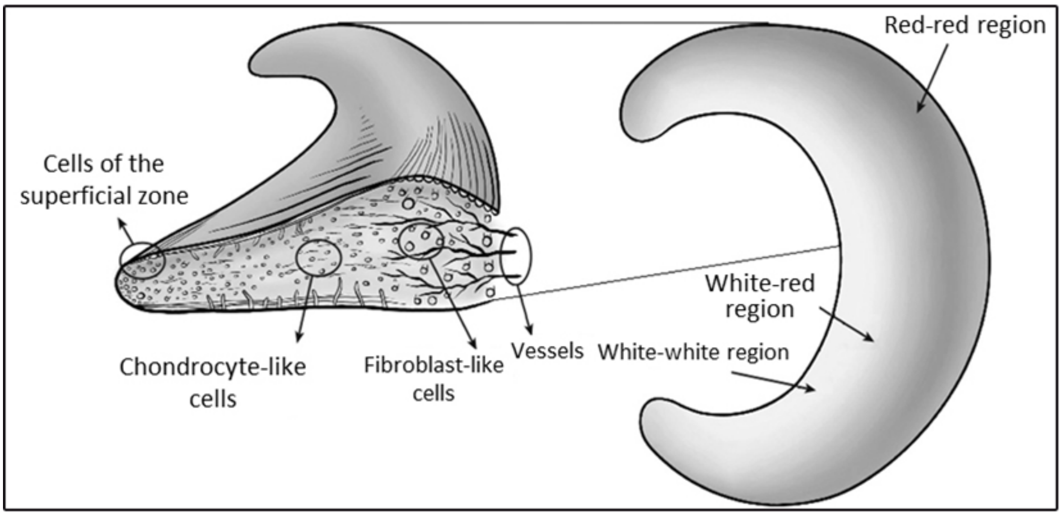

Figure 2 Regional cellular and vascular distribution of the meniscus [9]

(3) Meniscal Lesions and Development of Knee Osteoarthritis

Meniscal injuries can eventually lead to knee osteoarthritis and the vicious cycle of inflammation process induces further meniscal tears. An injured meniscus triggers the synovium to release various inflammatory cytokines, which further provoke degenerative changes within the matrix body and cause meniscal extrusion from the knee joint. These extrusions increase the stress on the tibia cartilage and further aggravate the injury [10]. Similarly, the collagen fibres are arranged randomly in the most superficial region, radially in the middle layer and circumferentially in the innermost layer. The circumferential fibers provide hoop-stress against the compressive loads exerted across the knee-joint. The collagen fiber distribution is shown in **Figure 3**.

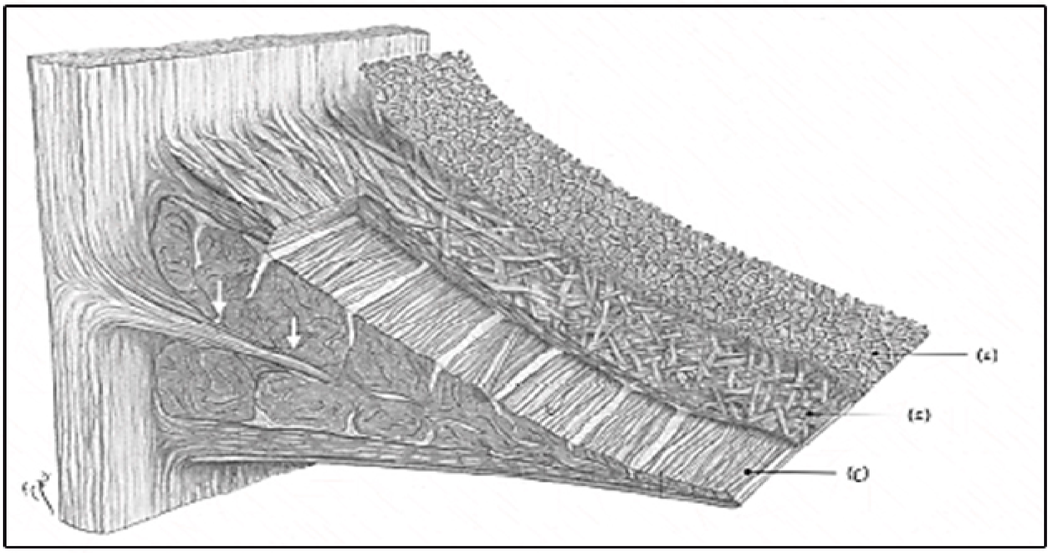

Figure 3 Ultrastructure of collagen fibers within the meniscus. Random arrangement in superficial layer, radial arrangement in middle layer and circumferential arrangement in the innermost layer [31]

(4) Meniscal Injury Patterns

All meniscal lesions can be classified into eight categories according to the Casscell's classification, namely i) vertical longitudinal (bucket handle), ii) vertical transverse (radial), iii) horizontal tear (cleavage), iv) oblique tear (flap), v) detachment of meniscal horns, vi) complex tear, vii) degenerative and viii) miscellaneous (discoid).

However, for therapeutic purposes, the meniscal injuries can simply be classified clinically into peripheral vascular and central avascular lesions. The pattern of meniscal lesions is also age-dependent. Traumatic injuries in the young and athletes usually result in longitudinal tear patterns or vertical radial full thickness tears pattern. These tears usually occur in the vascular red-red zones and are therefore more amenable to repair. On the contrary, degenerative tears in the elderly are usually horizontal, intra-substance and complex in nature. These lesions are less amenable to repair [11].

(5) Meniscal Treatment Options

Conventional treatments include conservative treatments, meniscal repairs, partial meniscectomies, total meniscectomies, partial meniscal substitute replacements, porous meniscal implants or total artificial meniscal replacements, allograft and autograft meniscal transplantations [12].

A partial meniscectomy is usually performed for irreparable or degenerative meniscal lesions. However, partial meniscectomy reduces the effective contact area between the femoral condyles and tibial platform and disproportionately increases the contact forces, predisposing the knee to osteoarthritis [12].

Consequently, more emphasis is placed on meniscal repair and reconstruction techniques. Repair procedures range from all inside, inside-out and outside-in techniques [13]. Meanwhile, reconstructive strategies restoring meniscal functions such as meniscal allografts, small intestinal submucosa (SIS) implants [14] and autogenous tendon grafts [15] have also been experimented [16].

The first free meniscal allograft transplantation, performed by Milachowski and Wirth in 1984, reduces pain and improves knee functions in young patients after a short follow-up. However, its chondro-protective effects have not been proven. Concerns of disease transmission, graft shrinkage and deteriorating material properties have hindered its widespread use [17]. Similarly, SIS [14] and autogenous tendon grafts [15] have given poor results.

(6) Mechanical Properties and Force Transduction of Meniscus

From Table 1 below, it can be seen that the posteromedial region of the meniscus has the lowest compressive properties and tensile modulus. These may be due to the lower proteoglycan content within this region, resulting in a lower charge density and lower resistance to deformation under compressive load. Proteoglycans and collagen fibers contribute to the compressive modulus and tensile stresses of the meniscus, respectively. These results, together with the relatively immobile posterior horns of the meniscus as shown above, would explain the predominance of traumatic tears in these regions.

Table 1 Compressive Modulus and Tensile Stiffness of the Human Meniscus [1, 18]

Study of the Human Meniscus	**Compressive Modulus (MPa)**	**Circumferential fibres Tensile Stiffness (MPa)**
Medial Superior		(Lateral meniscus)
Anterior	0.15 ± 0.03	124.58 ± 39.51
Central	0.10 ± 0.03	91.31 ± 23.04

Posterior	0.11 ± 0.02	143.73 ± 38.91
Medial Inferior		(Medial meniscus)
Anterior	0.16 ± 0.05	106.21 ± 77.95
Central	0.11 ± 0.04	77.95 ± 25.09
Posterior	0.09 ± 0.03	82.36 ± 22.23

(7) The Effect of Knee Flexion on Knee Contact Area and Joint Forces

The menisci occupy 60 % of the total contact areas between femur and tibia and distribute forces evenly across the knee joint. The contact area decreases 4 %, for every 30° of knee flexion with simultaneous increase in contact forces.

The knee meniscus transmits about 50 % and 85 % of the body weight, in full extension and in 90° flexion, respectively. In full knee flexion, the lateral meniscus and medial meniscus transmit 100 % and 50 % of the load respectively. It was found that meniscus micro motion during knee flexion permits optimal conformity during knee flexion and minimizes rotational injury.

With a weight-bearing dynamic MRI to study meniscus movement, Vedi *et al.* [19] found that while the anterior horns of the medial and lateral menisci moved through an average displacement of 7.1 mm and 9.5 mm, respectively, the posterior horns of the medial and lateral menisci only moved through an average displacement of 3.9 mm and 5.6 mm, respectively. The mediolateral radial displacement is 3.6 mm and 3.7 mm for the medial and lateral meniscus, respectively.

Its relative immobility makes the posterior horn of the medial meniscus more susceptible to injury. Being a secondary knee stabilizer, the meniscus confers significant stability in the ligament-deficient knees by virtue of its attachment anteriorly to the transverse ligament, peripherally to the capsular ligaments and centrally to the inter-articular area of the tibia. The meniscus may be torn centrally or peripherally as a result of misdirected rotatory force [20, 21].

(8) Contact Forces after Meniscectomy (Removal of Meniscus)

Following a total meniscectomy, total contact area decreases by 50 % and peak local contact load increases by 300 %, as reported by both Paletta *et al.* [22] and Kurosawa *et al.* [23].

2.1.3 Absorbable and Permanent Scaffolds

Meniscal scaffolds are mostly synthesized by tissue engineering techniques [10, 11].

Meniscal scaffolds can be categorized into 2 main groups: absorbable (degradable) and permanent. Absorbable scaffolds can be further classified into synthetic or natural scaffolds. Permanent scaffolds include allograft, xenograft and decellularised meniscal scaffolds. The radiological, arthroscopic, clinical outcomes studies for each category are examined below in short (up to 2years), medium (2 to 5 years) and long term studies (10 years and above) [24, 25, 26, 12].

(1) Absorbable synthetic scaffolds

Polyurethane, polyglycolic acid and polycaprolactone are the most commonly used absorbable synthetic materials in the fabrication of meniscal scaffolds [27]. The mechanical properties, architectural orientation and scaffolds bioactivity can be further enhanced with PGA or polyethylene terephthalate (PET) [28, 29,10].

Polyurethane is a highly porous, thermoplastic and biocompatible elastomer template which is able to bridge torn tissue in the red-red zone of the meniscus. Since it only degrades in 4 years, it is ideal for tissue engineering.

Verdonk *et al.* examined arthroscopic acellular polyurethane scaffold replacement in 52 patients who had partial meniscectomy. Cartilage stability was observed in 92.5% of the patients. 3 had cartilage degeneration and 9 had scaffold failure due to arthroscopic fixation failures [30]. Esposito *et al.* reinforced PLDLA with PCL in a 90 to 10 ratio (w/w) [31]. The polyester polymer scaffold was seeded with fibro-chondrocytes and implanted into NZ white rabbits. It is anchored at both meniscus horns using nylon sutures. At 12 and 24 weeks, the scaffold showed similar cellular distribution, circumferentially and radially, as the native meniscus. Koller *et al.* increased the bioactivity of HA/PCL scaffold by adding PET [32]. Koller also bonded PGA with PLGA (75:25) to produce meniscus-like scaffold. After seeding with allogenic meniscal cells, the regenerated menisci had similar biomechanical properties as the native menisci [33]. Meanwhile, Baker *et al.* electrospinned aligned scaffolds which are able to direct cell growth and has similar biomechanical properties as native meniscus [6]. Fisher *et al.* electrospinned circumferential scaffold and observed that the seeded bovine stem cells in the scaffolds resulted in circumferential cellular arrangement similar to that seen in native meniscus [3]. Chiari *et al.* used hyaluronic acid (HA) and polycaprolactone (PCL) in scaffolds to repair total and partial sheep meniscus defects [35]. In the absence of cell seeding, the implant still remained in position for 6 weeks with eventual successful integration of implant into native tissues.

Actifit implant is an acellular, synthetic, bioabsorbable meniscal scaffold composed of 80 % polycaprolactone (PCL) and 20 % polyurethane (PU). PCL can take 5 years to degrade by ester bond hydrolysis, while PU gets phagocytosed or integrated with the surrounding tissues over a long period of time. The interconnected pores encourage vessel ingrowth and meniscus regeneration. It is used clinically to treat partial meniscal lesions. Dynamic contrast MRI showed successful tissue ingrowths into scaffold 3 months in 81.4% patients. Despite having normal chondrocytic penetration into the substrate within a year, Baynet *et al.* reported all patients still needed at least 2 years to resume normal function [36].

In the short-term preclinical canine studies, Tienan *et al.* [37] and Klompmaker *et al.* [38] showed that there was complete vascular infiltration into the scaffold which had integrated with peripheral capsule, without inciting foreign body reaction. Verdonk *et al.* studied 52 patients with implanted PU scaffold after partial meniscectomy also showed 81.4% (35 of 43 implanted menisci) had stable cartilage at three months after tissue ingrowth with dynamic contrast-enhanced MRI. At two-year follow up, there was statistical significant improvement in all knee outcome clinical scores [30]. Similarly, in a two-year follow up by Efe *et al*. of 10 patients with PU meniscal scaffolds, all patients had improved knee outcome scores and satisfactory MRI findings on the scaffold and articular cartilage. One case of scaffold resorption and scaffold extrusion did not affect overall clinical outcome [39].

Kon *et al*. also reported outcome improvement using the IKDC and Tegner scores two years post-surgery. However, different clinical outcomes were observed if patients received other additional procedures such as realignment osteotomy, ligamentous, bony or chondral procedures [40, 41].

To show a similar degree of safety and effectiveness on the lateral knee compartment, Bouyarmane *et al*. also demonstrated improved pain scores on visual analogue scores

(VAS) and function outcome scores when PU was used in the lateral meniscus at two-year duration [42].

It was very important to note that there was no medium or long term studies to follow up on patients who had received absorbable synthetic scaffolds. A possible explanation was that most of these synthetic scaffolds had failed early during anchorage or while integrating with the tissue matrix before 2 years duration. Those patients who had regained function by 2 years would not return for further follow-up, while those patients with scaffolds which failed before 2 years would have been excluded from the studies.

(2) Absorbable biological scaffolds

Absorbable biological scaffolds, whether ECM-related or biological, were derived from Bovine Achilles' tendon, Collagen Meniscus Implant (CMI), silk fibroin, bacterial cellulose and Micro-channeled cellulose scaffold (MCCS) [28, 29, 10].].

Collagen Meniscus Implant comprised purified type I collagen isolated from bovine Achilles' tendon and glycosaminoglycans (GAGs). GAGs included chondroitin sulphate and hyaluronic acid. Chemical crosslinking and sterilization were done with formaldehyde and gamma-radiation, respectively.

In short-term studies of 2 years or less, Stone KR *et al.* showed that CMI supported new tissue ingrowth and assimilation over time. As it was being reabsorbed, CMI was gradually being replaced with immature collagen over 3 to 6 months in a phase I clinical feasibility study [43]. Reguzzoni *et al.,* after 6 months following CMI implantation, also demonstrated the proliferation of blood vessels and fibroblasts like cells [44]]. Rodkey *et al.,* in a two-year follow-up of eight CMI patients, showed that CMI was able to promote new tissue regeneration and symptomatic improvement [45]. Moher *et al*. also reported improvement on all clinical scores at two years when CMI was used in the lateral joint space [46].

In medium term studies, between 2 to 5 years, Bulgheroni *et al.* showed improvement in Lysholm and Tegner scores in 28 CMI patients. Radiographic evaluation did not show any failure at 5 years [47]. Steadman *et al*. at 5.8 years follow-up also reported improvement in Mean Lysholm and Tegner Activity Scores. MRI also showed preservation of chondral surfaces. Biopsies evaluation also did not revealed any evidence of infection, inflammation or immune reaction. On second look arthroscopy, it was estimated 60 % of meniscal defect was filled by the scaffold [48].

In a long-term 10-year follow-up of 25 CMI patients, Monllau *et al*. reported better pain relief and functional improvement, with significant improvement in Lysholm and VAS pain scores [49]. Zaffagnini *et al.* also obtained similar results in a 10-year follow-up [50].

Despite the limited studies above, Rodkey *et al.* conducted the only prospective multicenter randomized control trial comparing the clinical results of CMI with partial meniscectomy. 311 patients were followed-up at 4.9 years [45]. The patients were first divided into acute and chronic groups. The former had no prior meniscus surgery while the latter had previous meniscus surgery. They were then randomized to receive CMI or partial medial meniscectomy (control group). In the chronic group, biopsies of CMI performed at one year post-op showed that the implant was able to stimulate meniscus-scaffold matrix formation by the host. Patients regained more mobility and require fewer reoperations than in the chronic control group. However these improved clinical outcomes were not reflected in the acute groups.

There was also 2.7 times greater risk of reoperation in (acute group) patients with partial meniscectomy when compared to the CMI group.

Silk, which comprised fibrous proteins, were commonly used to tissue-engineer articular cartilage, ligaments and bones. Silk fibroins (SF) were selected for their biosafety profile, biocompatibility, versatility and biodegradability. Mandal *et al.* used silk fibroin from Bombyx mori silkworm cocoons to produce a multilayer, multiporous meniscal scaffold, with its external and internal layers seeded with fibroblasts and chondrocytes, respectively. The final scaffold product had an architectural morphology and cellular distribution similar to that of the native meniscus [51]. Although compressive and tensile moduli increased overtime, they still remained inferior to native meniscus. The durability of the porous scaffold in sheep specimen with medial meniscal defect was shown by Gruchenberg *et al.* to last for at least 6 months, without any macroscopic or histological abnormalities [52].

Yan *et al.* produced porous scaffolds which ranged from 8 to 16 % SF by weight, after leaching with granular sodium chloride and freeze drying. 16 % SF scaffolds were less porous and has a higher mechanical strength at 15.14 ± 1.7 MPa, comparable to that of a native meniscus. A scaffold-repaired defect had a higher failure modulus compared to the unrepaired defect [53, 54].

Bodin *et al.* used bacterial cellulose (BC), a polysaccharide synthesized by Gluconacetobacter xylinus, in blood vessel, cartilage and bone tissue engineering. It was shown that bacterial cellulose was biomechanically superior, highly hygroscopic and crystalline and had good biocompatibility [55]. The compressive modulus of BC at 10 % strain (1.8kPa) was five times higher than that of collagen meniscal implant (0.23 kPa). Martinez et al. showed that besides improving adherence and migration of seeded fibroblasts through the micro-channels, MCCS also facilitated collagen alignment with significantly higher cell proliferative counts than in the unmodified scaffold [56, 57].

Hydrogel scaffolds were made of N-isopropyl acrylamide or alginate. They had been widely used for their safe, biocompatible, viscoelastic, non-cytotoxic and insoluble features. Although their physical properties and versatility allowed for cell mixing and growth factors loading, they were not mechanically strong or bioactive [58]. Kobayashi *et al.* demonstrated encouraging results in rabbit studies when PVA-H meniscus implanted group rabbits was compared with meniscectomy groups in meniscus deficient knee. The group implanted with PVA-H menisci had normal articular cartilage and normal PVA-H implant even after 2 years post-surgery. However, osteoarthritis had set in one year and continued to progress in the meniscectomy group [59, 60].

Using projection stereolithography, Grogan *et al*. fabricated a 3D methacrylated gelatin (Gel MA)-based meniscus scaffold that mimicked collagen alignment [21]. The scaffold was able to direct cell growth after 3 weeks post meniscal cell seeding. Sarem *et al*. fabricated macroporous multilayered gelatin / chitosan scaffold. Chitosan in conjunction with gelatin, enhanced bioactivity of Chitosan and improved the gelatin’ s hydrophilicity of water retention and nutrient transfer [61]. Finally, Ishida *et al.* also showed the combination of PRP and gelatin enhances meniscal regeneration [62].

In conjunction with the positive results above, although the NICE guidelines in 2012 on partial knee meniscus replacement using biodegradable scaffold stated that the latter poses no safety concern, there was insufficient data to support its use over current standard procedures in both short- and long-term relief of symptoms. Thus its use had not been widely accepted. Meniscus allograft transplantation had also been advocated but long-term clinical results had been equivocal [63, 64].

c) Permanent Scaffolds

Permanent scaffolds included allografts, xenografts and decellularised meniscal scaffolds. Allografts and xenografts had similar biomechanical properties as the native meniscus but posed higher risks of disease transmission and immune rejection. They were therefore not accepted for use widely. On the contrary, Sandmann *et al.* had shown that decellularised meniscus scaffolds not only demonstrated good biocompatibility and biomechanical properties, but they also provided suitable regenerative microenvironment and meniscal geometry [65].

Acellular scaffolds can be obtained via physical, chemical, biological or combined methods of decellularisation. Physical means employ freeze thawing and sonication. Chemical decellularisation involved using detergents such as Sodium Dodecyl Sulfate (SDS), Ethylenediaminetetraacetic acid (EDTA), Triton X-100 or hypotonic buffers. Biological decellularisation used enzymatic digestion.

The vital steps were to retain as much collagen network and glycosaminoglycans content as possible, the former contributing to the tensile strengths while the latter contributing to the compressive strengths of the meniscus. In combination, both components maintained the viscoelasticity of the system [66, 67, 68].

Sonication methods and detergents had been used successfully to lyse cells without affecting the extracellular matrix [69]. Collagenase treatment created micro-pores within menisci but similar to sonication, it could denature GAGs and affect the compressive properties of the meniscus, as shown by Azhim *et al.* [70, 65]. Subsequently, Stabile *et al.* tried to improve scaffold porosity by applying oxidation [71]. Similarly, although SDS was effective in retaining collagen fibers while removing cells, it also removed GAGs from the proteins in the ECM, and adversely affected cellular ingrowth and tissue regeneration.

Fibro-chondrocytes [72], chondrocytes, fibroblasts, Bone Marrow Mesenchymal Stem Cells (BM-MSC) [73], were excellent cellular sources to seed the acellular meniscal scaffold. An optimal culture combination of meniscal cells and human Mesenchymal Stem Cells (hMSC) in a 3:1 ratio best preserved the meniscus integrity by promoting greatest synthesis of essential molecules. However, the thick fibrous collagen fibres in the ECM may also pose difficulties for cellular infiltration into the inner regions of the implanted meniscus [53].

2.1.4 Animal Studies for Meniscal Scaffolds

The following is a review of using sheep, dog and rabbit animal models to demonstrate the longevity and functionality of the meniscal scaffolds.

In sheep models, Martinez *et al.* [57] showed increased revascularization and scaffold remodeling at 3 months using collagen scaffold and autologous chondrocytes. Chiari *et al.* [35] also demonstrated superior tissue ingrowth and good mechanical strength in scaffolds made of hyaluronic acid and polycaprolactone.

Kelly *et al.* [58] showed that at 12 months that the outcome of hydrogel scaffold is much inferior to that of meniscal allograft, despite both implant groups showing signs of mechanical failure and significant cartilage degeneration Cartilage degeneration is reduced by Kevlar reinforced polycarbonate urethane scaffold as shown by Zur *et al.* [74]. Gruchenberg *et al.* [52] also showed that the use of silk fibroin scaffold can reduce cartilage degeneration, while inciting minimal inflammatory response.

In dog models, Toyonaga *et al.* [75] and Stone *et al*. [76] demonstrated good results with the use of Teflon and collagen based scaffold for meniscal replacement. Klompmaker *et al.* [38] and DeGroot *et al.* [77] had both shown good mechanical properties and superior regeneration with polyurethane scaffolds. Zhu *et al.* [78] showed faster meniscal regeneration with PLA/PGA scaffold which laden with hCMP-2 lentivirus transfected myofibroblast. In rabbit models, Messner *et al.* [79, 80] showed that recipients of medial meniscus replacement with polyurethane-coated PTFE (Teflon) and polyurethane-coated polyester (Dacron) prosthesis had better 3-month outcomes, in terms of shape retention and tissue ingrowth, when compared to meniscectomy group or uncoated PTFE groups. Interspecies and intraspecies comparison of regional aggregate moduli of the meniscus, performed by Sweigart *et al*. [81] had also showed that human posterior meniscus had the lowest compressive modulus at 0.1 MPa, while lapine anterior meniscus had the highest moduli at 0.45 MPa. These baseline values of compression properties provided the benchmark for future research and therapeutic efforts.

2.2 Partial and Total Meniscal Implants

The following is a review of partial and total meniscal implants [82]. In contrast to meniscal scaffolds, these meniscal implants have similar biomechanical properties as those of the native meniscus.

(1) Partial Meniscal Substitutes

Collagen Meniscus Implant (CMI) and Actifit were the two natural and synthetic porous meniscal implants, respectively, used for symptomatic postmeniscectomy patients, provided that there were residual peripheral meniscus tissues and minimal cartilage damage [38]. These had been in use in the CE European market. However they had not been approved by the FDA. Menaflex, formerly known as CMI, from ReGen Biologics was a natural meniscal substitute [20]. It was made of collagen TYPE I fiber from bovine Achilles tendon, supplemented with glycosaminoglycans to aid cellular ingrowth. It was resorbed over 12 months to 18 months and slowly replaced by the patients' native tissues. It was indicated in patients with meniscal tissue loss or meniscal tears.

Figures 4a, 4b and 4c below show, respectively, the gross implant, scanning electron microscope image and sagittal MRI images of the CMI at 12 months follow-up.

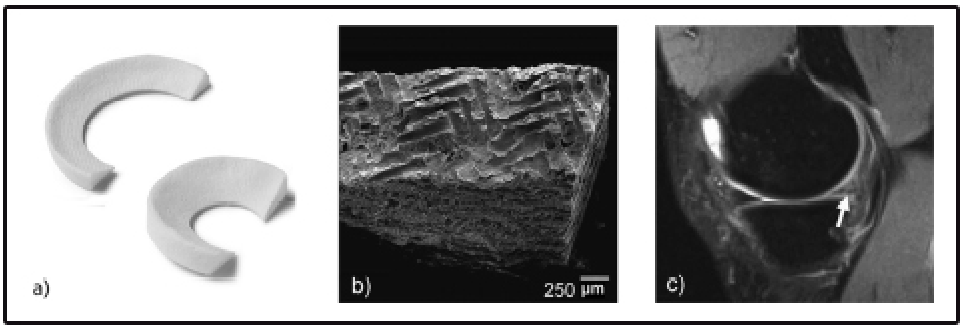

Figure 4 The CMI Partial Meniscal Implant. (a) Medial and Lateral CMI (b) SEM image of collagen within laminae (c) one-year follow-up sagittal MRI image. The white arrow points to the implant

Since 1997, there have been 18 studies showed results on 444 patients using CMI. Steadman *et al.* [48], in a 5.8 year Phase II feasibility follow-up studies of 8 patients, reported marked improvement in both Mean Lysholm and Tegner scores. Second-look arthroscopy shows regenerative tissues filling up 69% of defect and MRI shows no chondral surface degeneration. Zaffagnini *et al.* [50], in a ten-year follow-up cohort study comparing 8 CMI cases and 16 meniscectomy controls, also reported better knee outcome scores, lower VAS pain scores and less medial joint space narrowing in the CMI group. Similarly, Spencer *et al.* [12], in a one-year follow-up of 23 patients who underwent 14 medial and 9 lateral meniscus scaffold implantation, with either Actifit or CMI, reported significant improvement in knee scores post-surgically in 21 patients (93.1%). However, acute meniscus tear cases were not considered. Immediate meniscus load bearing capability and articular cartilage architectural quality were also not investigated. Bulgeroni *et al.* [47], in a five-year follow-up of 28 CMI patients, reported improved Lysholm and Tegner scores and stable radiographic results.

Rodkey *et al*. [45] in a prospective RCT, compared clinical outcomes in 311 patients who received medial CMI implantation and partial meniscectomy. 157 had acute tears and 154 had chronic tears. In both acute and chronic tear groups, pain scores, Lysholm knee scores and self-assessment scores improved from preoperative levels to 6 years postoperatively, but there was no statistical difference in between both tear groups. Overall, CMI implant group had improved knee activity and lower reoperation rates. However, Rodkey *et al.* [81] did not find any statistical significant difference in final clinical outcomes in the acute tear group treated with either CMI implant or simple meniscectomy.

Actifit is a synthetic implant from Orteq Bioengineering, United Kingdom. It is a biodegradable, porous, aliphatic polyurethane consisting of 80 % flexible polycaprolactone and 20 % stiff urethane. It is strong and degrades over 5 years. Its hydrolyzed non-toxic components is either excreted or safely integrated into the native tissue.

Figures 5a, 5b and 5c below show, respectively, the gross Actifit implant, scanning electron microscope images of Actifit and the MRI images of the Actifit implant 14 months post-surgery.

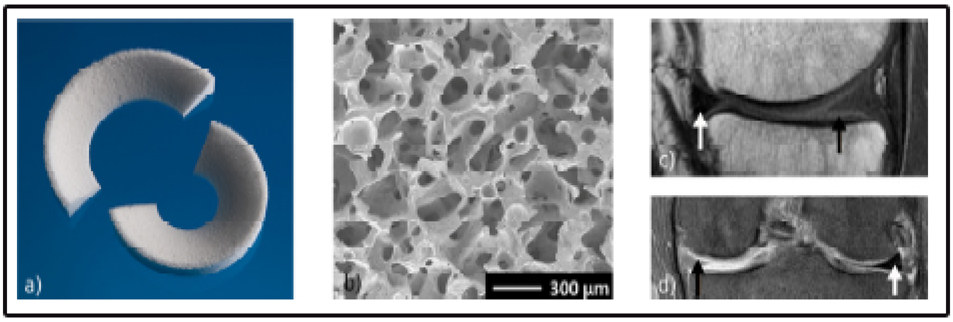

Figure 5 The Actifit Partial Meniscal Implant (a) Medial (top) and lateral (bottom) Actifit implant (b) SEM image shows the interconnected pores of Actifit 14-months post-operative (c) Sagittal and (d) coronal proton density MRI images of the Actifit. The images show preservation of construct architecture, with the Actifit implant emitting homogenous edema-like signal (black arrow) in comparison to native meniscus (white arrow)

Verdonk *et al.* [30] conducted a three-month prospective follow up study of 52 patients (34 medial and 18 lateral lesions) treated with Actifit polyurethane scaffold. MRI in 81.4% of patients and second-look arthroscopy in 97.7% patients showed tissue ingrowth and scaffold integration, respectively. These data showed that tissue regeneration was possible when acellular polyurethane scaffold was used to replace partial meniscus lesions.

Actifit, in contrast to CMI, performed more consistently on second look arthroscopy. It had good ingrowth of immature meniscus-like tissue with implant integration at 12 months. Compared to controls, chronic injury patient group using Actifit implant regained significantly more activity and had fewer reoperations compared to the acute injury group. This contrasted with results from Bulgheroni *et al.* [47] who showed better outcome in patients with acute lesions. Unfortunately, there had not been any randomized controlled trials performed comparing CMI or Actifit with meniscectomy, or any clinical trials directly comparing the two partial implants. Verdonk *et al.* [69] showed that 53 partial meniscectomised knees with ICTS grade < 2, having received Actifit scaffold, had improved pain scores and function 6 months postoperatively. These scores and function continue to improve up to 24 months in 90% of patients. Similarly,

Myers *et al*. [26] showed that Actifit implantation improved clinical outcomes at short-term follow up in patients with chronic post-meniscectomy symptoms of the medial or lateral meniscus. There was currently no medium- or long-term follow-up data. Actifit was found not to be useful in acute meniscal tears.

In a systematic review of scaffolds for partial meniscal replacement, Papalia *et al*. [83] found that both CMI and Actifit scaffold patients showed improved results, at medium term and short term, respectively, when compared to controls, following comprehensive search of medical databases.

Adverse effects seen in partial meniscectomy group, such as progressive cartilage degeneration and medial joint space narrowing, were not seen in CMI implantation group. [84, 69].

(2) The NUSurface Total Meniscus Implant

The NUSurface Meniscus Implant, shown in Figure 6 below, was a replacement indicated for patients with persistent knee pain following medial meniscectomy. The implant was made from polycarbonate-urethane (PCU) – a medical grade plastic. It was currently undergoing two clinical trials in the United States: The SUN (Safety Using NUsurface) trial and the VENUS (Verifying the Effectiveness of the NUsurface System) trial. This total meniscus implant was also useful for those with previous failed meniscus transplantation [64].

Figure 6 The NUSurface Total Meniscus Implant (a) Disc-shaped, free floating NUSurface total meniscus prosthesis. Ring-shaped reinforcement UHMWPE fibers are seen embedded inside (b) Fixation bolts at both ends (c) One-year follow up sagittal MRI image of the NUSurface replacement

Prior to NUSurface, Messner *et al.* introduced the use of Teflon and Dacron biomaterials [80, 81]. VanTienan *et al.* tried porous polyurethane scaffolds to promote tissue ingrowth and cellular differentiation [27]. Kobayashi *et al.* adopted the polyvinyl alcohol (PVA) hydrogels for permanent meniscal replacement. These has similar strength and viscoelastic properties as the native meniscus. However, the clinical durability and longevity results of the hydrogels had not been satisfactory [59, 60].

Kon *et al.* had also developed a porous meniscus scaffold replacement. The combined hyaluronic acid – polycaprolactone matrix was enhanced circumferentially with polylactic acid fibers [40, 41].

In summary, myriad options of biodegradable scaffolds ranging from synthetic (PU, PGA and PCL) to biological (Bovine Achilles' tendon, CMI, silk fibroin, bacterial cellulose and MCCS) were available. Most biodegradable scaffolds were biocompatible and demonstrated satisfactory tissue regenerative capability. However, most were disadvantaged by their obvious inferior mechanical properties, rendering immediate weight-bearing, rehabilitation and ambulation impossible. Meniscus implant slippage and dislodgement were also common postoperative problems which could cause problematic locking of the knees.

To circumvent these problems, we propose direct 3D printing of silicone meniscus implants which are customized for individual patients. A novel silicone 3d printer has also been custom-made to specifically 3-D print silicone meniscus. This silicone meniscus implant has the following unique properties: 1) it is customizable to function either as a partial or total meniscus implant, 2) it can be used for both acute and chronic meniscus injuries, as opposed to the current partial meniscal implants, CMI and Actifit which can only be used in chronic injuries, 3) it allows instantaneous weight bearing, 4) short rehabilitation periods of two to three weeks and 5) it minimizes the problems of infection and host-vs-graft rejection commonly seen in meniscus transplantation cases [63, 64]. After CMI or Actifit implantation, long rehabilitation periods are required to reduce the stress on the mesh-reinforced meniscus implants and to allow tissue in-growth and maturation. The use of 3D printed silicone meniscus can reduce the inconveniences and complications of long rehabilitation periods.

2.3 The Silicone

In 1901, Kipping coined the term "silicone" for the new compounds with generic formula R_2SiO. Commonly, in place of "R" above was a methyl group and the compound was known as polydimethylsiloxane (PDMS). The methyl group could be replaced by phenyl, vinyl and other groups [85].

The combination of organic branch to its inorganic backbone conferred its unique properties of biocompatibility, temperature and electrical resilience.

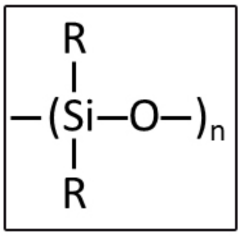

Figure 7 The Silicone generic formula R_2SiO

2.3.1 The Silicone Chemistry

Silicones are synthesized in 3-steps: a) chlorosilane synthesis, b) chlorosilane hydrolysis followed by c) polymerization and polycondensation [4, 86].

(1) Chlorosilane synthesis

In the first step, sand (SiO_2) is reduced at high temperatures to yield silicon metal, as shown in equation (1). In the second stage, methanol is reacted with hydrochloric acid to produce methylchloride, as shown in equation (2). Finally, this methylchloride stream is passed over the fluidized silicone metal powder bed, with a copper-based catalyst, at a temperature of 250°C to 350°C and at pressures of 1 to 5 bars, producing chlorosilane, as shown in equation (3).

$$SiO_2 + 2\ C \rightarrow Si + 2CO \qquad \text{Equation (1)}$$

$$CH_3OH + HCl \rightarrow CH_3Cl + H_2O \qquad \text{Equation (2)}$$

$$X\ Si + y\ CH3Cl \rightarrow Me_2SiCl_2 \qquad \text{Equation (3)}$$

(2) Chlorosilane hydrolysis

In the second stage, after separation by distillation, dimethyldichlorosilane is obtained and further hydrolysed to produce PDMS, as shown in Equation (4). PDMS condenses with HCL to give a mixture of linear and cyclic oligomers which must be further polymerized for future use.

$+H_2Ox\ Me_2SiCl_2 \rightarrow y\ HO(Me_2SiO)nH + z\ (Me_2SiO)m\text{-}HCl$ Equation (4)

(3) Polymerization and Polycondensation

In the final stage, cyclic polymerization and linear condensation processes of terminal SiOH are catalysed in the presence of acid or base compounds, chain substitutions and high temperatures and vacuum conditions. Catalyst removal is essential as it catalyse depolymerisation as well, as is shown in Equation (5).

$x\ (Me_2SiO)_4 + KOH \rightarrow (Me_2SiO)y + KO(Me_2SiO)zH$ Equation (5)

Labile catalysts have been developed which can self-decompose above the optimum polymerization temperature or overheating.

Linear condensation is catalyzed by many acids or bases to give long chains by intermolecular condensation of terminals SiOH, as shown in Equation (6). Longer chains are preferentially formed under high temperature or vacuum conditions.

-OSi---OH + HO---SiO-- → ---OSi----O----SiO-- + H_2O Equation (6)

2.3.2 Silicone Crosslinking Mechanism

Uncured silicone resin must be chemically crosslinked to be an elastomer. Crosslinking can be performed in 3 ways, via platinum-catalyzed addition curing, peroxide curing and condensation curing [85]. Curing agents, polymer side groups and catalysts are used in the formulation of these rubbers.

(1) Addition Crosslinking

Solid-silicone rubber (HTV), Liquid Silicones (LSR), 2 part silicone rubber (RTV-2), Silicone gels and UV curable silicone rubbers all utilize this principle of addition-curing.

The platinum-catalyzed hydrosilylation reaction starts with the addition of a crosslinker's silicon-hydrogen (Si-H) bond across the unsaturated carbon-carbon double bone (C=C) of the olefin to form a silicon-carbon (Si-C) bond during polymerization, as shown in Equation 7.

$$\mathrm{OME_2Si\text{-}CH{=}CH_2 + H\text{-}Si + Pt\ Cat \rightarrow OMe_2Si\text{-}CH_2\text{-}CH_2\text{-}Si} \qquad \text{Equation (7)}$$

The platinum catalysts are either contained together within the one-part silicones or contained separately from the cross-linker in a two-part silicone. A proposed mechanism, shown in Equation 8, has been the initial oxidative addition of the SiH on the platinum catalyst, followed by the proton transfer on the double bond and finally reductive elimination of the product [87].

$$\mathrm{{=}S\text{-}CH\text{-}CH2} \longleftrightarrow \mathrm{{=}S\text{-}CH2\text{-}CH2\text{-}Pt\text{-}Si{=}} \longleftrightarrow \mathrm{{=}Si\text{-}CH2\text{-}CH2\text{-}Si} \qquad \text{Equation (8)}$$

=Si-Pt-H

The advantages are that addition curing provides rapid curing without shrinkage problems or any by-products.

A major drawback of using the platinum catalyst is that it is costly and easily inhibited by catalyst poisons such as amine or organo-sulphur compounds, which are electrondonating substances. Thus, one must exercise extreme care when handling these catalysts in a two-part package.

The disadvantages of addition crosslinking are that side reactions, such as dehydrogenate silylation, redistribution of hydrosilanes, hydrogenation, isomerization and oligomerization of oleins, which often occur and can compromise the desired quantity and quality of the final silicone materials. Additional procedures may be required to remove the undesired impurities [87].

(2) Condensation Crosslinking

This method is used in room-temperature vulcanization (RTV) sealants and no mixing is required. As shown in the moisture-cured silicone extrusion paper [5], the process of moisture contact initiates the crosslinking process of oxime silicone in which the acetoxy groups (the hydroxyl end blocked PDMS) are hydrolysed to give silanols that allows further condensation to occur.

This excess silane ensures that all the chains are endblocked with 2OAc, with tin acting as a catalyst. However the by-products like acetic acid and water-soluble salt leads to corrosive problems and loss of adhesion, respectively.

To circumvent this problem, one part sealants which release less corrosive intermediate products like oximosilane and alkoxylane, have been developed.

(3) Peroxide Radical Crosslinking

Organic peroxides are employed to generate radicals which are used to crosslink with vinyl groups on polymer HCR in extrusion and injection molding at high temperatures. Post-curing treatment is required to remove the volatile residues which can act as depolymerisation catalyst.

2.3.3 Product Grade Silicone

Product Silicone Grades are classified based on the curing method, curing temperature and viscosity of the base polymer. They are classified into the following groups: 1) Solid Silicone rubber (HTV), 2) Liquid Silicone rubber (LSR), 3) two-part Silicone rubber (RTV-2), 4) one-part Silicone rubber (RTV-1) and 5) Silicone gels [88]. A summary table of these product grades silicones is shown in Table 2 below.

(1) Solid Silicone Rubber (HTV) –High Temperature Vulcanising Silicone Rubbers

They are cured at elevated temperatures via peroxide or addition cross-linking mechanism. To achieve its final mechanical strength, the cured rubber is mixed with reinforcing fillers like pyrogenic silica with BET surface area> 100m^2/g , precipitated silica, or inactive fillers like quarts or specific carbon black grades.

Their desirable properties include a good safety profile, a wide range of working temperatures (-50 to 200°C), biocompatible and good ageing resistance, making them suitable for a wide range of application areas ranging from automotive, electrical, construction, mechanical, food, healthcare and medical sectors.

(2) Liquid Silicone Rubber (LSR)- High Temperature Vulcanizing Silicone Rubbers

Standard forms of Liquid Silicone Rubber present in two components A and B. Component A has a Platinum catalyst and component B contains the curing agent with a high-functional polysiloxane. They are vulcanized by addition curing and exhibit shear thinning properties. All medical grade silicones belong to this category.

Their outstanding processing advantages lie with their consistency and curing mechanisms. Although cured by high temperatures, they have a lower viscosity compared to the solid silicone rubbers (HTV). Compared to the peroxide curing, the LSR do not release any curing byproducts.

LSR offer a wide range of application from automotive, mechanical and process engineering, electrical applications, construction, food, healthcare and medical sectors.

(3) 2-Part Silicone Rubber (RTV-2)-Room Temperature Vulcanising

RTV-2 silicones are used for mold-making materials. They are 2-part pourable, spreadable compositions that cure at room temperature forming highly elastic silicone rubber. There are 2 vulcanization methods: a) via condensation curing, where an organotin catalyst is used and alcohol as a byproduct is produced and b) addition curing, where a platinum catalyst is used and no byproduct is produced [89, 90].

Specialised silicone can be flash vulcanized by varying the UV intensity and exposure time. Most cured RTV-2 silicone rubbers can retain their properties between -50 °C and 200 °C.

The slow-acting Platinum catalysts offer a range of pre-mixed one-part system with a long shelf life, which only vulcanized at elevated temperature. Based on the polymer structure, these are similar to addition-curing RTV-2 silicone rubber grades and are thus classified as RTV-2.

The most useful electrical properties are thermal conductivity, insulation resistance, break down resistance and dissipation factor. At room temperature, the gas permeability of RTV-2 is around ten times higher than that of natural rubber. Another feature is the excellent release property of the cured rubber surfaces towards organic and inorganic materials. Its highly versatile property therefore allows it to be used in diverse industrial areas such as mold making, electronics, household appliances, mechanical and industrial process engineering, healthcare applications and solar photovoltaics.

(4) Silicone Rubber (RTV-1)- Room-temperature vulcanizing silicone rubbers

RTV silicone rubbers are used as adhesives and sealants. These one-part, ready to use systems consist of polydimethylsiloxane, curing agents, fillers and additives. After application, they are cross-linked by contact with atmospheric moisture releasing byproducts (amine, acetic acid or alcohol) in the process, with crosslinking starting from the surface and gradually progressing into the interior of the compound.

Their outstanding properties are ideal for almost all sealing, bonding and coating applications. This material has similarly a wide range of applications in different industries such as automotive, construction, household appliances, electrical and electronics, healthcare, medical and textile.

(5) Silicone Gels

These silicone gels are always addition-curing silicone grades which cure to form very soft vulcanizates, below the Shore a hardness range. They have particularly low crosslinking density and are often used as damping materials in medical applications or as encapsulation compound in the electrical and electronic applications.

Their advantages are that they are not influenced by temperature fluctuations and they exert only minimal stress on the encapsulated components. The silicone gels are suitable for various industries such as automotive field, transmission and distribution industry and in health care and medicine.

Table 2 Summary of Product Silicone Grades

Silicone types	HCR	LSR	RTV –(Room temperature vulcanizing)
Characteristic	High molecular weight High tear strengths and elongations	Low molecular weight Low blend viscosities well suited for automated production runs	Lower viscosity and less inhibitor
Equipment	Require high shear equipment for processing	Require equipment with precision control over mold cavity filling, temperature and ejection or extrusion control	
Use	Used for compression molding, transfer molding, injection molding and extrusion	Medical device, medical implants or medical disposables	RTV-2 used for industrial applications RTV-1 used for almost sealants, bindings and coating applications
Precautions	Peroxides by-product can affect stability and thus post-curing required	No byproducts	Amine, acetic acid or alcohol released as byproduct
Parts	2 parts-silicone Peroxide initiator or Pt cure system	2 parts-silicone Pt cure system	1 or 2 parts-silicone Cured by room temperature and moisture as 2nd component to cure

2.3.4 Uses of Silicone

Silicones are used in myriad applications. (Silicones Environmental Health and Safety Council, 1994). Less viscous silicone oils are used as syringe needles lubricants, fabrics water repellent, cosmetics cream modifiers, antifoam agents and stomach gas cures. More viscous oils are used as high temperature hydraulic and brake fluids.

Silicone medical devices include catheters, shunts, ocular lenses, soft tissue implants and tissue expanders, heart pacing devices, implantable infusion pumps, elastomer toes and fingers, incontinence and impotence devices and laryngeal implants. (Compton 1997). While the hardness of eye lens coating and scratch resistance in glass bottles are provided by highly cross-linked silicones, its water repellency is attributable to its low surface energy [91].

2.3.5 Silicone Implants

Silicones are thermoset liquid resins which are cured irreversibly by heat into a solid state. The key attributes of Liquid Silicone Rubber (LSR) which make it the ideal material of choice include its superior mechanical properties, fluid and electrical resistance.

Medical grade silicones, in addition, are selected for their biocompatibility and bio-implantability. The benefits of medical-grade LSR over other elastomeric materials include [92]:

1) its bio-inertness in compliance with ISO 10993, USP Class VI and RoHS standards, 2) its ability to be sterilized by a variety of methods such as Autoclave, ETO, E-beam and Gamma-radiation processes, 3) its thermal stability over a wide temperature from

65 °C to 230 °C and 4) its resilience, flexibility and capability to transfer mechanical force at extreme temperatures.

Medical grade silicone is a type of LSR which differs from non-medical (industrial) grade silicone mainly in the crosslinking systems used. The former used addition crosslinking system while the latter used peroxide crosslinking system.

Using the standard ISO 10993 which evaluates the biosafety of materials in contact with the body, medical grade silicones can be grouped into 3 categories, namely: limited exposure, prolonged exposure and permanent contact. Limited exposure products have less than 24-hour contact with skin, mucosal membranes or breached surface. Prolonged exposure products have surface contact or are implanted more than 24 hours and up to 30 days and require tests protocols for hemolysis, genotoxicity, toxicity and intramuscular implantation with histopathology. Permanent contact silicone products are implanted for more than 30 days and require test protocols for carcinogenicity, chronic toxicity and developmental toxicity.

Silicone was first used for urethral implantation in 1950 and subsequently for shunts and interphalangeal joint silicone replacement prosthesis. It was not until 1962 that silicone breast implant made its debut and its development continued through the 1990s.

Unfortunately, the use of silicones for meniscus replacement in knees have not been described in literature.

2.3.6 Silicone Molding Conventional Method

The conventional injection molding involves heating a thermoplastic polymer above its melting point and converting it into low viscosity molten fluid. This fluid is then injected into a mold of the desired shape, where it is left to cool below the freezing point of the polymer. In the final step, the mold is opened and the desired part recovered [93].
Contrary to conventional injection molding, the LSR is a two-part thermoset resin that is cooled before injection into a heated mold where it is heat cured in place. As opposed to a thermoplastic, once a thermoset is set in place, it cannot be melted again.

2.4 Silicone Additive Manufacturing Technology

Conventionally, silicone parts or end-products have been manufactured by the molding process or indirect casting. Molding process and mold fabrication pose high technical barriers since they are expensive and time consuming, especially when only small quantities of products are required.

The recent advent of various silicone 3D printing technologies allows potential space for flexible applications in robotics and rehabilitation devices.

This section provides a review on the state-of-the-art AM technology for silicone printing. Current available techniques for silicone 3D printing described in literature are Freeform Reversible Embedding, SLA-UV based (vat photo-polymerization), combined extrusion and ink-jetting, extrusion based techniques in combination with UV-cured, moisture-cured and heat cured technologies. A comparison of the resolution and printing speeds for available AM techniques is shown in Table 3 below. While piezoelectric-pneumatic jetting printing technology is able to achieve printing resolution of 600 µm with a printing speed of up to 100 mm/s, material extrusion has a wider range of printing resolution of 100 to 600 µm but only at a maximum printing speed of 20 mm/s.

Table 3 Comparison of the silicone printing features for available AM techniques

AM Technology	Resolution µm	Printing Speeds (mm/s)
Material Extrusion	100 – 610	1 – 20
Freeform Reversible Embedding	30- 700	2 – 20
Vat photo polymerization	100- 400	Not reported
Material Jetting	Not reported	5

Piezoelectric-Pneumatic Jetting	500-600	104

2.4.1 Freeform Reversible Embedding Technique

Hinton *et al.* first described in 2016 the 3D Printing of PDMS Elastomer in a Hydrophilic Support Bath via Freeform Reversible Embedding [94]. The experimental setup as shown in **Figure 8**, principles, proof-of-concept printing, pros and cons of this method are described below.

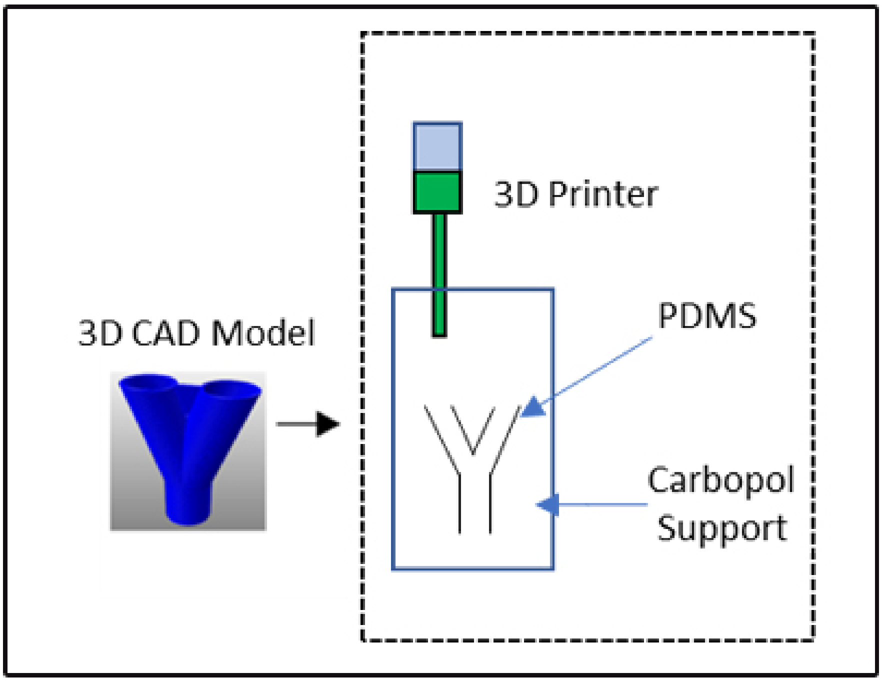

Figure 8 Experimental testbed of FRE using Carbopol (a) 3D Printing extrusion of hydrophobic PDMS resins into a hydrophilic Carbopol gel support

(1) The Experimental Setup for Freeform Reversible Embedding (FRE)

Hinton *et al* introduced this system in 2016 [94]. The PDMS 184 is first prepared In a 10:1 base to curing agent ration and degassed in a centrifugal mixer The support bath is prepared from a combination of Carbapol 940, ETD2020 and Ultrex30 [94].

The FRE printing process employed MakerBot 3D Printer and custom made syringe pump. The Solidworks CAD software is used first to design the 3D model. The Slic3r software then slices the STL files into 200um thick layers to generate G codes which are subsequently sent to the printer via Pronterface software. Before printing, the PDMS is contained in a 10cc syringed capped with a Nordson 400um ID 0.75 stainless steel extruder needle which is then placed in the bottom centre of the Cabapol support bath, with print speed set at 20 mm/s. The whole bath is placed at room temperature for three days or 4 hours in oven at 65 °C for curing of the PDMS. PBS is later used to release the print from the support.

(2) The Principles of Freeform Reversible Embedding

The working principle harness on unmixability of the hydrophobic PDMS in the hydrophilic Carbapol support. The freeform printings are then completed layer by layer. The Carbapol support acts like both as a Bingham plastic which yields and fluidizes during the movement of the printer needle and acts as solid during PDMS extrusion. After curing, PBS is used to release the PDMS and reduce the Carbapol yield stress.

(3) Proof of Concept of Freeform Reversible Embedding

As proof of concept, Sylgard 184 PDMS is used successfully to 3D print filaments and tubes, which are manifold and perfusable, as shown in **Figures 9a** to **9d**.

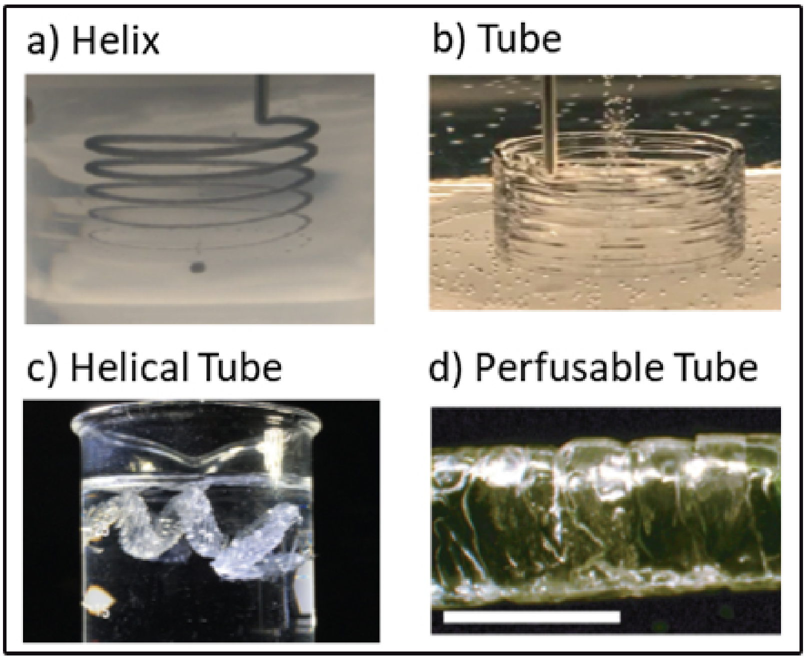

Figure 9 Representative FRE printed PDMS structures using the Carbopol support. (A) Helical path supported in the Carbopol gel (B) After curing, the released tube remains firm in printed geometry (C) The helical tube is supported within the Carbopol. (D) The manifold printed tube (scale bar is 4 mm)

(4) Pros and Cons of the Freeform Reversible Embedding

The advantages of this FRE printing system are as follows: 1) it can print wide range of biomaterials which are hydrophobic in nature, using a hydrophilic support, 2) the Carbapol supports are highly stable over long periods of time, 3) it has a high degree of accuracy and precision of printouts and 4) it has a low cost of implementation of its open-source hardware and software tools.

The disadvantages of this FRE printing system are that 1) it does not work well for lateral fusion, since no lateral pressure can be generated by the support. This is in contrast to the vertical fusion which can generate pressure to compress layer below, 2) Carbapol support may be trapped within the voids inside the print, 3) long curing times are necessary, 4) post curing is required and 5) the low elastic modulus of PDMS limits the number of 3D products that can be printed and 6) it cannot print medical grade silicone.

2.4.2 Moisture-Cured Extrusion Based Technique

Plott *et al.* in 2017 described the extrusion-based additive manufacturing of moisture-cured silicone elastomer with minimal void for pneumatic actuators [5]. The experimental setup as shown in **Figure 10**, principles, proof-of-concept printing, pros and cons of this method are described below.

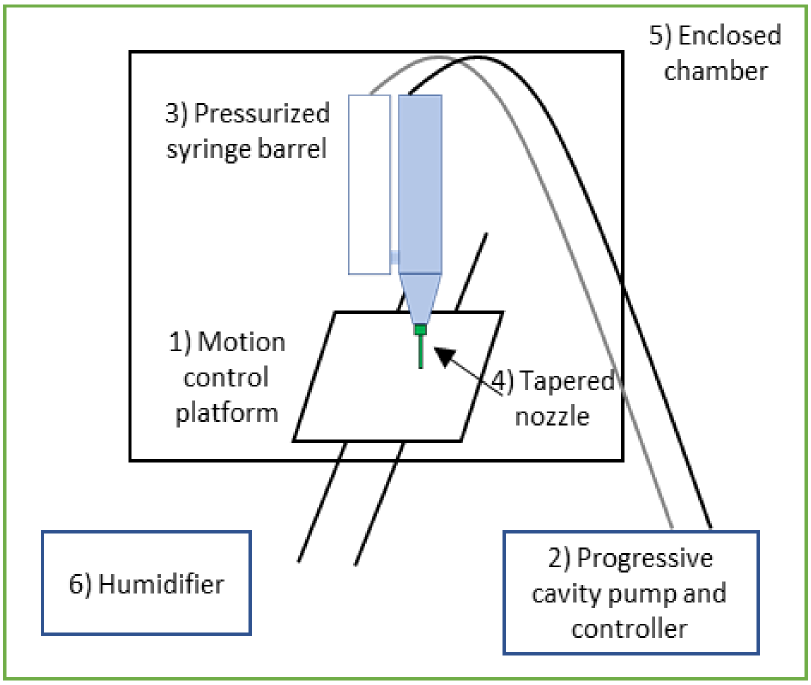

Figure 10 Experimental setup for moisture-cured extrusion-based silicone AM: legends: (1) 3D motion platform (2) pump and controller (3) pressurized syringe barrel (4) nozzle (5) enclosed chamber and (6) humidifier

(1) Experimental setup for moisture-cured extrusion-based technology

The moisture-cured extrusion has the following setup: 1) an enclosed interior chamber maintained at 75% humidity with a humidifier, 2) a 3-axes motion control platform based on an open-source FDM machine, 3) the chamber houses a clear syringe which is connected by a tapered (0.41mm) 22G nozzle to the pump and controller. The barrel pressure is set at 340kPa and calibrated to ensure accurate extrusion volume.

An open source 3D printing console Pronterface is used as a software-printer interface and Simplify3D used for tool path generation

In this setup, a one-part oxime silicone elastomer that is moisture-curable is used. It has a hardness of Shore 33A, a zero shear rate viscosity of about 62.5 Pa.s and a curing time of 24 h. It is of sufficient viscosity to be extruded out of the nozzle and to resist wetting out.

(2) The Principles of moisture-cured extrusion-based technology

The moisture-cured silicone extrusion process is based on its 1) material property, 2) the extrusion rate, 3) the resultant edge profile and 4) area in which extrusion takes place. After extrusion, the curing process is dependent on the silicone material, degree and duration of exposure to humidity. The viscosity of extruded silicone allows it to self-support, while minimal compressive force presses the silicone to fill the interstitial space for void less AM. However, the exposure time and degrees of humidity are not mentioned in the literature.

(3) Proof of Concept for the moisture-cured extrusion-based silicone technology

As a proof-of-concept, sphere-like balloons as in **Figure 11** and finger pneumatic actuators as in **Figure 12** were printed. While the balloons are able to expand diametrically up to 207 % with burst stress of up to 2.55 MPa, the actuators were able to oscillate up to 30,000 cycles before failure. These pneumatic actuators exhibited high elongation and fatigue life due to their near void-less construction.

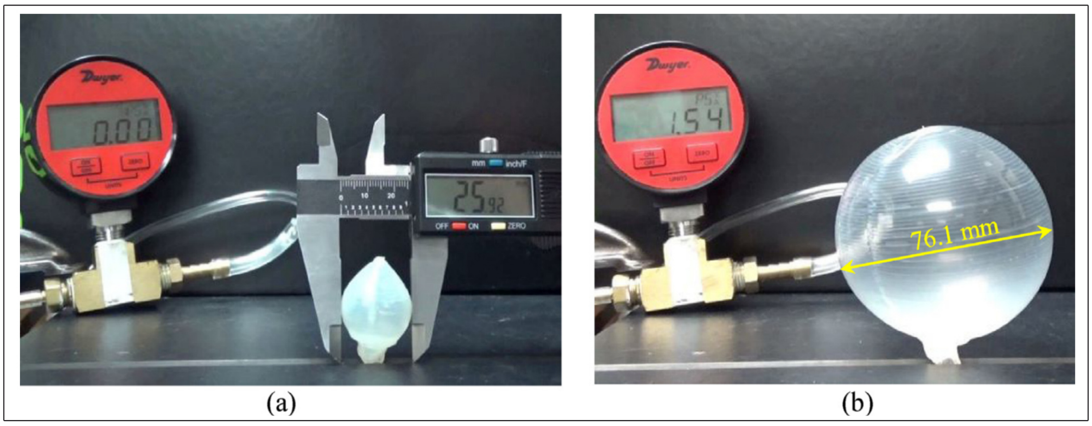

Figure 11 Burst pressure test of sphere-like balloon: (a) the initial diameter of 25.9 mm and (b) the inflated close-to-rupture balloon with the diameter of 76.1mm

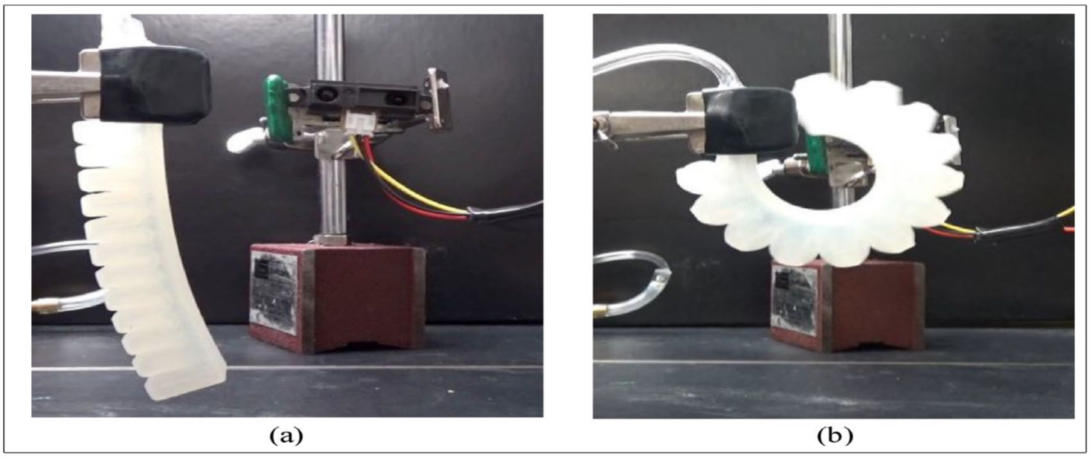

Figure 12 Finger pneumatic actuator in a (a) non-articulated and (b) fully articulated configurations

(4) Pros and Cons of the moisture-cured extrusion-based silicone technology

The advantages of this moisture-cured system are that 1) the printed balloons are capable of expanding up to 207 % and with a burst stress up to 2.55 MPa. The finger actuators are able to fully articulate 30,000 cycles before failure. The printouts are self-supporting, 2) the system has good fault tolerance and 3) it has unique part properties. The disadvantages are that 1) the system is unable to print heat-cured medical grade silicones, 2) long curing times with uneven degrees of curing since the curing commences from outermost layer to innermost layer, 3) Difficult to print parts with multi-material and 4) the system humidity sensitive

2.4.3 Combined UV-Extrusion and Ink-Jetting Technique

Plott *et al.* in 2018 described this hybrid additive manufacturing method for the fabrication of Silicone Bio-structures [6]. The experimental setup as in **Figure 13**, principles, proof-of-concept printing, pros and cons of this method are described below.

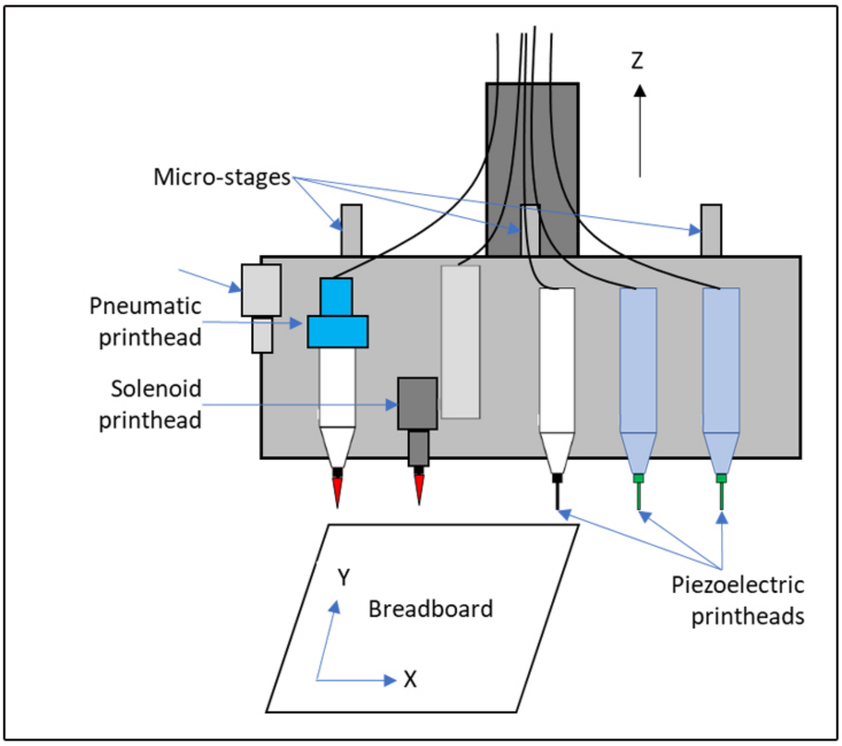

Figure 13 Experimental Setup of the Hybrid UV-Extrusion and Ink-Jetting system (a) Front view (b) Main components are shown with pneumatic, solenoid and piezoelectric print heads

(1) The Experimental Setup of the Hybrid UV-Extrusion and Ink-Jetting system

The hybrid pneumatic system comprises three different types of Nordson print-heads: 1) three piezoelectric-pneumatic jet print-heads 2) solenoid actuated extrusion jet print-heads and 3) one pneumatic extrusion jet print-heads and a 365 nm UV lamp.

Three voltage controller units actuate the piezoelectric stacks while one air-pressure controller regulate the extrusion based print-heads.

The open source Slic3r (slic3r.org) software creates the tool path extracted as G-code for printing on the 3-axis motion stage with multiple nozzles.

An organosiloxane polymer RTV 800-400 which is UV curable and has dual UV/moisture curing mechanism, was used. This polymer includes the photoinitiator, 3 wt % 2-hydroxy-2-methyl propiophenone and catalyses the polymerization process upon exposing to UV light for a few seconds. Atmospheric moisture helps to fully cure and attain the full mechanical properties in 7 days.

(2) The Principles of the Piezoelectric-pneumatic material jetting AM in the Hybrid system

The conventional inkjet printing method is capable of only printing fluid with maximum viscosity of 40 mPa.s. In this system described, fluids are considered only jettable if their Ohnesorge numbers Oh are between 0.1 and 1 (or $1<Z<10$ where $Z=Oh^{-1}$).

Medical grade silicones have viscosities of about 25,000 mPa.s and have Oh values greater than 1, making them impossible to be printed by conventional material jetting.

The new generation dual piezoelectric jetting mechanism of jetting print-heads can jet fluid droplets, with enough viscosity, force, frequency and volume in the order of pico-liters, of up to 1,000,000 mPa.s.

The pulsed voltage signal is shown in Fig 11. The print-head valve is normally open. An actuation voltage 95V pushes the sealing ball downwards and occludes the outflow orifice. A voltage drop opens the orifice and air back-pressure fills the orifice with fluid. A subsequent voltage rise up to the actuation voltage value again pushes the sealing ball downwards and jets out one droplet. The valve reopens with every new cycle, as shown in **Figure 14**.

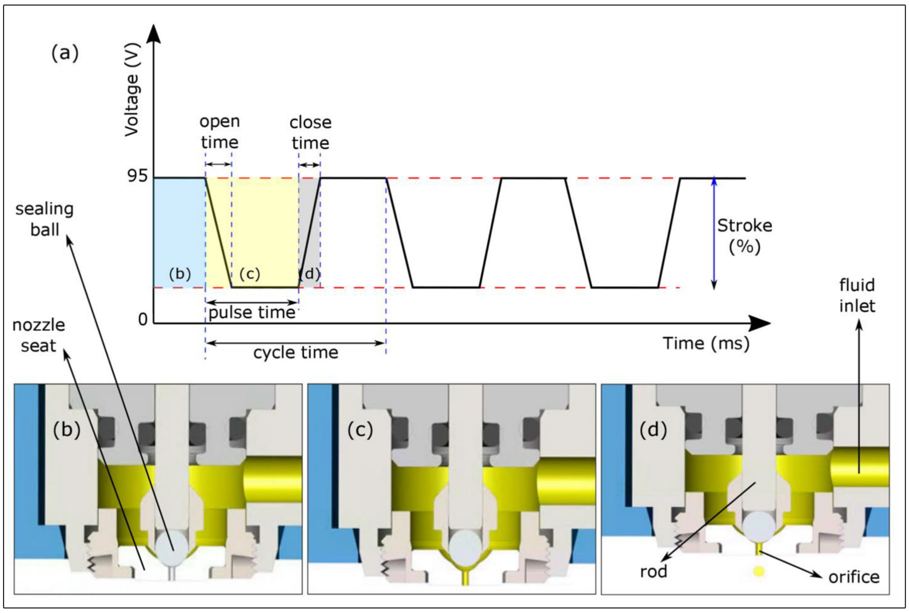

Figure 14 The working principle of the piezoelectric-based material jetting; (a) the plot shows the voltage signal sent to the piezoelectric stacks for three complete cycles, open time indicates valve opening rate, close time indicates valve closing rate, pulse time is the total time the valve is open, and the cycle time is the total duration of one open cycle plus one close cycle; (b) the duration that valve is closed is represented by blue region; (c) the duration of orifice opening and material filling is represented by yellow region; (d) the duration of ramp closing is represented by grey region

Two jetting elements, namely reverse piezoelectric and pneumatic force, combine to contribute to the total amount jetted. The first amount due to the reverse piezoelectric is controlled by the orifice closing time (CT) and the second amount jetted due to the pneumatic force is controlled by the pulse time as determined by the equation below. The open time indicates how long it takes to open the valve, the close time shows how long it takes to close the valve.

$$V = Qpzt \times CT + Qpne \times PT$$

Pulse time is the total time that the valve is opened, and the cycle time is total duration of one open/close cycle.

(3) The Principles of the Pneumatic Material Extrusion AM in the Hybrid system

Material extrusion is a flow-based technology, which deposit material onto a substrate or previous layers to fabricate solid freeform structures, using a robotically controlled nozzle. This pressure-actuated print head used compressed air to initiate deposition and curing is done by cooling, UV photo-curing or solvent evaporation. The nozzles are chosen for their ease of operations and maintenance.

The DOE analysis for this hybrid printing process found that specifically four factors namely pulse time, voltage, stroke and close time, are significant at 95 % confidence interval. When printing with optimized parameters, jetting and extrusion systems can achieved a XY resolution of 500-600um and 300-400um, respectively.

(4) Pros and Cons of the hybrid UV-Extrusion and Material Jetting system

The advantages of this hybrid system are as follows: 1) Compared to current systems, it prints at twenty times faster, 2) the extrusion system provides high quality of printing and the jetting system provides high velocity of printing, 3) viscous silicones can be printed with high throughput rate and high quality, and 4) it can print a wide range of materials of different viscosities and complicated parts. The drawbacks of this system are: 1) its inability to print medical grade heat-curable silicones and 2) post-curing of printouts are required.

2.4.4 Combined SLA-Low One-Photon Polymerization

Kim *et al.* in 2016 described this hydrostatic support-free fabrication of three-dimensional soft structures [95]. The experimental setup shown in **Figure 15**, principles, proof-of-concept printing, pros and cons of this method are described below.

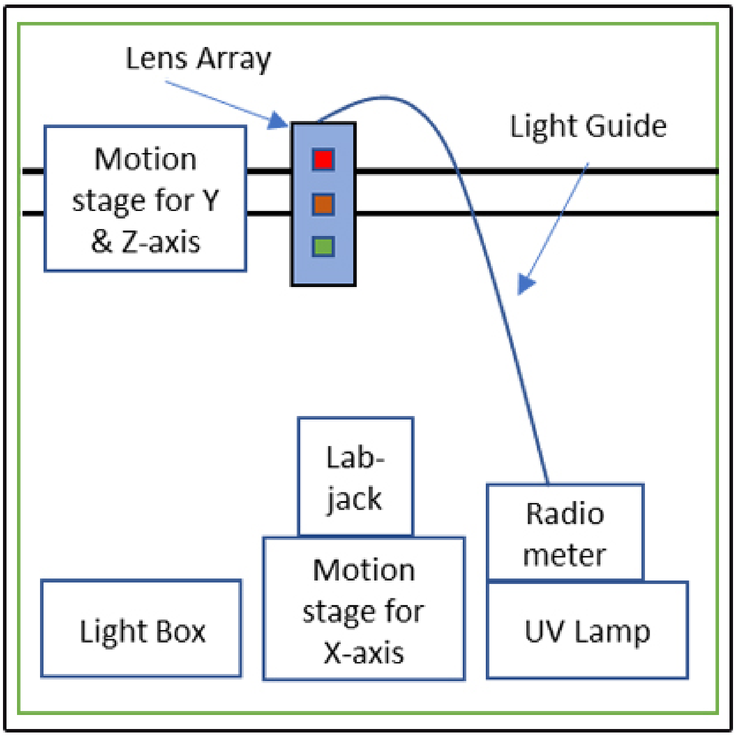

Figure 15 Schematic illustration of combined SLA-LOPP system. The configurable optical system consists of a UV lamp system, the optical lens array and 3-axis reconfigurable motion stage

(1) The experimental testbed of combined SLA-LOPP system

A two-part UV curable silicone is used to accomplish low one-photon polymerization (LOPP). The first part is the silicone resin and the second part is the UV activated photo-initiator, whose absorption spectra is measured by a spectrophotometer.

The configurable optical system consists of a UV lamp system, the optical lens array and 3-axis reconfigurable motion stage. The lamp system has a spectrum from 250nm to 650nm. The lens array consists of aspheric lens. The electric shutter controls the beam intensity and iris diaphragm aligns the beam. The band-pass filter is set at 365nm.

The system is constructed using 80/20 aluminium frame and linear sliders which are capable of achieving a resolution of 2.5um numerically controlled by G codes. The dual light guide system allows simultaneous operations with the lens array and radiometer.

(2) The principles of the combined SLA-LOPP system

The key principle of this method uses LOPP to initiate polymerization by focusing on a point below the resin surface, as opposed to surface one-photon polymerization in stereolithography.

UV curable silicone photopolymers undergo curing process by photo-polymerisation, requiring photo-initiators and reactive liquid monomers. The photo-initiator molecules absorbed photons from the UV source and are converted into the reactive initiator molecule which then react with monomer molecules forming polymerization initiating molecules. Through chain-propagation stage, the initiating molecules continue to elongate until chain termination process is reached. Cross-linking should be adequate to ensure that the polymerized molecules do not re-dissolve back into the liquid monomers [96]. To achieve hydrostatic support-free fabrication, the density of silicone resin, before and after curing, must be as constant as possible since a large fluctuation in density can cause unnecessary movement of cured parts.

(3) Proof of Concept of the combined SLA-LOPP system

H-shaped structures are printed as proof of LOPP concept, as shown in **Figure 16.**

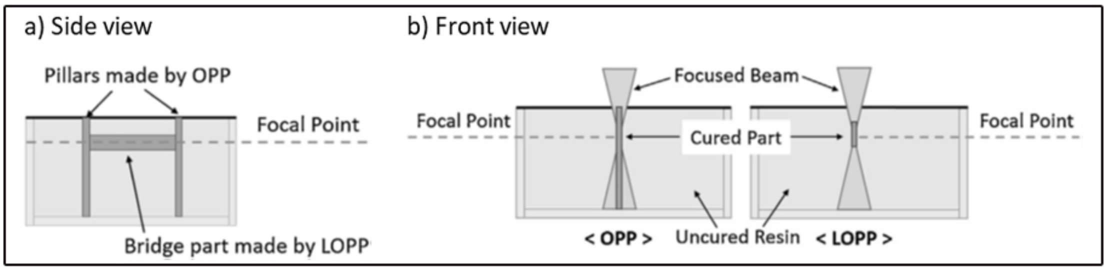

Figure 16. Schematic diagram of a) side view and b) front view of one-photon polymerization (OPP) and low one-photon polymerization (LOPP) of H-shape structure for proof of LOPP concept

(4) Pros and Cons of the combined SLA-LOPP system

The advantages of this system are that: 1) it can operate continuously, 2) it can print products of variable sizes, 3) using a wide range of substrate materials, for general and specific applications.

The disadvantages are that 1) post curing steps are necessary, 2) these post curing methods may not be appropriate for all materials, 3) limited geometrical resolution and accuracy since LOPP can only cure materials below the silicone resin surface, 4) special room and setups are necessary and 5) support structures are required for overhangs and 6) medical grade silicones cannot be printed.

2.4.5 Rep-Rep L280 Series

This L280 series is the newest addition to the silicone 3D printer family built by German Rep-Rep Company for liquid additive manufacturing solely using EVOLV3D LC 3335 Liquid Silicone Rubber A and B components (non-medical grade) [97].

It has a build platform of (X)280mm- (Y)280mm-(Z)200mm, maximum print speed of 150 mm/s, print layer height of 0.22 mm to 0.9 mm, print bed temperature of 110 °C and nozzle diameter options of 0.23 mm, 0.4 mm or 0.8 mm. It also has a build-in halogen lamp of thermal cross-linking and a pre-nozzle mixer attached. Appendix A shows the complete specifications of Rep-Rep L280 series.

2.5 Research Gap

Conventional methods of production of silicone parts require the initial machining or additive manufacturing of molds. These are subsequently filled in with silicone resins and cured in place. These expensive methods are nevertheless time consuming and incapable of addressing hollow structures with complex internal architecture.

Additive manufacturing methods for silicone printing available till date involves a) inkjet deposition layer by layer of ultraviolet-curable silicone, which are subsequently UV cured (ACEO, Wacker, Munich, Germany) [98] and b) the extrusion of catalyst (part-A) into a silicone bath (Part-B), the former becomes suspended and cured within the latter. (Fripp Design, Sheffield, UK) [3].

Recently, Plott J et al at the University of Michigan were able to extrude moisture-cured silicone pneumatic actuators and sphere-like balloons [5]. Its research focused on the identification of process parameters, mainly mechanical strength and porosity, which support fabrication of void-less solid and thin-wall structures. These parameters are in turn influenced by layer height, flow rate and adjacent line spacing.

Most recently, Rep-Rep introduced their L280 series that can print non-medical grade silicone product, also within a maximum individual layered height of 1mm, within an enclosed chamber and staged heating elements.

Current research gaps include 1) lack of research on direct printing of heat-cure silicone implants, without support structures, using liquid silicone rubber, 2) the lack of research in the optimization of printing parameters and in the design of fine internal structure, such as micro-channels, of the silicone meniscus in extrusion-based AM, 3) lack of research into the shape-memory properties of silicone resin and 4) lack of research into the use of concurrent composite printings of various LSR silicone using two or more print-heads.

2.6 Summary

The meniscus is an important shock absorber and stabilizer of the knee. Various meniscal scaffolds and implants have been developed to replace a damaged meniscus but these are met with poor or inconclusive mid-term or long-term clinical results. The skin-safe silicone is an ideal option to be explored for implant production since it is biocompatible, non-cytotoxic and demonstrates similar mechanical properties suitable for weight bearing and loading. With the progress in AM silicone technology, more customized implants can be produced.

Chapter 3 – Silicone 3-D Printer Development and Silicone Standard Samples Characterisation

3.1 Introduction

Silicone has been widely used in the manufacture of medical devices and implants like biliary stents [99], cochlear implants [100], peripheral nerve sheaths [101], breast [102-105], chin, nose[106], testicular, and hand implants [107], interphalangeal joint replacement implants [108], knee prosthesis [109], cardiopulmonary bypass tubing [110] and silicone membranes [111]. They have also been recently used for the manufacture of microfluidics [112], lab-on-a-chip [113] and biosensors [114]. However, it has not been described or used to manufacture silicone meniscus implants for the knees. Meanwhile, most information in literature are on the general properties of silicone resins but little on the rheological properties. Takahashi et al. studied the rheological behavior of several silicone resins in the un-crosslinked state and found that the temperature dependence of the viscoelastic behavior can be described by a Williams-Landel-Ferry (WLF) equation [131]. This chapter extends the rheological basis and understanding of silicone resin into the design and manufacture of 3D silicone printer.

3.1.1 Silicone material specification

The Ecoflex liquid silicone rubber (LSR) used is a water-white translucent, two-part, low-viscosity platinum-catalyzed LSR that cures when exposed to room temperature or can be accelerated by heat (Smooth-On®). Both Ecoflex 30 and Ecoflex 50 are chosen for its safety, biocompatible profiles and cost. 1A and 1B material are mixed in a 1:1 ratio by weight or volume and cured at room-temperature with negligible shrinkage. Ecoflex was evaluated based on the requirements of ISO 10993-10, Biological evaluation of medical devices, Part 10: Tests for irritation and skin sensitization.

Ecoflex 30 has a mixed viscosity of 3,000 cps (3Pa.s), specific gravity of 1.07 g/cc, specific volume of 26.0 cu.in./lb, pot life of 45 minutes, cure time of 4 hours, Shore Hardness of 00-30, Tensile strength of 200 psi, 100% Modulus of 10 psi, 900% Elongation at Break, 38 pli Die B Tear Strength and 0.001in/in of shrinkage. All values are measured after 7 days at 23^{0}C.

Table 4. Ecoflex Sample technical data (from SDS Smooth-On Supplier)

	Mixed Viscosity (cp)	Specific Gravity (g/cc)	Specific Vol. (cu. in./lb.)	Pot Life (min)	Cure Time (h)	Shore Hardness	Tensile Strength (psi)	100% Modulus (psi)	Elongation at Break (%)	Die B Tear Strength (pli)	Shrinkage (in./in.)
Ecoflex 50	8000	1.07	25.9	18	3	00-50	315	12	980	50	<0.001
Ecoflex 30	3000	1.07	26.0	45	4	00-30	200	10	900	38	<0.001

3.1.2 Experimental setup

The experimental setup for Liquid Additive Manufacturing (LAM) is shown in **Figure 17 a**.

Liquid additive manufacturing (LAM) is an **additive manufacturing** technique which deposits a liquid or high viscous material (e.g **Liquid** Silicone Rubber) onto a build surface to create an object which then vulcanised using heat to harden the object.

The system consists of five key components: (1) a motion control platform based on an open-source 3D printing machine (Model Core X-Y), (2) a syringe-pump extruder (Model Maker Shed Discovery extruder) to dispense the silicone with an accuracy of 0.05 μm , (3) a static mixer connected the double barrel syringe with tubing (TIUB05C, SMC, Japan), (4) stainless nozzles with tip size ranges from 20 to 21 gauges (inner diameter from 0.5 mm to 0.6 mm), (5) heating elements on the printer nozzles and platform with their controllers. **Figure 17b** shows the schematic drawing of the printer.

a)

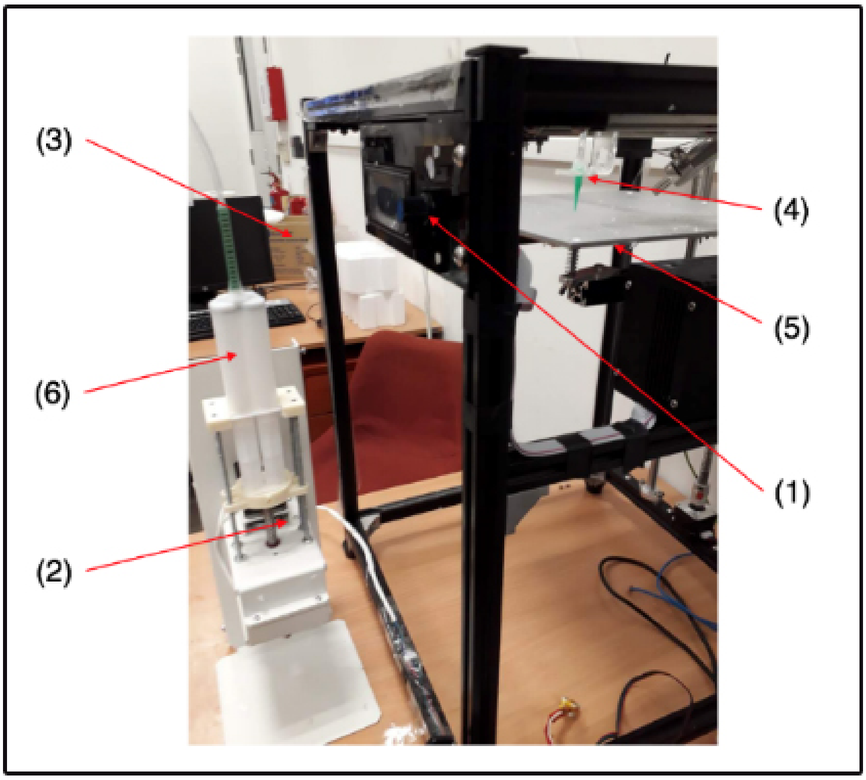

b)

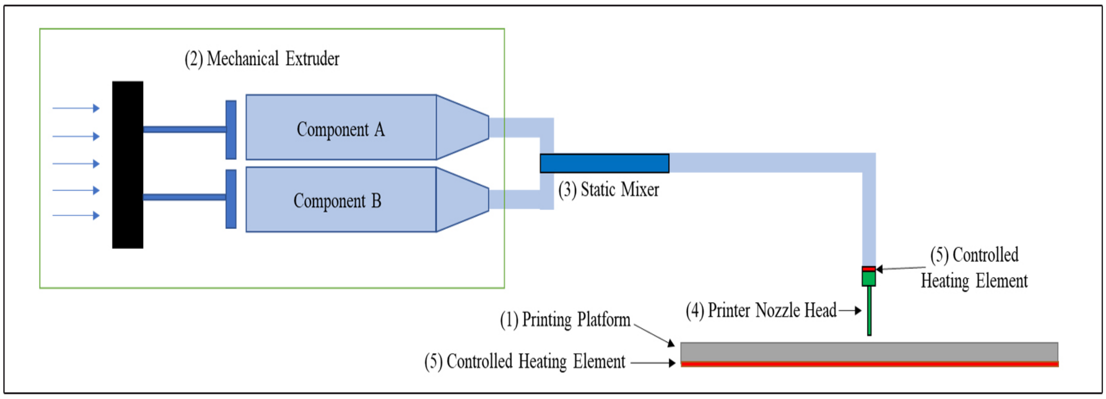

Figure 17 a) Experimental setup for heat cure extrusion-based LSR AM printer: (1) motion control platform, (2) extruder, (3) static mixer, (4) print head, (5) heating elements, b) schematic diagram of LSR 3D printer

Before printing, Parts A and B of the Ecoflex LSR were added into the double barrel syringe with a mix ratio of 1:1 by volume. The LSR were subsequently passed through a static mixer before extrusion through the heated nozzle head and heated platform. The open-source 3D printing software (Repetier-Host by Hot-World GmbH & Co. KG) was used to control the 3D printer while the open-source software Slic3r was used to generate the tool path. Currently, the German Rep-Rep L280 series printer is the only commercially available LAM silicone 3D printer. The comparison table of the specifications of our silicone 3D printer compared to those of the L280 series is presented in Appendix A. (Disclosure of Technology NTU 2019-065).

There are currently three groups of commercial 3D printers which utilized heat for curing in their respective systems, namely the FDM printer, the Rep-Rep L280 series silicone LAM printer and the Cell-Link BIOX series Bio-printer. However, the duration and intensity of heating and the placement and design of the heaters are important determinants for successful printouts.

In contrast to a typical Fused Deposition Modelling (FDM) 3D printer, which requires extruder heating of filaments at above 200 °C, our silicone printer requires specific extruder heating temperature of not more than 60 °C and the narrow gelation temperature range is specific to any individual liquid silicone rubber. Bed temperatures are set to 70 °C and 110 °C for FDM and the silicone printers, respectively.

The only similar silicone LSR printer used in Liquid Additive Manufacturing (LAM) launched in November 2018 and commercially available was the Rep-Rep L280 series silicone LSR printer. A comparison of the specifications of L280 printer and our silicone printer is presented in the Table. A major difference in the design of these two extrusion-based LAMs is that in the L280 printer, both stages of heating take place post-extrusion with a halogen lamp and on the heated platform. In contrast, the first stage of heating in our silicone printer starts in the nozzle prior to extrusion and the second stage of heating continues post-extrusion on the heated platform.

Although BIO X bioprinter from CellLink has modular pneumatic extruder heads and thermoplastic extruder heads set to 60 °C and 250 °C, respectively, the design and placement of these BioX heaters around these extruders predisposes silicone LSR to prematurely cure and clog up the nozzles. Unfortunately there is no post-extrusion heating mechanism.

3.1.3 Process parameters

In this study, a few key process parameters, such as the LSR flow rate (Q), nozzle-to-substrate distance (h), were first selected and fixed to simplify the optimization process. Before the silicone meniscus is 3D printed, several trial runs were conducted to find a suitable range of the process parameters. Subsequently, the meniscus were printed using various combinations of extruder and bed temperatures. The printouts were then analyzed to determine the optimal temperature combinations.

The first stage in determining the optimal nozzle diameter involves the fabrication of cylinders and T-bones. Deformation and voids are checked within each printed specimen.

The second stage involves the determination of optimal combination of both platform (T_1) and nozzle (T_2) temperatures via the printing of meniscus specimens.

3.1.4 Rheology test

The TA Texas Instruments DHR2 rheometer is used for monitoring gelation in silicone systems since the measurement is instantaneous and can be monitored as a function of time. The 40 mm steel Peltier parallel plate is used as the testing geometry. The DHR 2 rheometer is manufactured by TA instruments and operates in parallel-plate mode. It comprises a magnetic bearing, drag cup motor, force rebalance transducer (FBT), optical encoder and reader and true position sensor (TPS).

The 40mm Peltier parallel steel plate geometry is fitted after instrument inertia calibration, bearing friction correction and geometry inertia calibration have been done.

For the experiments, the two components Parts A and B of each silicone resin Ecoflex 30 and Ecoflex 50 (cross-linker with catalyst and polymer) were manually mixed according with the Smooth-On manufacturer's datasheet. The rheological characterization of silicone rubbers were done in triplicates with a 40mm Peltier parallel steel plate rheometer (TA Texas Instrument) operating in both steady and oscillation modes at different isothermal temperatures (30 °C – 80 °C) according to DIN 53529, similar to ASTM D 5289.

The selected temperatures of 30, 35, 40, 45, 50, 55, 60, 65, 70, 75 and 80 °C were controlled by the Peltier device with a cooling pump at an accuracy of ±0.1°C. Characterization of the rheological behavior of the silicone rubbers in triplicates was done with a 40 mm Peltier steel plate parallel-plate rheometer (TA Texas Instruments DHR 2 Rheometer) operating in both steady and oscillation modes. For dynamic oscillatory rheological studies, the samples were subjected to increasing strain rates of

0.00 to 3.00 s^{-1} at a constant frequency (1 Hz) to establish the linear viscoelastic range of the samples [116].

The temperature ramp mode is selected to determine the curing times, complex viscosities and complex moduli of Ecoflex 30 at various temperatures. The values of curing times, complex viscosities and moduli, obtained from 30 °C to 80 °C, are plotted and the calibration curves extrapolated for Ecoflex 30 resins. Here, the torsion geometry is used with normal force control of 2N, tolerance of 1.75N, gap change limit down of 5000 μm and gap change limit up of 2000 μm. In the temperature ramp mode, to examine the curing effects on the mechanical behavior of LSR, from 30 °C to 100 °C, the ramp rate is set at 5 °C/min, 200 sample points are collected, and the control strain is set at 0.025 % and constant angular frequency set at 3 rad/s. The data is collected and a plot of G’, G’’ and tan (delta) against temperature and time is performed [117].

Using a frequency range of 0.01 to 100 rad/s, the frequency mode is used to ascertain the viscoelastic properties of the silicone resin in steady shear and dynamic state. The heat treated material was pressed to disc shape at 70 °C. All samples were dried at room temperature for 12 hours [118, 119, 120, 116, 117].

3.2 Rheological Characterization of Liquid Silicone Rubber

3.2.1 Gelation Times

The silicone sample begins as liquid when both components A and B are mixed and are characterized by very low values of both G' (storage modulus) and G" (loss modulus).

Storage modulus (G') is a measure of **elastic** response of a material. It measures the stored energy. **Loss modulus** (G") is a measure of viscous response of a material. It measures the energy dissipated as heat.

In sol state, G" is greater than G'. When gel forms, G' crosses G" at gel point and eventually exceeds G". The gel point is described below.

The gelation time, in the manufacture of the thermoset resin, is the time interval between the addition of the catalyst into the liquid adhesive system and the formation of a gel. The printing extrusion time should be less than the gelation time to avoid clogging of the liquid silicone rubber within the syringe, tubing and nozzle.

The TA Texas Instruments DHR2 rheometer is used to measure the storage and loss moduli. The rheometer has 2 raw signals, namely the torque and the angle delta δ. The former measures the complex modulus G*, while the latter measures the phase difference between the oscillating strain and stress waves. The rheometer can subsequently calculate the G' and G" and tan delta, where

$G' = G^* \cos\delta$ and $G'' = G^* \sin\delta$, and $\tan\delta = G''/G'$

A low viscous liquid starts with an initial small torque signal and a near 90° initial phase angle. When gelation begins, the torque increases and G" becomes measureable but G' is not yet measureable in the early stage. The stress and strain are 90° out of phase. And $G' = G^* \cos 90^0 = 0$ and $G'' = G^* \sin 90° = G^*$

When gel point is reached, G" decreases and G' increases, as the unattached chains and loose ends contributing to the viscous signals are now incorporated into the purely elastic gel.

The initial small storage modulus G', prior to reaching the gel point, is due to the stretched deformation and physical mesh between the silicone polymer chains, especially at low frequencies. Longer polymers have higher molecular weights, more meshes and crosslinks and longer relaxation times, thus increasing both the viscosity and storage modulus G', in relation to G".

For ideal end-linked polymer gels, the critical gel point is the intersection point where the elastic and viscous moduli are equal (G'= G"). This intersection point is a liquid to solid state phase transition and is not reliant on measurement parameters.

However, this intersection point is dependent on the applied frequency when there are network defects and physical entanglements in non-ideal gels.

Winter in 1987 proposed the definitive criterion for the intersection point determination. This intersection point is taken to be the point when both moduli exhibit a power law dependence on the applied frequency over a wide range of frequencies. The ratio of the shear moduli, tan ɵ, is independent of the frequency

$$G', G'' \propto \omega^n \qquad G''/G' = \tan \delta = \tan (n \boldsymbol{\pi} / \mathbf{2}) \qquad \text{Equation (9)}$$

For ideal gels, at critical gel point, the shear moduli are equal and n = 0.5, as shown in Equation 9.

For imperfect gels, the phase angle $\delta = n\pi / 2$ will be frequency-independent and n lies between 0.5 and 1, with n taking on larger values for gels which contain more defects. After the intersection point, the storage modulus becomes larger than the loss modulus. Finally, as the reaction nears completion, the storage and loss moduli approach their equilibrium values. Stiffer silicone rubbers will have higher storage modulus G' and a smaller phase angle.

All the experiments in this study are conducted within the linear viscoelastic region, where the responses obtained are from intact silicone structure. In this linear region, the measured moduli are independent of the applied strain.

Firstly, it can be seen from **Figures 18 to 21** that, for silicone resin Ecoflex 30, when the temperature is held at 40 °C in time sweep studies, the storage modulus G' crosses the loss modulus G" at the gelation time of 805 s. This gelation time decreases to 452.5 s at 45 °C, 187.0 s at 50 °C and 163.2 s at 55 °C. The Figures for silicone resin Ecoflex 50 are shown in Appendix A.

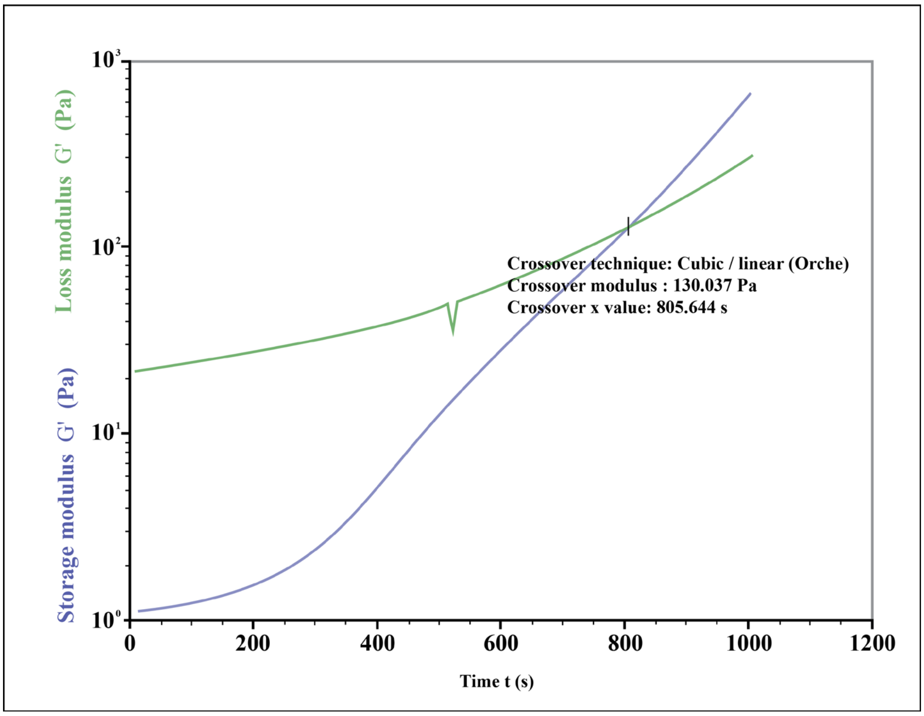

Figure 18 Time Sweep of silicone Ecoflex 30 at 40℃. Gelation time occurs at 805 s

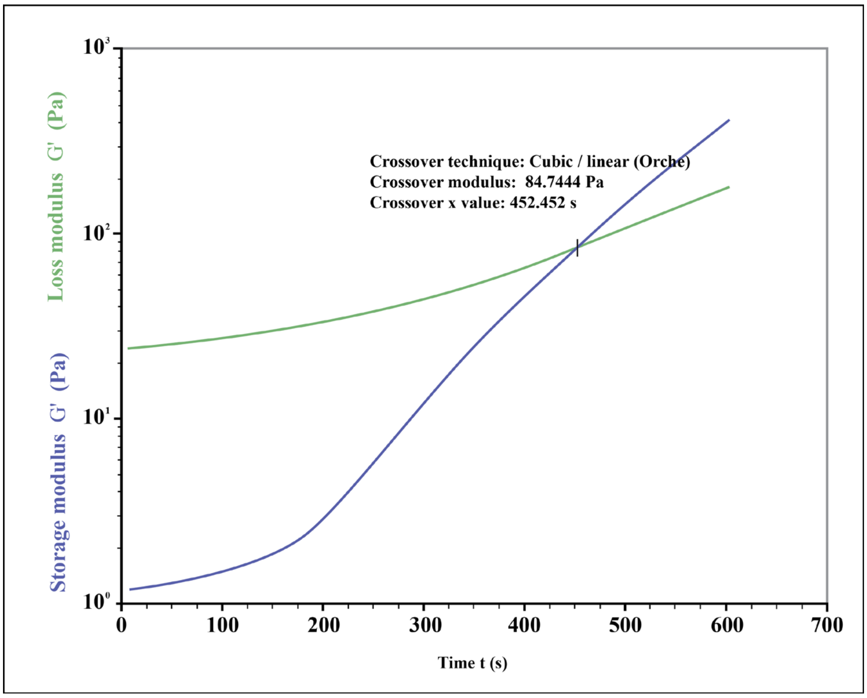

Figure 19 Time Sweep of silicone Ecoflex 30 at 45℃. Gelation time occurs at 452.4 s

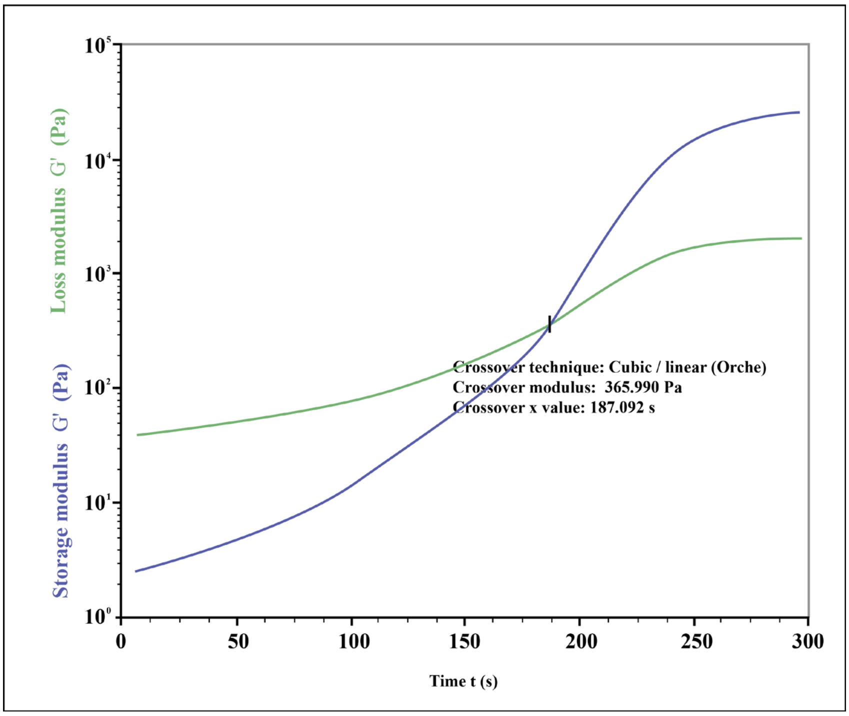

Figure 20 Time Sweep of silicone Ecoflex 30 at 50℃. Gelation time occurs at 187.1 s

Gelation Time of Ecoflex 30 at 55°C

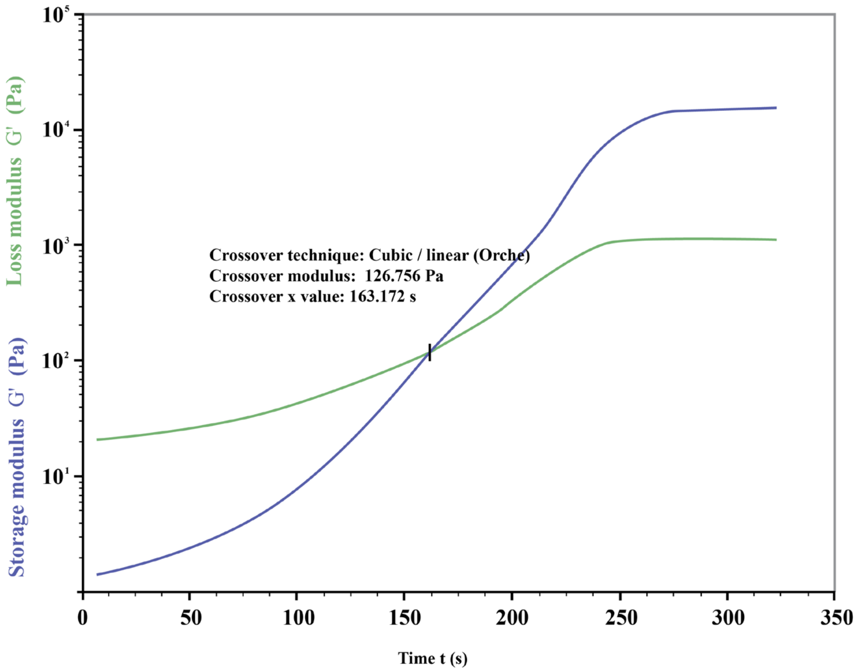

Figure 21 Time Sweep of silicone Ecoflex 30 at 55℃. Gelation time occurs at 163.2 s

The exponential decrease in curing time at higher temperature indicates an increase in silicone network crosslinking and faster curing speed. The gelation times are then plotted against their respective curing temperatures and the calibration curves specific to Ecoflex 30 and Ecoflex 50 can be drawn. An inverse exponential relationship is observed between the curing times and applied temperatures. For instance, when the temperature is increased from 30 °C to 40 °C, the gelation time is halved from about 1500 s to 750 s for silicone Ecoflex 30, while that of Ecoflex 50 falls from 3500 s to 1000 s. These curing times are then plotted against their respective temperatures to produce the calibration curve show in **Figure 22** below.

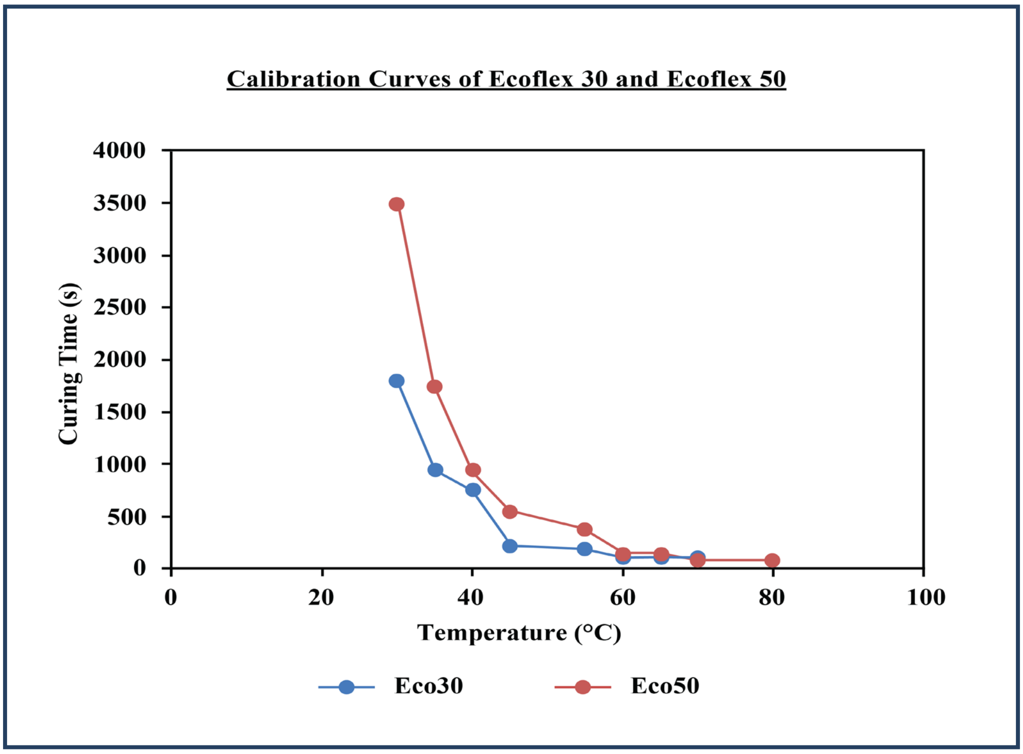

Figure 22 Plot of Curing times (s) of Ecoflex 30 (brown line) and Ecoflex 50 (blue line) versus temperatures (℃). Curing times markedly decrease with an increase in temperature.

By referring to the calibration curves, one can achieve great flexibility in selecting or combining various silicone resins or various temperatures in printing different layers or regions of any silicone medical products.

Following instance, to print a medical grade silicone product with an estimated print time of 900 s, one may select a combination of temperature and silicone resin to ensure the final printed layer is extruded way before 900 s, when there is a great likelihood that the resin cures and clogs up the nozzle. In this example, we can either apply a heating temperature of 35 °C to Ecoflex 30 or 40 °C to Ecoflex 50. Either heating method to the nozzle provide a sufficient estimated curing time of 1000 s.

Secondly, the plot of complex viscosities versus temperature of particular resin also provides vital information for the adjustment of the printing parameters. At a temperature of 50 °C, the complex viscosity Ecoflex 30 increases rapidly, with its curing time dropping drastically to 187 s, from a curing time of 805 s at 40 °C. Therefore, for rapid curing of any particular layer or region, one must ensure that the printing process at any stage has not taken more than 180 s.

Thus, the same CAD model can be printed using different permutations of printing parameters to achieve different properties at different layers or different regions. The estimated time for completion to print a certain CAD model can be obtained from the slicer.

At a temperature of 40 °C, the window of opportunity for extrusion starts from 600 s and ends 1000 s and has a duration of about 400 s. This critical period allows modulation of heating parameters and extrusion to obtain a silicone extrudate such that it is neither too liquid nor viscous, for optimal inter-laminar bonding with the previous extruded layers or substrate surfaces.

At a temperature of 55 °C, this window of opportunity for extrusion starts earlier at 150 s and only lasts for about 100 s. There is thus a very short working (printing and curing) time before the silicone resin cures. At this higher temperature, a shorter curing time can be used in conjunction with a faster print speed.

In addition to adjusting heat intensity, the curing speed can also be varied using silicones of variable viscosities. Contrary to expectation, when exposed to the same curing temperature, the less viscous specimen (Ecoflex 30) has a faster curing time when compared to the more viscous specimen (Ecoflex 50). When T90 starts to level off, increasing the temperature is ineffective in accelerating the reaction.

As shown in **Figures 23**, when heated to 40 °C, Ecoflex 30 has a gelation time of 805 s with a crossing modulus of 130 MPa. At 50 °C, it has a gelation time of 185s with a crossing modulus of 365 MPa. While the gelation times were shortened by 10 min over this 10 °C increase in temperature, the complex moduli were also lowered from 28 mPa to 8 mPa. However, there was a reciprocal steep increase in complex viscosity from 5 Pa.s to over 40 Pa.s. Similar trend is observed for Ecoflex 50, as shown in **Figures 24.**

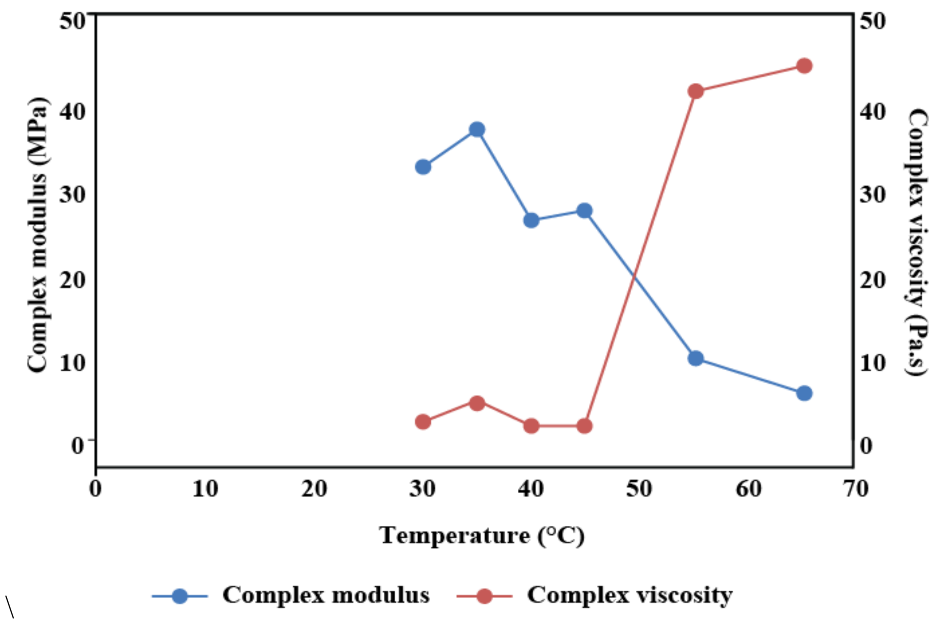

Figure 23 Plot of Complex Viscosity of Ecoflex 30 (red line) and Complex viscosity (blue line) versus temperature (℃). Complex Viscosity of Ecoflex 30 increases with temperature

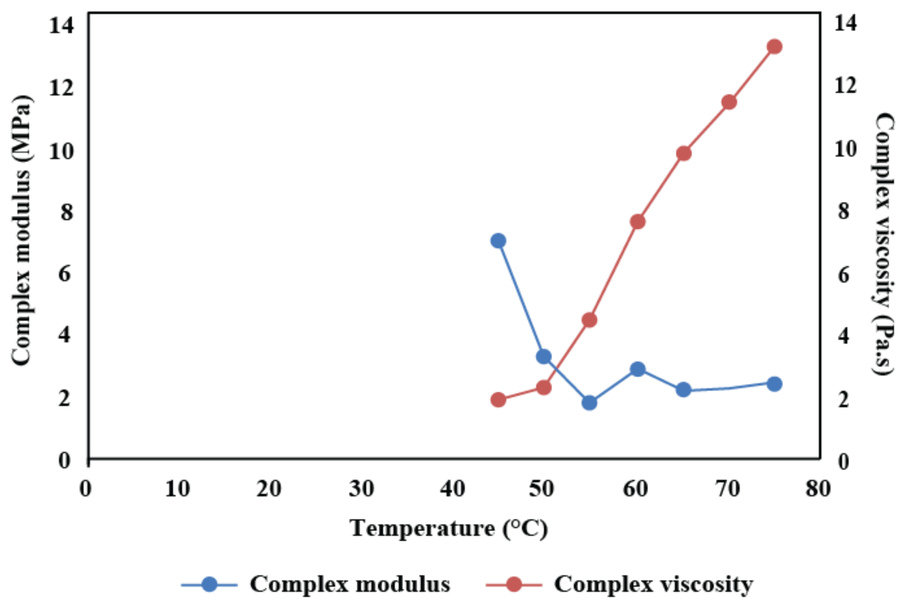

Figure 24 Plot of Complex Viscosity of Ecoflex 50 (brown line) and Complex viscosity (blue line) versus temperature (℃) Complex Viscosity increases with temperature. Complex Viscosity of Ecoflex 50 increases with temperature

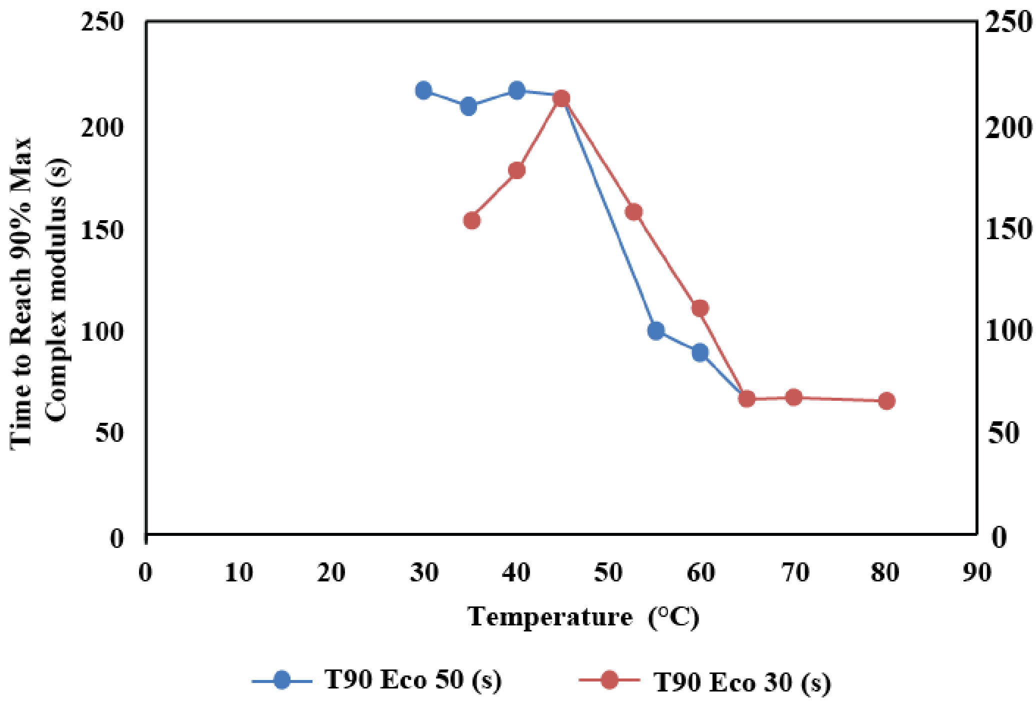

Figure 25 Plot of Time to reach 90 % maximum complex moduli (T90) vs temperature (℃). Both Ecoflex 30 and Ecoflex 50 show similar trend. Increasing heating temperatures above 40 ℃ decreases T90.

When heated below 60 °C, contrary to expectation, the more viscous Ecoflex 50 demonstrated longer curing times when compared to Ecoflex 30. When heated above 60 °C, both Ecoflex 30 and Ecoflex 50 have similar curing times. As the temperature increases, the complex viscosity decreases according to the temperature dependence of the viscous properties of the silicone resin. However, at even higher temperatures, the viscosity paradoxically increases due to the higher crosslinking rates.

3.2.2 Steady Shear Flow and Transient Shear Response

The steady shear flow measurements determine the fluid shear viscosity. Eight samples each of both Ecoflex 30 and Ecoflex 50 LSR samples are placed between the Peltier plate and hot platform. At various temperatures of 40, 50, 60, 70, 80 °C, viscosity is plotted against increasing times at a constant frequency of 1 Hz and the results are shown in the time sweep study in Table 5.

Transient measurements are necessary to evaluate the time-dependent response of the material, and to determine when the system reaches steady-state conditions. Five samples each of both Ecoflex 30 and Ecoflex 50 LSR samples are placed between the peltier plate and hot platform. At various temperatures of 40, 50, 60, 70, 80 °C, shear stress is plotted against increasing strain rates from 0 to 3 (1/s) at a constant frequency of 1 Hz). The shear stress versus strain figures, for both Ecoflex 30 and Ecoflex 50 samples, at 40, 50, 60, 70 and 80 ° C, are shown in **Appendix A**.

3D printing of the silicone meniscus implants is dependent on uninterrupted extrusion of silicone. Their viscous behaviours under different shear rates determine their flow characteristics.

Samples of Ecoflex 30 and Ecoflex 50 were tested under steady shear flow. Figure 26 shows rheological properties of Ecoflex 30 and Ecoflex 50 LSRs at 50 °C. Both Ecoflex 30 and Ecoflex 50 showed non-Newtonian behavior. At lower shear rates, shear stress is proportional to its shear rate.

At shear rates of 0.5 s^{-1}, the Ecoflex 30 viscosity decreases exponentially, until it levels off at high shear rate of 3 s^{-1}. For Ecoflex 30, the so-called zero-shear rate viscosity is around 3 Pa.s, when the viscosity is independent of increase in shear rate.

El Kissi et al. [121] reported similar behavior for PDMS solutions. We showed in **Figure 26** here a dramatic decrease in the viscosity of both Ecoflex 30 and Ecoflex 50 LSRs, from about 200 to 20 Pa.s, and from 500 to 5 Pa.s, respectively, over the shear rate range 0.01-5 s^{-1}.

At extremely high shear rates, viscosity becomes independent of shear rate, approaching infinite-shear rate viscosity. However, this infinite-shear rate viscosity is not usually measurable, since silicone degradation occurs before sufficiently high shear rates can be obtained. Shear thinning pseudoplastic behaviour is observed with Ecoflex 50 under steady shear flow above 3.5 s^{-1}. The decreasing viscosity with increasing shear rates is utilized for the current extrusion nozzle design.

Steady Shear Flow Study for Ecoflex 30 and Ecoflex 50

a) Ecoflex 30

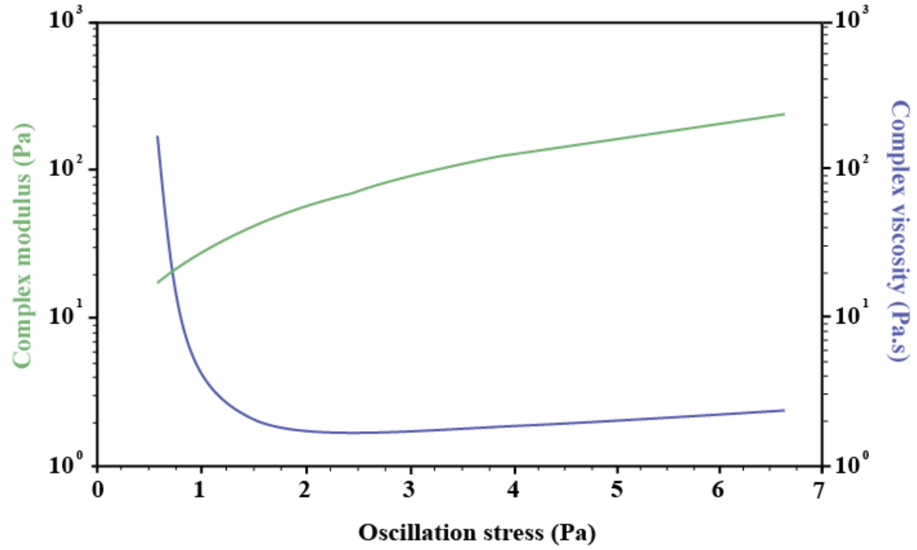

Figure 26 (a) Ecoflex 30 complex viscosity and complex modulus versus shear stress. Viscosity of Ecoflex 30 decreased with increasing shear stress

b) Ecoflex 50

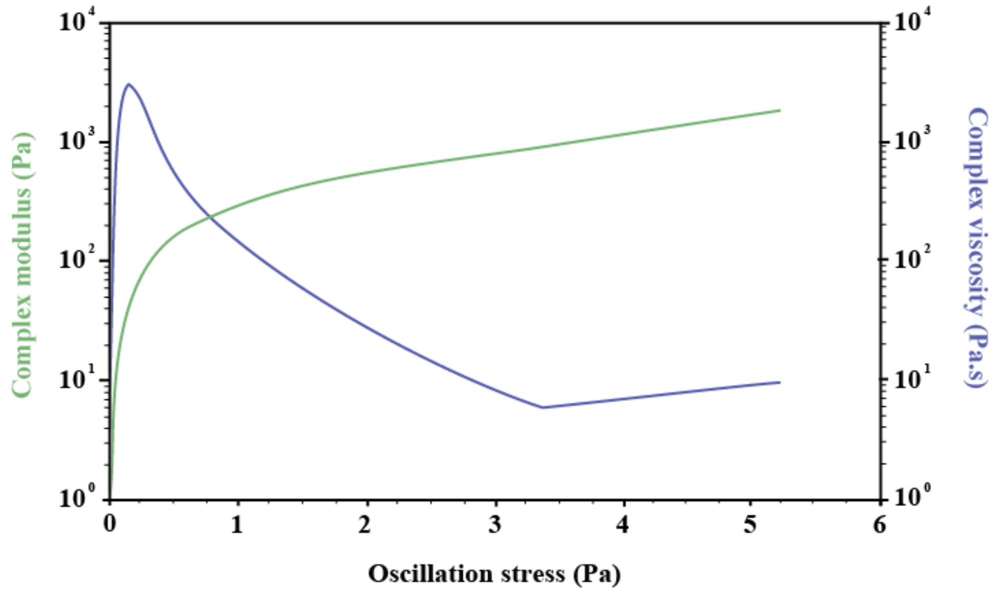

Figure 26 (b) Ecoflex 50 complex viscosity and complex modulus versus shear stress. Viscosity of 50 decreased with increasing shear stress

It is important to study the transient shear behavior for rheologically complex materials.

The study of transient shear behavior is important for the design of silicone printer and process optimization. The shear stress responses of Ecoflex 30 and Ecoflex 50 LSRs were measured as a function of shear rate and time to examine the transient behavior of Ecoflex 30 and Ecoflex 50 LSRs. Both Ecoflex 30 and Ecoflex 50 LSR show Bingham pseudoplastic shear thinning behavior on the first 250 seconds, as shown in **Figure 27.**

When samples were tested in shear rate ranges between 0.5< çù < 10 s^{-1}, shear thinning was observed for all temperature ranges. Generally, the effect of shear rate is quite significant on the flow behavior of Ecoflex 30. For example, at 55 °C, the viscosity of Ecoflex 30 decreases from 3 000 Pa.s at 0.05 s^{-1} to almost 2 Pa.s at 2.5 s^{-1} (**Figure 27a**), and the viscosity of Ecoflex 50 decreases from 300 Pa.s at 0.05 s^{-1} to almost 2 Pa.s at 2.5 s^{-1} (**Figure 27b**). This effect represents a depression of three orders and two orders of magnitude of viscosity, for Ecoflex 30 and Ecoflex 50, respectively, over a shear rate range of less than 3 s^{-1}.

Transient Shear Behavior for Ecoflex 30 and Ecoflex 50

(a) Ecoflex 30

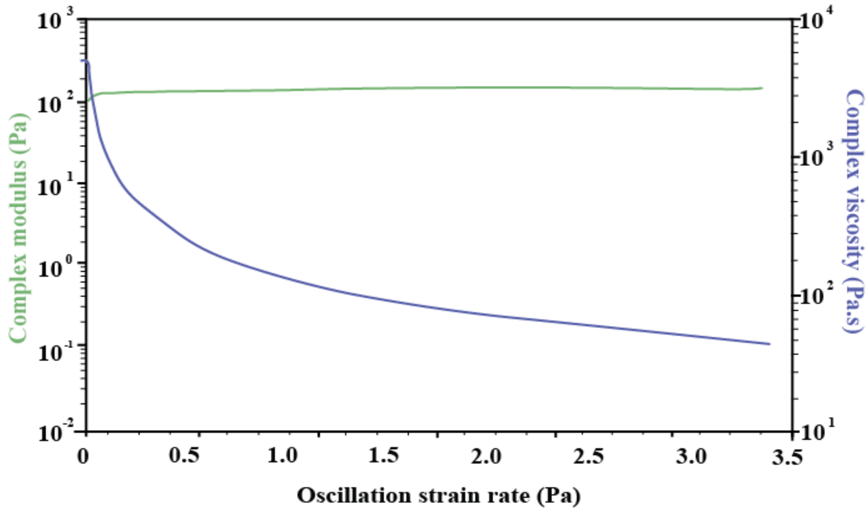

Figure 27 (a) Ecoflex 30 Complex viscosity and shear stress versus strain rate. Ecoflex 30 showed shear-thinning behavior

(b) Ecoflex 50

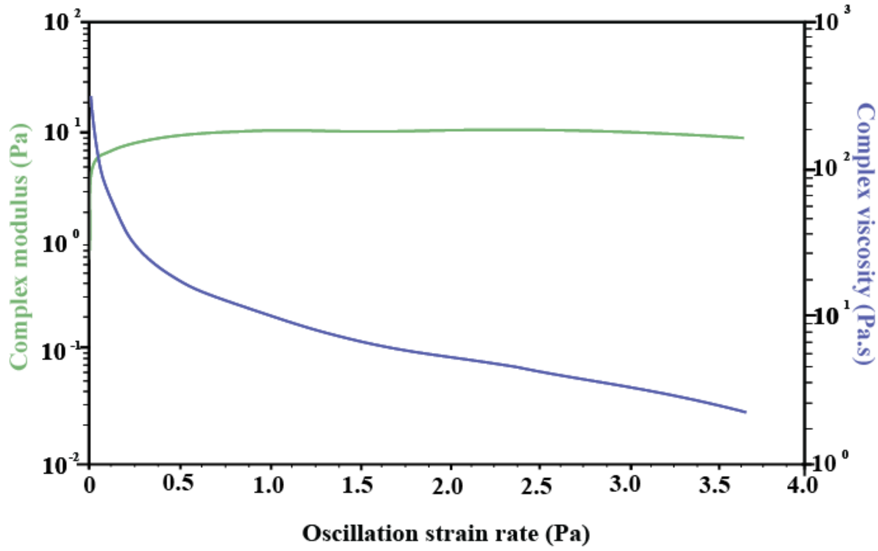

Figure 27 (b) Ecoflex 50 complex viscosity and shear stress versus strain rate. Ecoflex 50 showed shear-thinning behavior

3.2.3 Dynamic Flow Response

Five samples each of both Ecoflex 30 and Ecoflex 50 LSR samples are placed between the peltier plate and hot platform. At temperatures of 40, 50, 60, 70, 80 °C, modulus is plotted against increasing stress at a constant frequency of 1 Hz. at 40, 50, 60, 70 and 80 °C. These are shown in Appendix A.

In the dynamic test, test samples are subject to oscillating stress or strain to measure the storage modulus G’ and loss modulus G’’. Mechanical properties such as the storage modulus G’ and the viscous modulus G” are derived through oscillatory shear measurements, while storage and loss moduli were plotted against increasing stress at various temperatures, as shown in the temperature ramp table.6 (Performed time sweep and temperature ramps modes, ramp rate of 5 □C/min, constant strain of 0.025% and constant angular frequency of 10 rad/s were used).

The complex modulus G* represents the total resistance versus the applied strain. The dynamic test starts with the determination of the linear viscoelastic range where the complex moduli G* is constant over a wide range of stress. This shows that the internal structure of silicone is intact. Stress sweeps which were carried out for both Ecoflex 30 samples and Ecoflex 50 samples found this linear viscoelastic region to be from 35 Pa to 50 Pa range for Ecoflex 30 and 100 Pa to 150 Pa range for Ecoflex 50. This is shown in Figure 9 (Appendix A) and Figure 19 (Appendix A) for Ecoflex 50 and Ecoflex 30 LSRs, respectively.

Five samples each of both Ecoflex 30 and Ecoflex 50 LSR samples are placed between the peltier plate and hot platform. At various temperatures of 40, 50, 60, 70, 80 □ C, modulus is plotted against increasing frequency range from 0.01 to 100 rad/s at a constant oscillation strain rate of 0.03%.), as shown in the frequency sweep results Tables 7 and 8, for Ecoflex 30 and Ecoflex 50, respectively.

A frequency sweep test was performed to establish the viscoelastic behavior Ecoflex 30 and Ecoflex 50. Both samples demonstrated elastic and viscous responses. **Figure 28** shows the elastic G' and viscous *G*" moduli for both Ecoflex 30 and Ecoflex 50 LSRs over the frequency range 1-100 rad/s. Ecoflex 30 has both higher elastic and higher viscous modulus (**Figure 28a**), when compared to those of Ecoflex 50 (**Figure 28b**). Ecoflex 30 samples also demonstrated a greater elastic response than viscous response over the entire range of frequencies.

<u>Dynamic flow response for Ecoflex 30 and Ecoflex 50</u>

a) Ecoflex 30

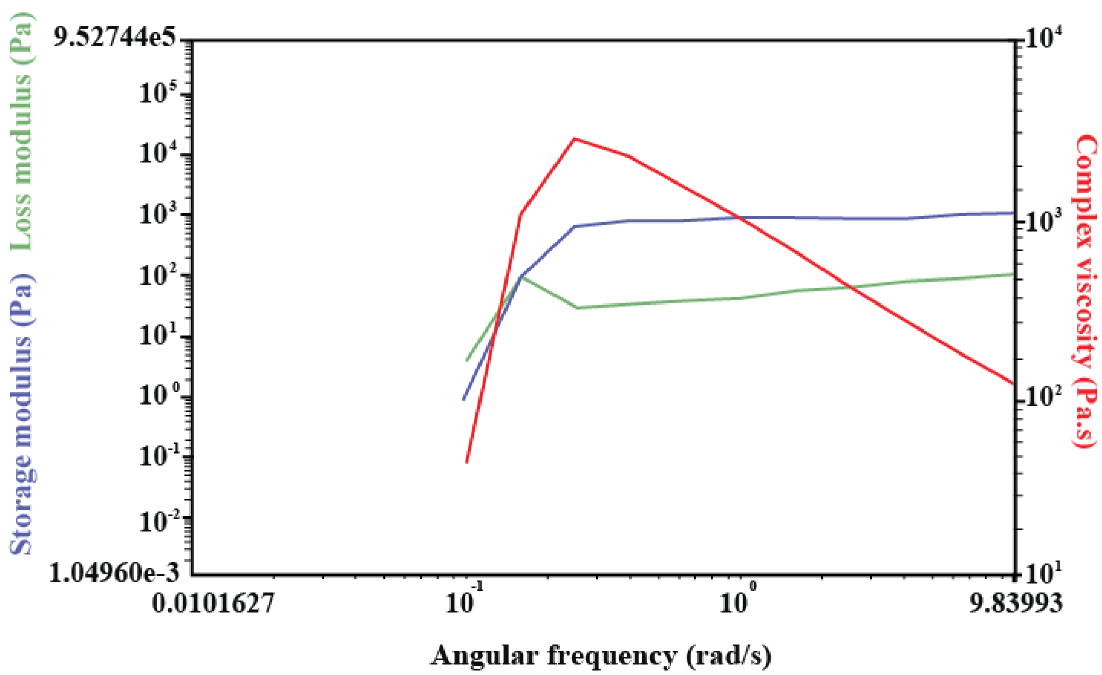

b) Ecoflex 50

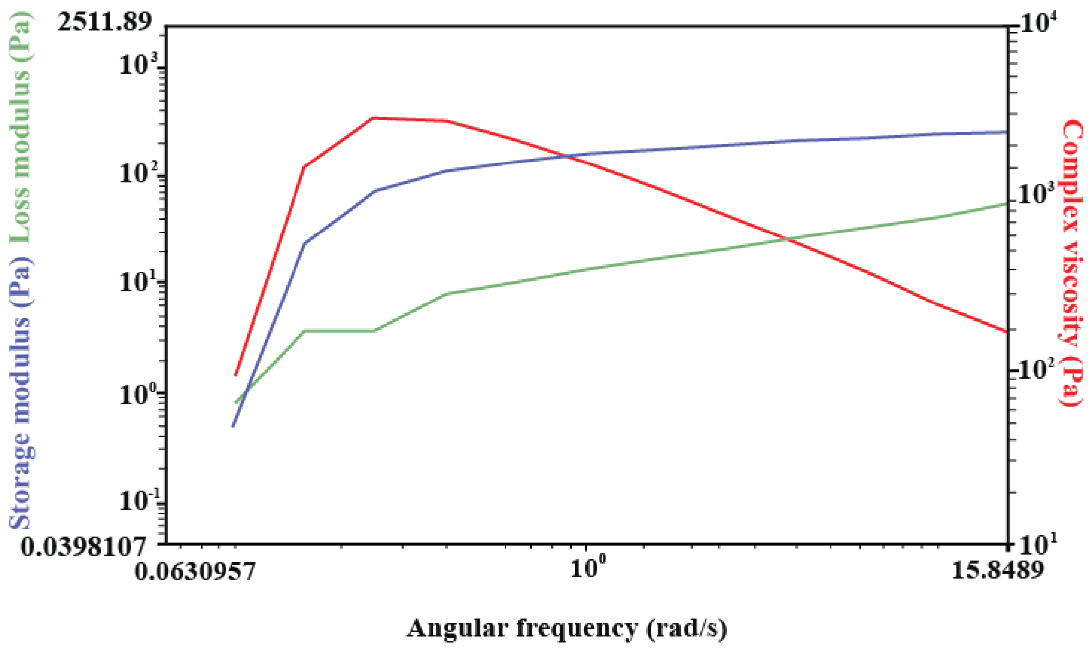

Figure 28 (a) Ecoflex 30 and (b) Ecoflex 50 storage modulus, loss modulus, complex viscosity vs. angular frequency. Ecoflex 30 and Ecoflex 50 have higher elastic moduli than viscous moduli over the entire range of frequency.

3.2.4 Frequency Dependence of Elastic Response of Silicone Rubbers

Ideal silicone rubbers exhibit pure elastic behaviour, independent of frequency, with higher magnitude of elastic modulus when compared to its viscous counterpart. With imperfect gel networks, the silicone response becomes frequency dependent, causing an increase in both storage and loss moduli [122].

At low frequency, the polymer has time to rearrange according to Brownian motion and measurements portray the elastic deformation of the gel network at equilibrium. As the physical interactions are created and broken faster than the deformation rate, they do not store elastic energy. At high frequency, there is not ample time to rearrange. Physical interactions persist longer to restrict the polymer movement and store elastic energy. As the frequency approaches zero, the elastic modulus represents the contribution mainly from the chemical crosslinking in the gel, owing to the extremely short lifetime of physical interaction.

At higher frequencies, the solvent and polymer interactions increase both the storage and loss moduli. At the highest frequency, the contribution of physical interactions is inseparable from those of chemical crosslinkings.

At lower temperatures of 40 °C and 45 °C, shown in **Figures 29** and **30**, respectively, the silicone Ecoflex 30 demonstrate complete elastic response, with G' higher than G", independent of frequency, at lower oscillation frequency ranges of 0.1 Hz and 10 Hz. The observed storage modulus reflects a major contribution from chemical crosslinks.

At higher temperatures of 50 °C and 55 °C, **shown in Figures 31 and 32**, respectively, the silicone Ecoflex 30 showed elastic response, with G' higher than G", independent of frequency, at higher oscillation frequency ranges of between 1 and 100 Hz. At higher frequencies, the contribution of physical entanglements and local polymer chain interactions to both the storage and loss moduli is indistinguishable from that of chemical crosslinkings.

Regardless of the curing or heating temperatures used, the final extruded silicone has only reached a "stable" state when both the observed storage moduli G' and loss moduli G" have plateaued and these values will only then reflect the effect of chemical crosslinking. The magnitude of both storage and loss moduli also increased with increase in curing temperature.

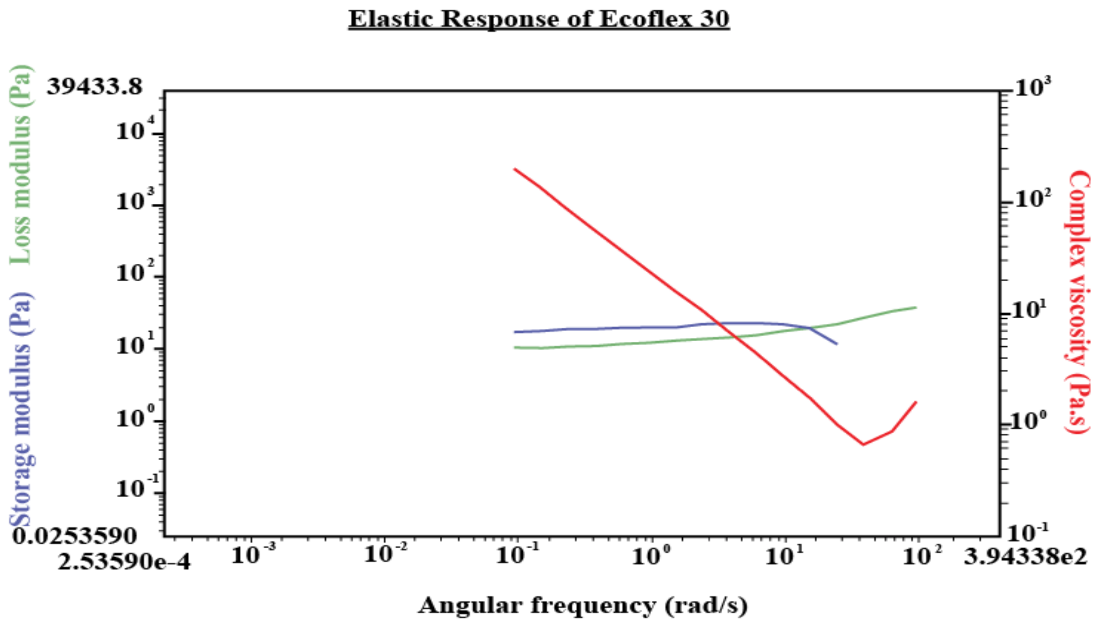

Figure 29 Frequency Sweep of silicone Ecoflex 30 at 40 ℃. "Stable" state is achieved at lower frequency when heated at lower temperature.

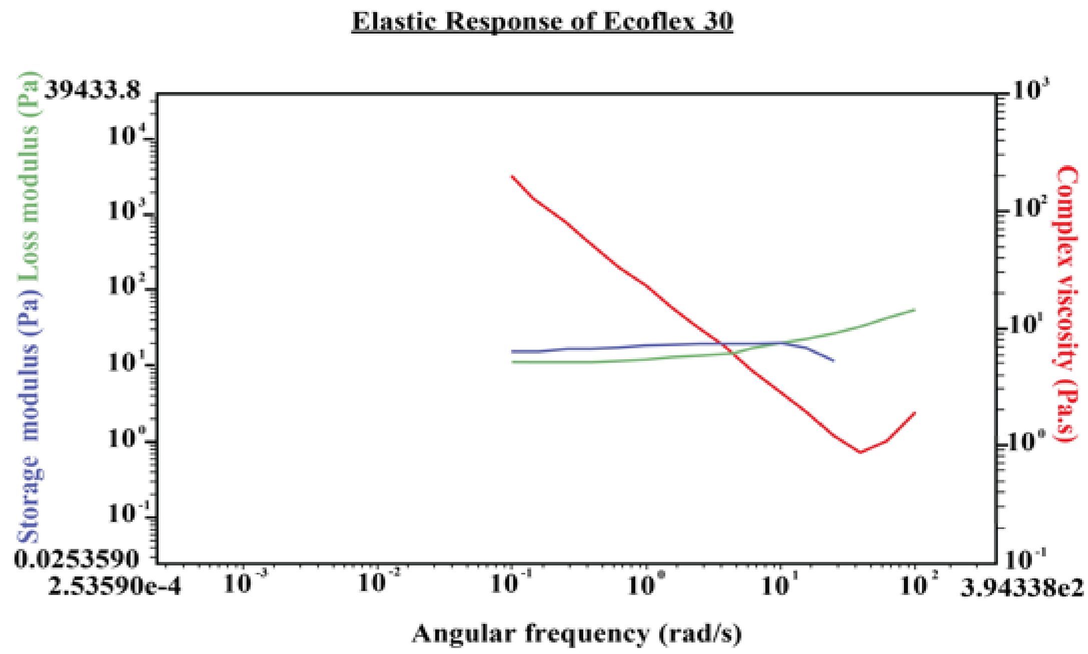

Figure 30 Frequency Sweep of silicone Ecoflex 30 at 45 °. "Stable" state is achieved at lower frequency when heated at lower temperature.

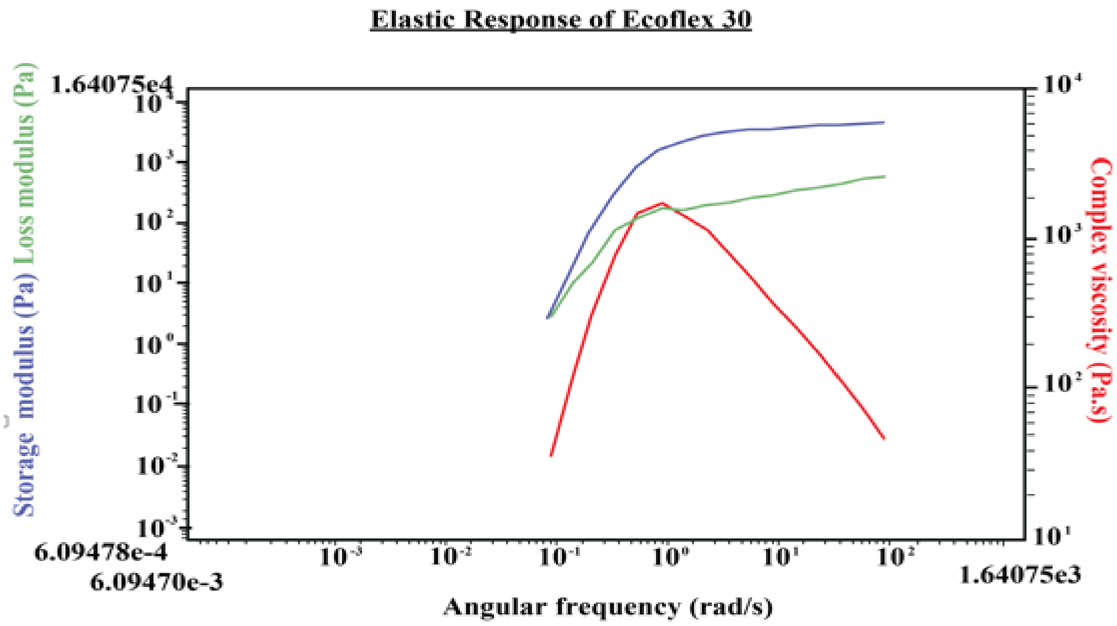

Figure 31 Frequency Sweep of silicone Ecoflex 30 at 50°. "Stable" state is achieved at higher frequency when heated at higher temperature

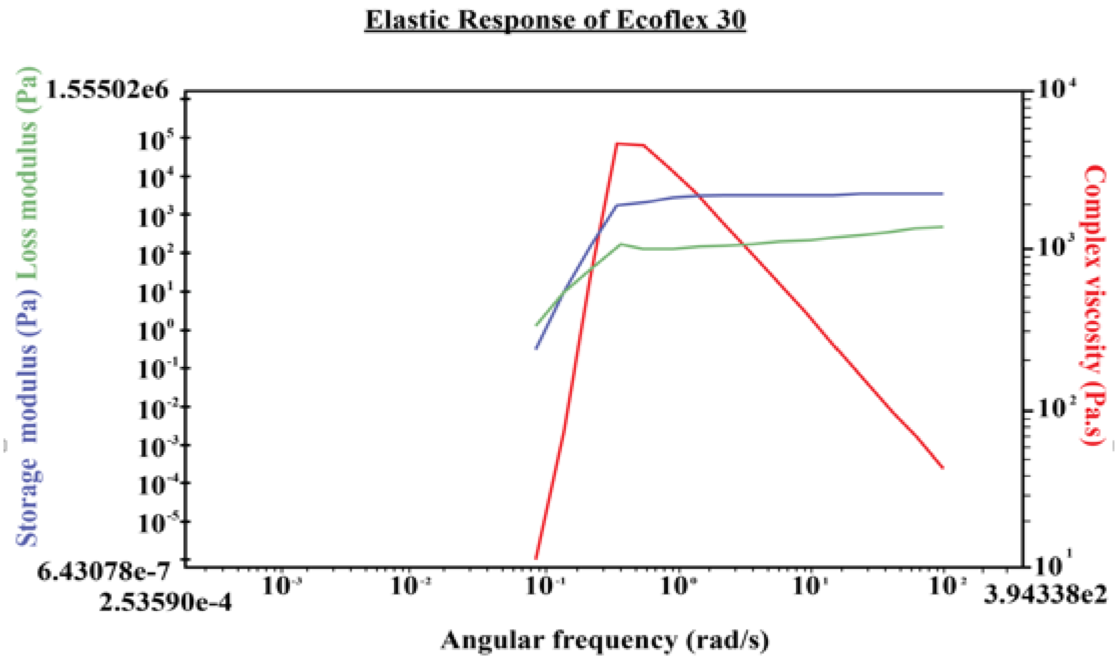

Figure 32 Frequency Sweep of silicone Ecoflex 30 at 55℃. "Stable" state is achieved at higher frequency when heated at higher temperature.

Table 5 *Time sweep rheology data for Eco30 and Eco50 samples.*

	Storage modulus (Pa)	Loss modulus (Pa)	Tan(delta) tan(	Angular frequency (rad/s)	Oscillation torque (µN.m)	Step time (s)	Temperature (°C)	Raw phase	Oscillation displacement (rad)	Complex viscosity (Pa.s)
1 ECO30	34.631	30.943	0.893	10.000	19.644	62.054	30.003	45.943	0.0009985	4.644
2 ECO30	38.972	42.208	1.083	10.000	24.760	117.898	34.998	50.916	0.0009965	5.744
3 ECO30	153.586	156.635	1.019	10.000	96.093	608.548	36.991	46.816	0.0009790	21.936
4 ECO30	97.186	89.971	0.925	10.000	54.582	186.237	50.007	44.802	0.0009356	13.243
5 ECO30	159.701	163.389	1.023	10.000	86.497	80.654	55.018	46.858	0.0008455	22.847
6 ECO30	1010.930	448.852	0.444	10.000	427.526	99.305	59.985	24.068	0.0008509	110.609
7 ECO30	1543.420	461.978	0.299	10.000	599.764	68.333	65.016	16.718	0.0008185	161.107
8 ECO30	7181.850	600.973	0.083	10.000	3275.890	130.246	69.991	4.7715	0.0009990	720.691
1 ECO50	109.598	145.516	1.327	10.000	81.283	3600.500	29.999	54.703	0.0009978	18.217
2 ECO50	153.082	151.512	0.989	10.000	95.785	1775.540	35.000	45.962	0.0009947	21.538
3 ECO50	509.542	502.285	0.985	10.000	321.283	1198.320	37.000	44.948	0.0009894	71.548
4 ECO50	351.666	344.738	0.980	10.000	217.395	819.532	44.994	44.963	0.0009755	49.245
5 ECO50	284.276	282.491	0.993	10.000	176.132	459.461	50.016	45.484	0.0009732	40.076

6 ECO50	486.849	473.578	0.972	10.000	290.345	266.932	55.011	44.586	0.0009423	67.918
7 ECO50	83.222	82.977	0.997	10.000	49.427	186.268	60.007	47.276	0.0009577	11.750
8 ECO50	233.458	220.072	0.942	10.000	130.028	74.401	65.018	44.123	0.0009004	32.083
9 ECO50	408.167	405.527	0.993	10.000	218.386	24.788	75.033	45.269	0.0008375	57.536
10 ECO50	70.956	70.628	0.995	10.000	38.842	43.524	80.013	47.656	0.0008896	10.011

Table 6 Temperature ramp rheology data for Eco30 and Eco50 samples.

	Storage modulus (Pa)	**Loss modulus (Pa)**	**Tan(delta) tan(**	**Angular frequency (rad/s)**	**Oscillation torque (µN.m)**	**Step time (s)**	**Temperature (°C)**	**Raw phase**	**Oscillation displacement (rad)**
t50 ECO30	66.280	78.483	1.184	10.000	40.192	186.444	53.211	52.747	0.0008921
	97.260	91.971	0.945	10.000	51.944	192.617	53.310	45.408	0.0008803
t50 ECO50	75.972	81.536	1.073	10.000	46.516	415.933	57.037	49.605	0.0009508
	89.646	87.156	0.972	10.000	52.124	422.142	57.131	46.380	0.0009476
t55 ECO30	139.636	152.239	1.090	10.000	77.696	130.335	57.199	48.847	0.0008410
	233.070	200.847	0.861	10.000	113.316	136.515	57.300	41.563	0.0008193

t55 ECO50	111.603	111.692	1.001	10.000	64.805	167.73	57.896	46.765	0.0009252
	141.144	124.085	0.879	10.000	76.979	173.871	57.993	42.680	0.0009205
t60 ECO30	258.867	262.778	1.015	10.000	133.385	68.353	61.226	46.162	0.0008014
	494.641	371.811	0.751	10.000	213.573	74.452	61.341	37.291	0.0007619
t60 ECO50	130.879	149.745	1.144	10.000	79.243	148.988	62.570	50.305	0.0008912
	187.625	178.844	0.953	10.000	102.092	155.265	62.674	44.647	0.0008780
t65 ECO30	31.603	49.895	1.578	10.000	22.183	86.976	66.560	63.382	0.0008698
	63.524	62.622	0.985	10.000	31.252	93.110	66.648	47.727	0.0008082
t65 ECO50	190.458	195.848	1.028	10.000	106.471	74.580	66.341	46.803	0.0008674
	297.752	240.591	0.808	10.000	145.621	80.687	66.460	39.561	0.0008438
t70 ECO30	60.536	63.421	1.047	10.000	30.051	37.240	65.729	49.618	0.0007899
	124.576	83.547	0.670	10.000	50.407	43.369	65.816	35.302	0.0007630
t70 ECO50	129.857	130.525	1.005	10.000	72.901	49.652	70.932	46.636	0.0008886
	189.285	160.852	0.849	10.000	96.382	55.873	71.048	41.359	0.0008667

Table 7 Frequency sweep rheology data for Eco30 samples.

	Storage modulus (Pa)	Loss modulus (Pa)	Tan(delta) tan(	Angular frequency (rad/s)	Oscillation torque (µN.m)	Step time (s)	Temperature (°C)	Raw phase	Oscillation displacement (rad)	Complex viscosity (Pa.s)	Complex modulus (Pa)	Oscillation stress (Pa)
t30	0.831	1.25915	1.514	0.100	0.379	247.905	29.999	56.592	0.0005502	170.109	17.010	0.575
	1.935	5.84633	3.020	1.000	1.573	76.267	29.994	72.264	0.0005611	19.7958	19.795	0.708
	103.584	262.083	2.530	100.000	154.455	5.960	29.995	154.774	0.0005497	2.35722	235.722	6.651
t40	8.147	2.48393	0.304	0.100	1.686	248.220	40.011	16.956	0.0004334	204.825	20.482	0.688
	0.458	4.41045	9.613	1.000	1.116	76.8624	40.008	84.910	0.0005516	23.995	23.995	0.826
	2.280	305.405	133.893	100.000	181.852	5.9764	39.997	155.086	0.0005489	1.608	160.837	4.277
t45	16.911	12.201	0.721	0.100	7.897	66.043	45.001	35.809	9.04E-04	208.536	20.853	0.628
	19.803	13.1085	0.661	1.000	10.323	180.847	45.000	33.570	1.040E-03	23.748	23.748	0.822
	-183.435	59.8273	-0.326	100.000	230.587	248.156	45.001	175.085	7.880E-04	1.929	192.945	5.070
t60	0.168	0.263722	1.569	0.100	0.130	65.821	59.998	57.572	9.940E-04	3.127	0.312	0.010
	1539.060	96.7571	0.062	1.000	552.996	180.524	59.993	3.595	8.570E-04	1542.100	1542.100	44.007
	2830.150	472.076	0.166	100.000	1000.110	247.793	59.998	60.003	1.010E-03	28.692	2869.250	96.562
t65	1.129	4.33259	3.835	0.100	1.337	65.877	64.986	64.986	7.130E-04	13.795	4.477	0.106

	1005.630	56.5336	0.056	1.000	412.608	180.064	65.008	3.216	9.780E-04	1007.220	1007.220	32.836
	1346.570	299.693	0.222	100.000	381.990	247.098	65.006	19.753	1.030E-03	44.774	1379.520	47.318

Table 8 Frequency sweep rheology data for Eco50 samples.

	Storage modulus (Pa)	**Loss modulus (Pa)**	**Tan(delta) tan(**	**Angular frequency (rad/s)**	**Oscillation torque (µN.m)**	**Step time (s)**	**Temperature (°C)**	**Raw phase**	**Oscillation displacement (rad)**	**Complex viscosity (Pa.s)**	**Complex modulus (Pa)**	**Oscillation stress (Pa)**
t35	0.066	0.371	5.583	0.100	0.157	65.720	34.998	79.916	9.140E-04	3.778	0.377	0.012
	0.546	3.101	5.676	1.000	1.307	180.069	35.002	80.853	9.110E-04	3.149	3.149	0.104
	-134.105	224.073	-1.670	100.000	257.423	245.768	34.997	159.643	8.740E-04	2.611	261.138	8.304
t40	0.020	0.102	4.953	0.100	0.043	65.923	39.989	78.863	1.000E-03	1.040	0.104	3.470E-03
	0.168	0.865	5.127	1.000	0.364	180.043	40.005	82.266	9.970E-04	0.881	0.881	0.029
	-194.944	60.504	-0.310	100.000	238.675	246.427	40.005	175.113	8.020E-04	2.041	204.118	5.458
t50	0.200	0.180	0.900	0.100	0.111	65.859	50.008	42.066	9.110E-04	2.694	0.269	8.920E-03
	0.760	1.139	1.497	1.000	0.558	180.483	49.995	57.927	9.100E-04	1.369	1.369	0.045
	-160.010	64.814	-0.405	100.000	217.185	247.352	50.004	174.125	7.510E-04	1.726	172.639	4.711

t55	0.106	0.208	1.967	0.100	0.097	65.893	54.993	63.173	9.930E-04	2.343	0.234	7.760E-03
	5.866	3.807	0.649	1.000	2.683	180.549	55.001	33.215	9.220E-04	6.993	6.993	0.214
	-111.461	137.593	-1.234	100.000	237.502	247.920	54.993	167.568	8.870E-04	1.770	177.075	5.236
t70	0.403	1.043	2.583	0.100	0.431	65.880	70.007	68.863	8.450E-04	11.189	1.118	0.034
	3218.650	180.541	0.056	1.000	1252.490	180.573	69.999	3.205	8.520E-04	3223.710	3223.710	99.671
	4515.860	786.372	0.174	100.000	1725.030	247.077	69.992	10.978	9.180E-04	45.838	4583.820	152.703

Table 9 Frequency sweep rheology data for Eco30 and Eco50 samples.

	Storage modulus (Pa)	**Loss modulus (Pa)**	**Tan (delta)**	**Angular frequency (rad/s)**	**Oscillation torque (µN.m)**	**Step time (s)**	**Temperature (°C)**	**Raw phase**	**Oscillation displacement (rad)**	**Complex viscosity (Pa.s)**	**Complex modulus (Pa)**	**Oscillation stress (Pa)**	**Oscillation strain rate (1/s)**
1 ECO30	27.728	26.695	0.962	6.309	16.699	206.709	24.996	46.100	1.080E-03	6.100	38.490	0.226	3.586
2 ECO30	15.088	14.764	0.978	1.584	9.380	187.725	29.996	44.623	1.070E-03	13.319	21.110	0.749	0.056
3 ECO30	27.952	26.226	0.938	10.000	15.833	214.143	35.001	48.961	1.090E-03	3.832	38.329	1.388	0.056
4 ECO30	21.295	17.732	0.832	10.000	10.960	213.906	39.988	47.634	1.090E-03	2.771	27.711	1.007	0.140
5 ECO30	21.478	16.491	0.767	3.981	11.716	201.435	45.003	38.588	1.060E-03	6.802	27.079	0.954	0.140

6 ECO30	7.715	8.899	1.153	0.158	2.972	109.152	54.983	49.080	6.020E-04	74.319	11.778	0.236	3.180E-03
7 ECO30	1.761	2.842	1.613	0.158	1.191	108.976	60.007	58.235	8.510E-04	21.096	3.343	0.094	5.040E-04
8 ECO30	126.475	116.657	0.922	0.158	6.880	109.039	64.993	42.684	9.550E-05	1085.630	172.061	0.547	5.040E-04
1 ECO50	0.124	0.570	4.574	0.630	0.242	170.352	39.994	79.639	9.980E-04	0.926	0.584	0.019	7.960E-03
2 ECO50	0.096	0.335	3.473	3.473	0.144	157.127	45.007	75.230	9.970E-04	0.876	0.349	0.024	7.040E-03
3 ECO50	0.512	0.542	1.058	0.398	0.308	156.842	49.994	47.033	9.100E-04	1.875	0.746	0.024	6.000E-03
4 ECO50	0.845	0.954	1.128	0.251	0.515	137.624	55.009	48.569	9.670E-04	5.077	1.275	0.041	7.960E-03
5 ECO50	1.170	1.299	1.109	0.251	0.695	137.654	60.011	48.061	9.510E-04	6.96118	1.748	0.055	7.960E-03
6 ECO50	0.495	0.803	1.621	0.1	0.368	65.984	65.008	58.360	9.320E-04	9.44188	0.944	0.029	3.110E-03
7 ECO50	0.403	1.043	2.583	0.1	0.431	65.880	70.007	68.863	8.450E-04	11.1898	1.118	0.034	3.070E-03
8 ECO50	12.449	3.925	0.315	0.1	2.758	65.833	75.001	17.503	5.040E-04	130.537	13.053	0.219	3.090E-03

3.3 The Design and Development of Customized Silicone 3D Printer

3.3.1 Design of the Printer

The first most important criterion is to have an Discovery extruder pump connected to an open-source Core-XY 3d printer which is operating on open-source Marlin firmware. These open-sourced features allow 1) the customization of the 3D printer to extrude silicone, 2) the modulation of heating parameters to regulate heating at various stages of extrusion and 3) modification of printing and extrusion speeds.

The firmware is a type of computer program that controls the device's specific hardware and provides a standardized operating platform for the device's more complex software The second most important criterion is to have adjustable heater blocks and platforms which are controllable and modifiable to provide the required heating temperatures at various stages of printing.

To establish connection between the printer and extruder, the first step requires the RAMPS platform to be first plugged onto the Arduino Mega board. The second step involves connecting the wires of the Discovery Extruder to RAMPS. The third step involves adjustment of the Marlin Firmware to synchronize the Extruder and the Core-XY Printer. Finally, the extruder tip is mounted onto the printer.

The Discovery extruder operates on a stepper motor-based drive system, thus the Discovery extruder can be "plugged into" any stepper motor driver/controller on the microcontroller electronics board. The Core XY uses its own Marlin firmware based on the open standard Arduino and RAMPS electronics.

To connect the Discovery wiring, the four screws of the electrical connector are loosened on the second extruder port typically labeled E1 (extruder 1 is usually E0) and the stripped wires are slid under them in the same color arrangement as the other motors in the printer.

3.3.2 Hardware

The essential hardwires are the Arduino Mega 2560 and RAMPS 1.4 platform of the Core-XY 3D printer and the Discovery Extruder. .

(1) Arduino Mega 2560

The Arduino board links the power supply to the stepper motors which controls the movement of the 3D printer axis and extruders. This open-source computing platform comprises a simple input/output board and a development environment that implements the processing and wiring language. It has a AT mega 2560 microcontroller and contains 54 input/output pins, a 16 MHz crystal oscillator, USB connection, power jack, an ICSP header and reset button

Thus, it is needed for the project to control the movement of the 3D printer axis and the extruder through stepper motors. A 12 V 10 A power is necessary to power the system. The Arduino Mega 2560 board is shown below in Figure 33.

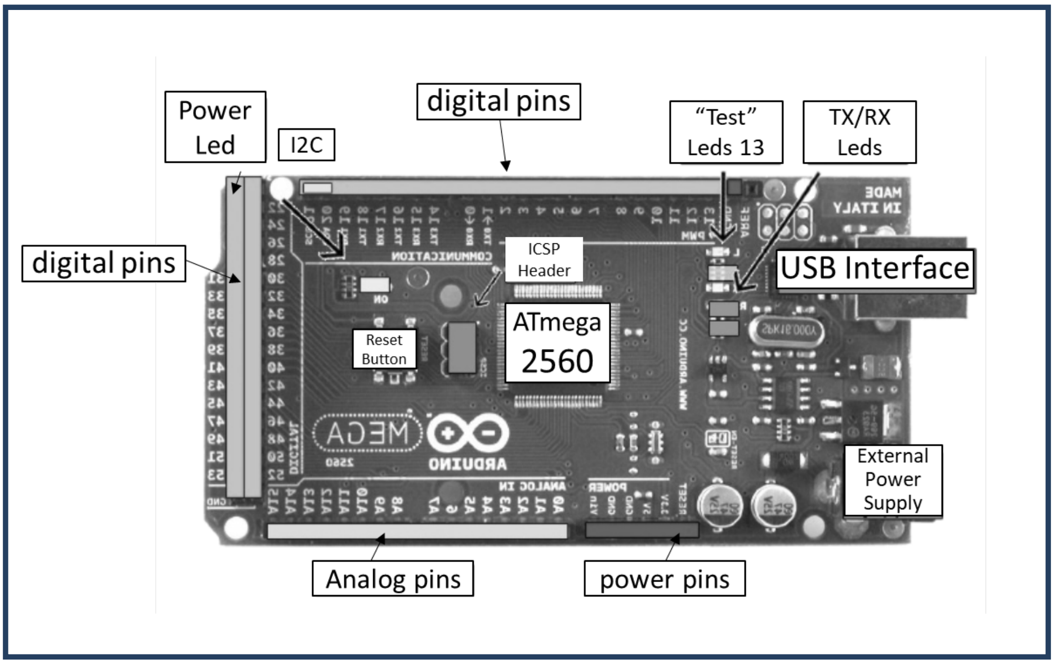

Figure 33 The Arduino Mega 2560 board

(2) RepRep Arduino MEGA Pololu Shield (RAMPS)

RAMPS links Arduino to other electrical components. It consists of a RAMPS 1.4 shield, an Arduino Mega 2560 board, and a maximum of five Pololu Stepper drivers. It can control up to 5 stepper motors with 1/16 stepping precision and interface with a hotend, a heat bed, a fan (or a second hot end), a LCD controller, a 12 V power supply, up to three thermistors, and up to six end stoppers. The schematic diagram of the RAMPS 1.4 is shown in Figure 34.

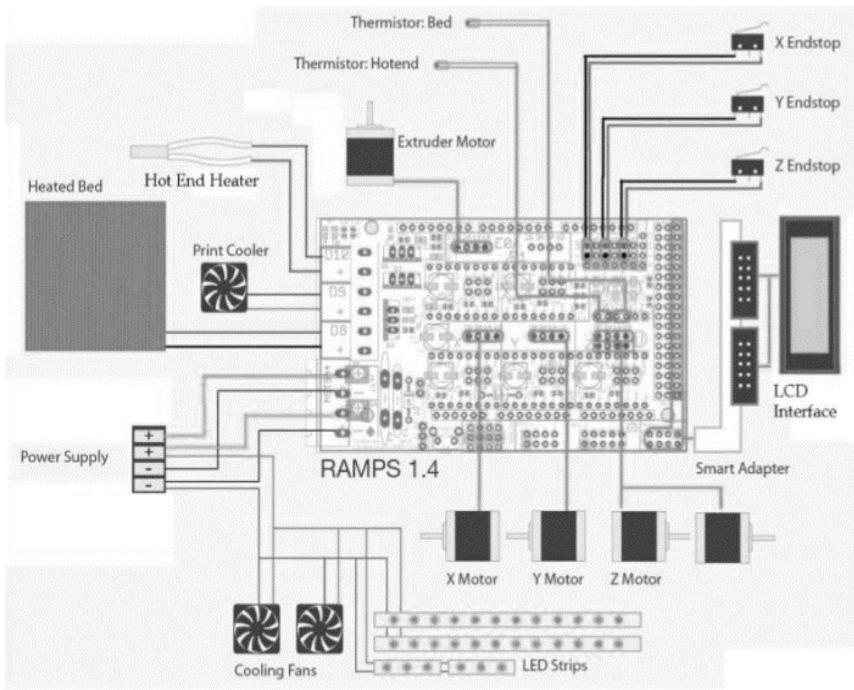

Figure 34 Schematic Diagram of the RAMPS 1.4

There are a few modifications that will need to be made to the printer's firmware in the 3D printer microcontroller. These include adjusting the temperature control for the Discovery extruders and any additional heating blocks.

To modify the printer's firmware, one needs to first download the firmware and Arduino IDE control software to the computer. The Arduino control software will allow the computer to interface with the electronics board of the 3D printer.

Connect the computer to the USB port of the RAMPS board. Next open the Arduino IDE program and select Tools > Board > and Arduino Mega 2560 (or other if your printer is based off another Arduino microcontroller). Next, select Tools > Serial Port > and then choose the option labeled USB TTY. Finally, open the firmware.

Now to make the necessary modification in the firmware code. Go to the tab titled configuration.h (same for all firmwares) and find the line of code (use the find and replace tool):#define MIN_EXTRUDER_TEMP 60. This command tells the 3D printer not to operate unless the extruder has reached at least 60°C. In Repetier there is also a user interface minimum that can be changed but not necessary: #define UI_SET_MIN_EXTRUDER_TEMP 0

These are the only changes to the firmware necessary to get the Discov3ry and 3D printer to work together. It is recommended to start with the firmware that comes with the printer. If one is using a RepRap or other printer using the generic firmwares, then it may require other printer specific modifications. Now click the Verify/Compile button and if it is successful, then click the Upload button. Save the INO file on your computer as backup and future reference. The printer electronics are now ready to extrude paste after the extruder tip is mounted.

3.3.3 Software

The softwares, which are essential to operate the 3D Printer, and Discovery Extruder include the Repertier-Host software and Marlin firmwares.

(1) Repertier-Host

The Repetier-Host is an open-source host software, which is compatible with Marlin and other firmwares. It communicates in classic ASCII mode or binary Repetier-

Protocol and includes the fast Slic3r slicer. It has a STL composer which places, rotates and scales the STL files on the print-bed and stores or slices it. The STL files are then automatically converted to G-Codes which can be previewed visually and modified before being sent to the 3D printer.

(2) Marlin Firmware

Marlin is an open source firmware for the RepRep family of 3D printers. Marlin firmware runs on the 8-bit Amel-AVR microchip embedded within the Arduino Mega 2560 in RAMPS 1.4 platform. This firmware is the operating system for all control, data monitoring and manipulation functions. It coordinates in real-time, the steppers, heaters, sensors, lights, LCD displays and other processes in the 3D printing process.

Marlin can only receive, read and print in G-codes. From a PC or Secure Digital (SD) card, many commercially available host soft-wares like Repetier Host, Pronterface, Octoprint, Cura or Simplify3d can generate the G-codes by first “slicing” the 3D CAD models. Subsequently, Marlin can use these G-codes to further instruct the printers. The movement commands received by Marlin is added to the movement queue, which is processed by the “stepper interrupt”, converting linear movement into precisely-timed electronic pulses to the stepper motors.

A slower second-interrupt controls the heaters and sensors, while the main loop commands processing, updates display and controller.

3.3.4 The Heat-Cured Extrusion-Based Printing Process

This section covers a) the conversion of MRI DICOM file to .stl format for 3D Printing, b) Slicer settings input, c) Stepper driver calibration and d) Selection of printing parameters.

3.3.4.1 Image Processing for Customized Meniscal Implant- MRI/CT

Image processing is first performed by the conversion of the MRI-CT DICOM file images into 3D Printable STL files [122]. The following stages of conversion are involved:

(1) Preparing the DICOM dataset

The first stage involves importing of MRI/CT dataset using the 3D Slicer. This is followed by the generation of 3D visualization by selecting the volume rendering module which is a built-in module that generates an interactive 3D visualization from the dataset. By analyzing the 3D volume, we are able to access and analyze the quality of the dataset. This analysis can be fine-tuned by selecting the Scalar Opacity Mapping.

The 3D Slicer is an open source software available on multiple operating systems used to analyze, visualize medical images and generate 3D volumes that can be used for 3D printing.

(2) Creating the 3D Volume (segmentation)

The Editor module is selected to create and edit the label maps which the 3D volume will be based. Different color codes representing different organs are first chosen for the label maps. There can be as many labels as is necessary, each one segmenting different regions, then merging them into one single volume, or create individual models from each label map. The editing of the selected label map can be subsequently performed by the paint effect, draw effect, wand effect and other editing features. The 3D model can then be created by selecting "make model' icon and saved as .stl file.

(3) Preparing for printing

The above .stl file is first imported for further cleaning using Meshmixer. Meshmixer is a free software by Autodesk and is widely used for 3D printing. It can be used to edit the segmentation and facilitate 3D printing. The "reduce the triangle counts" and "plane cuts" functions can help to provide clean, sharp edges and close up gaps and fill holes. At this point, flaws can be fixed and gaps can be bridged in the model. Finally, one can use Meshmix function to make, align and scale a base for the model before the .stl file is exported to Repertier-Host for printing. The Repertier open-source software downloaded on the PC is used to interface with the Marlin firmware of the Core XY printer. It contains the Slicer program and requires further input setting as shown in the following section.

3.3.4.2 Slicer Settings Input

The Slicer setting parameters are selected to give a layer height less than or equal to 80% of the nozzle diameter and extrusion width which is greater or equal to the nozzle diameter. For example, with a 0.5mm nozzle, the maximum layer height is 0.5X 80% = 0.4mm and the extrusion width should be 0.5mm or greater. The extrusion volume is estimated by slicing software based on the settings. The lower limit of the layer height

and widths are determined by the extrusion value required to ensure that the perimeter of the product is completely filled with no gaps in the middle and no infills.
The Cartesian printer has a build volume set at X_225 mm, Y_145 mm and Z_150 mm. For the purpose of printing a silicone meniscus implant, the following Print Settings have been input as follows: first layer height of 0.4mm, 3 vertical shells, 3 top and 3 bottom horizontal shells, 100 % of filled density with concentric fill patterns, 3 skirt loops at a distance of 20 mm from the print object, without any support. The speeds for print moves are set as follows: 20 mm/s for all perimeters, 20 mm/s for all infills, 60mm/s for bridges and 20mm/s for gap fills. The following filament settings have been input as follows: filament diameter of 3 mm, extrusion multiplier of 1, extruder temperature of 60 °C and bed temperature of 110 °C. The Printer Settings have been input as Start G-code: i) G28: home all axes, ii) G1 Z5 F5000; lift nozzle and iii) M92 E6000-8000; Set ESTEPS for Discov3ry extruder.

In the extrusion process, the double-barrel syringe, each containing 20ml of part A silicone resin and 20 ml of part B curing agent, is first mounted onto the Discovery extruder which runs on a NEMA 17 stepper motor, and runs at 1600 motor steps per second.

The extruder drive is chosen to provide sufficient torque to push the silicone resin via the static mixer, through a 30 cm length of polyurethane tubing with inner diameter of 2.65 mm and finally the nozzle at the printing speed and sufficient resolution so that individual extruder micro-steps are not visible in the print.

3.3.4.3 Stepper Driver Calibration

The stepper driver calibration involves the XY steps, Z steps and E steps calibration.

(1) X-Y steps

This drive gear has a 10.8 mm diameter. One full rotation of the drive gear will advance a silicone resin length equal to its circumference, which is pi x 10.8mm or approximately 33.93 mm. Equation (10)

The motor rotates 1.8 degrees per step, so it takes 360 / 1.8 = 200 steps for a full rotation. Since you are using 16x micro stepping, this is multiplied to 200 x 16 = 3200 steps.

Thus, one ends up with steps per mm value of 3200 / 33.93 = 94.31 steps/mm.

In the belt and pulley system, the XY steps per mm, which is influenced by the motor, pulley and belt characteristics, can be calculated from Equation (11):

X-Y steps/mm = (motor steps per revolution x driver micro step) / (belt pitch x pulley number of teeth) Equation (11)

(2) Z steps

Most RepRap printers use a pair of threaded rods for the Z axis.

The distance with which the Z axis moves for each revolution of the motor, knowing the amount of rotation and distance per rotation (thread pitch), is calculated from Equation (12) :

Z steps / mm = (motor steps per revolution x driver microstep) / thread pitch

Equation (12)

In the NEMA 17 stepper motor with standard pitch M8 threaded rod, the Z-steps per mm is calculated as (200 x 16) / 1.25 = 2560.

(3) E steps

"Wade" extruders use a NEMA motor to drive a large reduction gear that turns a "hobbed bolt." Direct-drive extruders typically use a motor with a planetary gearbox to turn a drive gear, such as the popular MK7.

The standard formula is E steps per mm = (motor steps per revolution x driver micro-step) X (big gear teeth / small gear teeth) / (π x hob effective diameter) Equation (13)

A classic Wade with a 39:11 gear ratio will perform = (200 x 16) / (7 x 3.14159) = 515.91. To perform an E step calibration, firstly, the extruder body is made a reference point and a 100mm mark is made at the polyurethane tubing. The printer is directed to print 80mm of silicone and the distance is measured from the body to the point.

New E steps = old E steps x (80 / distance actually moved) Equation (14)

This value is then input into firmware. Marlin supports M92 E*nnn* to set this value temporarily. Repeat from Step 3 until one gets between 96-104 mm.

3.4 Characterization of Standard Ecoflex Silicone Specimens

This is the first study to show that direct 3D Printing of silicone is possible using a novel heat-cured extrusion-based technology and that adequate mixing and polymerization of the two-part Ecoflex resin is possible, as opposed to what was claimed by Liravi et al. [6]. The present novel system harnesses on the variable curing rates and viscosities of the Ecoflex silicone resins to print these silicone constructs. This paper is divided into 3 parts. The first section investigates the effect of 3D printing parameters (nozzle diameter, nozzle temperature and bed temperature) on the dimensional accuracy and mechanical properties of 3D printed silicone parts. The second section investigates the reliability and failure properties of 3D printed silicone samples according to ASTM D575 [14] standards under monotonic (strain rates of 12, 120, 360, 720 and 1000 mm/min) and 1000-cycle compressive loading and the third part studies the biocompatibility of 3D printed silicone by extraction method according to ISO 10993-12 for different extraction time (10, 20, and 30 days) and extract volume/surface area ratios (1x, 2x, and 3x).

3.4.1 Materials and Methods

(1) Material

Ecoflex silicone elastomeric kit, Ecoflex 30 and Ecoflex 50 were used. This two-part liquid elastomeric kit consists of a polymer base (dimethyl siloxane) and crosslinking curing agent (oligomeric dimethyl siloxane) and platinum catalyst. By mixing the two parts at equal ratios by weight/volume, the silicone elastomeric can be extruded and cured optimally. Similar to PDMS elastomer, the Ecoflex elastomer was assumed to have a Poisson's ratio of 0.5.

(2) Sample dimension

For compression tests, both standard cylindrical and 3D printed cylindrical specimens were used. The design of specimen mold was based on ASTM D575 [124]. It consists of a top plate with ten cylindrical holes (each hole measuring 13 mm in height and 28 mm in diameter) and a plain rectangular base. This plastic mold does not bind with silicone elastomeric during the curing process. A schematic drawing of cylinder is shown in **Figure 35.**

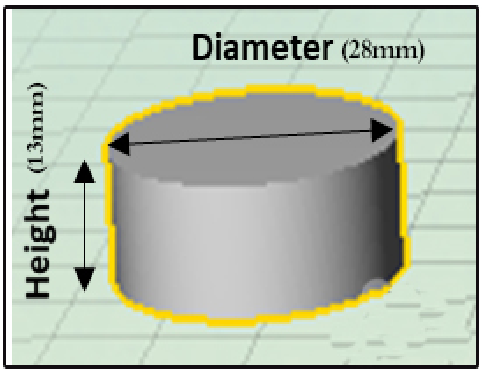

Figure 35 CAD drawing of cylindrical silicone sample

3.4.2 Mechanical Characterization of Silicone samples

The ASTM standards Test Methods for Rubber Properties in Compression D575-91 was performed for the compression test of silicone samples [124]. The ASTM Standard Test Methods for Vulcanized Rubber and Thermoplastic Elastomers—Tension D412-16 [4] was performed for the tensile test of silicone samples [123].

3.4.2.1. Compression Test

The compression test is performed in accordance with the ASTM Standard Test Methods for Rubber Properties in Compression Designation: D575 – 91. Test Method A [124].

The test measures the compression stiffness of the silicone sample. Deflection is the change in thickness of the specimen upon application of a compressive force. Test Method A—Compression Test of Specified Deflection—A compression test in which the force required to cause a specified deflection is determined was used.

The following information was reported: a) Deflection demonstrated as a percentage of the original thickness of the specimen, b) Description of the 3 samples and type of test specimen, including dimensions, c) Description of test method and apparatus.

The universal tensile testing instrument (Instron Model 5586) was used to perform the compression test on 3D printed silicone specimens measuring 28 mm in diameter and 13 mm in height. The testing room temperature was maintained at 23 °C and the specimens were kept in the room for 3 hours before testing.

The test was carried out following ASTM D575 Test Method A using Instron 5569. The top compression plate was connected to a load cell (500 N) to record the compression force and displacement transducer was used to record the compressive displacement. Data collection of load and crosshead position was done with Bluehill Testing Software at constant crosshead displacement rates of 12, 120, 360, 720 and 1000 mm/min. The experimental setup allows the sample to freely expand laterally under compression. The samples were compressed up to 70 % strain and engineering stress and strain were obtained. The setup is shown in **Figure 36**.

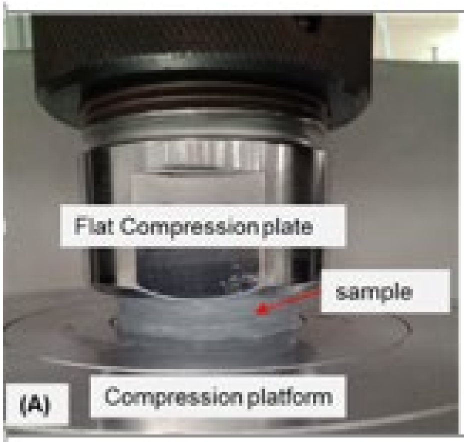

Figure 36 Experimental apparatus used for the static compression of standard sample. Silicone sample is placed between compression plate and platform. Compression test is then performed.

For standard samples, the stress was obtained as the ratio of compression force recorded by the load cell to the average cross-sectional area of sample. The strain was obtained as the ratio of compressive displacement and sample thickness. All tests were done in triplicates for each Ecoflex elastomer. All values recorded in tables were the mean values with standard errors.

3.4.2.1.1 Monotonic compressive test

The stress-strain response curve of the silicone elastomer under monotonic compressive loading up to failure is shown in **Figure 37a** and **Figure 37b** for Ecoflex 30 and Ecoflex 50 LSRs, respectively. Johnstone et al [125] similarly observed similar stress-strain trend. A linear elastic region is obtained at low strain level and a nonlinear region is obtained at higher strain level before failure. In the linear region with low initial gradient, when the load is first applied, the material is not stiff, as a large increase in strain only resulted in a small increase in stress. In the non-linear region with high gradient, a large stress increment can result from a small strain increment. This pattern is different from those of natural rubbers where the initial slope is very high and from those of elastic undamageable material, where the initial gradient is near zero [126]. The inbox of the linear region allows a closer look of **Figure 37** up to 40% strain and statistical analysis using student's unpaired t-test shows that Ecoflex 50 has a higher modulus at any point of strain values when compared to Ecoflex 30 ($p < 0.05$). The transition range occurs at 55 % for Ecoflex 50 compared to 50 % for Ecoflex 30. The results indicate that a harder or more viscous LSR has a higher transition range.

The load-displacement curves of the standard samples of both Ecoflex 50 and Ecoflex 30 LSRs are also included in Appendix A. The two moduli, calculated from the slope of stress-strain curves of the standard samples of Ecoflex 50 and Ecoflex 30 LSRs are presented in **Figure 38**. Compressive modulus of Ecoflex 50 is statistically significantly higher than that of Ecoflex 30 ($p < 0.05$) using student's unpaired t-test. The compressive modulus of Ecoflex 50 and that of Ecoflex 30 are approximately 0.35 MPa and 0.25 MPa, respectively and these values are higher than those of the anteromedial region of the native human meniscus, which has the highest compressive modulus of 0.16 MPa, as shown in Table 1.

This higher transition range and compressive modulus of the standard silicone sample reflect its suitability as a load-bearing base material. The relationship between elastic modulus and LSR viscosity is different in both the linear and nonlinear region. A comparison of the initial linear slopes of stress-strain graphs in Figure 37a and 37b also shows that a higher compressive modulus is achievable with Ecoflex 50, which has higher viscosity and shore hardness.

Table 10 Monotonic Compression Test for Ecoflex 30 and Ecoflex 50 standard samples

1-cycle compression test	diameter (mm)	height (mm)	Load (N)	displacement (mm)	Strain	stress (kPa)	Compressive modulus (N/mm2)
STD-E30			(n = 5)	(n = 5)	(n = 5)	(n = 5)	(n = 5)
sample 1	28	13	680.96954	9.1	0.7	1105.914	266.1784
sample 2	28	13	793.62262	9.10038	0.7	1288.867	251.0056
sample 3	28	13	855.48999	9.09962	0.7	1389.341	257.3448
sample 4	28	13	763.87775	9.12038	0.7	1240.56	221.7243
sample 5	28	13	653.22083	9.09956	0.7	1060.85	249.6344
Mean			749.436	9.103988	0.7	1217.106	251.919
SD			82.694	0.0091		134.298	16.72742
STD-E50			(n = 5)	(n = 5)		(n = 5)	(n = 5)
sample 1	28	13	562.06824	9.1	0.7	981.68382	310.4455
sample 2	28	13	961.38092	9.1	0.7	1457.224	376.5596
sample 3	28	13	949.14362	9.1	0.7	1541.438	353.3929
sample 4	28	13	1103.59595	9.10031	0.7	1792.273	358.7124
sample 5	28	13	696.50671	9.10006	0.7	1364.338	312.4824
Mean			854.539	9.100074	0.7	1427.391	342.3185
SD			219.606	0.000134		295.662	29.4531

Monotonic Compression Test for Ecoflex 30 standard samples

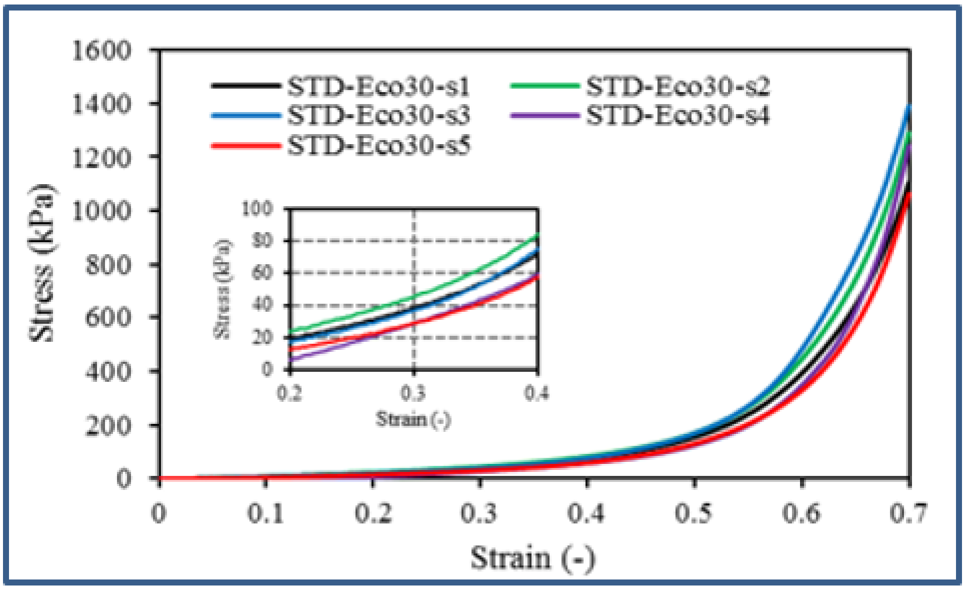

Figure 37 a) Stress-strain curves of monotonic compression for Ecoflex 30. Linear region is observed up to 30% strain. Transition range occurs at 50% for Ecoflex 30

Monotonic Compression Test for Ecoflex 50 standard samples

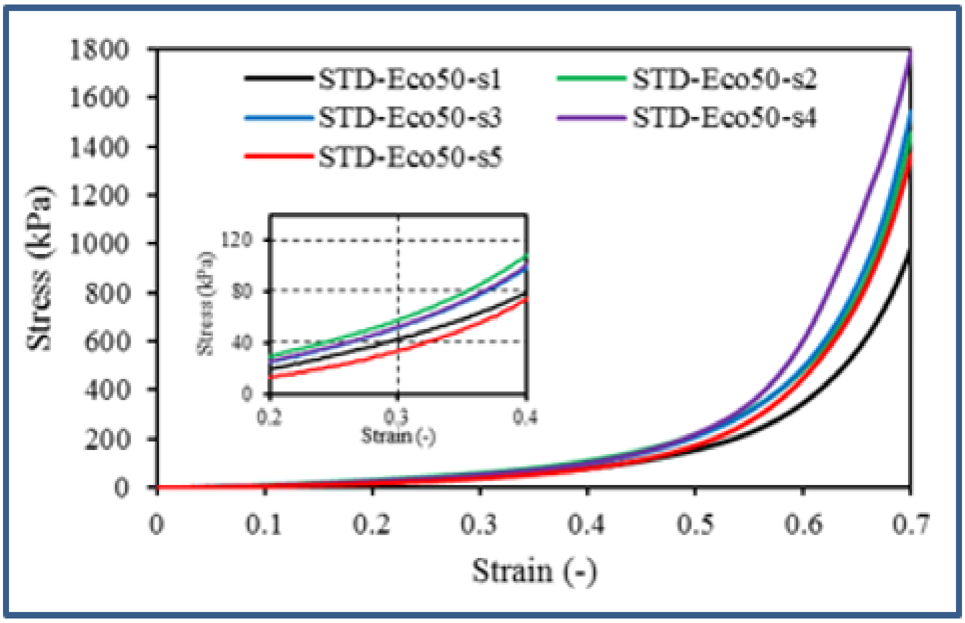

Figure 37 b) Stress-strain curves of monotonic compression for Ecoflex 50. Linear region is observed up to 30% strain. Transition range occurs at 55% for Ecoflex 50

Compressive Modulus of Ecoflex 30 and Ecoflex 50 standard samples

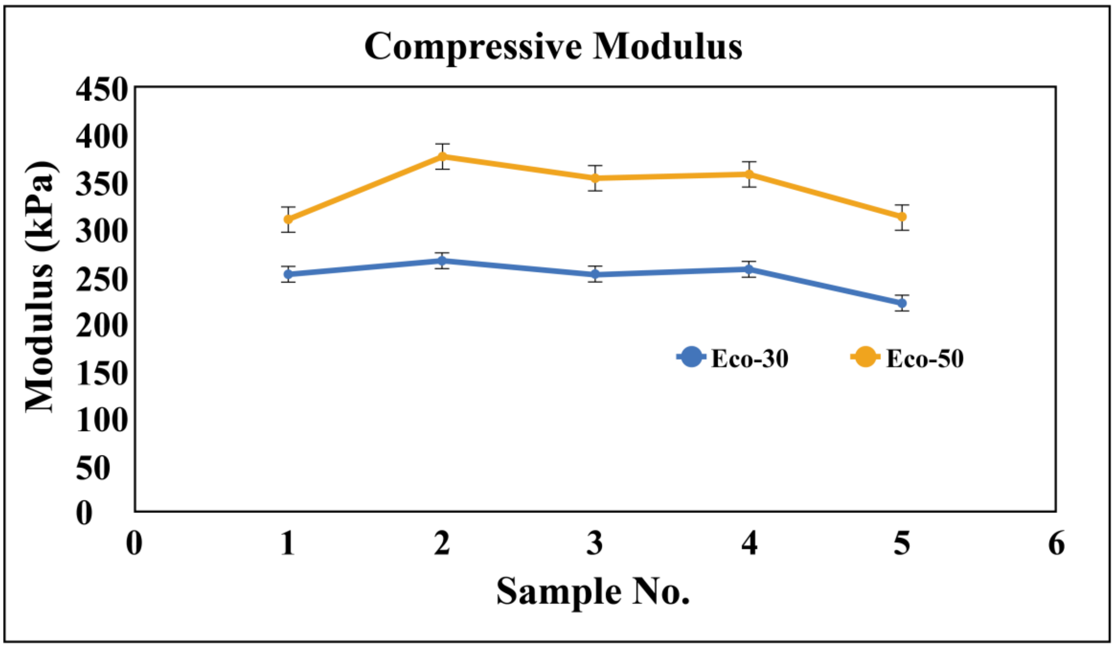

Figure 38 Graphical representation of the compressive modulus for different standard sample with the standard error bars with 95% confident interval. In general, Ecoflex 50 standard samples have higher compressive modulus than Ecoflex 30

3.4.2.1.2 Cyclic compression test

The sample was compressed from 0% to 70% strain and then released back to 0% strain for 4 and 1000 cycles, as shown in **Figures 39** and **40**, respectively. The maximum number of 1000 cycles is selected to closely mimic the number of steps a sedentary person or post keyhole surgery would take in a day. Four cycles is chosen to investigate Mullin's effect and hysteresis. Mullin's effect, or stress softening, was observed when a lower force was required for compression to the same displacement. Most of this softening occurs in the first compression and after a few cycles a steady state is reached.

The modification of mechanical properties of silicone elastomer with the number of cycles was observed and compared for Ecoflex 30 and Ecoflex 50 under different strain rates. With four-cycle compression and up to 25% strain, different strain rates did not seem to have any significant effect on the modulus. Transition range occurred at 35% strain and 30% strain, respectively, for Ecoflex 30 and Ecoflex 50 samples. Mullin's effect, with a right shift of the curves, can also be observed with lower strain rates at 12 mm/min and 120mm/min. With 1000-cyclic compression at 1000 mm/min, there was a gradual upward shift of the curves, known as strain-stiffening. This characteristic of strain-hardening was apparent in both

Ecoflex 50 and Ecoflex 30, with compressive moduli increasing to a maximum at 400th to 500th cycles before gradually reducing to 70%-80% of the maximum at 1000th cycle. Ecoflex 50 demonstrated double the magnitude of strain-stiffening when compared with Ecoflex 30, as shown in **Figure 40**. From Fig 40a, compression test for Ecoflex 30 standard samples show maximum stress of 0.3 MPa is achieved at strain of 0.5. From Fig 40b, compression test for Ecoflex 50 standard samples show maximum stress of about 0.6 MPa is achieved at strain of 0.5. This maximum stress value of Ecoflex 50 is almost double that of Ecoflex 30. The phenomenon of strain-stiffening can be explained microscopically by the slippage of small segments of crosslinked silicone chains pass its neighbors but may recover their initial conformation during unloading. With increasing number of cycles, some crosslinks are broken and the deformation becomes plastic. Since Ecoflex 50 is more viscous the Ecoflex 30, crosslinks are more extensive making slippage of silicone segments more difficult and thus conferring greater durability to the silicone products.

The strain stiffening in biopolymer networks can, generally speaking, be attributed to 1) the properties of the fibers; 2) the cross-links that mediate the interfiber force and the network microstructure. This strain stiffening behaviour can be explained in terms of two fundamental mechanisms: 1) the pulling out of stress-path undulations undulations in the localized paths of high axial forces that develop as the network is deformed to large strain. This bending-dominated mechanism that can be characterized by a power-law dependence with exponent 3/2 of the shear modulus, G, on stress, T and 2) finite strain effects induced by reorientation of the stress path. This stretch-dominated finite strain effect gives rise to a power-law relation between G and T with exponent 1/2. The three-dimensional dynamic finite-element model (45) indeed demonstrates that the dynamic behavior of cross-links (cross-links being allowed to unbind and rebind) affects the nonlinear response of enthalpic networks. The rupture of cross-linking gives rise to strain softening, while re-binding of crosslinking gives rise to strain stiffening. The predominance of either stiffening mechanisms is determined by the characteristic ratio, which is in turn related to material properties (bending and axial stiffnesses) of the network constituents [127].

Table 11 4-cycle Compression Test for Ecoflex 30 and Ecoflex 50 standard samples

4-cycle compression test	diameter (mm)	height (mm)	Load (N)	displacement (mm)	strain	stress (kPa)	Compressive modulus (N/mm2)
STD-E30			(n = 5)	(n = 5)	(n = 5)	(n = 5)	(n = 5)
sample 1	28	13	131.8486	6.999425	0.538417308	0.214126086	0.1634
sample 2	28	13	230.6588	6.9821	0.537084615	0.374596818	0.2217
sample 3	28	13	183.4774	6.99315	0.537934615	0.297972808	0.1828
sample 4	28	13	189.8003	6.9979	0.5383	0.308241387	0.1985
sample 5	28	13	150.1099	6.9783	0.536792308	0.243782986	0.1713
Mean			177.179	6.99	0.5377	0.2877	0.1875
SD			38.231	0.0094	0.00073	0.062	0.0232
STD-E50			(n = 5)	(n = 5)	(n = 5)	(n = 5)	(n = 5)
sample 1	28	13	253.7441	6.998275	0.538328846	0.412088039	0.2497
sample 2	28	13	330.5022	6.98215	0.537088462	0.536745498	0.2829
sample 3	28	13	396.2739	6.993175	0.537936538	0.643560714	0.3065
sample 4	28	13	304.8944	6.983	0.537153846	0.495157662	0.2465
sample 5	28	13	323.4657	6.978325	0.536794231	0.525318011	0.2607
Mean			321.776	6.986	0.53746	0.52257	0.2692
SD			51.337	0.0083	0.00064	0.0833	0.0252

4-Cycle Compression Tests for Ecoflex 30 standard samples

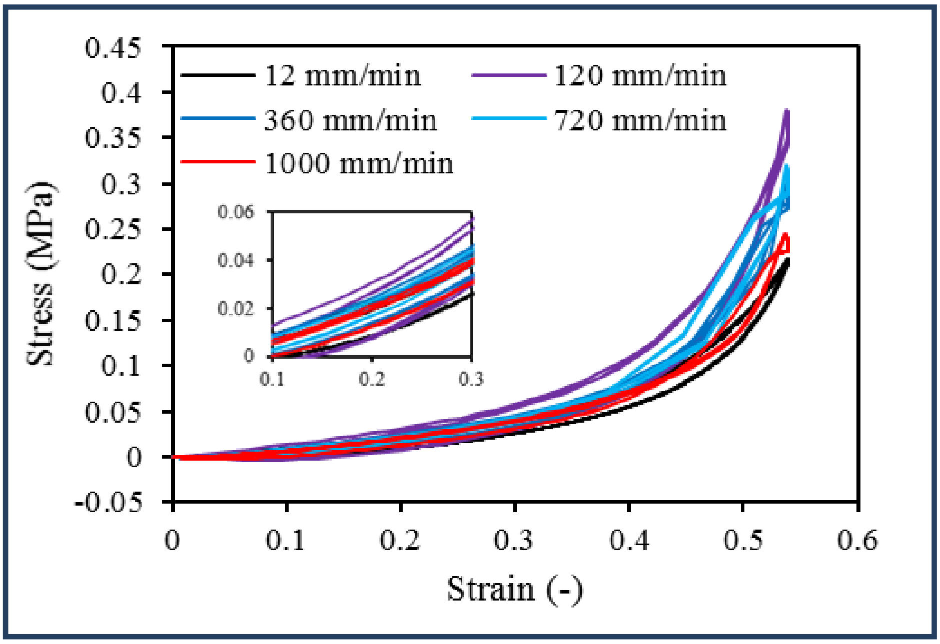

Figure 39 a) Stress-strain curves of cyclic compression of standard samples. Four-cycle compression of Ecoflex 30 at strain rates of 12, 120, 360, 720, and 1000 mm/min. Hysteresis is observed for all strain rates.

4-Cycle Compression Tests for Ecoflex 50 standard samples

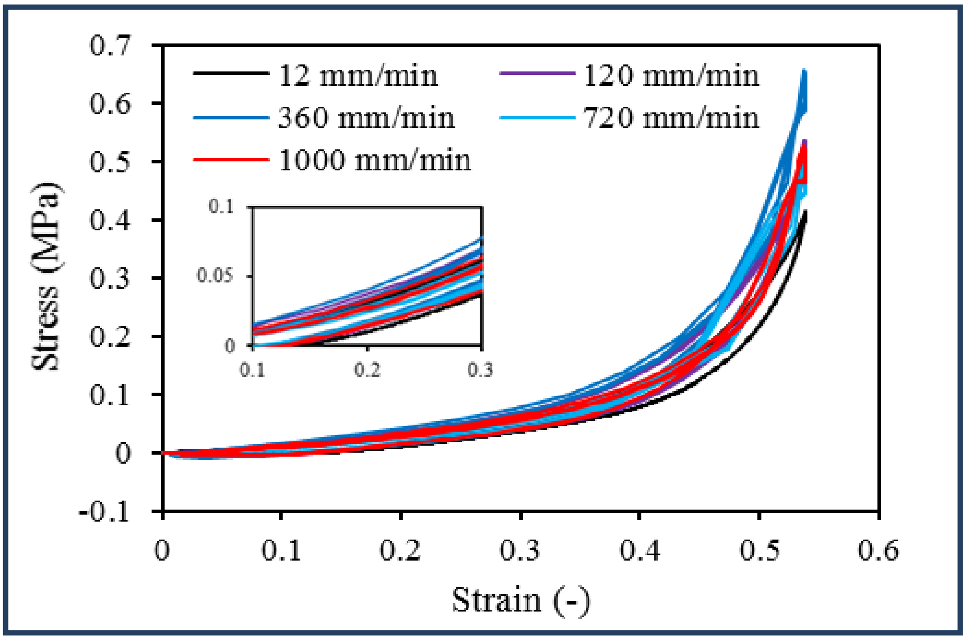

Figure 39 b) Stress-strain curves of cyclic compression of standard samples. Four-cycle compression of Ecoflex 50 at strain rates of 12, 120, 360, 720, and 1000 mm/min. Ecoflex 50 samples are twice stiffer and stronger than Ecoflex 30 samples

Table 12 1000-cycle Compression Test for Ecoflex 30 and Ecoflex 50 standard samples

1000-cycle compression test	diameter (mm)	height (mm)	Load (N)	displacement (mm)	strain	stress (kPa)	compressive modulus (N/mm2)
STD-E30			(n = 5)	(n = 5)	(n = 5)	(n = 5)	(n = 5)
sample 1	28	13	350.8679	6.9965	0.538192308	0.569820007	0.6075
sample 2	28	13	326.0009	7.00005	0.538465385	0.529435252	0.5817
sample 3	28	13	324.2238	7.00005	0.538465385	0.526549188	0.6331
sample 4	28	13	320.2613	7.00005	0.538465385	0.520113969	0.6049
sample 5	28	13	322.218	7.00005	0.538465385	0.523291709	0.5845
Mean			328.714	6.999	0.5384	0.5338	
SD			12.569	0.00158	0.0001221	0.02041	
STD-E50			(n = 5)	(n = 5)	(n = 5)	(n = 5)	(n=-5)
sample 1	28	13	183.088	7.000025	0.538463462	0.29734041	1.2368
sample 2	28	13	186.5053	7	0.538461538	0.302890208	1.2338
sample 3	28	13	183.8716	7.00005	0.538465385	0.298613	1.0801
sample 4	28	13	186.4084	6.999925	0.538455769	0.30273284	1.1412
sample 5	28	13	181.7306	7.00005	0.538465385	0.295135952	1.1672
Mean			184.32	7.00001	0.538	0.299	
SD			2.095	5.18E-05	3.99E-06	0.0034	

1000-Cycle Compression Tests for Ecoflex 50 standard samples

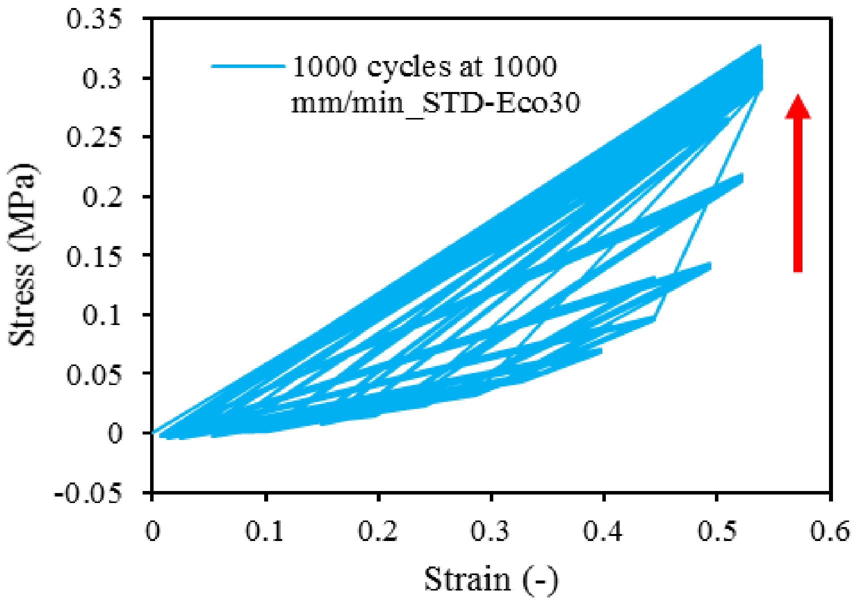

Figure 40 a) Stress-strain failure curves of 1000-cyclic compression of Ecoflex 30 standard samples at 1000 mm/min. Ecoflex 30 showed strain-stiffening with cycling,

1000-Cycle Compression Tests for Ecoflex 50 standard samples

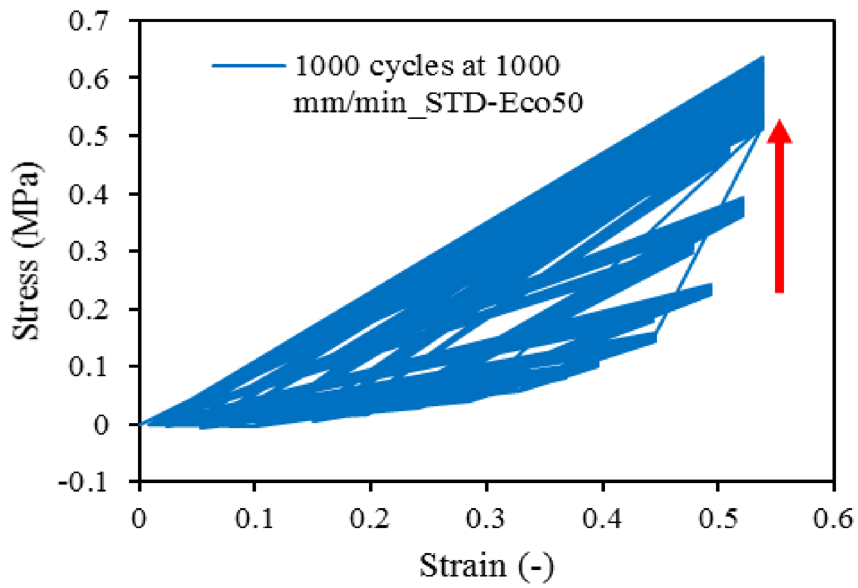

Figure 40 b) Stress-strain failure curves of 1000-cyclic compression of Ecoflex 50 standard samples at 1000 mm/min. Ecoflex 50 showed strain-stiffening with cycling. Ecoflex 50 samples has about twice the Young's modulus of Ecoflex 30 samples.

Table 13 Compressive Moduli for both Ecoflex 30 and Ecoflex 50 standard samples

Standard Sample	Compressive Modulus (kPa)	
	STD-Eco30	STD-Eco50
1	251.919	310.4455
2	266.1784	376.5596
3	251.0056	353.3929
4	257.3448	358.7124
5	221.7243	312.4824
Average	249.6344	342.3185
S.D.	16.72742	29.4531

Table 14 Compressive modulus for all samples as obtained by the slope of the stress-strain curve in linear viscoelastic region (i.e. strain range 0.3-0.5)

	Mean (SD) (kPa)		
sample type	Standard	3D Printed	
Eco-30	249.63 ± 16.72	218.61 ± 22.76	p = 0.039
Eco-50	342.31 ± 29.45	298.85 ± 20.44	p = 0.026
	p = 0.00028	p = 0.00037	

3.4.2.2 Tensile Test

The tensile test is performed in accordance with the ASTM Standard Test Methods for Vulcanized Rubber and Thermoplastic Elastomers—Tension Designation: D412 – 16 [123]. For the tensile test, the clamps were attached to the movable crosshead and to the base of the Instron machine. The upper clamp was attached to a 500N load cell (accuracy <0.025%) mounted to the mobile crosshead, while the lower clamp was attached to the static base plate. The silicone dumbbell specimens (Die D), with the measurements shown below, were molded and 3D printed. The specimens were then clamped between the stationery clamp and the movable crosshead clamp. **Figure 41** shows the measurement for the ASTM Die D Silicone Dumbbell Ecoflex Specimen.

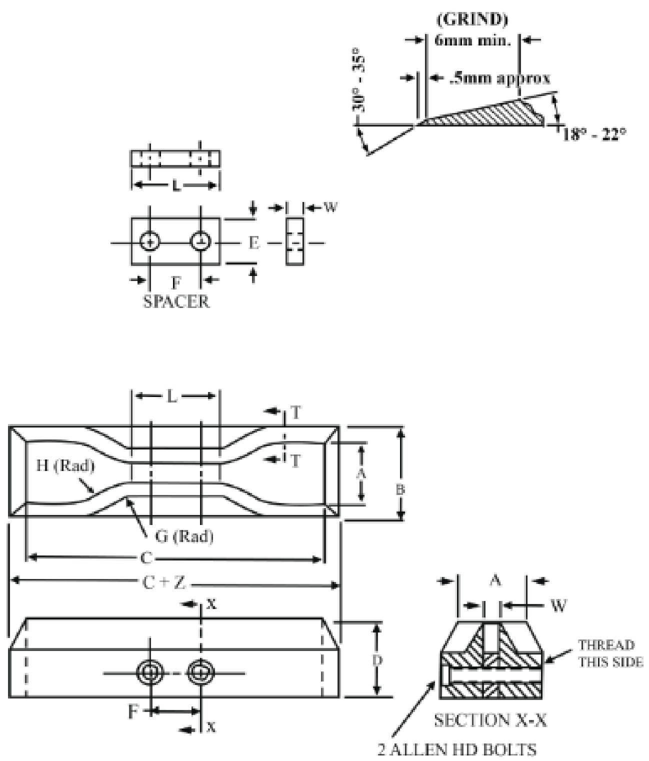

Dimensions of Standard Dumbbell Dies[A] (Metric Units)

Dimension	Units	Tolerance	Die A	Die B	Die C	Die D	Die E	Die F
A	mm	±1	25	25	25	16	16	16
B	mm	max	40	40	40	30	30	30
C	mm	min	140	140	115	100	125	125
D	mm	±6[B]	32	32	32	32	32	32
D-E	mm	±1	13	13	13	13	13	13
F	mm	±2	38	38	19	19	38	38
G	mm	±1	14	14	14	14	14	14
H	mm	±2	25	25	25	16	16	16
L	mm	±2	59	59	33	33	59	59
W	mm	+0.05, -0.00	12	6	6	3	3	6
Z	mm	±1	13	13	13	13	13	13

[A] Dies whose dimensions are expressed in metric units are not exactly the same as dies whose dimensions are expressed in U.S. customary units. Dies dimensioned in metric units are intended for use with apparatus calibrated in metric units.

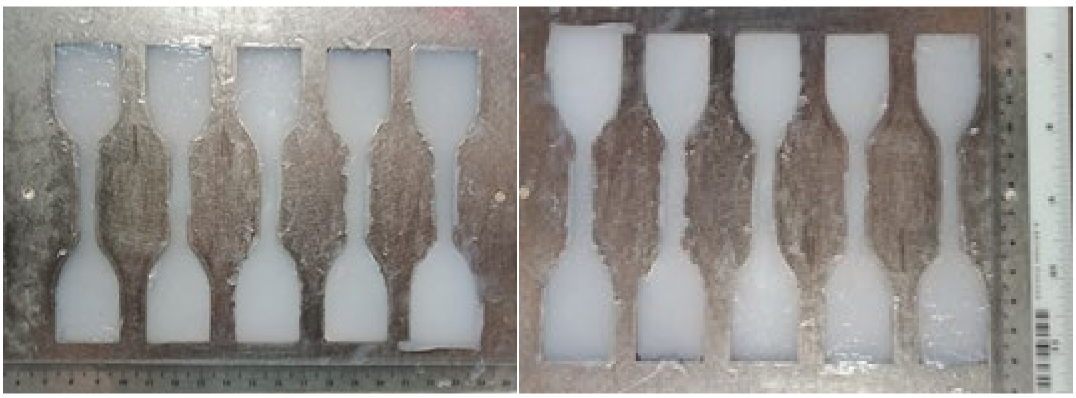

Figure 41 The ASTM Die D Silicone Dumbbell Specimen

The dumbbell specimens between the clamps were subjected to a pull by the crosshead moving upward at a rate of 150mm/min. The resistance offered by the silicone specimens is sensed by the Instron 2630-100 Series Clip-On Extensometer. The Instron® Bluehill® 2 modular applications software was employed to set the testing protocol and capture data every 100 ms. Samples, at room temperature (23°C), were compressed in between the clamps before fine position control was used to increase the tension manually to achieve a starting load of 0 N.

The clamps were distracted vertically upwards at the rate of 150 mm/min until failure occurs. The tensile strengths and elongation at breaks were measured. The tensile strengths and elongation at break of both molded and 3D printed samples are shown in **Figures 42a and 42b**, respectively.

ASTM D412-16 tests showed the tensile strengths of molded and 3D Printed Ecoflex 30 specimens to be (0.152 +/- 0.020) N/mm^2 and (0.117 +/- 0028) N/mm^2. The difference between both Ecoflex 30 groups was not considered to be statistically significant ($p = 0.058$)

The tensile strengths of molded and 3D Printed Ecoflex 50 specimens were found to be (0.312 +/- 0.020) N/mm^2 and (0.189 +/- 0.047) N/mm^2, This difference was found to be statistically significant ($p = 0.006$).

Comparison of the tensile strength of both molded Ecoflex 30 (0.152 +/- 0.020) N/mm^2 and molded Ecoflex 50 (0.312 +/- 0.020) N/mm^2 also showed significant differences ($p = 0.0004$).

There are also significant differences between the tensile strengths of 3D Printed Ecoflex 30 (0.152 +/- 0.020) N/mm^2 and 3DP Printed Ecoflex 50 (0.312 +/- 0.020) N/mm^2 ($p = 0.0004$).

The differences elongation at break, for both the molded silicone and 3D printed silicone groups, in both Ecoflex 30 and Ecoflex 50, were not statistically significant.

In conclusion, the tensile properties of both molded and 3D Printed silicone groups are comparable. These resilient properties are important for the design of meniscus anchorage which may need substantial elongation and traction during implantation and ambulation.

Table 15a Tensile Test for Ecoflex 30 and Ecoflex 50 standard samples

Tensile Test ASTM-412	width (mm)	thickness (mm)	Load (N)	Displace ment (mm)	Stress (N/m m2)	Strain (%)	tensile modulus (N/mm2)
			n = 5	n = 5	n = 5	n = 5	n = 5
3DP E30 Sample 1	6	4.43	6.202	268.137	0.413	412.519	0.100
3DP E30 Sample 2	6	4.02	10.654	429.304	0.710	660.468	0.107
3DP E30 Sample 3	6	3.98	8.192	354.971	0.546	546.109	0.100
3DP E30 Sample 4	6	4.1	6.839	260.637	0.455	400.981	0.113
3DP E30 Sample 5	6	4.26	6.678	173.138	0.445	266.366	0.167
Mean		4.158	7.713	297.238	0.514	457.288	0.117
SD		0.204	1.803	97.93	0.12	150.66	0.028
			n = 5	n = 5	n = 5	n = 5	n = 5
3DP E50 Sample 1	6	4.01	15.090	333.554	1.006	513.160	0.196
3DP E50 Sample 2	6	4.37	16.400	313.554	1.093	482.391	0.2266
3DP E50 Sample 3	6	4.49	18.950	339.971	1.263	523.032	0.2415
3DP E50 Sample 4	6	4.23	13.458	444.387	0.897	683.673	0.1312

3DP E50 Sample 5	6	4.16	12.935	370.221	0.862	569.571	0.1514
Mean		4.252	15.366	360.337	1.024	554.365	0.18934
SD		0.186	5.063	51.19	0.16	78.758	0.047
			n = 5	n = 5	n = 5	n = 5	n = 5
Mold E30 Sample 1	6	3.97	8.9025	250.804	0.593	385.853	0.1538
Mold E30 Sample 2	6	4.35	8.0156	225.846	0.534	413.032	0.1294
Mold E30 Sample 3	6	4.49	8.3796	272.137	0.558	418.673	0.1334
Mold E30 Sample 4	6	4.37	8.5083	211.887	0.567	325.981	0.174
Mold E30 Sample 5	6	4.11	10.306	261.971	0.687	403.032	0.168
Mean		4.258	8.822	244.529	0.588	389.314	0.7586
SD		0.211	0.887	25.101	0.059	33.573	0.019
			n = 5	n = 5	n = 5	n = 5	n = 5
Mold E50 Sample 1	6	3.96	15.955	246.137	1.063	378.673	0.2809
Mold E50 Sample 2	6	4.16	24.183	327.471	1.612	503.801	0.32
Mold E50 Sample 3	6	4.38	17.431	288.804	1.162	444.314	0.2616
Mold E50 Sample 4	6	4.37	23.107	342.887	1.540	527.519	0.292
Mold E50 Sample 5	6	4.06	22.565	239.137	1.504	367.904	0.409
Mean		4.186	20.648	288.88	1.376	444.44	1.563
SD		0.186	3.694	46.656	0.246	71.779	0.3127

Table 15b

Tensile Strengths - Mean (SD) N/mm^2			
sample type	Mold	3D Printed	
Eco-30	0.152 ± 0.020	0.117 ± 0.028	P = 0.058
Eco-50	0.312 ± 0.057	0.189 ± 0.047	P = 0.006
	P = 0.0004	P = 0.0195	

Table 15c

Elongation - Mean (SD) %			
sample type	Mold	3D Printed	
Eco-30	1179.74 ± 113.73	900.72 ± 296.76	P = 0.3563
Eco-50	1346.80 ± 217.51	1092.25 ± 155.13	P = 0.06
	P = 0.1665	P = 0.2375	

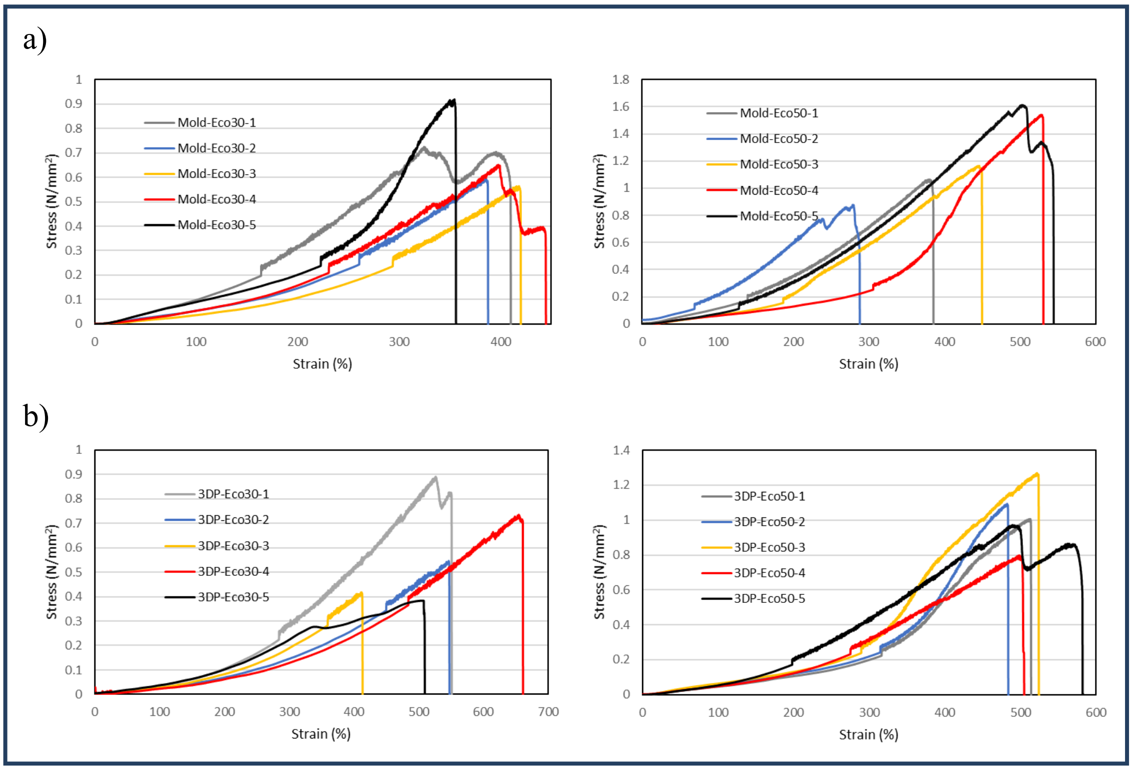

Figure 42 Tensile graphs for a) molded and b) 3D printed Ecoflex 30 silicone specimens. There is no statistical significant difference between molded and 3D printed groups, in both Ecoflex 30 and Ecoflex 50 groups.

3.4.3 Determination of Biocompatibility of Silicone Specimens

3.4.3.1 Cell Proliferative Assay

Following implantation of biomaterials, the following host reactions can be observed and these include injury, blood-material interactions, inflammation, foreign body reaction, and fibrosis/fibrous capsule development. In the initial phase of implantation, there is protein adsorption to the biomaterial surface and subsequent matrix formation on and around the biomaterial.

To investigate the extent of foreign body reaction, L929 fibroblastic cells were seeded and allowed to proliferate in culture medium on molded or 3D-printed silicone samples for 24, 72, and 120 hours. 3 samples were tested for each unique condition. The cells were seeded after washing steps to investigate cell adhesion or attachment behavior to the silicone samples. The data from **Figure 43b** shows that cells remained spherical in shape and did not form an extended morphology typical of attached cells in a 2D culture. The results point to a negative response for fibrosis/fibrous capsule development even when fibroblasts were in direct contact with silicone surface up to 120 h. However, the fibroblasts continued to exhibit contact-inhibited growth for up to 120 h and started to form clusters on the silicone surface due to the low cytotoxicity of the silicone samples, as shown in **Figure 43a**. **In Figure 43a**, the cell proliferation assay uses a water-soluble tetrazolium salt to quantify metabolic activity by producing an orange formazan product that is soluble in tissue culture medium upon bio-reduction by cellular dehydrogenases. The amount of formazan produced is directly proportional to the number of living cells and is measured by absorbance at 460 nm.

Cell Proliferative Assays

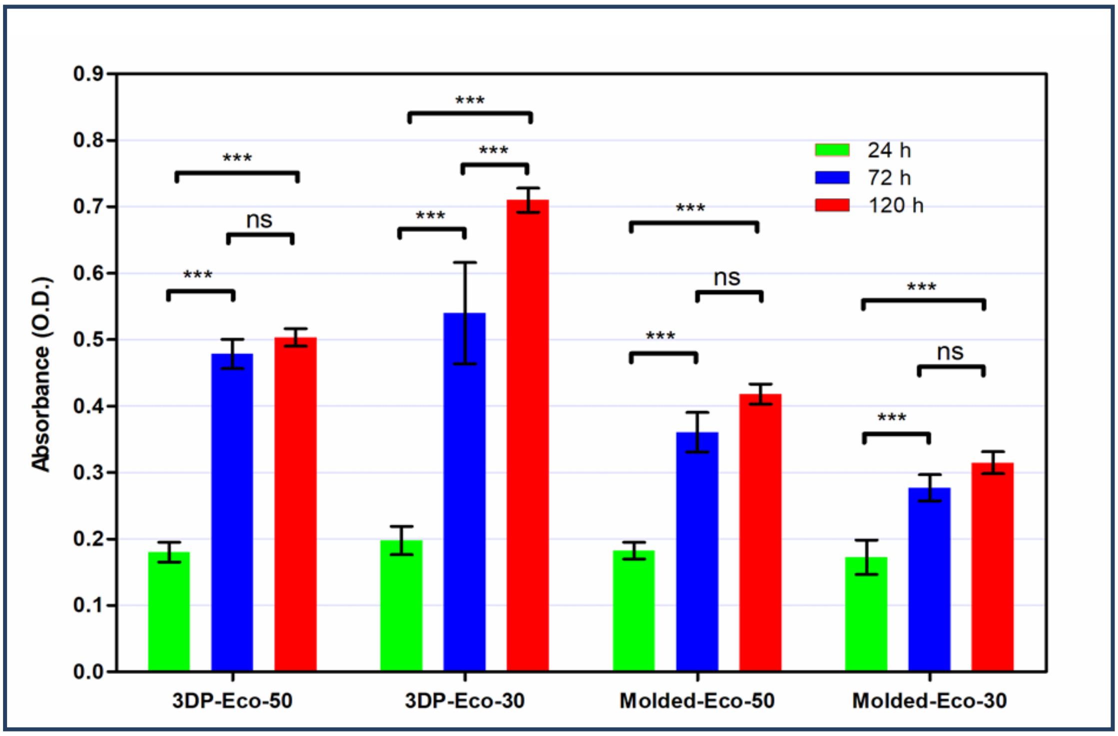

Figure 43 (a) Cell proliferation of seeded L929 cells on printed/casted Ecoflex50 / Ecoflex30 substrates after 24, 72, and 120 h culture was quantified based on the WST-8 cell proliferation assay. 3 samples were tested for each unique condition. For 3D printed samples, cells continue to proliferate and there was statistically significant differences found across all the groups after 24, 72 and 120 hours. Similar results were obtained for molded samples, except that there was no statistical significant difference in cell numbers between 72 and 120 hour groups. In general, Ecoflex 50/Ecoflex 30 silicon samples were found not to be cytotoxic to L929 cells.

Table 16 Cell Proliferation over 24, 72, and 120 h cultures.

	3DP-Eco50	**3DP-Eco30**	**Molded-Eco50**	**Molded-Eco30**
24 h	0.180 ± 0.015	0.198 ± 0.021	0.182 ± 0.012	0.172 ± 0.026
72 h	0.478 ± 0.022	0.540 ± 0.076	0.361 ± 0.030	0.277 ± 0.208
120 h	0.503 ± 0.013	0.710 ± 0.018	0.418 ± 0.015	0.315 ± 0.016

Live/Dead® Cell Viability Assay

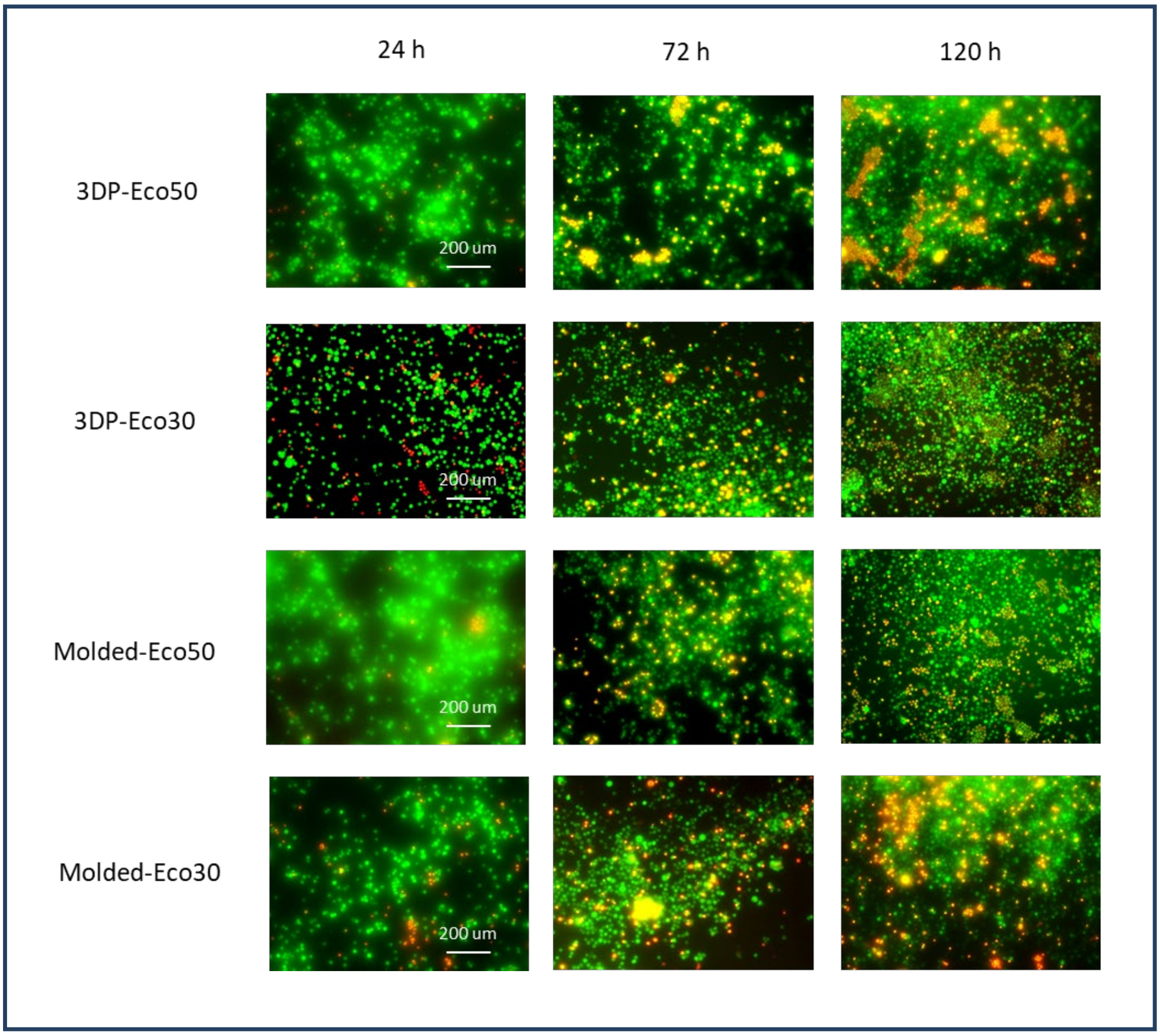

*Figure 43 (b) Fluorescent images of seeded L929 cells on printed/casted Ecoflex 50 / Ecoflex 30 substrates after 24, 72, and 120 h culture. Cells were stained with the Live/Dead® cell viability assay. Statistical significance between groups was assessed using two-way ANOVA followed by Bonferroni post-tests. ns = $p>0.05$ and *** = $p<0.001$. Cell proliferation continues at and after 24, 72 and 120 hours. In general, Ecoflex 50 / Ecoflex 30 silicone samples were found not to be cytotoxic to L929 cells.*

3.4.3.2 Cytotoxicity Test via Extraction Method (ISO10993-12)

Cytotoxicity test by extraction according to ISO10993-12 [132] is used widely in most in vitro biocompatibility studies. However, the extraction parameters in ISO10993-12 such as extraction medium, extraction time, extraction volume to surface area should be modified to simulate in vivo degradation. In this cytotoxicity study, we examined and compared between molded and 3D printed silicone samples for extraction times of 10, 20, and 30 days, and extraction volume/surface area ratios of 1x, 2x, and 3x. Positive control refers to extraction medium without any samples. 3 samples were tested for each unique condition. Results from quantitative cell proliferation assays indicated a statistically non-significant difference between almost all 3D printed and molded for both Ecoflex 30 and Ecoflex 50 samples for all 3 extraction volume/surface area ratios tested (**Figure 44**). This points to the non-toxic nature of the 3D printed silicone as no toxic chemicals were released over the extraction period. The same observation was made for longer periods of observation up to 30 days of extraction time (**Figure 45**). Thirty days of extraction time is chosen as this is the time limit for implantable devices. The results are extremely promising and highlight the long-term biocompatibility and stability of the 3D silicone using cell culture medium as extraction medium.

Cell Proliferation Assay (Extraction concentration)

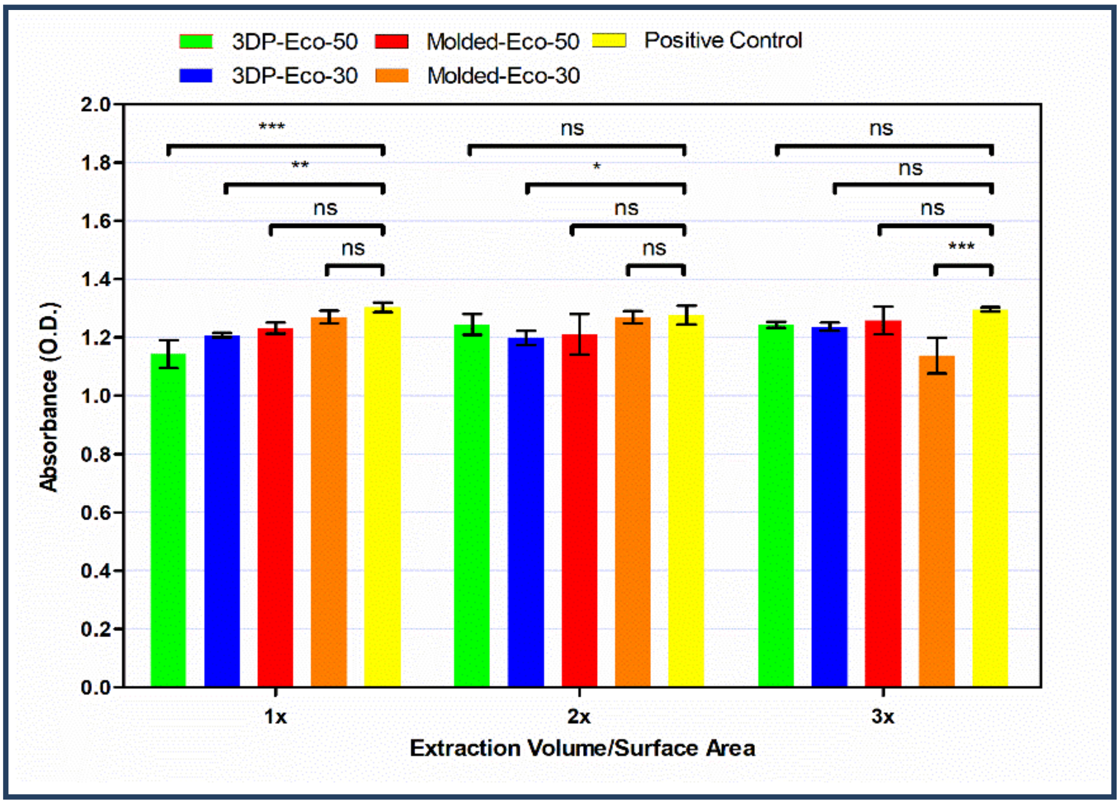

*Figure 44 Cytotoxicity results under different extraction volume/surface area ratios for extracts collected from standard silicone samples: 3D printed Ecoflex 50 / Ecoflex 30, molded Ecoflex 50 / Ecoflex 30 and positive control. Positive control refers to extraction medium without any samples. 3 samples were tested for each unique condition. Cell proliferation of L929 cells after 24 h incubation with extract was quantified based on the WST-8 cell proliferation assay. Statistical significance between groups was assessed using two-way ANOVA followed by Bonferroni post-tests. ns = $p>0.05$, * = $p<0.05$, ** = $p<0.01$, and *** = $p<0.001$. There is no statistical significant difference observed among different groups exposed to different extraction concentration*

Cell Proliferation Assay (Extraction time)

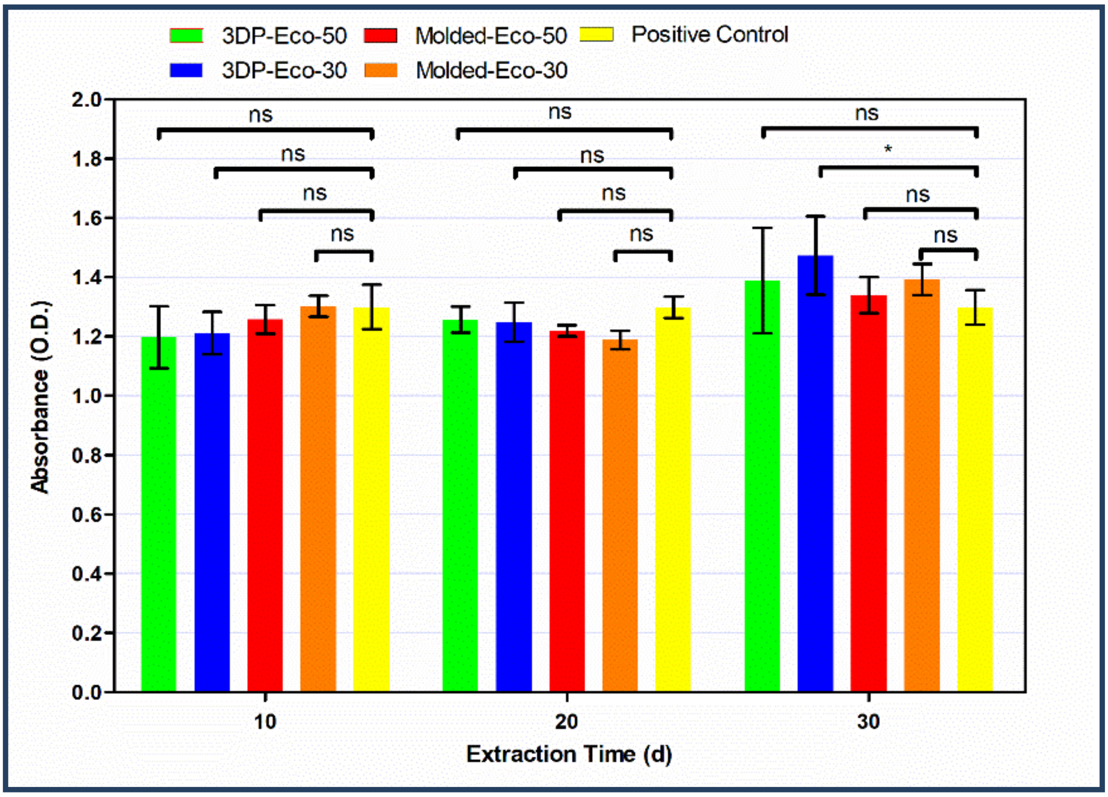

*Figure 45 Cytotoxicity results under different extraction time for extracts collected from standard silicone samples: 3D printed-Ecoflex-50 / Ecoflex 30, molded-Ecoflex-50/Ecoflex 30 and positive control. Positive control refers to extraction medium without any samples. 3 samples were tested for each unique condition. Cell proliferation of L929 cells after 24 h incubation with extract was quantified based on the WST-8 cell proliferation assay. Statistical significance between groups was assessed using two-way ANOVA followed by Bonferroni post-tests. ns = p>0.05, * = p<0.05. There is no statistical significant difference in cell proliferative numbers among 3D printed and molded groups exposed to extraction times of 10, 20 and 30 days.*

Table 17 Cell proliferation of L929 cells after 24 h incubation with extract was quantified

	Extraction Volume/	Surface Area		Extraction Time (d)		
	1x	2x	3x	10	20	30
3DP-Eco-50	1.143 ± 0.048	1.245 ± 0.036	1.243 ± 0.011	1.197 ± 0.105	1.257 ± 0.044	1.389 ± 0.179
3DP-Eco-30	1.208 ± 0.007	1.198 ± 0.024	1.237 ± 0.014	1.212 ± 0.071	1.248 ± 0.066	1.473 ± 0.132
Molded-Eco-50	1.232 ± 0.019	1.211 ± 0.070	1.258 ± 0.048	1.258 ± 0.048	1.219 ± 0.019	1.339 ± 0.061
Molded-Eco-30	1.27 ± 0.022	1.269 ± 0.020	1.138 ± 0.061	1.302 ± 0.036	1.188 ± 0.032	1.393 ± 0.053
Positive Control	1.303 ± 0.017	1.277 ± 0.033	1.296 ± 0.007	1.300 ± 0.075	1.298 ± 0.036	1.298 ± 0.058

Chapter 4 – Optimization of Printing Parameters

4.1 Determination of Critical Printing Parameters

In this chapter, critical printing parameters are optimized for Ecoflex 50 silicone printing. Printing parameters are critical in the determination of quality and accuracy of printouts. In the first section, I will first examine which of the following parameters are critical in determining the quality of Ecoflex 50 silicone printouts, namely: print speed, nozzle sizes, nozzle temperature, bed temperature and nozzle tip-bed distance. These set of selected optimal parameters are then further optimized using Design of Experiments (DOE) and Analysis of Variance (ANOVA) and their interactions studied using Regression Analysis.

4.1.1 Effect of Print Speed and Nozzle Diameter on Printing

(1) Print Speed

The optimal combination of print speed and flow rate is one of the most important factors affecting printing success. In this study, the optimal flow rate was estimated to be 1.2 ml/min, after E-steps and printing speeds adjustment. A simple structure of three-layer T-bone was first printed to determine the optimal print speed with this flow rate. The length of the T-bone closely resembles the length of the meniscus, as is indicated in the toolpath being generated. The ends of the T-bones act as reservoirs for extrudate droplets as the print-head decelerates and reverses direction in the printing process.

T-bone, shown in **Figure 46**, was designed with a height of 3 mm, overall width of 19 mm, overall length of 55 mm, narrow length portion of 6 mm and narrow width portion of 6 mm.

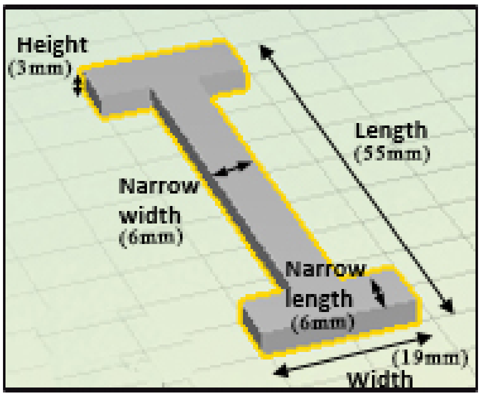

Figure 46 Schematic illustration of T bone

In this section, print speeds, v, are varied from 10 mm/s to 30 mm/s with 5mm/s intervals, were used to print the silicone. Other process parameters were fixed (T_1 = 40 °C, T_2 = 100 °C, Q = 1.2 ml/min, and d = 0.60mm), and 3 specimens were printed with each set of parameters.

The top view images of selected 3D printed silicone T-bone fabricated under different printing speeds were displayed in **Table 18**, with other parameters being held constant. With increasing print speeds, the extrudate diameter gradually diminishes until it was extruded in fine thread or droplet forms. At a high print speed, v = 30 mm/s, only silicone droplets were extruded on the previous layers of the specimen. On the other hand, the lowest print speed v = 10 mm/s resulted in maximal silicone overflow and a low print speed v = 15 mm /s resulted in moderate silicone overflow along the print path. Overall, this experiment shows that a printing speed at 20 mm/s produce the best printout results.

Determination of optimal printing speed

Table 18 Printed specimens of T-bone using different speeds. Optimal extrusion with high printing accuracy is achieved with printing speed of 20 mm/s. Scale bar: 1cm.

Printing Speed mm/s	Printed Specimen Top-view	Printing Outcomes
10		Geometry : Severe overflow at the stem and edges of T-bone Accuracy: poor
15		Geometry : Moderate over-extrusion Accuracy: moderate
20	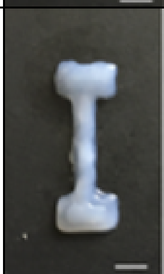	Geometry : optimal extrusion Accuracy: high
25		Geometry : Mild spotting and mild under-extrusion at edges Accuracy: moderate
30		Geometry : Spotting and severe under-extrusion Accuracy: poor

(2) Nozzle Diameter

Subsequently, a series of cylinders was printed to determine the optimal inner nozzle diameter for printing. As shown in **Figure 47**, the cylinder has a diameter of 28 mm and height of 13 mm. These cylinders resemble the circular toolpaths taken by the print-heads when printing the anterior and posterior horns of the meniscus.

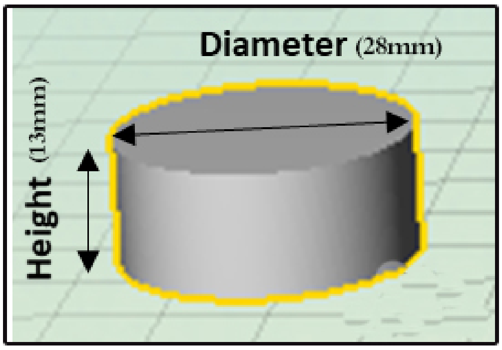

Figure 47 Schematic illustration of 3D printed cylinder

In this section, nozzles with seven different internal diameters, i*d,* (0.41, 0.51, 0.60, 0.70, 0.90, 1.21 mm) were used to print the silicone cylinders. In the meantime, other process parameters were fixed with the following values: T_1 = 40 °C, T_2 =100 °C, Q = 1.2 ml/min, and v = 20 mm/s.

Results of top view images of printed silicone cylinders are shown in **Table 19**. With the increasing nozzle diameters (internal), the best printout results of silicone cylinders were obtained using nozzles with inner diameters of 0.51 mm and 0.60 mm. There was minimal overflow in these two cases and heights of about 1 cm can be achieved with these diameters. When nozzle diameters (internal) of d = 0.7 mm to d = 1.12 mm were used for printing, there were over extrusion in all the silicone printouts.

Based on these results, the printing speed of 20 mm/s, nozzle inner diameters of 0.51mm and 0.60 mm, nozzle temperatures of 60 °C and 70 °C, bed temperatures of 100 °C and 110 °C have been adopted for the printing of the silicone meniscus

Determination of Optimal Nozzle Diameter

Table 19 Printouts of 3D printed cylinder (a) top view and (b) side view. Optimal printings are achieved with nozzle diameters of 0.51mm and 0.6mm. Scale bar 1cm

Nozzle diameter (mm)	Specimen Printout Top-view	Specimen Printout Side-view	Printing Outcomes
0.41		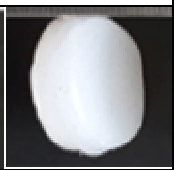	Geometry : inadequate extrusion Accuracy : unable to achieve height
0.51		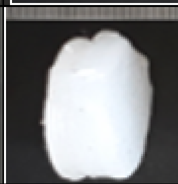	Geometry: accurate in diameter and height. Accuracy: accurate
0.60		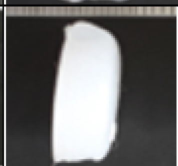	Geometry : accurate in diameter and height Accuracy : accurate
0.70		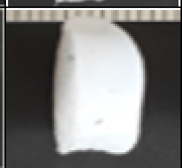	Geometry : slight overflow of silicone Accuracy: moderate
0.90		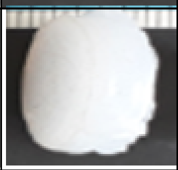	Geometry : moderate overflow Accuracy: moderate
1.12		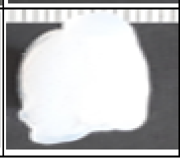	Geometry: Severe overflow Accuracy: poor

4.1.2 Effect of Nozzle Temperature and Bed Temperature on Printing

(3) Nozzle Temperature

The selection of optimal nozzle temperature is of paramount importance since each liquid silicone rubber has its own unique curing temperature. Using the calibration curve data obtained above from the rheological experiments, the optimal temperature is selected from the range where there is a marked change in viscosity. Printing is commenced at a temperature 20 °C lower than the curing temperature. If the extrusion is too fluid, the nozzle temperature is increased by 10 °C every 2 to 3 layers until a steady stream of extrudate is achieved. On the contrary if the infill becomes discontinuous or extrudate becomes intermittent, the nozzle temperature must be reduced. Nozzle temperatures ranging from 40 °C to 80 °C have been used. The print is continuously monitored and the optimum nozzle temperature is noted for the specific liquid silicon rubber.

(4) Bed Temperature

Optimum printer bed temperature is essential to provide adequate printer bed adhesion. This is estimated to be around the T 90°C value obtained from the rheological calibration curve. The first layer of silicone extrudate stream must adhere to the printer bed and achieve adequate curing to receive and bond with the subsequent layers of extrudate.

After allowing for 10 minutes of thermal equilibrium, a starting print temperature of the first layer with the bed temperature 10 °C warmer will ensure good gelation and adhesion to the platform bed or substrate. If the first layer is soft, wets the glass platform or adheres poorly, one should increase the temperature by 3 °C to 5 °C and restart the printing process. If the first layer has interrupted lines or shrinks, one should reduce the bed temperature.

To discover the effects of temperature variation on the silicone meniscus fabrication, a series of experiments were conducted. Heated platform temperatures from 80 °C to 110 °C have been used.

4.1.3 Temperature and Meniscus Fabrication

The effect of temperature on meniscus fabrication is shown in **Table 20**. Several combinations of the nozzle and bed temperatures were selected to fabricate the silicone meniscus, with nozzle temperatures ranging from 40 °C to 80 °C and platform temperatures ranging from 80 °C to 110 °C.

In general, nozzles with larger inner diameters can extrude greater volumes of silicone. Tight control over its flow rate and curing temperatures is recommended to avoid over-extrusion or inadequate curing or warpage. Similarly, using too high a nozzle or bed temperatures can result in nozzle clogging, uneven or under-extrusion of the liquid silicone rubber, as shown in the final two sets of meniscus printouts, when T_1 is 70 °C or 80 °C and T_2 is at 110 °C.

Nevertheless, the first three sets of printed meniscus showed silicone resin overflow from various angles due to inadequate curing. Once the height of 10 mm is reached, some uncured silicone may overflow due to the gravity. The final two sets of printout results showed either voids or imperfections with rough droplet deposition instead of smooth extrusion of silicone stream. The best meniscus print results were printed with a nozzle / print bed temperatures combination of 60 °C / 100 °C or 60 °C / 110 °C and using nozzles with inner diameter of 0.51mm.

Meniscus printed under varied combinations of temperatures and nozzle diameters

Table 20 Top view images of the 3D printed silicone meniscus. Optimal meniscus printing achieved with a combination of nozzle temperature of T1 (60 °C), bed temperature T2 (100 / 110 °C) and nozzle diameter of 0.60 mm. Scale bar: 1cm

T1	T2	0.51mm	0.60mm	Outcome: Print meniscus
40	80	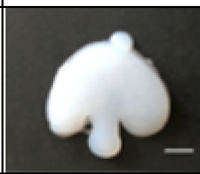	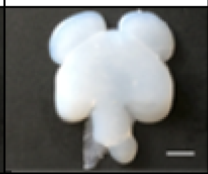	Geometry: severe overflow Accuracy: poor
40	90			Geometry: severe overflow Accuracy: poor
50	100			Geometry: moderate overflow Accuracy: poor
50	110			Geometry : shape achieved Accuracy: good
60	100			Geometry: satisfactory Accuracy: good
60	110		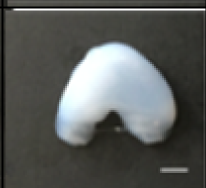	Geometry : satisfactory Accuracy: good
70	110			Geometry: under extrusion Accuracy: poor
80	110	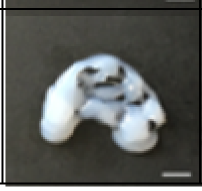	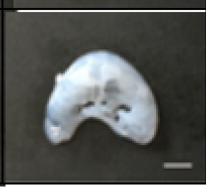	Geometry :under extrusion Accuracy: poor

4.2 Determination of Printing Parameters Interaction using Design of Experiment for Regression Analysis and Analysis of Variance of Printing Parameters

To best fit a set of observe data, linear or non-linear regression analysis is used to determine the value of the coefficients of the function. Empirical model is used to predict the output parameters under a set of controlled experimental variables. This involves three steps:

1. Performing designed statistical experiments

2. Approximating the coefficients of the mathematical model

3. Predicting the response and evaluate the adequacy of the model

The significant variables for the in house developed 3D silicone printers are nozzle diameter *ND*, nozzle temperature *NT* and bed temperature *BT*. The values for these variables were selected after preliminary experiments and their three levels in the factorial design are listed in Appendix B.

Table 21 Factors for regression analysis

Factor		Values		
		(-1)	(0)	(1)
ND	**Nozzle diameter (G)**	20	21	22
NT	**Nozzle temperature (^{o}C)**	40	50	60
BT	**Bed temperature (^{o}C)**	70	90	110

The generate polynomial equation used to evaluate the key factors and their effects on the printed dimensions of the sample is shown below:

$$y = a_0 + \sum a_i x_i + \sum a_{ii} x_i^2 + \sum \sum_{i<j} a_{ij} x_i x_j + \varepsilon \qquad \text{Equation (15)}$$

where y is the response or dependent variable investigated, a_i is a correction constant coefficient, a_i, a_{ii} and a_{ij} are coefficients for linear, quadratic and interaction effect, x_i and x_j is the independent variables, namely, nozzle diameter, nozzle temperature and bed temperature. ε is the random error. This equation assumes that third order interactions of the independent variables are insignificant. The significance of the formulae is evaluated using Analysis of Variance (ANOVA) which uses test statistics called the F statistic to test the null hypotheses. From the F distribution table, with probability of 5 %, if the F value of the formula is lower than critical value, the formula is then concluded to be significant in relating the inputs and output. The p value is the probability that the derived empirical formula is not significant where R^2 is a measurement of the fit of the data from 0 to 1 with 1 being the perfect fit.

4.2.1 Regression Model

The second-order regression models, which considered only the significant model terms, were obtained for the printed samples dimensions (C_l, C_w, C_h, L_w and L_h). C_l, C_w, C_h, L_w and L_h denotes length of printed cube, width of printed cube, height of printed cube, width of printed strut and height of printed strut, respectively. Using statistical analysis, insignificant model terms were removed as they have limited influence to make the empirical formulae efficient. The empirical formulae for the printed dimensions in terms of the key process parameters and their coefficient is given by:

$$C_l = 12.21 - 0.61NDBT \qquad \text{Equation (16)}$$

$$C_w = 12.25 - 0.73NDBT \qquad \text{Equation (17)}$$

$$C_h = 3.78 - 0.804\,ND + 1.02\,BT - 0.82\,NDBT \qquad \text{Equation (18)}$$

$$L_w = 1.73 - 0.50NDBT \qquad \text{Equation (19)}$$

$$L_h = 0.77 + 0.11\,BT \qquad \text{Equation (20)}$$

For Equation (16) to Equation (20), the following statistical analysis is obtained

For C_w, the model F value of 8.46 and p-value of 9.72×10^{-5} indicates that the model is significant ($p < 0.05$). There is only 5 % chance that a model F value could become this large due to noise. If the p-value of the factor is larger than 0.05, the factor is not significant in affecting C_w, hence in this case, ND is the significant factor. The second order interactions, C_w^2 and interaction between ND and NT are significant as well. The predicted R^2 (0.82) indicate a good fit of the experimental data to the developed empirical formula and is in good agreement with the adjusted R^2 (0.72).

Based on these equations, only the nozzle diameter *ND* and bed temperature *BT* have significant effect on the printed silicone structures dimensions. To rank the process parameters in order of importance, sensitivity analysis is used to determine the most significant input parameters based on the output. This is obtained from the partial derivative of the output with respect to the input variables. If the sensitivity is positive, the dimensions will increase with an increase in this process parameter, whereas negative sensitivity states the opposite. The sensitivity analysis results are shown in **Figure 48**. Both the heights of the printed cube and struts have positive sensitivity towards bed temperatures, indicating that a higher construct is possible with higher bed temperatures.

For Figure 48, Using Equation 15, for illustration, assuming we get

$C_w = k_1 + k_2NT + K_3BT + K_4ND + K_5NT^2 + K_6BT^2 + K_7ND^2 + K_7NTBT + K_8NTND + K_9BTND$ Equation (21)

To get the sensitivity with respect to each variable, we partially differentiate with respect to that specific variable. For example, for C_w sensitivity to NT (shown in Figure 53), we need to partially differentiate Equation (21) with respective to NT

Sensitivity Analysis of Printed Dimensions to Process Parameters

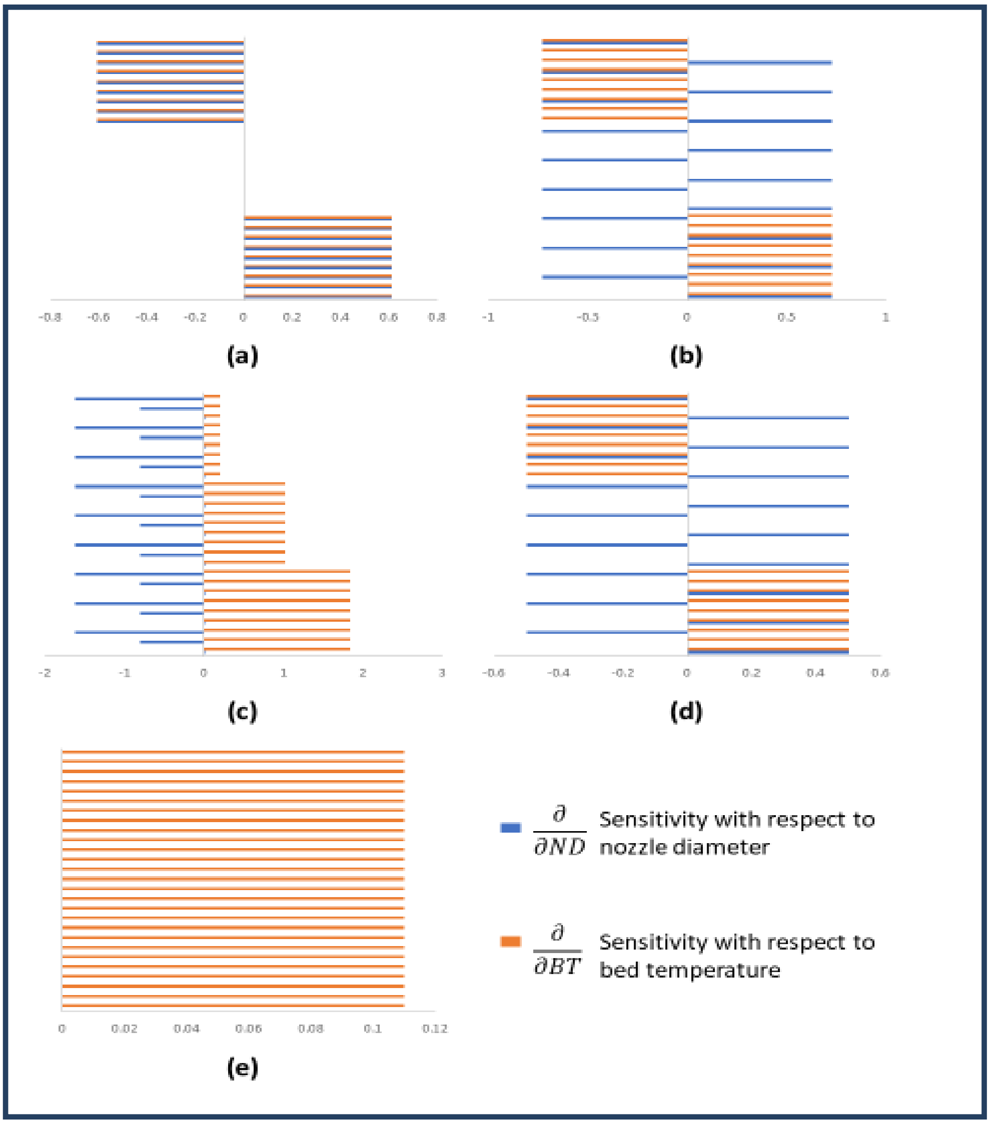

Figure 48. Sensitivity of printed dimensions to process parameters (a) C_l – length of printed cube (b) C_w – width of printed cube. (c) C_h –height of printed cube. (d) L_w – width of printed strut. (e) L_h – height of printed strut

4.3 Printing of Benchmarked Part with Inclined Surface

In order to further differentiate the printing effects between the 2 nozzles with d = 0.51mm and 0.60 mm, two additional complex polyhedrons with 4 converging slopes. The shapes and dimensions of the polyhedron, shown in Figure **49a** and **49b**, approximates 50 mm × 40 mm × 20 mm. They have a depth of 10mm. The slopes of the widths and lengths were inclined at 45 degrees and 30 degrees to the horizontal, respectively. Using Repertier-Host software, the stl file of the polyhedron was sliced to 20 layers and the slopes were printed from the 11th layer. **Figure 50** shows the top view image of the polyhedron which is fabricated using previous optimal AM process parameters obtained (T_1 = 40 °C, T_2 = 100 °C, Q = 1.2 ml/min, v = 20 mm/s, d = 0.51 mm and 0.61 mm). Overall, the layer-by-layer printed architecture can be clearly observed on both of the polyhedrons and the dimensions of these two printed parts were close to the CAD values. When printing was performed with 0.60 mm nozzle instead of 0.51 mm nozzle, there was slight silicone resin overflow at the superior edges due to inadequate curing and over extrusion. Nevertheless, this printing demonstrated that void-less silicone polyhedron with slopes can be reliably achieved.

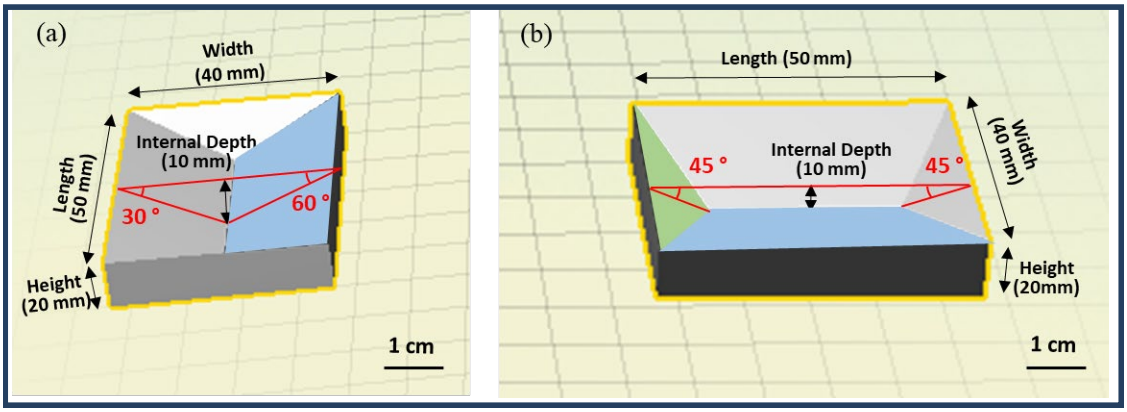

Figure 49 Schematic illustration of a polyhedron samples with four converging slopes and three different angles of inclination (indicated in red): 30, 45, and 60°. The shape and dimensions of the polyhedron are shown in Figure 54 a and b, which approximates 50 mm × 40 mm × 20 mm with a 10 mm interior depth. The Slic3r software slices the polyhedron into 20 layers, while the slope begins on the eleventh layer. The surfaces slopes are colored in grey, green and blue. The inclination angle of 30 ° is made between grey slope and horizontal surface. The inclination angle of 45 ° is made between green slope and horizontal surface. The inclination angle of 60 ° is made between blue slope and horizontal surface.

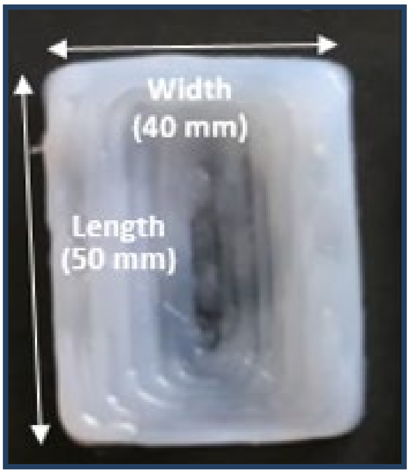

Figure 50 Top view of the printed polyhedron. Scale bar

Chapter 5 – Characterization of 3D Printed Silicone Meniscus

The physical, biochemical, mechanical and biocompatible profiles of 3D printed silicone meniscus should be similar to those of their molded counterparts.

In this chapter, we have used Phosphate Buffered Saline (PBS) absorption test, surface profilometry, Fourier transform infrared (FTIR) spectroscopy, X-Ray Dispersive Spectroscopy (XRDS), Scanning Electron Microscopy (SEM), Thermo-Gravimetric Analysis (TGA), Differential Scanning Calorimetry (DSC) to determine and compare material properties between molded and 3D printed silicone samples. Physicochemical analysis was performed by SEM and XRDS to observe surface level morphological changes and elemental composition changes on the surface of 3D Printed and molded samples, respectively. SEM is used to assess the surface morphology of the silicone implant samples and to investigate the relative changes in surface roughness [129]. XRDS was used to analyze the chemical composition in the top layer of the sample. FTIR is used for detection of chemical changes and surface hydroxylation in defective or damaged samples. TGA and DSC are used to analyze the thermal stability of the silicone implants. ASTM 575 compression testings and cyclic loading up to 1000 cycles [128] are used to assess the mechanical stability and robustness of the silicone meniscus implants. The PBS absorption test [130], together with surface roughness measurement, determines the degree of hydrophobicity of the silicone samples [131]. The former measures the swelling content of the silicone sample, while the latter is a line-profiling method which provides a quantitative picture of the sample surface by using a high-resolution probe to detect the peaks and valleys of the surface topography. The degree of hydrophobicity determines the affinity for attachment of the extracellular matrix and subsequent cell adhesion, proliferation and differentiation [131]. Despite using biocompatible liquid silicone rubbers, the final silicone printout implant must also be evaluated for its biocompatibility. Cell viability and proliferation assays [132] using L929 fibroblastic cells are used to assess the cyto-compatibility of the silicone meniscus.

5.1 Physical Characterization

5.1.1. Dimensional Accuracy Analysis and Surface Profilometry

In this dimensional accuracy study, four printed silicone samples were used. **Figure 51a** shows the overlapped view of the scanned printed silicone meniscus and the CAD model. Here, it is observed that the exterior dimensions, such as the lengths and widths, of the printed meniscus, matched well with the CAD model. **Figure 51b** shows the color-mapped shape deviation of the scanned sample. Based on the analysis result, it is found that the average root-mean-square (RMS) deviation of the four scanned samples from the CAD model is around 0.9017 mm, with standard deviations ranging between 0.8804 and 0.9142 mm. The standard deviation values come from 4 different scanned samples. Each sample is scanned and analyzed to obtain a root-mean-square (RMS) shape deviation value and a standard deviation of shape deviation value. Average RMS shape deviation value is calculated by averaging the 4 RMS shape deviation values from the 4 samples. The standard deviation of the shape deviation is a measure of variation from the mean value. The standard deviations of the 4 scanned samples range between 0.8804 and 0.9142 mm.

Figure 51c shows the color-mapped tolerance analysis of the scanned sample. It is found that all samples have 92% to 94% of the printed geometry falling within a tolerance of ± 2 mm, which is indicated as green region. Although 6% to 8% (as indicated as red and blue) of the printed geometry are beyond the accepted tolerance limits, this does not affect the functionality of the printed knee meniscus as these are non-critical regions. Although 6% to 8% of printed geometry are beyond the accepted tolerance limits, this does not affect the functionality of the printed knee meniscus as these regions are non-critical areas. These results are similar to those of Bortolotto *et al.* [133], that showed the use of inexpensive printer does not necessarily imply inaccuracy of the 3D printing process. The absolute and relative differences, between test objects (CAD models) and 3D printed copies, are 0.23 mm and 0.55 %, respectively.

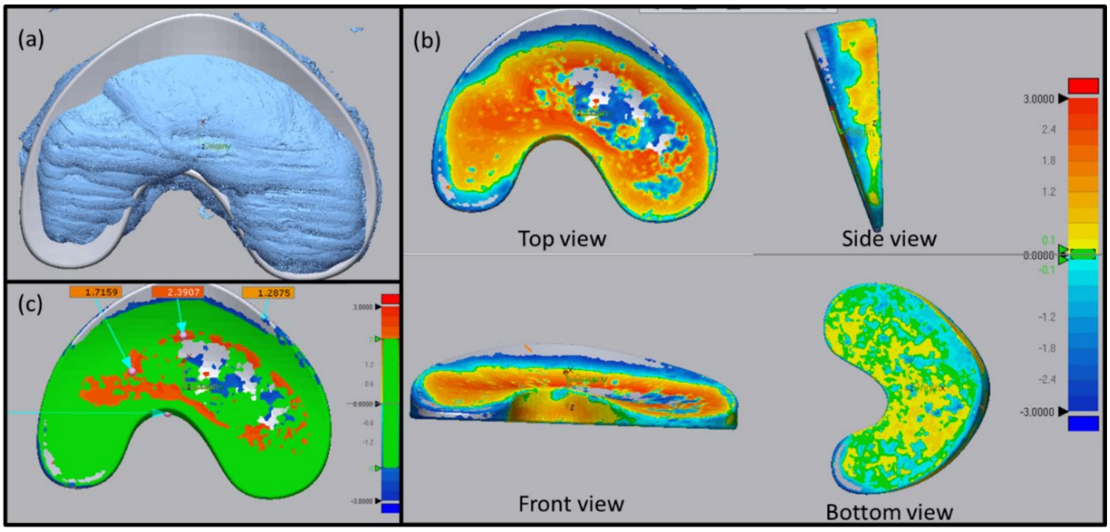

Figure 51 (a) Overlapped view of CAD model and scanned data. (b) Different view of color-mapped shape deviation of the scanned data. (c) Color-mapped tolerance analysis of the scanned data, green indicates within tolerance of ± 2 mm, whereas blue and red indicate out-of-tolerance. All units in mm. The peripheral rim of the meniscus superiorly and central horn-body junction show out-of-tolerance regions.

It is well known that extrusion-based 3D printing technique tend to introduce voids between the adjacent filaments especially for polymeric material. However, the extent of porosity in the 3D printed silicone parts are not well studied. In this study, porosity of the 3D printed silicone knee meniscus is evaluated using μ-CT. **Figure 52a** shows the cross-sectional view of the 3D printed silicone knee meniscus. Tiny pores are observed which may be caused by air bubbles present in the silicone feedstock. Unlike polymeric materials shown in **Figure 52b**, there is no noticeable groove formed between the roads of two adjacent filament. This is probably due to the less viscous property of the silicone that make it easier to fill the gap in between two roads of filaments. The average porosity is found to be 0.27 ± 0.13 % which indicates an almost fully-dense 3D printed silicone part is achievable using this extrusion-based technique. Using CT scan analysis, the porosity is determined from the black spots within the reconstructed image. 5 samples are measured. The image pixel size is 24.25 micrometers, which means anything smaller than 24.25 micrometers cannot be captured.

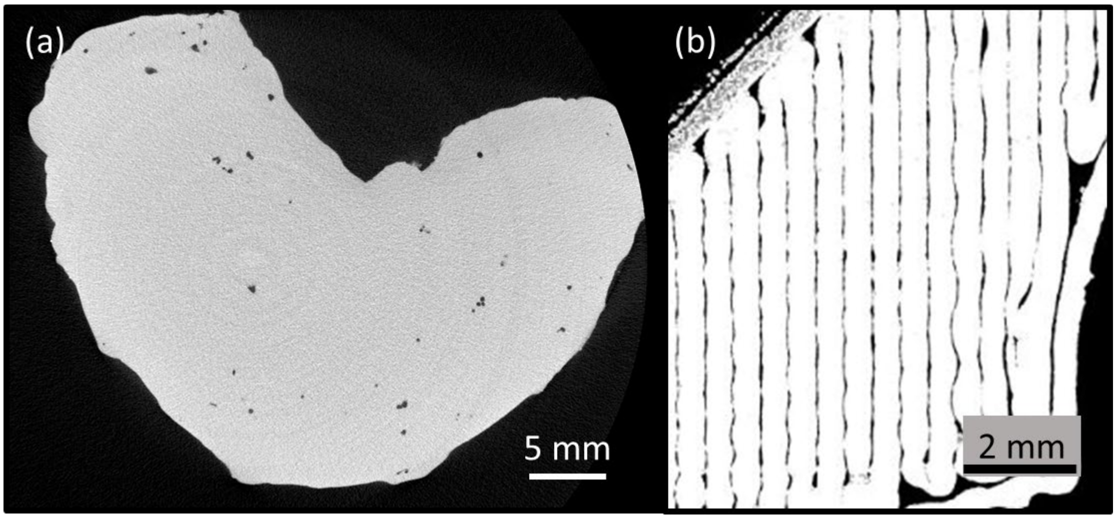

Figure 52 (a) cross-sectional view of 3D printed silicone knee meniscus with some tiny pores, no noticeable grooves are formed between silicone extrudates (b) clear groove between roads of filaments in the 3D printed polymeric material resulting of the extrusion-based technique [25]

This surface-profiling method used a high-resolution probe to detect and provide quantitative measurements of the peaks and valleys of the surface topography. Scans were taken across surface of the anterior horn, body and posterior horns, in triplicates, of the silicone meniscus implants. The results are shown in **Figure 53** indicating there is no statistically significant difference in surface roughness between both molded and 3D-Printed Ecoflex 30 and Ecoflex 50 silicone implants. The optical images for both 3D printed and molded silicone samples are shown in **Appendix E**.

Surface Roughness Measurement

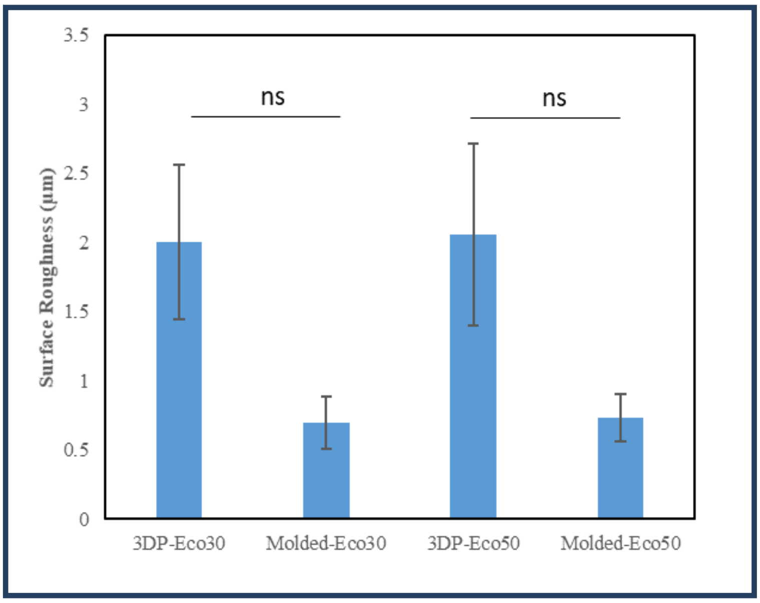

Figure 53 Surface Roughness (µm) of Ecoflex-30 and Ecoflex-50, manufactured by molding and 3D printing. There is no statistical significant difference between 3D printed and molded Ecoflex 30/Ecoflex 50.

Table 22 Surface roughness data and p values

Samples	3DP-Eco30	Molded-Eco30	3DP-Eco50	Molded-Eco50
	1.25	0.691	1.57	0.963
	2.17	0.467	2.99	0.685
	2.59	0.932	1.62	0.551

Mean	2.003333	0.696667	2.06	0.733
SD	0.559603	0.189878	0.657926	0.171589
P values	> 0.05 (ns)		> 0.05 (ns)	

5.1.2 Scanning Electron Microscopy

SEM showed that different manufacturing methods of the silicone meniscus implants resulted in distinct surface patterns. The surfaces of implants are not textured in both groups. Figures 54 and Figures 55 showed SEM of Ecoflex 50 and that of Ecoflex 30, respectively. **Figure 54a, c and e** representatively showed the smooth, irregular, and diffuse surface patterns on molded silicone implants, while **Figure 54b, d and f** showed the regular, wavy, mosaic surface patterns on 3D printed silicone implants. In both groups, SEM did not show any tear, fracture or heavy metal contamination. The layer-by-layer configuration is obvious in 3D printed specimens.

Scanning Electron Microscopy

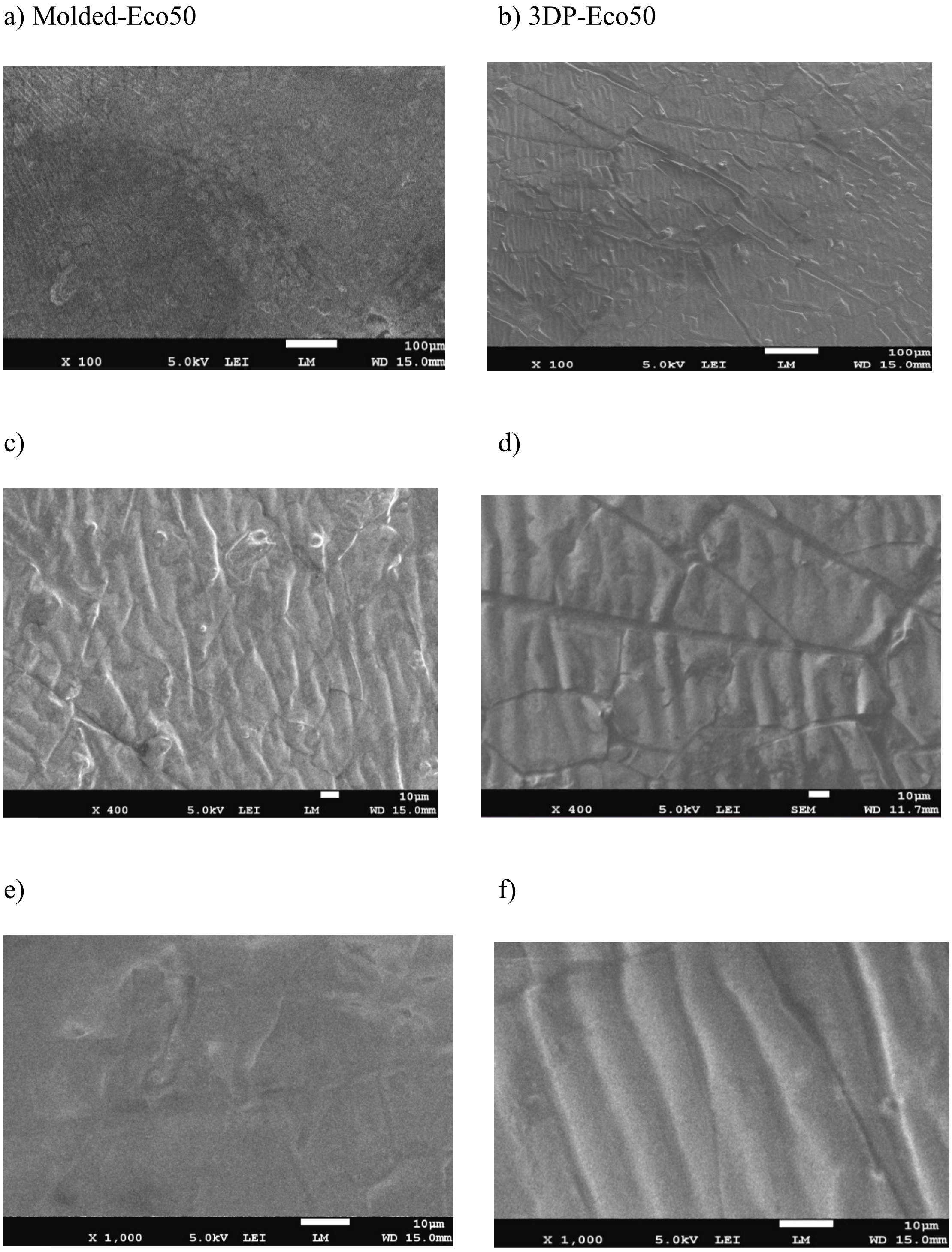

Figure 54 Representative SEM pictures of Ecoflex 50 (magnification 100x, 400x and 1000x) showing the different surface patterns of (a, c, e) molded silicone and (b, d, f) 3D printed silicone. A more orderly track is observed on the surface of 3D printed silicones

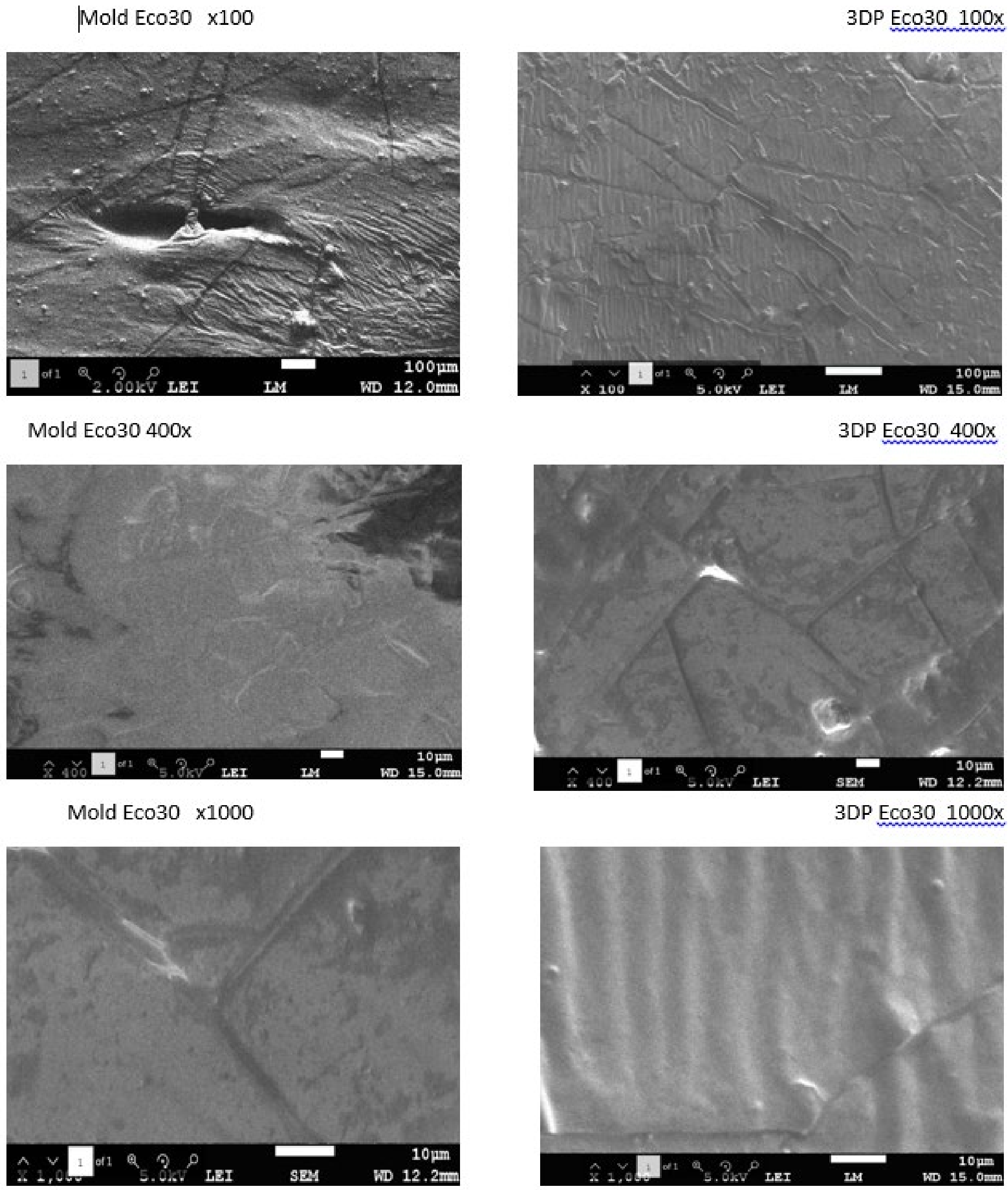

Figure 55 Representative SEM pictures of Ecoflex 30 (magnification 100x, 400x and 1000x) showing the different surface patterns of (a, c, e) molded silicone and (b, d, f) 3D printed silicone. A more orderly track is observed on the surface of 3D printed silicones

5.1.3 PBS Absorption Test

The PBS absorption tests showed that the water content of both silicone implants Ecoflex 30 and Ecoflex 50 increased rapidly within the first 24 hours and stabilized thereafter, as shown in **Figure 56**. These results shown are in concordance with those of Gong's study [134], which proved that water diffusion, and absorption of silicone rubber material followed Fick's law. Fick's law expresses moisture content c(t) as a function of the diffusion coefficient D and the maximum moisture content c_s in wt% at the absorption equilibrium as in **Equation 22** shown below. In this study, the maximum moisture content Cs were calculated to be 0.36 % for Ecoflex30 meniscus implants and 0.47 % for Ecoflex 50 meniscus implants. These values were slightly higher than the Cs value 0.23 % in Gong's study which assumed that diffusion only occurs from the top and bottom surfaces of their used silicone rubber samples. There is no significant difference between water contents after 24 hour post soak and those after one-week post soak data, which clearly demonstrated that the water contents have already stabilized within 24 hours of soaked period. This indicates that the meniscus implants should also have attained its final size and shape within 24 hours of arthroscopic insertion into the knee joint. This has important surgical implication since excessive swelling post-implantation of the meniscus can cause obstruction and locking of the knees.

$$c(t) = c_s - c_s \frac{8}{\pi^2} \sum_{k=1}^{20} \frac{1}{(2k-1)^2} \exp[-\frac{(2k-1)^2 D\pi^2 t}{d}] \qquad \text{Equation (22)}$$

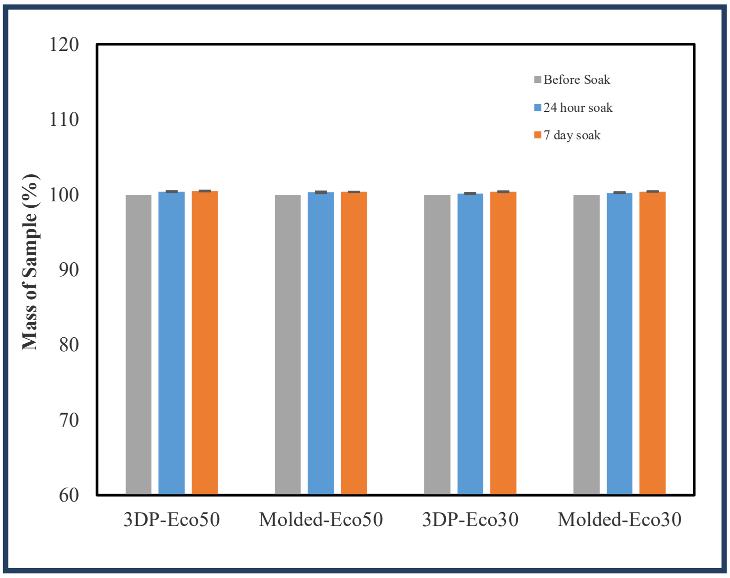

Figure 56 Phosphate Buffer Solution (PBS) absorption test for silicone meniscus implants Ecoflex 50 and Ecoflex 30. There is no statistically significant difference in the masses of 3D printed and molded Ecoflex 30 and Ecoflex 50 meniscus groups, before soak and after 24-hours and 7-day soak.

Table 23 PBS absorption data and p values

Samples	**Before Soak (referenced as 100%)**	**24-hour Soak (% Mass)**	**7-day Soak (% Mass)**
3DP-Eco50	100	100.4011861	100.5232862
	100	100.3320053	100.4482072
	100	100.3995794	100.4206099
	100	100.3419147	100.4223652
	100	100.5168493	100.5375233
Mean	100	100.398307	100.4703984
SD	0	0.073549617	0.056083422
P values		< 0.001 (***)	< 0.001 (***)
Molded-Eco50	100	100.2233389	100.3768844
	100	100.4666667	100.3866667
	100	100.3119067	100.339029

	100	100.3017833	100.3703704
	100	100.1909612	100.3309994
Mean	100	100.2989313	100.36079
SD	0	0.106868383	0.02439999
P values		< 0.001 (***)	< 0.001 (***)
3DP-Eco30	100	100.241303	100.3820631
	100	100.1978239	100.4154303
	100	100.1457726	100.3748438
	100	100.3703356	100.3989674
	100	100.0626174	100.2713421
Mean	100	100.2035705	100.3685293
SD	0	0.114537918	0.056556536
P values		< 0.001 (***)	< 0.001 (***)
Molded-Eco30	100	100.1968781	100.4078189
	100	100.3356606	100.3759398
	100	100.2962268	100.4257248
	100	100.2767892	100.3954132
	100	100.1587722	100.4101614
Mean	100	100.2528654	100.4030116
SD	0	0.07296526	0.018579113
P values		< 0.001 (***)	< 0.001 (***)

5.2 Biochemical Characterization

5.2.1 FTIR

FTIR was used to analyze the change of the molecular structure and functional groups on the surface and in inner parts of the silicone 3D printed and molded parts. The FTIR results are depicted in **Figure 57**. The absorption peaks at 3000 cm^{-1} and 1400 cm^{-1} correspond to the stretching of methyl CH_3 group and asymmetric Si-CH_3 stretching, respectively. The peaks at 1255 cm^{-1} and 1000 cm^{-1} are attributable to the Si-CH3 and Si-O-Si bonds, respectively. The prominent peak at 800 cm^{-1} points to the stretching of Si-CH3. All these peaks are specific to silicone LSRs.

It can be observed from both **Figure 57a and 57b** that both FTIR spectra of 3D printed and molded Ecoflex 30 and Ecoflex 50 silicone samples show exactly the same peaks, indicating that the heat-curing processes within the silicone printer, at heating temperatures of less than 120 °C, did not alter the chemical composition of the Ecoflex silicone and the passage of silicone resins through the syringe, tubing and nozzle did not contaminate the silicone resins.

FTIR of 3D printed and molded Ecoflex 30/ Ecoflex 50

a) b)

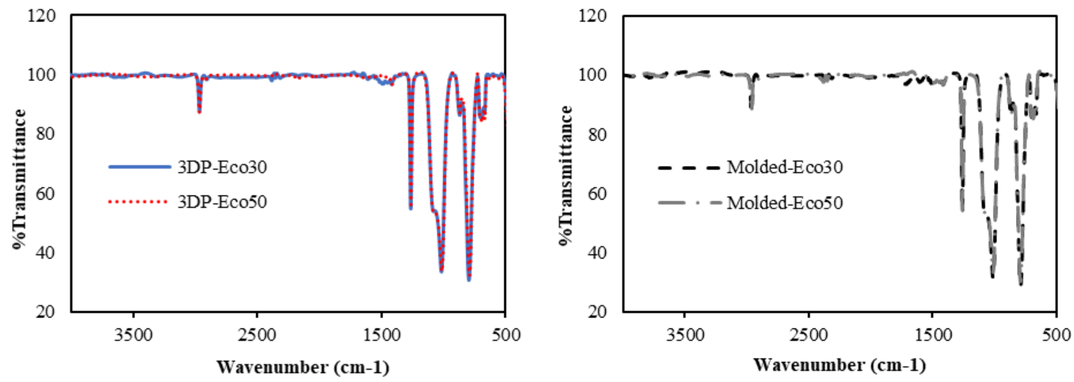

Figure 57 FTIR absorbance spectra of a) 3D printed silicone implant and b) molded silicone sample. Both 3D printed and molded silicone meniscus show identical absorbance peak, indicating that neither the 3D printing nor molding process disrupts the molecular structure of Ecoflex 30 and Ecoflex 50 meniscus.

5.2.2 TGA/DTG/DSC

Compositional analysis TGA measures sample mass in relation temperature or time. It is used to determine the composition of elastomers, for example, moisture, solvents, plasticizers, polymers, carbon black or inorganic fillers.

The TGA analysis of Ecoflex silicone elastomer has three steps (**Figure 58**). The DTG curve (the first derivative of the TGA curve) is used to delineate the correct temperature range for the evaluation of subsequent steps. The first step below 300 °C corresponds to the loss of 3.1% mass, a relatively small amount of relatively volatile components, mainly un-crosslinked crosslinkers. The second step of silicone sample pyrolysis happens between 300 °C and 550 °C. This second step corresponds to a pyrolysed polymer content of about 59.937 % in the molded silicone sample and 61.95 % in the 3D printed sample (**Table 5**). The residual silica content is 40.063 % in the molded sample and 38.05 % in the 3D printed sample.

At 600 °C, nitrogen is switched to air to oxidize the carbon black formed during the pyrolysis reaction. The content of carbon black filler can be determined in the third step, between 600 °C and 700 °C and is measured to be about 40.03 % in molded silicone samples and 38.05 % in 3D printed silicone. The final residue is made up of inorganic fillers such as silicates of oxides.

Appendix G shows a comparison DSC, TGA and DTG of both the molded and 3D printed Ecoflex 30 and Ecoflex 50 specimens. There is a slightly greater heat flow requirement for Ecoflex 50 specimens in comparison to Ecoflex 30 specimens as shown in the DSC graphs. This is in concordance with the greater activation energy postulated and calculated previously and could be due to the greater meshwork and stronger crosslinks in Ecoflex 50. However there was no obvious difference in TGA and DTG for all Ecoflex 30 and Ecoflex 50 specimens.

a) Ecoflex-50 Molded Silicone Meniscus

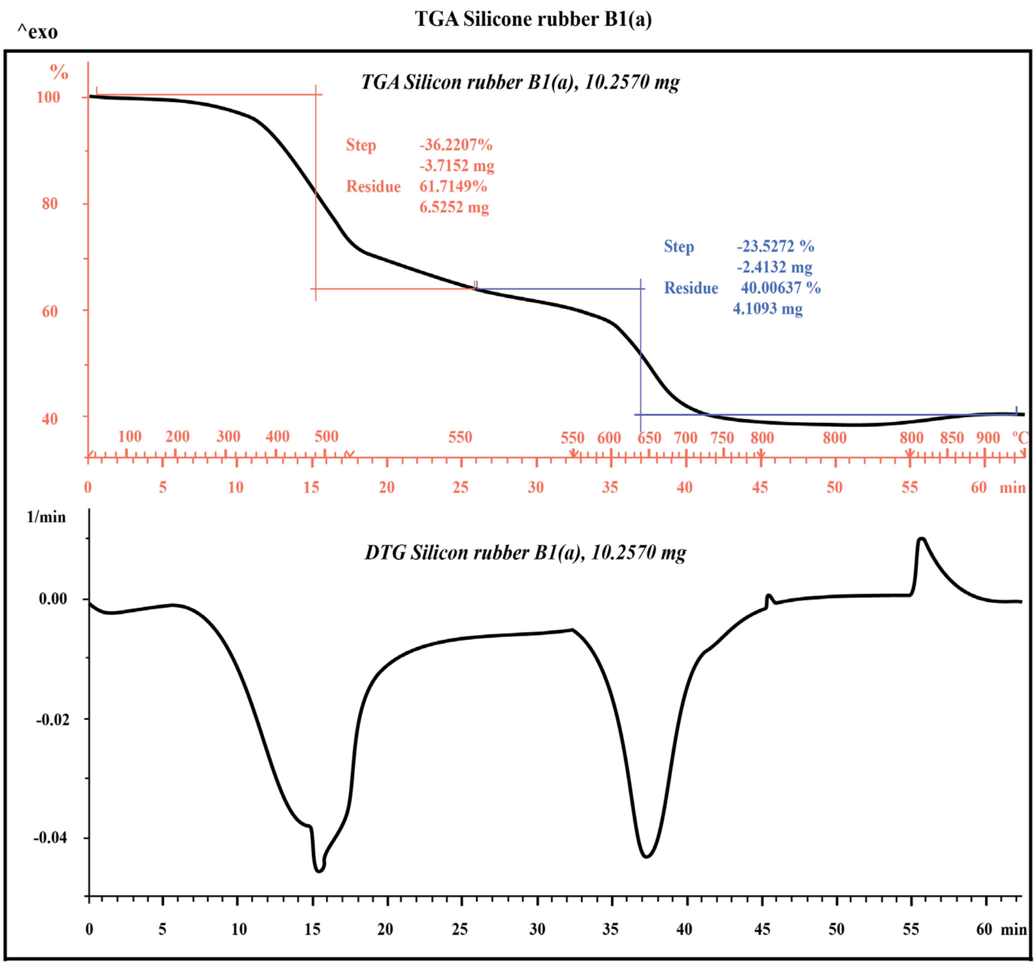

DSC Silicone rubber B1(b)

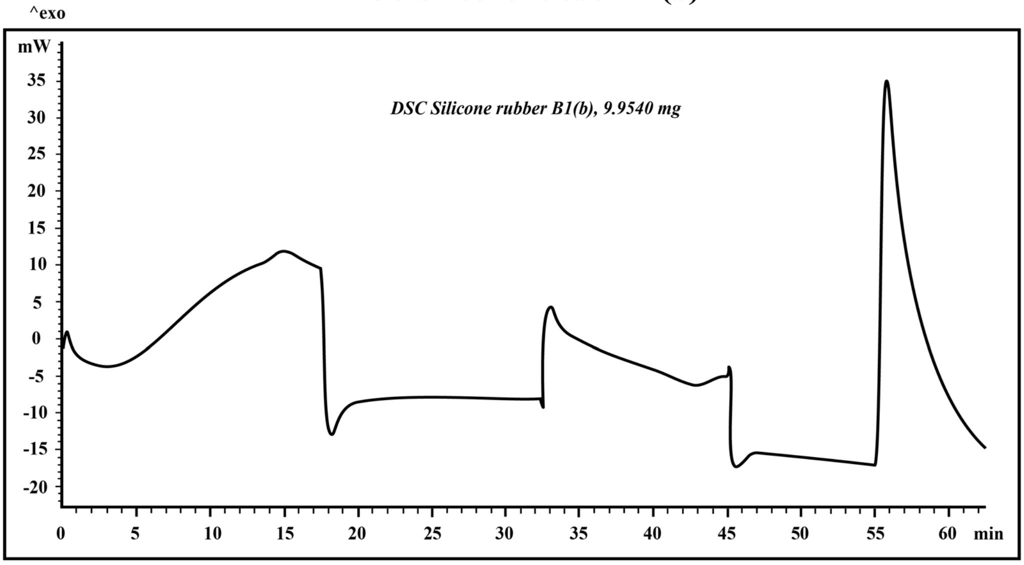

b) Ecoflex-50 3D-Printed Silicone Meniscus

Silicone B2

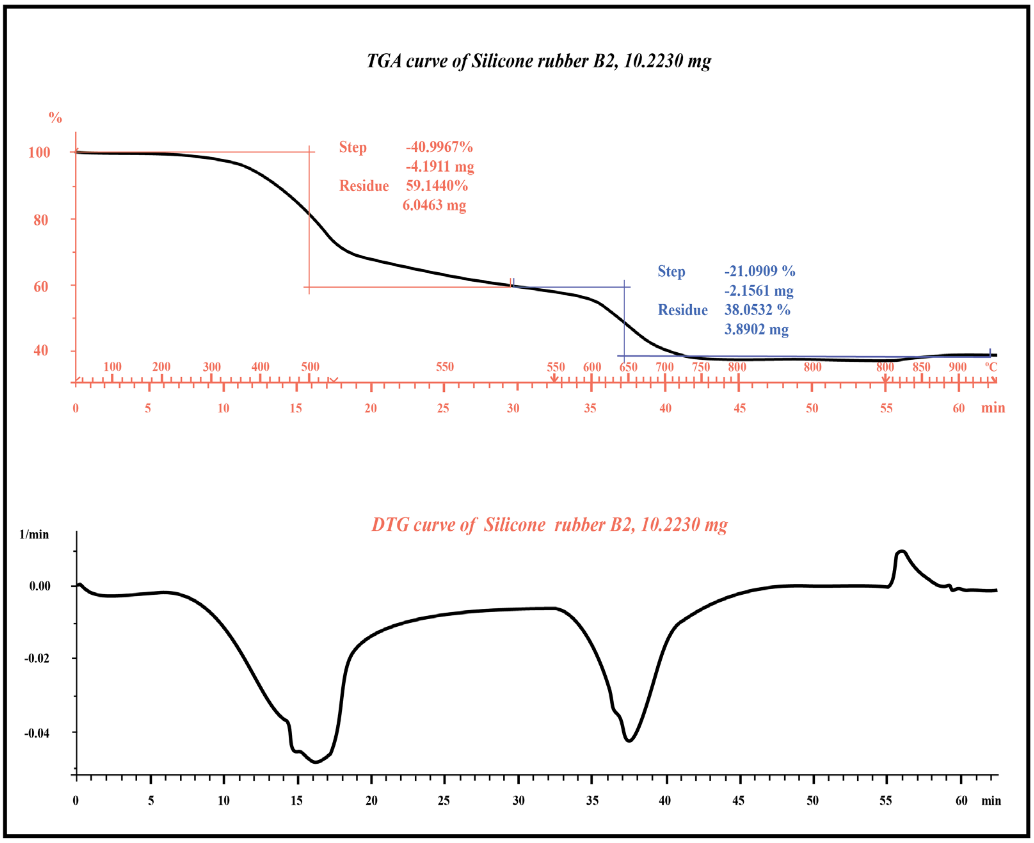

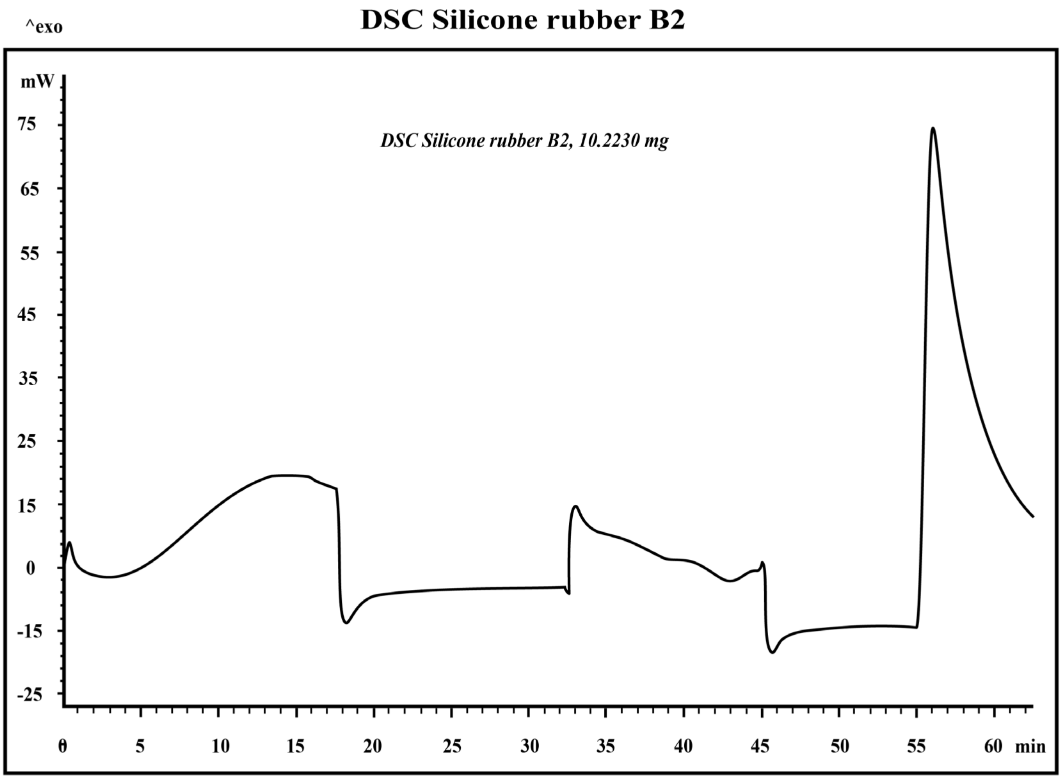

Figure 58 TGA/DTG/DSC curves of (a) molded and (b) 3D-Printed silicone Ecoflex 50 measured from 30 °C to 700 °C at a heating rate of 20 °C/min. The TGA curve (red) measures the loss of mass and the DSC curve (black) provides information about endothermic and exothermic effects. Similar % polymer degradation are observed in both 3D printed and molded silicone samples. Same number (2) of DTG peak, exothermic and endothermic peaks are registered in both 3D printed and molded silicone samples.

Table 24 % polymer content of material and % residual silicates / oxides

Samples	**% Polymer content**	**% Oxides residual silicates**
Ecoflex-50 Molded Silicone implant	59.937	40.063
Ecoflex-50 3D printed Silicone implant	61.95	38.05

5.2.3 X-Ray Fluorescence Spectroscopy

X-Ray Fluorescence Spectroscopy (XRFS) uses silicon-based detectors to detect characteristic secondary x-rays produced as a result of the incident primary X-ray beam impacting on the silicone specimens.

The atomic composition of the molded silicone and 3DP Silicone Implant are shown below in **Table 25**. The energy table of silicone is adapted from http://www.shimadzu.co.jp/surface/.

Both molded and 3D-printed Ecoflex 50 silicone implants show similar silicone composition of 99.7 % and 99.8 %, respectively (element 14 Si, K alpha-1.740, K beta-1.829, Kab-1.84). The sulphur, iron and copper elements detected are likely additives within the resins. There were no carbon-black fillers in both groups. There was no heavy metal contamination observed in both groups. **Appendix F** shows the XRFS curves for both molded and 3D-printed silicone samples.

Table 25 Atomic Composition obtained for molded and 3D Printed Silicone Implant

Samples	**Si (%)**	**S (%)**	**Fe (%)**	**Cu (%)**
Eco50 molded implant	99.739	0.253	0.005	0.003
Eco50 3D-printed implant	99.816	0.174	0.005	0.01

5.3 Mechanical Characterization

5.3.1 Weibull Failure Plot Model of 3D Printed Meniscus

The purpose of Weibull Failure Plot is to determine the probability of failure and the maximum failure strength a 3DP silicone meniscus sample is able to bear prior to failure. The failure data of the silicone meniscus implants showed moderate variability and the two-parameter Weibull distribution (e.g. exponential, lognormal, Weibull distribution, etc.) can used for the reliability analysis [135] due to its versatility [136,137].

An example is the Weibull proportional hazard model, which can be used to calculate the reliability of a component considering the effect of operational conditions (such as temperature, dust or humidity) [138]. Most Weibull family distributions have a characteristic shape on the Weibull probability plot (WPP). For instance, a two-fold Weibull mixture is an S-shape and a two-parameter Weibull distribution is a straight line [139]. Hence, the WPP can provide a systematic procedure to determine which model is more appropriate for a specific data set.

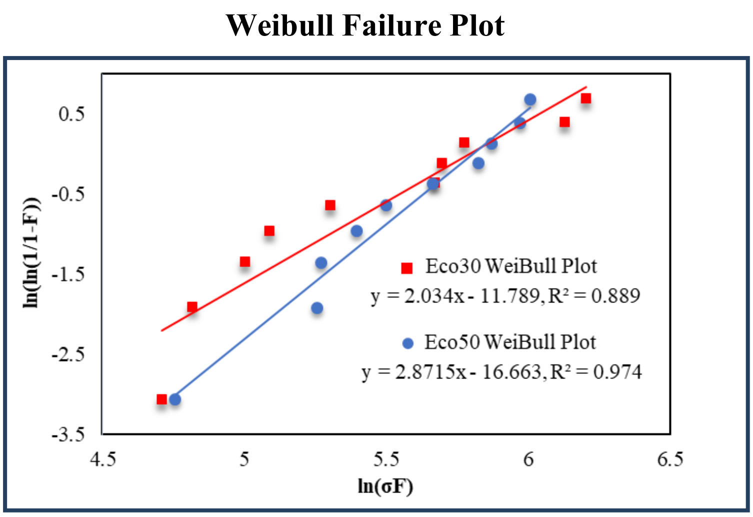

Figure 59 Weibull Failure Plot for 3DP Ecoflex 50 and Ecoflex 30 meniscus implants. Ecoflex 50 meniscus samples demonstrate higher strengths and lower failure rates than Ecoflex 30 meniscus samples

For only 1 in 10^6 samples of meniscus to fail, ($F= 10^{-6}$), at 1000 x of cyclic loading and max strain rate of 1000 mm/min, a typical daily walking frequency of a sedentary person or patient who has undergone key-hole meniscus surgery undergoing crutch-assisted ambulation , the maximum stress that Ecoflex 50 ($\boldsymbol{\sigma F_{50}}$) and Ecoflex 30 ($\boldsymbol{\sigma F_{30}}$) silicone meniscus implants can take, ($\boldsymbol{\sigma F_{50}}$), is 2.696 MPa and 0.369 MPa, respectively, as shown in **Figure 59**.

- X axis = natural log of strength at failure= ln (strength at failure)
- Y axis = natural log of the natural log of (1/ 1-F)

  = ln (ln (1/1-F))

  F = cumulative probability of failure

  i = sequence number of test after ranking of failure strength

  N = total number of test.

  F = (*i*-0.5) / N

This type of behavior is described by Weibull statistics, in which flaws are assumed to be randomly distributed throughout the tested volume. The probability of failure of a material is given by:

$P = 1 - \exp [-V/V_0 (\sigma/\sigma_0) m]$ Equation (23)

where *m* is the Weibull modulus, *V* is the tested volume, σ is the failure strength, and V_0 and σ_0 are scaling constants.

By rearranging and taking the natural logarithm of both sides of Equation (23), the following equation is obtained:

$\ln [\ln (1/1-P)] - \ln V/V0 = m \ln \sigma - m \ln \sigma_0$ Equation (24)

For a constant tested volume, Equation. (24) is reduced to:

$$\ln [\ln(1/1-P)] = m \ln \sigma + k$$ Equation (25)

where *k* is a constant. The Weibull modulus, *m*, is then determined graphically as the slope of the "Weibull plot" of ln[ln(1/1−*P*)] against ln σ.

$y = \ln (\ln (1 /(1\text{-}F)) = mx + c$

$\ln (\ln (1/1\text{-}\ 10^{-6})) = -13.8155 = 2.8715x - 16.663$ $\quad x = \ln (\boldsymbol{\sigma}\mathbf{F}_{50}) = 0.9916420$

$e^{0.9916420} = 2.696$ MPa

$\ln (\ln (1/1\text{-}\ 10^{-6)}) = -13.8155 = 2.034x - 11.789$ $\quad x = \ln (\boldsymbol{\sigma}\mathbf{F}_{30}) = -0.99582$

$e^{-0.99582} = 0.369$ MPa

The null hypothesis for no differences between Ecoflex 30 silicone printouts and Ecoflex 50 silicone printouts was rejected. Higher strengths were associated with Ecoflex 50 silicone meniscus printouts. Weibull analysis showed both groups had parameter b values, Weibull modulus, greater than 1. This implies that the failure rates of both groups of samples increase with time, as expected.

However, the higher b value (Weibull modulus) in Ecoflex 50 showed that it has a lower failure rate than that of Ecoflex 30. This is probably due to the earlier breakage of intermolecular bonds in Ecoflex 30 samples as a result of its greater percentage elongation.

Weibull analysis also revealed that parameter a (the characteristic strength), which indicates the highest failure stress, at a probability of 63.2 %, ranges from 4.75 to 5.97

N/mm^2 for Ecoflex 30 and ranges from 4.71 to 6.20 N/mm^2 for Ecoflex 50. The higher values of a were associated with Ecoflex 50 samples and lower values with Ecoflex 30 samples, following the same pattern with the results based on the means.

5.4 Biocompatibility Cytotoxicity Tests

5.4.1 Cytotoxicity Test via Extraction Method (ISO10993-12)

Cytotoxicity test by extraction according to ISO10993-12 [144] is the most widely used test in most in-vitro biocompatibility studies. However, the extraction parameters in ISO10993-12 such as extraction medium, extraction time, extraction volume to surface area should be modified to simulate in vivo degradation. In this cytotoxicity study, we examined and compared between molded and 3D printed meniscus samples for extraction time of 72 hours. 3 samples were tested for each unique condition. Results from quantitative cell proliferation assays indicated a statistically non-significant difference between almost all 3D printed and molded samples (**Figure 60**). This points to the non-toxic nature of the 3D printed silicone as no toxic chemicals were released over the extraction period. The results are extremely promising and highlight the long-term biocompatibility and stability of the 3D silicone using cell culture medium as extraction medium.

Cell Proliferation Assays

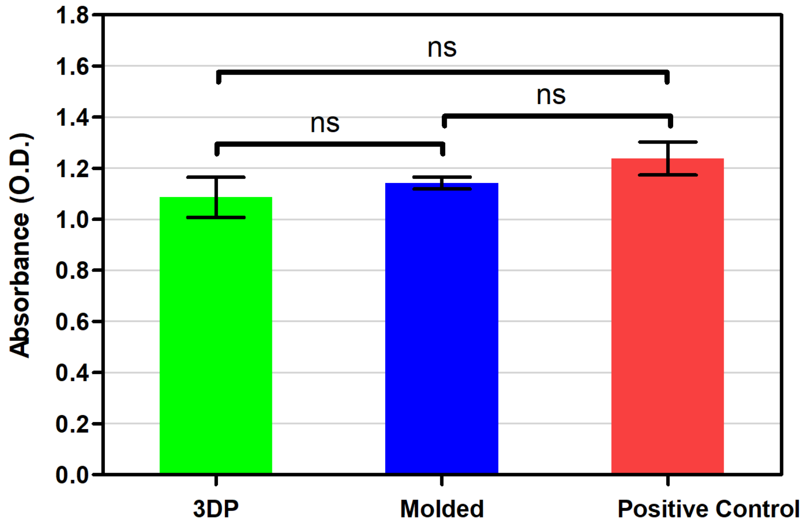

Figure 60 a) Cytotoxicity results under different extraction volume/surface area ratios for extracts collected from different meniscus samples: 3D printed, molded and positive control. 3 samples were tested for each unique condition. Cell proliferation of L929 cells after 24 h incubation with extract was quantified based on the WST-8 cell proliferation assay. Statistical significance between groups was assessed using two-way ANOVA followed by Bonferroni post-tests. ns = p>0.05. There is no statistical significant difference between 3D printed and molded meniscus groups.

Cell Proliferation Assays

	3D-Printed	Molded	Positive Control
Fluorescent Images	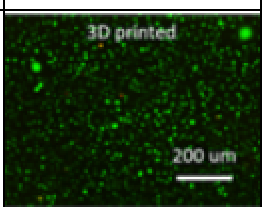	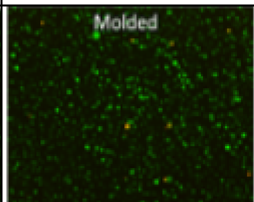	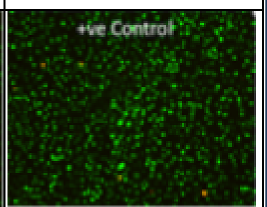
Optical Images			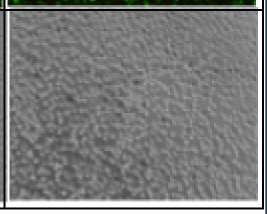

Figure 60 b) Fluorescent images of L929 cells seeded on 24-well plate after 24 h incubation with extract. Cells were stained with the Live/Dead® cell viability assay. There is no statistical significant difference between 3D printed and molded meniscus groups.

Table 26 Cell Proliferation after incubation with extract from different meniscus samples: 3D printed, molded and positive control

	3DP	**Molded**	**Positive Control**
Absorbance (O.D.)	1.086 ± 0.078	1.142 ± 0.023	1.239 ± 0.065

Chapter 6 – Potentials and Challenges of 3D Printing of Silicone Meniscus

In this chapter, the first section provides an in-depth discussion into the preparation of MRI DICOM files, its conversion into 3D printable stl files by segmentation, prior to printing. The second section looks into the design of micro-reservoir and micro-channels and the third section looks at a method to incorporate shape-memory properties within the meniscus. Finally, the chapter concludes with an implementation flow chart of the entire process chain.

6.1 Preparation of 3D meniscus stl files from Magnetic Resonance Imaging (MRI) Images

6.1.1 MRI DICOM data set preparation and file conversion

The first step starts with the import of the dataset in MRI DICOM format. These datasets are in axial views and as the Slicer3r program analyzes the images, additional sagittal and coronal views are generated. To generate the 3D visualization, the **"*volume rendering*"** option is chosen from the drop-down list in the ***DICOM*** module. From the "***preset***" select option, modulation to the opacity, color and gradient transfer can be made. Once the "***region of interest (ROI)"*** is cropped under the ***"voxel based cropping"*** and the "***visibility"*** key is turned on, the computer will generate the 3D visualization in the background. By manipulating the range slider under the "***Shift***" parameter and ***"Scalar Opacity Mapping",*** one can have additional control over the threshold of the transfer function. This volume rendering of the dataset stacks up the dataset, applies color and opacity over them to generate a "pseudo-3D image" which provides a detail preview of what the actual 3D image will look like and helps to the viewer to anticipate printing problems. This Pseudo-3D volume, however, cannot be used for printing.

6.1.2 Creation of the 3D Volume of meniscus (segmentation) for actual printing and Label Map

The second step of creating the 3D volume for actual printing, begins with selection of ***"Editor"*** module to create and edit label maps on which the 3D volume is based. The ***"color table"*** is a color code to manage the label map. A label map is the generation of a printable 3D volume block from basic voxels. In the ***"Create and Select Label Maps"*** and under ***"Per-structure volume" tab,*** select ***"Add Structure"*** to initiate a range of options of color codes for the label map. For example in Fig 1 to Fig 3 below, blue color can be assigned for meniscus label and brown color for bone label. This label map once created will be listed under ***"Per-structure volume"*** tab.

The following "effects" can be used for the editing of the selected label maps: ***"Paint Effect", "Draw Effect", "Wand Effect", "Level Tracing Effect", "Rectangle Effect", "Erase Label" and "Threshold Effect".*** After editing, clicking on the ***"Make Model"*** button generates a 3D printable object which can be saved in file and exported in printable .stl (stereolithography) formats.

6.1.3 Using Autodesk Meshmixer to fine-tune edit and prepare segmented files for printing

Finally, import the saved .stl file model and use AUTODESK MESHMIXER to clean up the model, reduce the triangular counts if necessary, check for any segmentation flaws and again re-export it as .stl to be print ready.

The 3 steps used in processing customized patient bio-modelling involve 1) acquisition of data, 2) processing of image and 3) printing of model. Each step is prone to errors and may cause distortions in the final printouts.

Following imaging, the CT / MRI DICOM data is converted via an image segmentation process into STL file format. This segmentation process involves voxel clustering into various regions of interest (ROI). This process can performed automatically, manually or both. Manual segmentation, while being the most accurate method, has the greatest source of error since it requires a great deal user experience and knowledge of anatomy.

Thresholding, shown in **Figure 65,** is the most common image segmentation algorithm. Firstly, the desired threshold intensity is chosen. Only voxels with equal or higher intensities are included in the segmented volume, while others are discarded. Edge detection and region growing are other segmentation method where a seed voxel may be made to grow repeatedly into adjacent voxels until a stopping threshold is met.

Thresholding with Label Maps

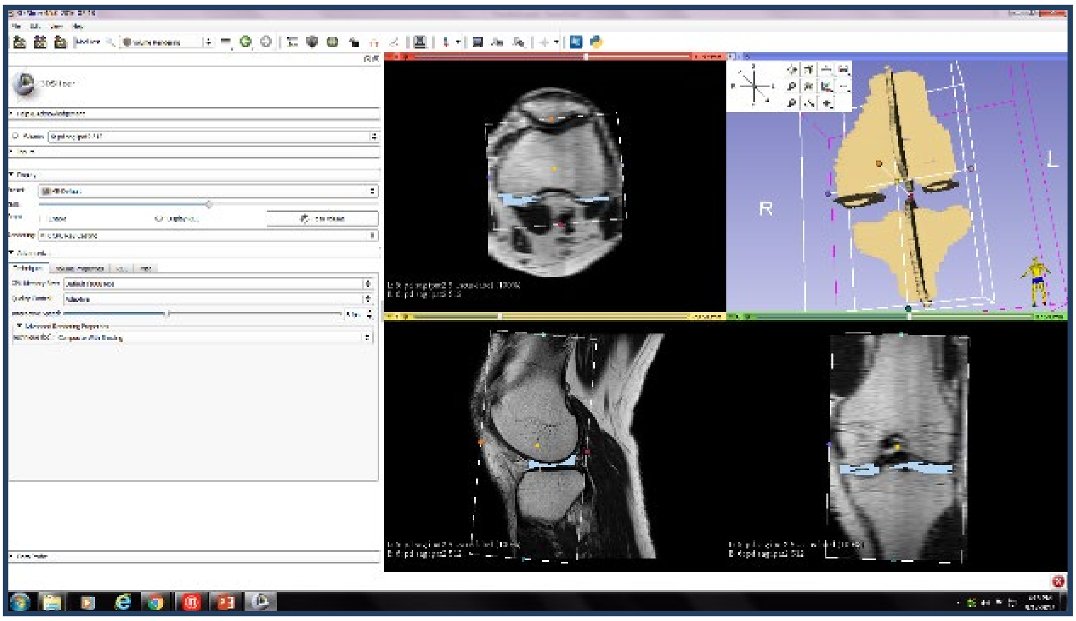

Figure 61 Label Map, Blue for meniscus. Brown for bone. Adapted from [122]

Considering this vagueness, threshold-based segmentation may pose various problems:

1) Scanned regions of same density can still erroneously pose different threshold depending on their position in the image volume

2) Boundaries with similar or overlapping intensities are difficult to delineate

3) As only one threshold value can be assigned to one voxel, its value is automatically determined by the predominant tissue type that fills the voxel. For instance, if 55 % of the voxel is filled predominantly by fat, then the whole voxel will be assigned the threshold value of fat. This further compromises the accuracy of threshold based segmentation

4) Substantial subjective interpretation is required in assigning threshold values. This problem is especially significant when the voxel intensity distribution over the image is non-uniform.

6.1.4 Challenges in Segmentation

Prior to be printable, the patients' DICOM imaging data has to be converted to a 3D virtual model, a 3D mesh. The file format most commonly used is the STL (Standard Tessellation Language) file format. Many programs exist that are able to convert DICOM data to STL files. Toolpath of the intended printout can subsequently by generated, as shown in **Figure 66**. Commercial software, such as Surgicase CMF© are FDA- and CE-approved whereas free programs, available online do not have the approval. Table 27 from Stratasys Technical Application Guide offers a comprehensive overview of the various software for viewing DICOM images.

Table 27 Software For Viewing DICOM Images

Name	Dicom Import	3D visualzation	STL creation	STLfixing	STL editing	FDA clearance	Thresholdingding	AutoSegmentation	Free
Osirix	+	+							+
InVesalius	+	+	+	+			+	+	+
ITK Snap	+	+	+				+	+	+
Mimics	+	+	+	+	+	+	+	+	
Mimics Inprint	+	+	+	+	+	+	+	+	
Vitrea	+	+	+			+	+	+	
Seg3D	+	+	+				+	+	+
3Dslicer	+	+	+				+		+
DeVIDE	+	+	+				+	+	+
TurtleSeg	+		+						+

Bucking et al provided an overview of various softwares with segmentation tools which are applicable to any part of the body is shown in Table in Appendix H. However the quantification and direct comparison of print accuracies using these softwares, have not been performed and detailed. Using FDM printing, the group was able to demonstrate a mean error of 0.78%, 1.3% and 2.53%, between CAD model and 3D printed phantom ribs, liver and lung, respectively. This is shown in Table 28.

Table 28 Quantification of print accuracy based on comparing size of anatomical landmarks between computer model and 3d print

Phantom	Feature	Measured in silico (mm)	Measured in 3D Print (mm)	Percentage Error
Ribs	Superior Rib thickness	14.4	14.1	2.1%
	Interspinous process distance	110.1	110.4	0.3%
	Spine Depth	75.8	78.2	0.5%
	Middle Rib length	187.2	187.5	0.2%
	Mean Error			0.78%
Liver	Total height	99.5	99.1	0.4%
	Total Width	201.1	198	1.6%
	Total Depth	135.1	132.5	1.9%
	Mean Error			1.3%
Lung	Bronchus length	75.2	74	1.6%
	Bronchus thickness	10.8	10.5	2.9%
	AP lung base	114.5	118	1.7%
	AP pericardium	57.5	60	4.3%
	Mean Error			2.53%

Free programs able to convert volume-imaging data to a printable virtual mesh do not provide equivalent results. Variations were noted in the three plane of space with a systematic difference between free programs and the commercial FDA-approved one. While the length and width were less than a millimeter different to the reference, the dimension that most varied was the length with a difference reaching −2.06 mm with itk-Snap. Geometric data also varied significantly, the number of triangles composing the meshes being much different from the reference, resulting in variable file sizes. Algorithms used by the programs are not the same. In the era of 3D printing made directly accessible in surgical departments, great attention should be paid to the accuracy of the models created with free software.

Toolpath generation during 3D printing

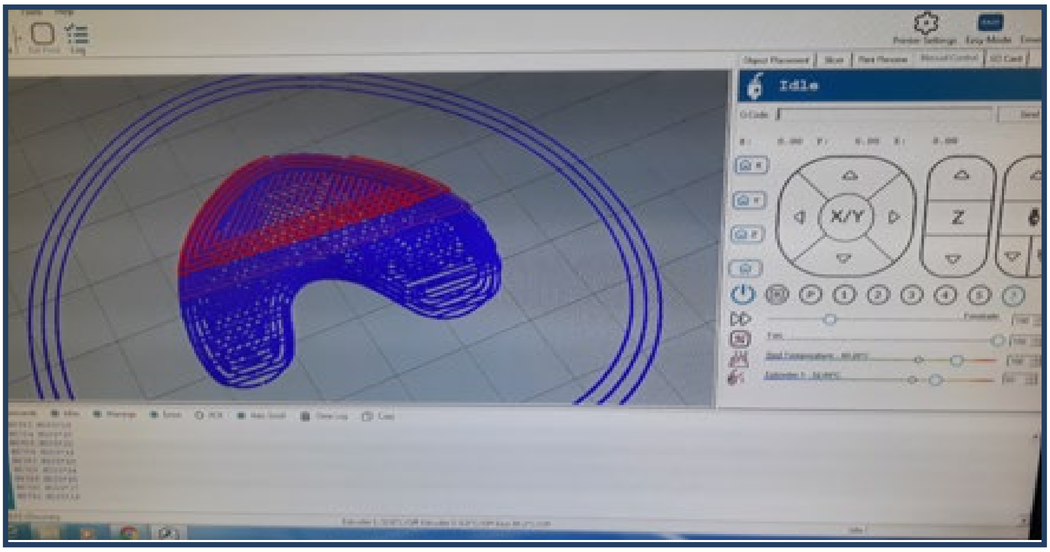

Figure 62 Tool path generated for meniscus

6.2 Design of Micro-reservoir and Micro-channels

In Chapter 2, a comprehensive review has been provided on the partial meniscus implants, namely CMI and Actifit and on the total meniscus implant, NUSurface. The main challenges faced with partial meniscus implants are that they are not mechanically sound to immediately withstand the body weight of patients post-operatively and their incorporation into the remaining meniscus tissues also proved to be formidable. NUSurface is currently in the end of Phase II Clinical Trial approved by the US FDA.

A new biocompatible silicone implant has been designed to overcome these difficulties. It is durable, flexible, highly elastic and has comparable tensile strength and Young's modulus to native menisci (100 to 150 MPa), it has comparable mechanical properties to the native meniscus. (Provisional Patent No: 2018-265-01-SG PRV)

The novelty of the current silicone meniscus invention, with features not provided by current technologies, are as follows: 1) it is 3D printable and customized to individual needs, 2) it can be inserted via minimally-invasive surgery, 3) the reservoir and micro-channels are incorporated to allow slow-release of drugs, platelet-rich plasma and lubricants and 4) it is refillable. Contrary to the current available partial meniscus implants which are indicated for use in settings of chronic meniscus injuries, our silicone meniscus can be used in both acute and chronic injury settings. Furthermore, it allows immediate weight-bearing after arthroscopic insertion. Silicone meniscus can be 3D printed or molded. The printing or molding process can be temporarily paused and later resumed, to allow extrusion of molten sugar mixed with honey, heated to 80°C and extruded in the desired location of the meniscus. The reservoir is designed to 1cm in its greatest dimension and the micro-channels at 300 um in diameter. The designed prototype is shown in **Figure 63.**

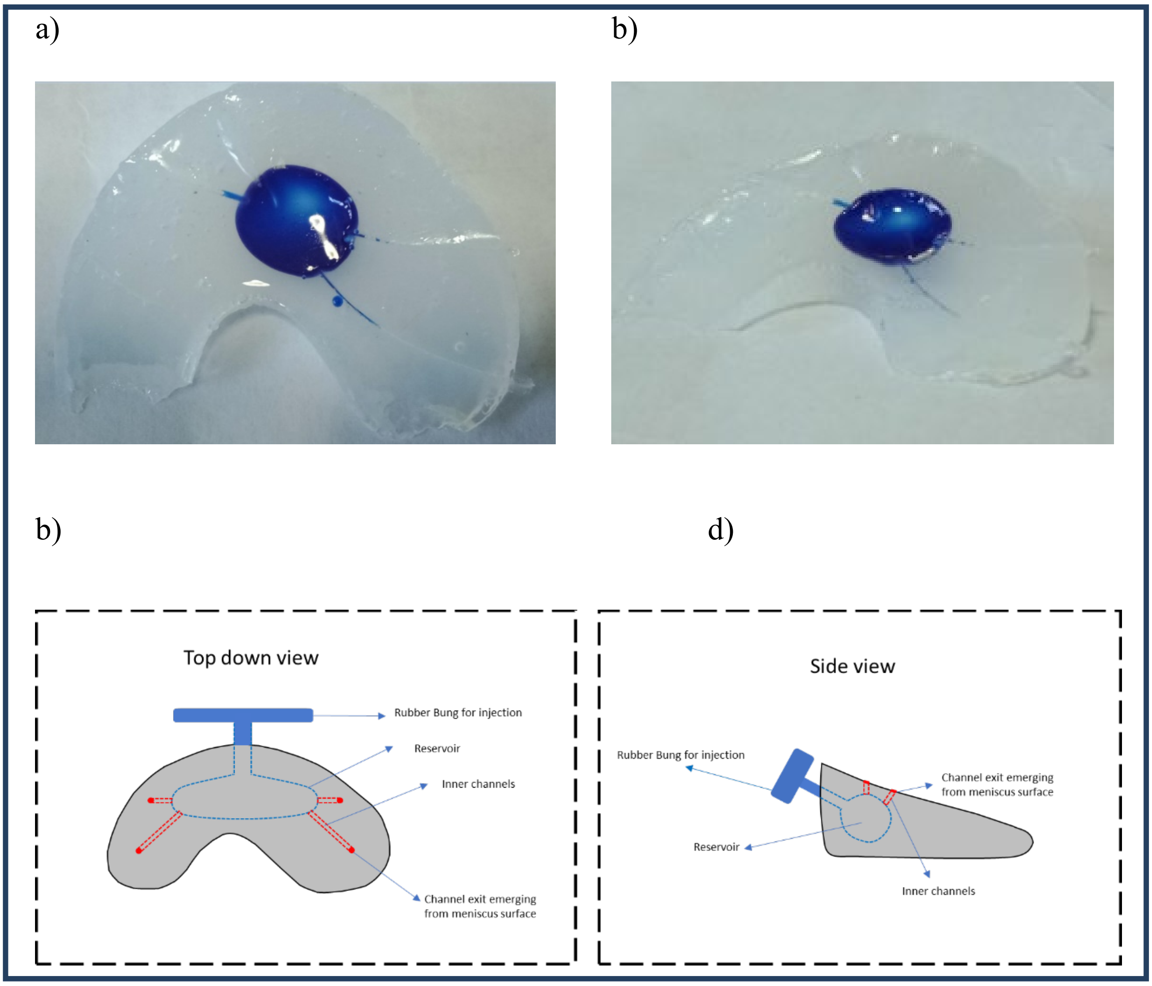

Figure 63 (a) Front and (b) side view of meniscus with incorporated reservoir and micro-channels (c) and (d) Schematic illustration of front and side view of meniscus

6.3 Incorporation of Shape-memory properties within the silicone meniscus

Thermoplastic polyurethanes are used as shape memory polymers in smart fabrics and materials in their own right. They are synthesized by polymerization combining diisocyanates and diols [142].

Nanocomposites have been prepared from immiscible blends of thermoplastic polyurethane (TPU) and polydimethylsiloxane (PDMS) rubber with nHA nanofiller [158].

The mechanical and physical properties (ie plastification and crystallinisation) are affected by the basic chemical monomer composition but also the length and sequence of the hard and soft segments. Shape recovery via thermal induction is the most common mechanism for shape-memory polymers (SMPUs).

In the relaxed state, the soft and hard segments partially segregate but coexist in the polymer. Below the glass transition temperature, Tg, the soft segments are quite immobile due to low kinetic energy. Above Tg, SMPU transforms easily from glass state to rubber state.

The hard segments act as pivot points for shape recovery and soft segments absorb external stress applied on the SMPU.

The deformed shape of a sample can be fixed by cooling the deformed sample to a temperature below Tg, under constraints, to restrict the mobility of the soft segments.

The original shape of the SMPUs can be recovered if the material is heated back to temperature above Tg, without constraints, to increase the mobility of the soft segments.

Polyurethane-based SMPs have many advantages over other types of shape-memory polymers, namely ease of processing, low cost of materials and production, large recovery strains up to 1000%, flexible shape-recovery temperature range, excellent chemical properties and biocompatibility for most SMPU.

6.3.1 Materials and Methods

6.3.1.1 Materials

A Si-TPU composite is made in 80:20 ratio (wt %) (80%Si-20%TPU). 40ml of Ecoflex 30 Liquid Silicone Rubber (Smooth-on) base agent and TPU pellets (PU Corporation) were first heat blended at 150°C in a 250 ml glass beaker. This first mixture was then rapidly cooled down to 23°C within 5 minutes, after which it is mixed and evenly stirred with 40ml of Ecoflex 30 resin curing agent before being poured into a meniscus mold.. This mold is then heated to 60°C to expedite curing. Molded Si-TPU is a proof of concept showing that shape-memory properties can be incorporated into silicone. Additional modifications can subsequently be made to future generations of silicone printers to print shape-memory silicone medical implants or devices.

Similarly, a 60%Si-40% TPU can be made in a 60:40 ratio (wt%) (60%Si-40%TPU). The maximum proportion of TPU that can be mixed with the silicone is 45%:55% (wt%) beyond which the mixture becomes cement-like which makes heating, mixing and blending impossible. (Shape-memory silicone-Disclosure of Technology : NTU TD 2019-061)

6.3.1.2 Experimental Methods

Light Microscopy. Light microscopy using Zeiss Axioskop Mat microscope with Olympus ACH 1x lens at 20x magnification was used to see surface morphology and characterisation..

X-ray Fluorescence Spectroscopy. It is used for non-destructive chemical analysis of atomic composition of the Si-TPU specimens.The XRFS instrument is EDX-8000 with Rhodium anode operated at an ultra-high vacuum of ~10-9 mbar. The X-ray gun is operated at 10 kV, 300 W.

Scanning Electron Microscopy. It is used for detailed three-dimensional and topographical imaging. Field Emission SEM is carried out using JEOL JSM-7600F equipped with electron gun operated in the voltage range of 15-25 kV in high vacuum mode. The Si-TPU samples platinum-sputtered were analysed in backscattering mode only.

Fourier Transform Infrared Analysis. It is used to determine the chemical bonding and composition of Si-TPU specimens. FTIR is carried out using Shimadzu IR Prestige-21 model equipped with the MIRacleTM single reflection horizontal attenuated total reflection (ATR) accessory having diamond-zinc-selenium ATR prism. The IR spectrum (4000-600 cm^{-1}) was used.

Thermogravimetric Analysis. TGA is carried out from room temperature to 700 $_{o}C$ using TA Instruments Thermo-Gravimetric Analyzer Q50 model with controlled heating rate of 10 °C/min. It is used to determine thermal properties and stability of the Si-TPU specimens. DSC analysis is used to explore heat capacity changes during phase transitions. Further study on phase transition is performed using METTLER-TOLEDO DSC1 Model with similar regulated heating rate of 10 °C/min.

Mechanical Properties Compression and tensile properties of the specimens were investigated. The specimens were made out of aluminum mold and subsequently tested with Shimadzu universal testing machine at ambient temperature. Compression tests were performed at 1-cycle and 4 cycles at crosshead speeds at 12mm/min, 120mm/min, 360 mm/min, 720 mm/min and 1000 mm/min. Tensile tests were done at 4-cycles also at the above crosshead speeds. The samples are stretched to 100% of the original effective length.

Thermogravimetric Analysis. TGA is carried out from room temperature to 700 ºC using TA Instruments Thermo-Gravimetric Analyzer Q50 model with controlled heating rate of 10 °C/min. DSC analysis is used to explore heat capacity changes during phase transitions. Further study on phase transition is performed using METTLER-TOLEDO DSC1 Model with similar regulated heating rate of 10 °C/min.

Mechanical Properties Dumbbell specimens were punched out of the molded tensile sheets, and tensile properties were measured per ASTM D 412 standard using a Shimadzu universal testing machine at ambient temperature and at 4 cycles at crosshead speeds at 12mm/min, 120mm/min, 360 mm/min, 720 mm/min and 1000 mm/min. The samples are stretched to 100% of the original effective length.

Shape-Memory Behaviour: Length Recovery Specimen. The length and shape recovery tests were done to determine the memory and recoverability of the specimens. The effective length of the specimen between the clamps (25mm) are first marked and measured. The length recovery specimen is first heated to 80°C for 15 minutes before stretching to 50mm (100% of effective length) on the tensile clamps. This strain length is maintained for 15 minutes at room temperature (23°C). Subsequently, the stretched Si-TPU meniscus is then released from clamps and any retraction was measured after 30 minutes. Finally, the Si-TPU meniscus is heated to 80°C for 30 minutes and the effective length again was measured.

Shape-Memory Behaviour: Shape Recovery Specimen. The Si-TPU specimen is first removed from the mold, heated to 80°C and wrapped around an 8mm diameter glass-rod. This curled configuration is maintained for 15 minutes at room temperature (23°C). The curled meniscus is removed from the glass rod and any outward springing is noted and measured after 30 minutes. Finally, the Si-TPU is heated to 80°C for 30 minutes and Percentage recovery was determined as a ratio of the recovered length to the tensile deformation.

Cytotoxicity Elution Test Studies. The purpose of this study was to investigate the influence of extract concentration on cytotoxicity. MEM α supplemented with 10% FBS was used as extraction medium for incubation of cylindrical Si-TPU samples (1.56 cm diameter, 0.5 cm height) for 72 hours under cell culture conditions. To investigate the influence of the extract concentration on cytotoxicity, extracts were prepared with different volumes of extraction medium (1.5, 3, and 4.5 mL).

50,000 L929 cells were seeded in 24 well plates and incubated for 24 hours to allow attachment. Then the culture medium was replaced with 500 µL of extracts. The positive control medium was the corresponding extraction medium incubated under cell culture condition along with the silicon samples. After incubating the cells with extraction medium for 24 hours, all medium in the wells were replaced with fresh medium mixed with 10% WST-8 cell proliferation assay. The assay was incubated for 4 hours and measured on a microplate reader (Molecular Devices) at 450 nm.

6.3.2 Results and Discussion

6.3.2.1 Light microscope and SEM studies

Light microscopy in F**igure 68** shows the white layer of TPU blend enveloping the individual silicone strands and the dark TPU granules on the surface. SEM in **Figure 69** also shows the round TPU granules scattered across the surface of the mosaic silicone plates.

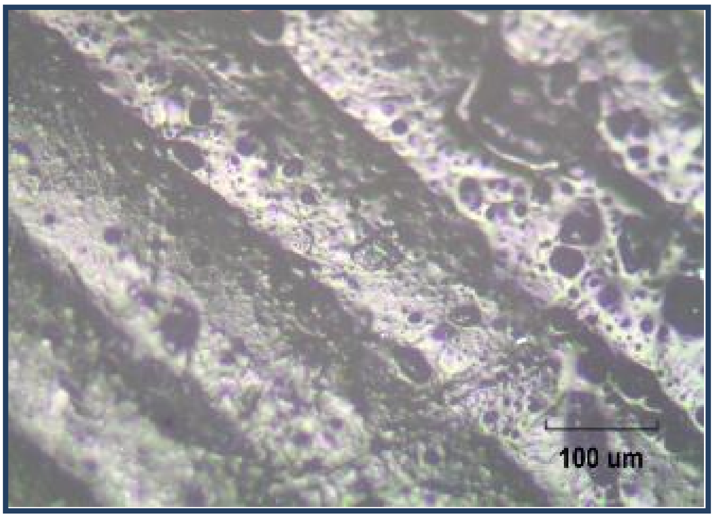

Figure 64 Widefield microscopy 20x magnification. Light microscopy shows the white layer of TPU blend coating the individual silicone strands surface

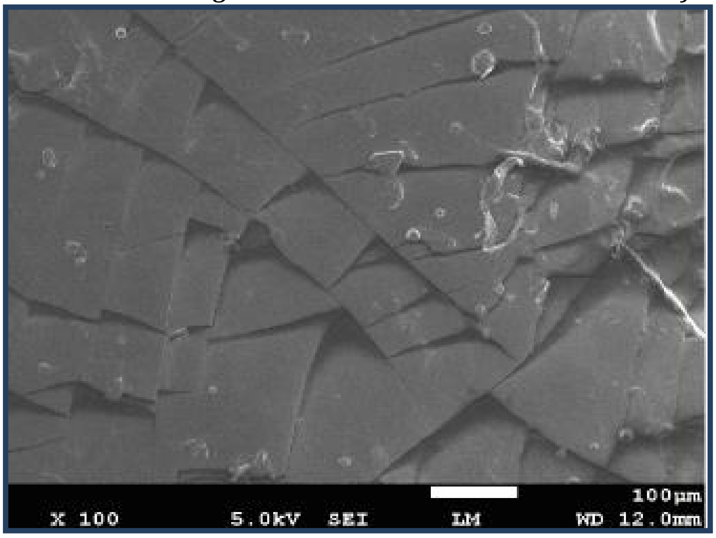

Figure 65 SEM 100x of Si-TPU. TPU granules are seen scattered on surface of the mosaic silicone plates. There is no disruption of the silicone plates by the TPU granules.

6.3.2.2 FTIR

The overlay FTIR spectra of both the 80%Si-20%TPU composite and pure 100% silicone rubber is shown below in **Figure 66**. The features in the Si-TPU composite, differentiating them from pure 100% silicone rubbers, are the peaks at 1730 cm^{-1}, 1535 cm^{-1} and 1367 cm^{-1}, signifying urethane –C=O vibration, N-H bending and CH_3 deformation, respectively.

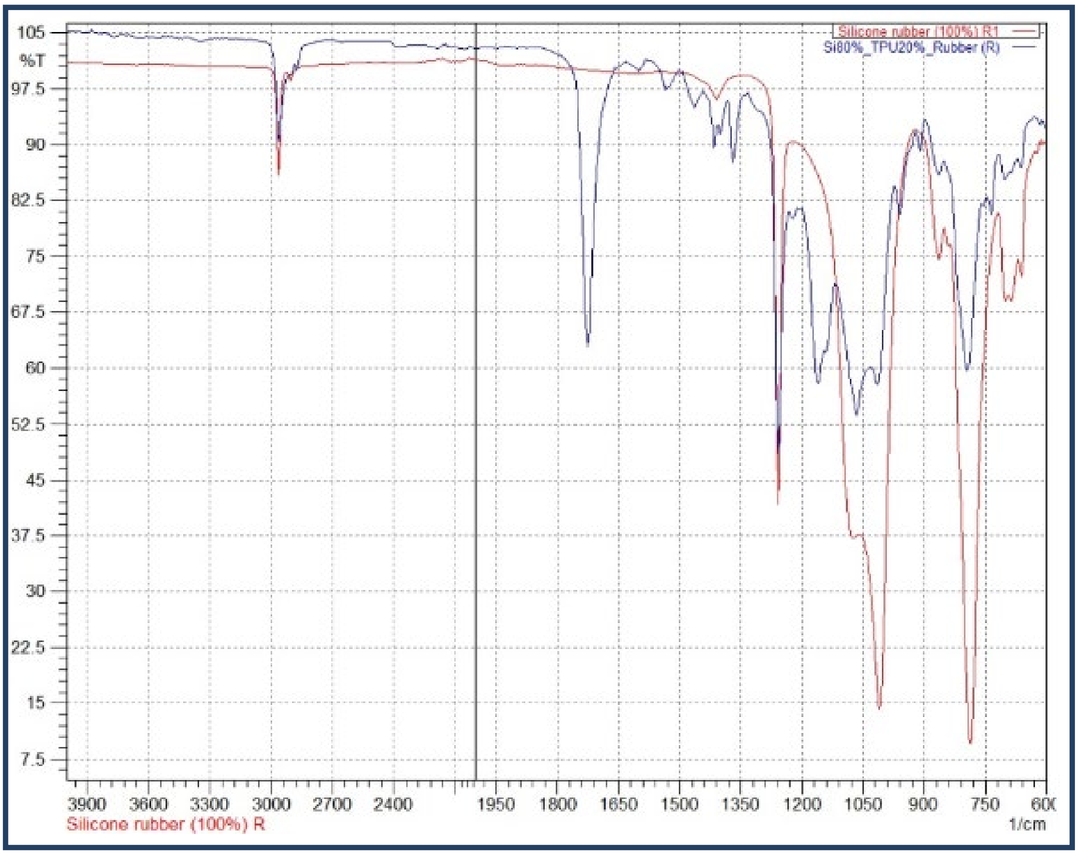

Figure 66 Overlay spectra of pure Si (blue) and Si-TPU (brown). Characteristic peaks of Si-TPU occur at 1730 cm^{-1}, 1535 cm^{-1} and 1367 cm^{-1}. These represent urethane –C=O vibration, N-H bending and CH_3 deformation, respectively.

6.3.2.3 Energy Dispersive X-ray Fluorescence Analysis

Atomic composition of pure Silicone sample is measured to contain 29.77% of SiO2, 0.011% of SO3, 0.006% of CaO, 0.001 of CuO and 70.213% of C. On the other hand, atomic composition of Silicone 80%-TPU 20% sample is measured to contain 9.806 % of SiO2, 0.001% of SO3, 0.001% of CaO, 0.001 of CuO and 90.19 % of C. The XRFS spectra showed high carbon content (90.19%) in the polyol segments in the Si-TPU composite. This is in contrast to the 70.2% carbon content in Ecoflex silicone rubber.

XRFS of Si-TPU

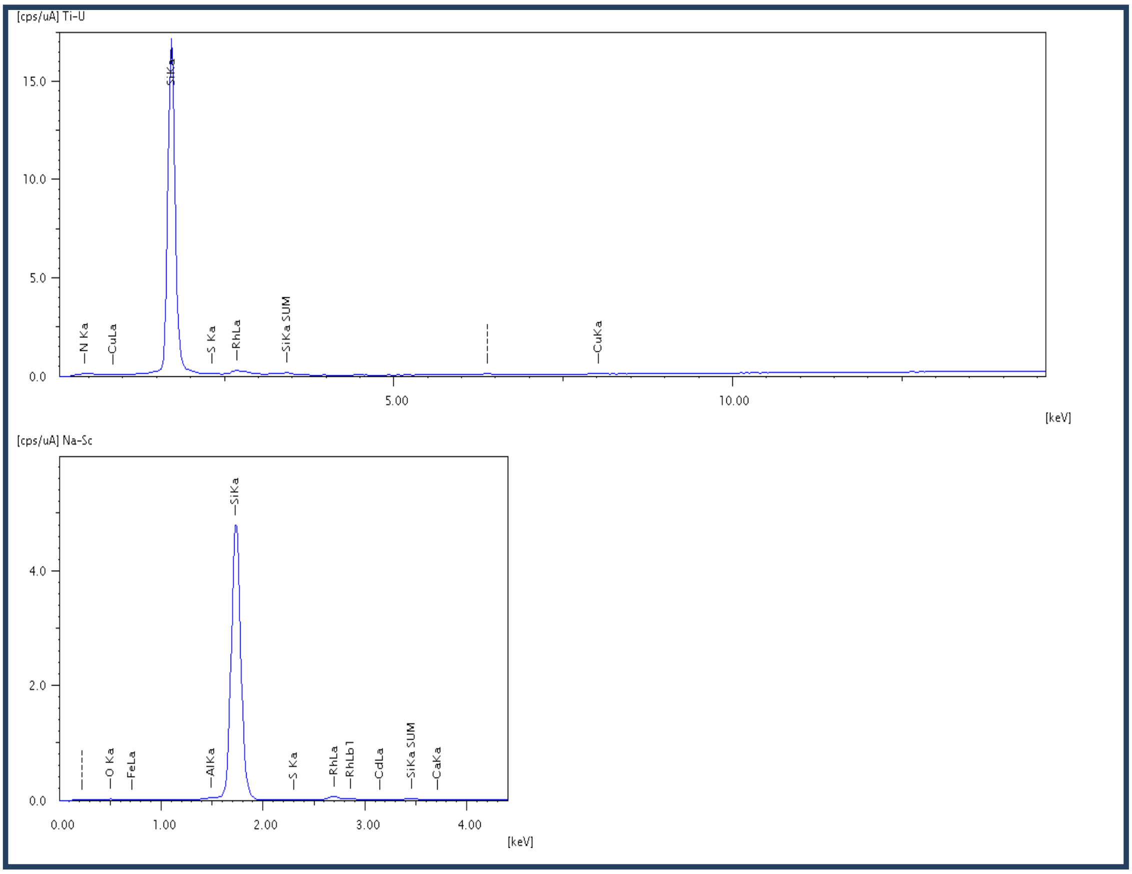

Figure 67 The XRFS spectra showed characteristic Si-K alpha peaks at 1.7 kev characteristic for silicone component

6.3.2.4 Thermal Stability

Thermogravimetric (TG) and derivative thermogravimetric analysis (DTG) curves of Si-TPU and Si in nitrogen atmosphere are shown in **Figures 68 and 69** and the thermal degradation of polyurethane occurs in two stages, according to the two DTG peaks. First is the degradation of hard segment of the TPU, between 400°C and 500°C. It occurs as urethane groups first undergo de-polymerization, resulting in individual monomers, which then further decompose to produce carbon dioxide. The second degradation is due to the polyol chain scissioning, between 500°C and 550°C.

For 80%Si-20%TPU rubber, the initial decomposition temperature (T_0) and the maximum decomposition temperature (T_{max}) are at 400°C and 600°C respectively. These are in contrast to the T_0 and T_{max} of pure Ecoflex silicone rubber, which are at 330°C and 700°C respectively. Appendix E shows the combined DSC, TGA and DTG of pure silicone, 80%Si-20%TPU and 60%Si-40%TPU.

Proximate Analysis of Rubber (Polymer, Carbon Black and Filler by TGA)

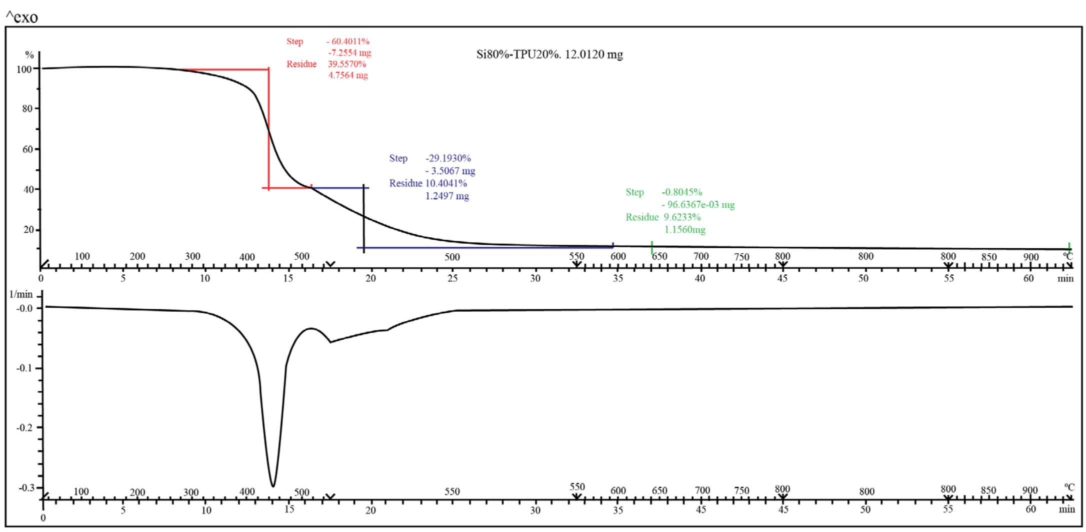

Figure 68 TGA and DTG graph of Si80%-TPU20%. 2-stage degradation of TPU is shown above, as indicated by a sharp and second obtunded peak in the DTG graph. First stage de-polymerization occurs between 400°C and 500°C. The second stage degradation is due to the polyol chain scissioning, between 500°C and 550°C. Polymer and filler content is measured to be 80.59% and 0.02%. There is no carbon black.

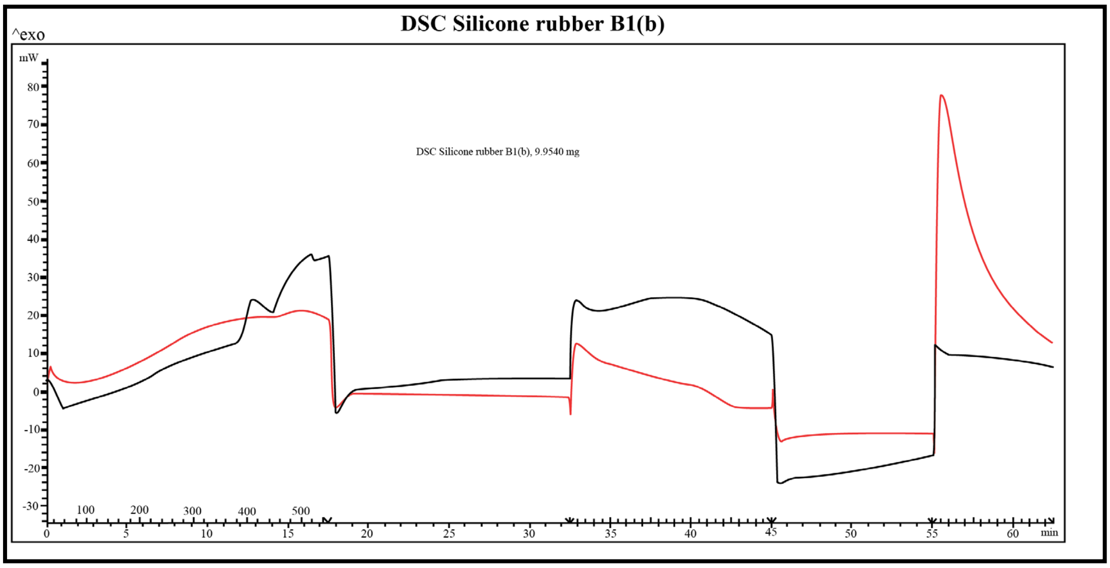

Figure 69 Overlay DSC curves of Si 80%-TPU 20% (black line) with pure Silicone samples (red line). Both show similar endothermic and exothermic profiles during the tests.

6.3.2.5 Mechanical Properties

For monotonic compressions, strain hardening effects are observed in both sets of pure silicone and 80%Si-20%TPU with increasing strain rates from 12 mm/min to 1000 mm/min. The addition of 20% and 40% TPU increases compressive modulus of pure silicone meniscus by up to 10-fold and 20-fold, respectively (**Figure 70b, d, and f**). This may be attributable to the shape fixity and retaining properties of the TPU.

For cyclical loading, the addition of 20% TPU did not significantly change the compressive modulus of the meniscus (**Figure 70a and c**). However, the addition of 40% TPU increased the modulus of pure silicone meniscus by about 10-fold (**Figure 70e**).

This is in contrast to the monotonic scenario above. This may be explained by the shape fixation property of TPU, being somewhat disrupted by the cyclical loading process.

Comparing monotonic to cyclical compressions, for pure silicone, there is a 3-fold increase in modulus (strain hardening effect) during cyclical loading (**Figure 70a and b).** For Si-TPU components, a 3-fold decrease in modulus for 20% TPU and a 2-fold increase in modulus with cyclical loading (**Figure 70c-f**). With increasing strain rates, strain-hardening effects are also observed at cyclical loading.

Table 29 Compression Test for pure Silicone and Si-TPU

1-cycle Compression-Test	Specimen Dimension (cm)	Strain Rate (mm/min)	Force (N)	Displacement (mm)
Si-TPU (60-40)	l x b x h		(n = 5)	(n = 5)
sample 1	4 x 2 x 1	12	893.426	3.00003
sample 2	4 x 2 x 1	120	917.217	3.00003
sample 3	4 x 2 x 1	360	1064.88	3.00003
sample 4	4 x 2 x 1	720	1288.24	3.00003
sample 5	4 x 2 x 1	1000	1550.49	3.00003
Si-TPU (80-20)	l x b x h		(n = 5)	(n = 5)
sample 1	4 x 2 x 1	12	386.224	3.00003
sample 2	4 x 2 x 1	120	508.17	3.00003
sample 3	4 x 2 x 1	360	625.258	3.00003
sample 4	4 x 2 x 1	720	764.874	3.00003
sample 5	4 x 2 x 1	1000	916.057	3.00003
Si -(100)	l x b x h		(n = 5)	(n = 5)
sample 1	4 x 2 x 1	12	51.3728	3.00003
sample 2	4 x 2 x 1	120	57.9627	3.00003
sample 3	4 x 2 x 1	360	70.2667	3.00003
sample 4	4 x 2 x 1	720	85.2331	3.00003
sample 5	4 x 2 x 1	1000	98.629	3.00003

4-cycle Compression-Test	Specimen Dimension (cm)	Strain Rate (mm/min)	Force(N)	Displacement(mm)
Si-TPU (60-40)	l x b x h		(n = 5)	(n = 5)
sample 1	4 x 2 x 1	12	1846.4	3.00003
sample 2	4 x 2 x 1	120	2128.76	3.00003
sample 3	4 x 2 x 1	360	2614.09	3.00003
sample 4	4 x 2 x 1	720	3108.28	3.00003
sample 5	4 x 2 x 1	1000	3653.73	3.00003
Si-TPU (80-20)	l x b x h		(n = 5)	(n = 5)
sample 1	4 x 2 x 1	12	116.825	3.00003
sample 2	4 x 2 x 1	120	166.295	3.00003
sample 3	4 x 2 x 1	360	199.717	3.00003
sample 4	4 x 2 x 1	720	301.221	3.00003
sample 5	4 x 2 x 1	1000	349.209	3.00003
Si -(100)	l x b x h		(n = 5)	(n = 5)
sample 1	4 x 2 x 1	12	202.006	3.00003
sample 2	4 x 2 x 1	120	250.441	3.00003
sample 3	4 x 2 x 1	360	293.287	3.00003
sample 4	4 x 2 x 1	720	288.137	3.00003
sample 5	4 x 2 x 1	1000	347.118	3.00003

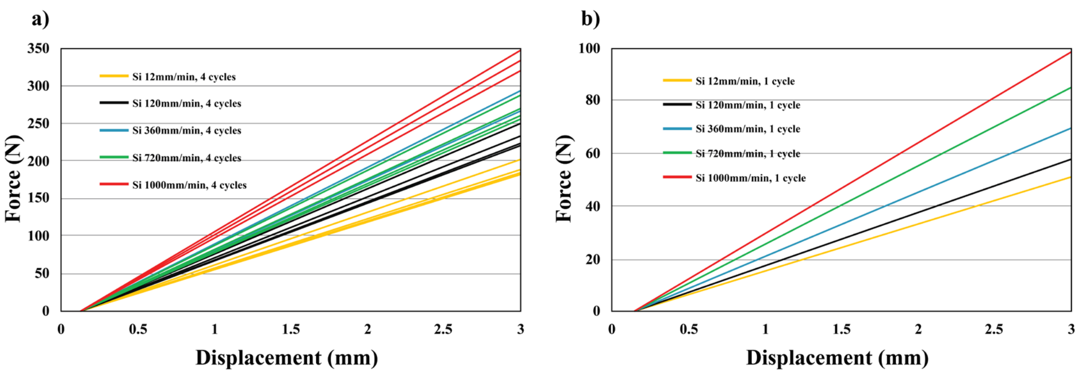

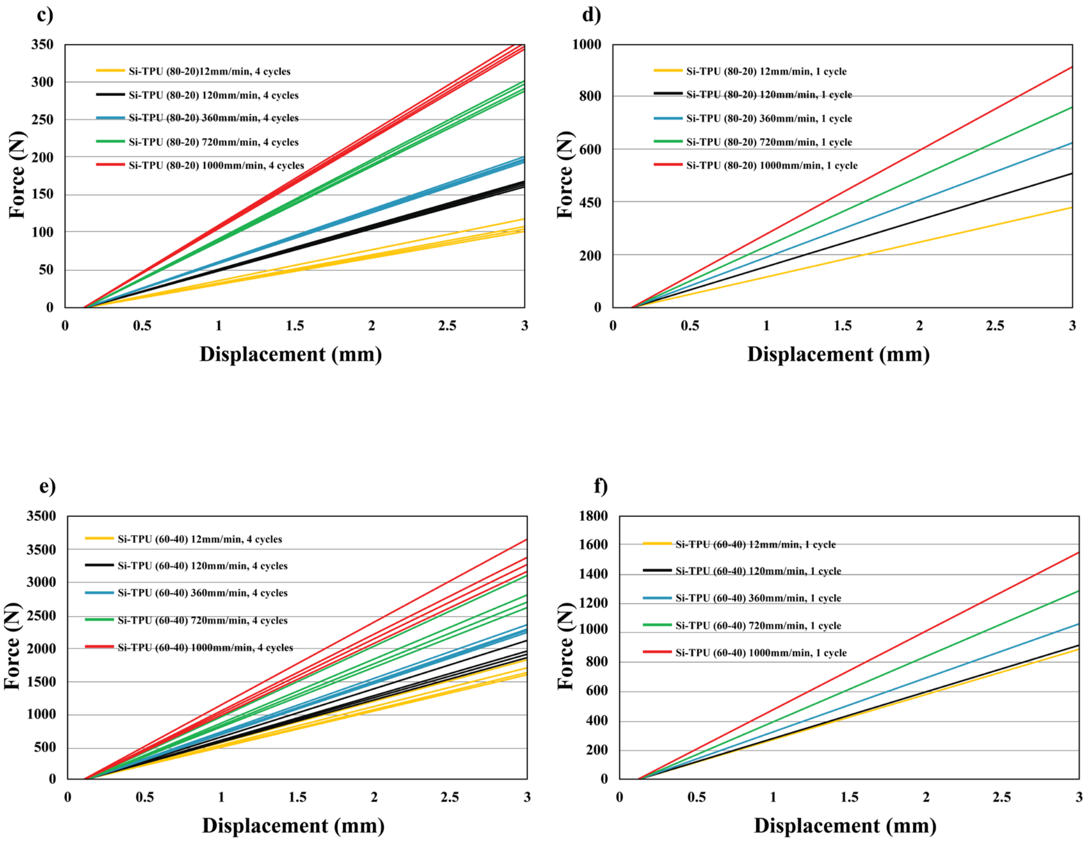

Figure 70 Compression data for (a and b) Pure silicone, (c and d) Si-TPU (80%-20%), and (e and f) Si-TPU (60%-40%) for 4-cycle (a, c, and e) and 1-cycle (b, d, and f) compressions. In monotonic compression, the addition of both 20% and 40% TPU increases the compressive modulus of pure silicone meniscus by up to 10-fold and 20-fold respectively. However in cyclical compression, only the addition of 40% TPU has the effect of increasing the compressive modulus by up to 10-fold.

Tensile modulus decreases from pure silicone, 80%Si-20%TPU and 60%Si-40%TPU, in that order. The difference was not statistically significant between pure silicone and 80%Si-20%TPU groups during 4 cycle loading. However, tensile modulus decreases by half for 60%Si-40%TPU group during 4-cycle loading. Therefore, an increase in % composition of TPU in the composite decreases the tensile modulus of the Si-TPU composite at all strain rates.

Table 30 Tensile Tests for pure Silicone, Si80%-TPU20% and Si60%-TPU40%

4 cycle Tensile-Test	Specimen Dimension (cm)	Strain Rate (mm/min)	Force(N)	Displacement(mm)
Si-TPU (60-40)	l x b x h		(n = 5)	(n = 5)
sample 1	4 x 2 x 1	12	1.475016	30
sample 2	4 x 2 x 1	120	1.519521	30
sample 3	4 x 2 x 1	360	1.75635	30
sample 4	4 x 2 x 1	720	1.831055	30
sample 5	4 x 2 x 1	1000	1.853307	30.00002
Si-TPU (80-20)	l x b x h		(n = 5)	(n = 5)
sample 1	4 x 2 x 1	12	3.480911	30
sample 2	4 x 2 x 1	120	3.530185	30
sample 3	4 x 2 x 1	360	3.695488	29.9993
sample 4	4 x 2 x 1	720	4.150073	29.99463
sample 5	4 x 2 x 1	1000	3.739993	29.99967
	l x b x h			
Si -(100)			(n = 5)	(n = 5)
sample 1	4 x 2 x 1	12	3.883044	30
sample 2	4 x 2 x 1	120	4.116694	30
sample 3	4 x 2 x 1	360	4.197756	30
sample 4	4 x 2 x 1	720	4.293124	30
sample 5	4 x 2 x 1	1000	3.873507	30

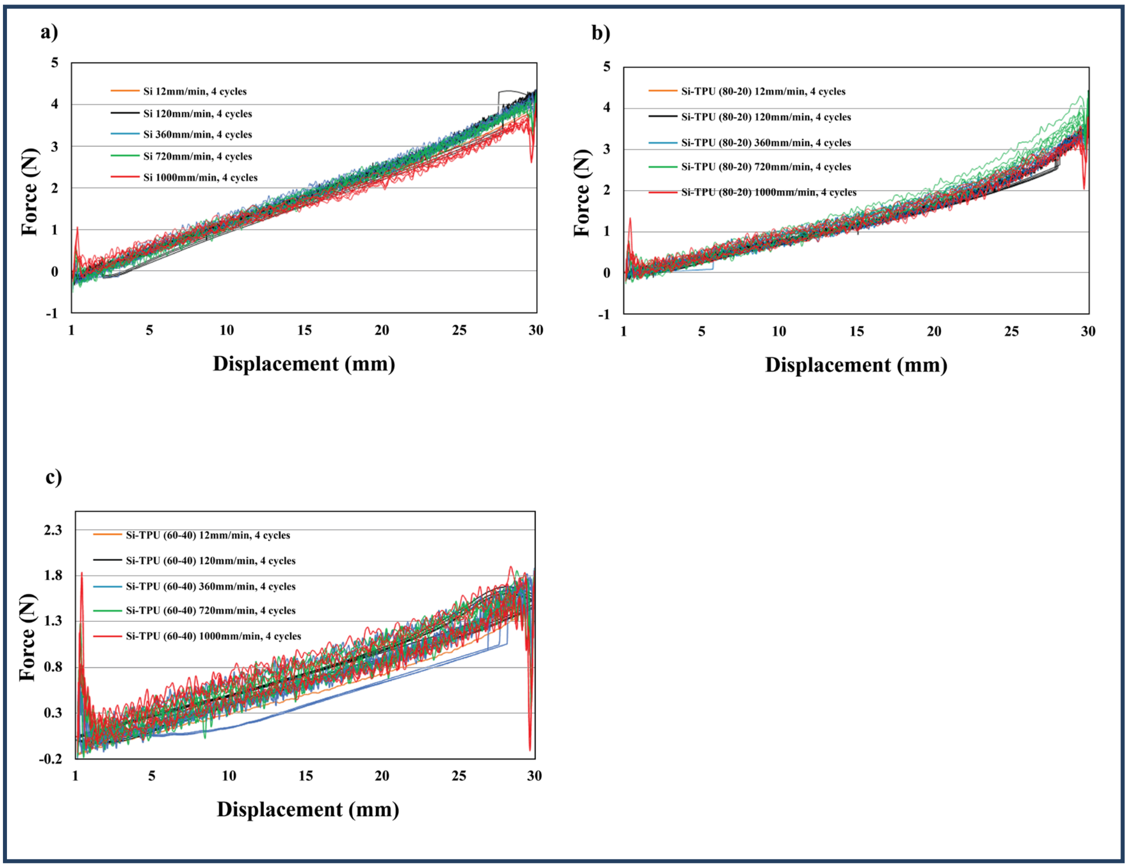

Figure 71 Tensile test graphs for (a) pure silicone, (b) Si-TPU (80%-20%), and (c) Si-TPU (60%-40%) for 4-cycle tension tests. An increase in % composition of TPU in the composite decreases the tensile modulus of the Si-TPU composite at all tested strain rates.

6.3.2.6 Shape memory behavior

Shape memory capability can be imparted to the silicone meniscus by blending with thermoplastic polyurethane (TPU), conferring silicone the ability to be in-elastically deformed and recover subsequently to their original shape using external heat stimuli. **Figure 72** presents a schematic illustration of the shape memory mechanism. Reshaping capability is applied in the design of sutures and stents for minimally invasive surgery, sensors, actuators and robotics. Conventionally, shape memory polymers (SMP) are manufactured by extrusion and casting.

Shape-Memory Mechanism of Si-TPU composite

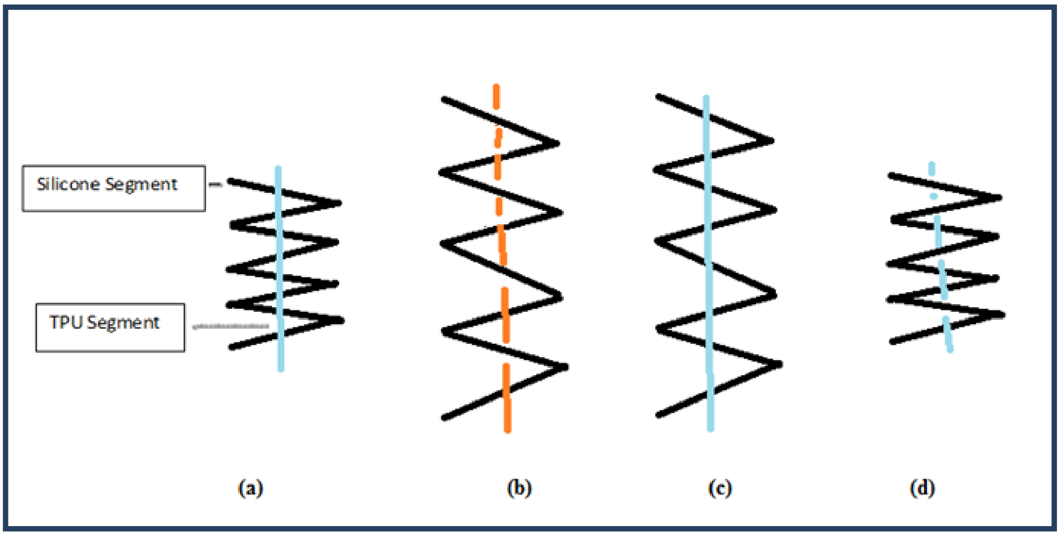

Figure 72 Schematic Illustration of mechanism Shape-Memory Biocompatible Silicone Polymer. a) Native silicone (elastic segment) and TPU (transition segment) are entangled together. b) Stretching at temperature above Tg of TPU (TPU transition segment softens and deforms easily, while the silicone elastic segment deforms and stores elastic energy) c) Transient shape is maintained at temperature below Tg of TPU (TPU transition segment becomes hard at low temperature and prevents recovery of the silicone elastic segment) d) Original shape is recovered after heating. TPU transition segment softens and elastic energy is released from the silicone elastic segment

The shape memory behavior of the Si-TPU meniscus are demonstrated below in **Figure 73** showing the sequence of recovery in length and in **Figure 74** showing the sequence recovery in shape. The shape memory properties can be expressed in terms of shape fixity ratio and shape recovery ratio [143]. The shape fixity ratio, Rf, is calculated to be 100 % and 98 %, for 60%Si-40%TPU and 80%Si-20%TPU, respectively. The shape recovery ratio, Rr, is calculated to be 85% and 95%, for 60%Si-40%TPU and 80%Si-20%TPU, respectively.

Length Recovery

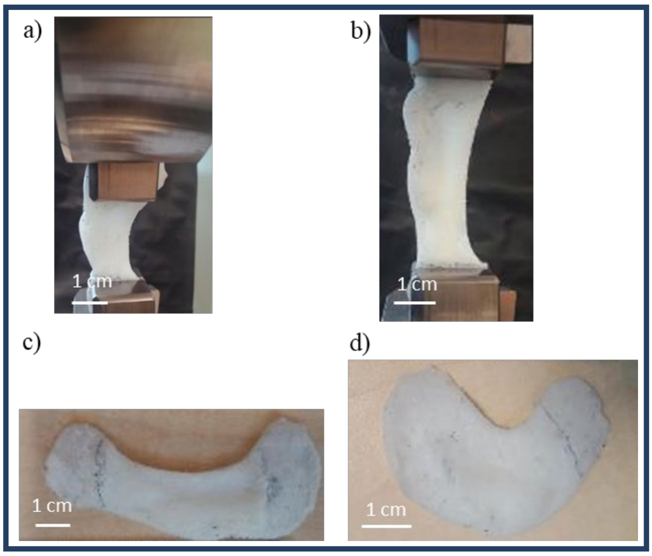

Figure 73 Length recovery of Si-TPU meniscus. a) A 40mm long Si-TPU meniscus specimen clamped with effective length 25 mm, between clamps, at room temperature 23°C. b) Si-TPU meniscus specimen heated first to 80 °C, then stretched to 50mm, continue to maintain at this strain length for 15 minutes at room temperature. c) Si-TPU meniscus specimen released from clamps and observed to have minimal retraction. d) Si-TPU meniscus specimen returned to effective length of 25mm, after being heated to 80 °C

A full shape recovery in all three dimensions was achieved from a curled position, after heating up to 80°C. These results further illustrated that the silicone has a greater contribution towards the SMPU recovery component, while the TPU has a greater contribution towards the SMPU fixity component.

Shape Recovery

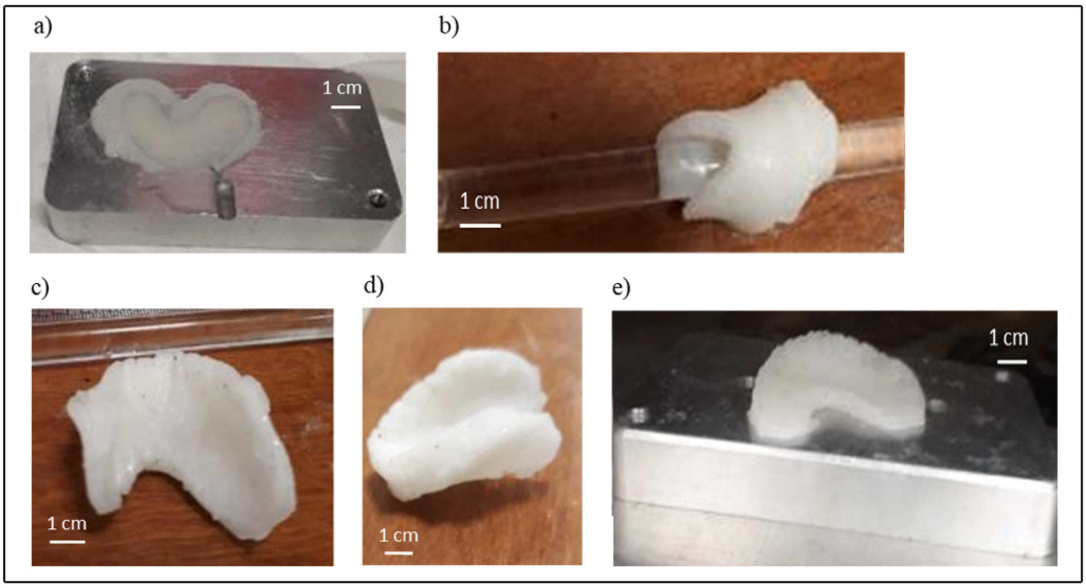

Figure 74 Shape-recovery of Si-TPU meniscus. a) Molded Si-TPU meniscus specimen b) Si-TPU meniscus-specimen heated first to 80 °C, then wrapped around glass rod and maintained in this configuration for 15 minutes at room temperature. c)Si-TPU meniscus-specimen maintained curled-up shape (front-view). d) Si-TPU meniscus-specimen maintained curled-up shape (side-view). e) Si-TPU meniscus-specimen returned to original shape upon heating to 80 °C

6.3.2.7 Cytotoxicity Test via Extraction Method (ISO10993-12)

In this cytotoxicity study [146], we examined and compared between molded Si-TPU standard samples for extraction time of 72 hours. 3 samples were tested for each unique condition. Results from quantitative cell proliferation assays indicated a significant decline in cell viability for 1.5- and 3.0-mL extraction volumes but a statistically non-significant difference for 4.5 mL extraction volumes between positive controls and extracts from Si-TPU samples, as shown in **Figure 75**. This indicates potential of the Si-TPU as biocompatible implants as long as certain threshold limits are not exceeded. Further modification to manufacturing process will be in place to improve on biocompatibility of Si-TPU samples.

Cell Proliferation Assay

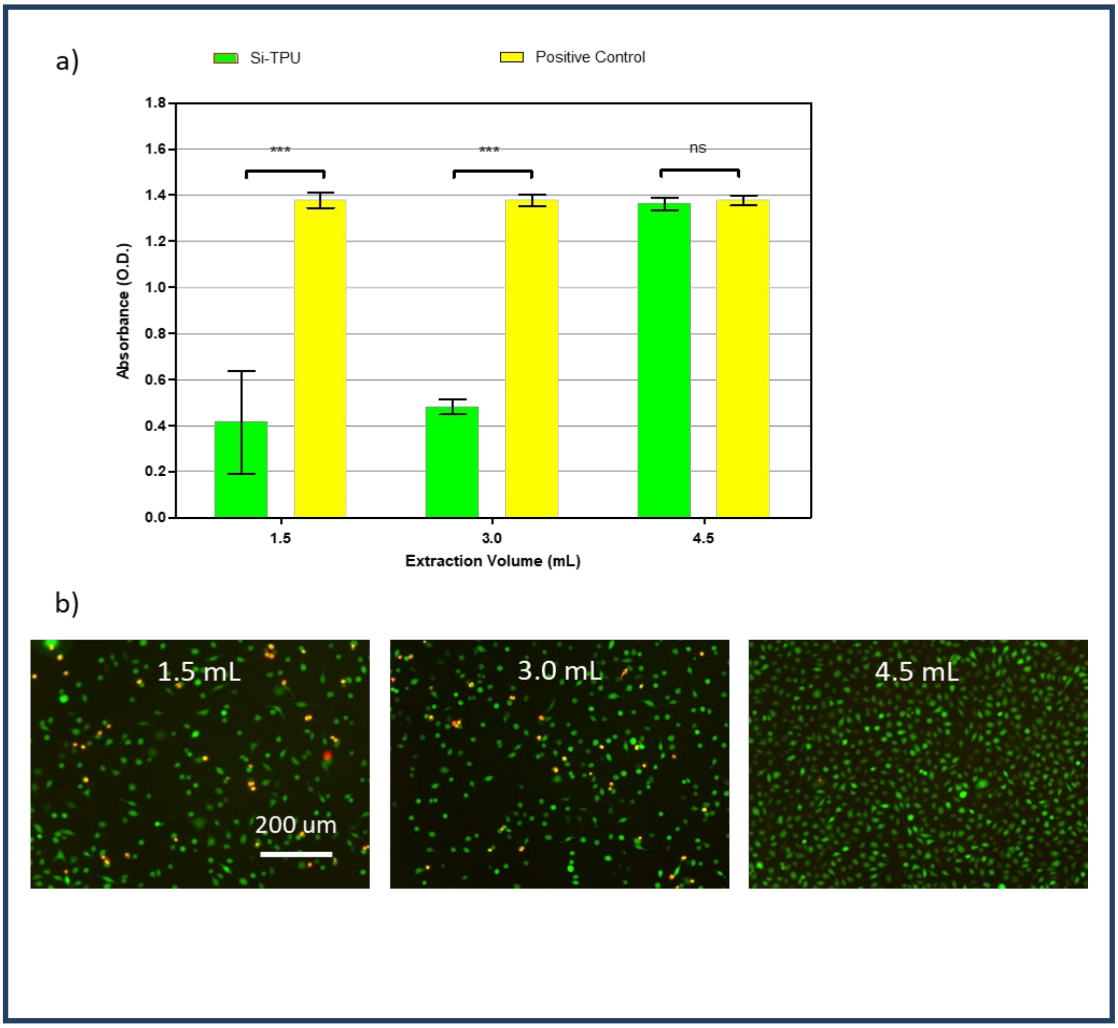

Figure 75 a) Cytotoxicity results under different extraction volumes for extracts collected from Si-TPU samples. Cell proliferation of L929 cells after 24 h incubation with extract was quantified based on the WST-8 cell proliferation assay. 3 samples were tested for each unique condition. Statistical significance between groups was assessed using two-way ANOVA followed by Bonferroni post-tests. ns = p>0.05. b) Fluorescent images of L929 cells seeded on 24-well plate after 24 h incubation with extract. Cells were stained with the Live/Dead® cell viability assay

6.4 Workflow Implementation

The workflow implementation of the 3D printing of silicone meniscus can be summarized in the flow chart below. The first step involves obtaining the MRI in DICOM format of the knee meniscus from the individual. Secondly, this DICOM format is converted into STL 3D printable version. Finally the silicone meniscus is printed with optimized parameters of the silicone 3D printer.

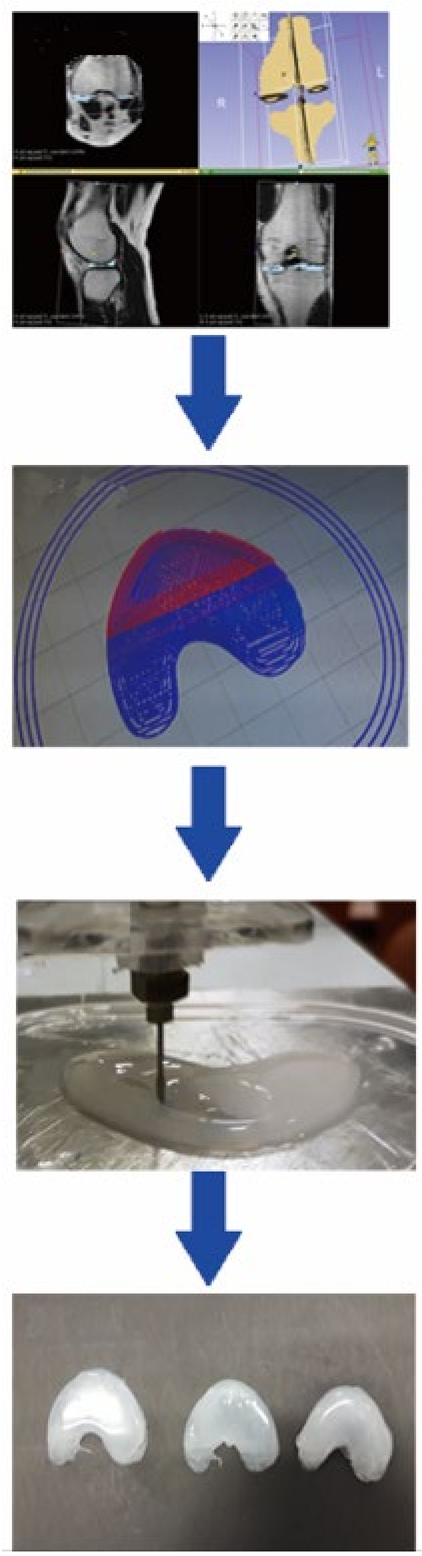

Figure 76 Workflow Implementation i) Data conversion stage: MRI of knee in DICOM format is collected and converted to stl printable format. 2) Slicing Stage: Slicing of the model is executed and G-codes generated are sent to the printer. Toolpath of the meniscus generated is shown here. 3) 3D Printing stage: Liquid Additive Manufacturing of silicone meniscus using optimized process parameters. 4) 3D printed silicone meniscus.

Chapter 7 - Conclusion & Future Works

7.1 Conclusion

7.1.1 3D Silicone Printer

A customized heat-cured extrusion based has been developed successfully, based on the rheological properties of the specific liquid silicone resin of interest and employing an open-source hardware printer (Core X-Y) and software. Rheology is an important method in determining the modulus, curing times and viscosity of silicone resins. The rheological values obtained here are unique for each series of LSR and they are important in defining the nozzle diameters, nozzle and platform temperatures. Direct 3D printing is demonstrated without support structures using Ecoflex, a skin-safe medical grade FDA approved Liquid Silicone Rubber, with pre-extrusion heating at the nozzle and post-extrusion at the platform. The placement of heating el**ements,**intensity and duration of heating are all important determinants of a successful printout. Therefore, all medical grade silicones, which are heat-curable, can be printed with this printer. Rheological studies will also prove invaluable for composite silicone printing, composite material printing, overlay printing and the design of multiple nozzles for silicone printer. Easily accessible and inexpensive open-source Core XY printer hardware and Repetier-Slic3r software allow printing of biomedical silicone models for educational, training and teaching purposes initially. Current insufficiencies which can be improvised are 1) improvement of heating mechanisms and environment, 2) the ability to print taller constructs, 3) mixing of LSR components and 4) accuracy of extrusion pump

7.1.2 Characterization of Standard Silicone Samples

Standard Ecoflex silicone samples and Ecoflex silicone meniscus were printed out using the optimal nozzle internal diameter, in the range of 0.5 mm and 0.6 mm and optimal bed temperatures, between 100°C and 110°C. Both are major determinants on the accuracy and precision of the printouts in the x-y plane.

Characterization of the standard Ecoflex silicone samples demonstrated that they have similar biomechanical properties as the human native meniscus, making Ecoflex a suitable candidate with the potential to be explored for use as a meniscus implant. Ecoflex 30 and Ecoflex 50 SLRs have compressive moduli of about 0.25 MPa and 0.3 MPa, respectively, and these values have far surpassed the minimum compressive modulus of the human meniscus of 0.09 MPa in the posteromedial region and the maximum compressive modulus of the human meniscus of 0.16 MPa in the anteromedial region. Thirty days of cytotoxicity extraction studies also have proven the biocompatibility and stability of Ecoflex rubbers.

Both Ecoflex 30 and Ecoflex 50 demonstrated viscoelastic properties of strain hardening. At all strain rates, Ecoflex 50 silicone meniscus implants and standard samples consistently showed higher stiffness and high modulus when compared to their Ecoflex 30 counterparts, rendering the former a more suitable implant candidate. Finally, cytotoxicity tests showed that both Ecoflex 30 and Ecoflex 50 silicone implants are safe to fibroblasts and biocompatible.

7.1.3 3D Printed Silicone Meniscus

A silicone meniscus with dimensions of 4cm x 2 cm x 1 cm, which demonstrate similar mechanical properties as the conventionally heat-molded meniscus, was successfully directly 3D printed.

An accurate 3D printout of silicone meniscus, within 2% tolerance, can be printed using Ecoflex liquid silicone rubber, as measured by μ-CT. This 2% tolerance allows for antero-posterior and medio-lateral excursion of the meniscus during ambulation.The average porosity is found to be 0.27 ± 0.13% which indicates an almost fully-dense 3D printed silicone meniscus part is achievable using this extrusion-based technique. No grooves or voids are observed between lines of silicone extrudates and this is extremely important for the design and incorporation of reservoir and micro-channels within the meniscus. PBS absorption tests indicated that both the molded and 3D printed meniscus are able to tolerate prolonged immersion in physiological solutions, without swelling excessively. This is vital for its use as an intra-articular knee implant. Our characterization of the 3D printed and molded silicone meniscus concludes that the heat-cured extrusion-based 3D printing process does not alter the overall physical, biochemical, mechanical or biocompatible properties of the silicone meniscus implant printouts. Both the chemical and thermal stabilities of Ecoflex liquid silicone rubbers were demonstrated by FTIR and TGA/DSC, respectively. Although silicone rubbers decompose at temperatures of above 300°C and since Liquid Additive Manufacturing of silicone LSRs seldom exceed this heating temperature of 300°C, these heat profiles for different LSRs become critically important in cases of composite material and overlay printing, where different materials may require printing temperatures above 300°C and thus directly affecting silicone properties. Biocompatibility results of 3D printed silicone meniscus (ISO-109930) at 30 days are also very promising. Ecoflex can therefore be explored as a candidate for silicone meniscus implant fabrication.

In Weibull failure analysis of Ecoflex LSRs, the maximum stresses that Ecoflex 50 ($\boldsymbol{\sigma F_{50}}$) and Ecoflex 30 ($\boldsymbol{\sigma F_{30}}$) silicone meniscus can take, ($\boldsymbol{\sigma F_{50}}$), are 2.696 MPa and 0.369 MPa, respectively, such that only one in a million silicone meniscus samples fail in a typical sedentary person or in a patient undergoing crutch-assisted ambulation after arthroscopic surgery. These maximum stresses tolerable by silicone meniscus are still way above the maximum compressive moduli of the human meniscus of 0.16 MPa, further supporting the cause for its use as a meniscus implant option. The maximum tensile moduli of the silicone meniscus tested in this study is in the range of 0.1-0.2 MPa, when compared to the tensile moduli range of 2-40 MPa of human meniscus tested in various shapes and configurations reported in other studies. As the meniscus cushions mainly in knee compression while walking, the design of the silicone meniscus will be based more on its compressive rather than tensile properties. Finally, both Ecoflex 50 and Ecoflex 30 have Weibull modulus value greater than one, indicating that the implants will fail eventually with time.

7.1.4 Reservoir, Micro-channels and Shape Memory Incorporation

The silicone meniscus implants have been incorporated with reservoir and micro-channels and shape-memory properties. The reservoirs and micro-channels have been successfully fabricated by using mixed sugar and honey as sacrificial molds.

Shape memory behaviour have also been successfully incorporated into the silicone meniscus via addition of thermoplastic-polyurethane (TPU). Length recovery and shape recovery of Si-TPU have also been demonstrated. The shape memory properties of Si-

TPU have been confirmed by its high shape fixity ratio, Rf, of 100 % and 98 %, for 60%Si-40%TPU and 80%Si-20%TPU, respectively, and its high shape recovery ratio, Rr, of 85% and 95%, for 60%Si-40%TPU and 80%Si-20%TPU, respectively.

7.2 Future Works

As future works, we plan to improve on the 1) printing and heating capabilities of our silicone 3D printer, 2) expand on the evaluation of our silicone meniscus implant, 3) perform animal studies and 4) clinical trials.

In order to expand the printing capabilities of our heat-cured extrusion-based 3D silicone printer, including the future printing of shape-memory LSRs, we will include multiple nozzles driven by different mechanisms such as pneumatic, solenoid, and piezoelectric print-heads. We also plan to incorporate composite material printing, composite silicone printing, combining the printing of both silicone and thermoplastic polyurethane (TPU).

To achieve a better controlled curing platform and to achieve better resolution, we can employ an additional 3rd stage heating system using infrared light, halogen lamp or laser heating. The temperature can be better controlled in an enclosed chamber. This would greatly facilitate the development of 4D printing of silicone meniscus implants with shape memory behaviour and composite silicone printing. Finally, we will aim to achieve a printing resolution of 100-150 μm for our extrusion-based printing system in the future.

In terms of meniscus implant evaluation, we intend to expand and initiate animal testing for our 3D printed silicone meniscus implants, starting from smaller animal models such as mouse and rabbits to bigger animals such as goats in order to test for the in vivo applicability of our printed implants. Finally, the silicone meniscus is considered a class 3 medical device and will be assessed via suitable human clinical trials to proof its utility in treating meniscus pathologies in patients.

References

[1] Verdonk Rene, Philippe Beaufilis, The Meniscus, Springer Publication, 2010.

[2] H. Kurosawa, T. Fukubayashi, H. Nakajima, Load-bearing mode of the knee joint: physical behavior of the knee joint with or without menisci, Clinical Orthopaedics and Related Research, 149 (1980) 283‑290.

[3] T. Fripp, N. Frewer, L Green, Method and apparatus for additive manufacturing, US PATENT 2016/0263827.

[4] E. Selbertinger, F. Achenbach, B. Pachaly, Method for Producing Silicone Elastomer Parts, 2014 (PCT/EP2015/075329).

[5] J. Plott, A. Shih, The extrusion-based additive manufacturing of moisturecured silicone elastomer with minimal void for pneumatic actuators, Additive Manufacturing, 17 (2017) 1‑14.

[6] F. Liravi, E. Toyserkani, A hybrid Additive Manufacturing Method for the Fabrication of Silicone Bio-structures: 3D Printing Optimization and Surface Characterization, Materials & Design, 138 (2018) 46-61.

[7] M. Englund, A. Guermazi, L.S. Lohmander, The meniscus in knee osteoarthritis. Rheumatic Disease Clinics of North America, 35 (2009) 579- 590.

[8] M. Englund, E. M. Roos, H. P. Roos, L. S. Lohmander, Patient-relevant outcomes fourteen years after meniscectomy: influence of type of meniscal tear and size of resection. Rheumatology, 40 (2001) 631-639.

[9] M.C. Chambers, S. F. El-Amin III, Tissue engineering of the meniscus: Scaffolds for meniscus repair and replacement: A Review, Musculoskeletal Regeneration, 2 (2015) e 998.

[10] H. Pereira, A.M. Frias, J.M. Oliveira, J Espregueira-Mendes, RL Reis, Systematic Review: Tissue engineering and Regenerative Medicine Strategies in Meniscal Lesions, Arthroscopy, 27 (2011) 1706-1719.

[11] J.Vaquero, F. Forriol, Meniscus tear surgery and meniscus replacement, Muscles Ligaments Tendons Journal, 6 (2016) 71–89.

[12] J. Steadman, L. Matheny, S. Singleton, K. Briggs, N. Johnson, W. Rodkey, B. Crespo, K. Briggs, Meniscus Suture Repair: Minimum 10-Year Outcomes in Patients Younger Than 40 Years Compared With Patients 40 and Older, The American Journal of Sports Medicine, 43 (2015) 2222- 2228.

[13] J. L. Cook, D. B. Fox, P. Malaviya, J. L. Tomlinson, K. Kuroki, C. R. Cook, S. Kladakis, Long-term outcome for large meniscal defects treated with small intestinal submucosa in a dog model, The American Journal of Sports Medicine, 34 (2006) 32-42.

[14] L.L Johnson, J.A. Feagin, Autogenous tendon graft substitution for absent knee joint meniscus: a pilot study, Arthroscopy, 16 (2000) 191-196.

[15] R.J. Van der Wal, B.J. Thomassen, E.R.van Arkel, Long-term clinical outcome of open meniscal allograft transplantation, American Journal of Sports Medicine, 37 (2009) 2134-2139.

[16] G. Peters, C.J. Wirth, The current state of meniscal allograft transplantation and replacement, The Knee, 10 (2003) 19-31.

[17] H.N. Chia, M.L. Hull, Compressive Moduli of the Human Medial Meniscus in the Axial and Radial Directions at Equilibrium and at a Physiological Strain Rate, Journal of Orthopaedic Research, 26 (2008) 951- 956.

[18] V. Vedi, A.Williams, S. Tennant, E. Spouse, D. Hunt, W Gedrovc. Meniscal movement: an in-vivo study using dynamic MRI, The Journal of Bone and Joint Surgery (British Volume), 81 (1999) 37-41.

[19] A. Grassi, S. Zaffagnini, M. Muccioli, A. Benzi, M. Marcacci, Clinical Outcomes and complications of a collagen meniscus implant: a systematic review, International Orthopedics (SICOT), 38 (2014) 1945-1953.

[20] S. Grogan, ,P. Chung, P. Soman, P. Chen, M. Lotz, S. Chen, D. D’Lima, Digital micromirror device projection printing system for meniscus tissue engineering, Acta Biomaterialia, 9 (2013) 7218–7226.

[21] G.A. Paletta, Jr, T. Manning, E. Snell, R. Parker, J. Bergfeld, The effect of allograft meniscal replacement on intraarticular contact area and pressures in the human knee. A biomechanical study, American Journal of Sports Medicine, 25 (1997) 692–698.

[22] G. Filardo, L. Andriolo, E. Kon, M. Marcacci, F. de Caro, Meniscal scaffolds: results and indications, A systematic review, International Orthopedics, SICOT 39 (2015) 35-46.

[23] M.C. Chambers, S.F. El-Amin III, Tissue Engineering of the Meniscus: Scaffolds for meniscal repair and replacement, Musculoskeletal Regeneration, 2 (2015) e 998.

[24] K.R. Myers, N.A. Sagalione, A.D. Goodwillie, Meniscal scaffolds, The Journal of Knee Surgery, 27 (2014) 435–442.

[25] T.G. van Tienan, G Hannink, P. Buma, Meniscus Replacement Using Synthetic Materials, Clinical Sports Medicine, 28 (2009) 143-156.

[26] P. Gunatillake, R. Adhikari, Biodegradable synthetic polymers for tissue engineering, European Cells & Materials, 5 (2003) 1–16.

[27] W.M. Guo, S.Y. Liu, Y. Zhu, C.L. Yu, S.B. Lu, M.Yuan, Y.Gao, J.X Huang, Z.G.Yuan, J. Peng, A.Y. Wang, Yu Wang, J.F. Chen, L. Zhang, X. Sui, W.J. Xu, and Q.Y. Guo. Review article: Advances and Prospects in TE meniscal scaffolds for meniscal regeneration, Stem Cell International, Volume 2015, http://dx.doi.org/10.1155/2015/517520.

[28] R. Verdonk, P. Verdonk, W. Huysse, R. Forsyth, E.L. Heinrichs, Tissue ingrowth after implantation of a novel, biodegradable polyurethane scaffold for treatment of partial meniscal lesions, American Journal of Sports Medicine, 39 (2011) 774-82.

[29] A. Esposito, M. Moda, S. Cattani, G. Santana, J. Barbieri, M. Munhoz, T. Cardoso, M. Barbo, T. Russo, U. D'Amora, A. Gloria, L. Ambrosio, E. Duek, PLDLA/PCL-T scaffold for meniscus tissue engineering, BioResearch Open Access, 2 (2013) 138-147.

[30] Koller, S. Nehrer, P. Vavken, B. Kapeller, R. Windhager, C. Chiari, Polyethylene terephthalate (PET) enhances chondrogenic differentiation of ovine meniscocytes in a hyaluronic acid/polycaprolactone scaffold in vitro, International Orthopaedics, 36 (2012) 1953–1960.

[31] C. Chiari, U. Koller, R. Dorotka, C. Eder, R. Plasenzotti, S. Lang, L. Ambrosio, E. Tognana, E. Kon, D. Salter, S. Nehrer, A tissue engineering approach to meniscus regeneration in a sheep model, Osteoarthritis Cartilage, 14 (2006) 1056-1065.

[32] B.M. Baker, R.L. Mauck, The effect of nanofiber alignment on the maturation of engineered meniscus constructs, Biomaterials, 28 (2007) 1967-1977.

[33] C. Chiari, U. Koller, R. Dorotka, C. Eder, R. Plasenzotti, S. Lang, L. Ambrosio, E. Tognana, E. Kon, D. Salter, S. Nehrer, A tissue engineering approach to meniscus regeneration in a sheep model, Osteoarthritis and Cartilage, 14 (2006) 1056–1065.

[34] C. Baynat, C. Andro, J. Vincent, P. Schiele, P. Buisson, F. Dubrana, F. Gunepin, Actifit synthetic meniscal substitute: experience with 18 patients in Brest, France, Orthopedics & Traumatology: Surgery & Research, 100 (2014) 153-157.

[35] T. Tienen, R. Heijkants, J. de Groot, A. Pennings, A. Schouten, R. Veth, P. Buma, Replacement of the knee meniscus by a porous polymer implant: a study in dogs, American Journal of Sports Medicine, 34 (2006) 64-71.

[36] J. Klompmaker, R.P.H. Veth, H.W.B. Jansen, H.K.L. Nielsen, J.H. deGroot, A.J. Pennings, R. Kuijer, Meniscal repair by fibrocartilage in the dog: characterization of the repair tissue and the role of vascularity, Biomaterials, 17 (1996) 1685‑1691.

[37] T. Efe, A. Getgood, M.D. Schofer, S Fuchs-Winkelmann, D. Mann, J.R.J. Paletta, T. J. Heyse, The safety and short-term efficacy of a novel polyurethane meniscal scaffold for the treatment of segmental medial meniscus deficiency, Knee Surgery & Sports Traumatology Arthroscopy, 20 (2012) 1822-1830.

[38] E. Kon, C. Chiari, M. Marcacci, M. Delcogliano, D.M. Salter, I. Martin, L. Ambrosio, M. Fini, M. Tschon, E. Tognana, R. Plasenzotti, S. Nehrer, Tissue engineering for total meniscal substitution: animal study in sheep model, Tissue Engineering-Part A, 14 (2008) 1067-1080.

[39] E. Kon, G. Filardo, M. Tschon, M. Fini, G. Giavaresi, L. Reggiani, C. Chiari, S. Nehrer, I. Martin, D.Salter, L. Ambrosio, M. Marcacci, Tissue engineering for total meniscal substitution: animal study in sheep model - results at 12 months, Tissue Engineering-Part A, 18 (2012) 1573-1582.

[40] H. Bouyarmane, P. Beaufils, N. Pujol, J. Bellemans, S. Roberts, T. Spalding, S. Zaffagnini, M. Marcacci, P. Verdonk, M. Womack, R. Verdonk, Polyurethane scaffold in lateral meniscus segmental defects: clinical outcomes at 24 months follow-up, Orthopedics & Traumatology: Surgery & Research, 100 (2013) 153-157.

[41] K.R. Stone, W. Rodkey, R. Webber, L. McKinney, R. Steadman, Meniscal regeneration with co-polymeric collagen scaffolds. In vitro and in vivo studies evaluated clinically, histologically, and biochemically, The American Journal of Sports Medicine, 20 (1992) 104‑111.

[42] M. Reguzzoni, A. Manelli, M. Ronga, M. Raspanti, F. Grassi, Histology and ultrastructure of a tissue-engineered collagen meniscus before and after implantation.

Journal of Biomedical Material Research Part B: Applied Biomaterials, 74 (2005) 808-816.

[43] W. Rodkey, K. DeHaven, W. Montgomery, C. Baker, C. Beck, S. Hormel, J Steadman, B. Cole, K. Briggs, Comparison of the Collagen Meniscus Implant with partial meniscectomy- a prospective randomized trial, The Journal of Bone and Joint Surgery, American Volume, 90 (2008) 1413-1426.

[44] D.S. Kim, B.L. Tai, Hydrostatic support-free fabrication of threedimensional soft structures, Journal of Manufacturing Processes, 24 (2016) 391‑396.

[45] P. Bulgheroni, L. Murena, C. Ratti, E. Bulgheroni, M. Ronga, P. Cherubino, Follow-up of collagen meniscus implant patients: clinical, radiological, and magnetic resonance imaging results at 5 years, Knee, 17 (2010) 224‑229.

[46] J. Steadman, W. Rodkey, Tissue-engineered collagen meniscus implant: 5-to 6-year feasibility study results, Arthroscopy, 21 (2005) 515-525.

[47] J.C. Monllau, P. Gelber, F. Abat, X. Pelfort, R. Abad, P. Hinarejos, M. Tey, Outcome after partial medial meniscus substitution with the collagen meniscal implant at a minimum of 10 years follow-up, Arthroscopy, 27 (2011) 933-943.

[48] S. Zaffagnini, G. Maria, M. Muccioli, N. Lopomo, D. Bruni, G. Giordano, G. Ravazzolo, M. Molinari, M. Marcacci, Prospective long-term outcomes of the medial Collagen Meniscus Implant versus partial medial meniscectomy: a minimum 10-year follow-up study, American Journal of Sports Medicine, 39 (2011) 977-85.

[49] B. Mandal, S.H. Park, E. Gil, D. Kaplan, Multilayered silk scaffolds for meniscus tissue engineering, Biomaterials, 32 (2011) 639‑651.

[50] K. Gruchenberg, A. Ignatius, B. Friemert, F. von Lübken, N. Skaer, K. Gellynck, O. Kessler and L. Dürselen, In vivo performance of a novel silk fibroin scaffold for

partial meniscal replacement in a sheep model, Knee Surgery, Sports Traumatology, Arthroscopy, 23 (2015) 2218-2229.

[51] N. Kida, Y. Ikebe, Y. Takahashi, J. P. He, Y. Kaneko, Y. Yamasaki, R. Shimano, T. Arima, N. Nagaosa,Y. Tokura, Electrically driven spin excitation in the ferroelectric magnet $DyMnO_3$, Physical Review B, 78 (2008), 104414.

[52] L.P. Yan, J.M. Oliveira, A.L. Oliveira , S.G. Caridade, J.F. Mano, R.L. Reis, Macro/microporous silk fibroin scaffolds with potential for articular cartilage and meniscus tissue engineering applications, Acta Biomaterialia, 8 (2012) 289-301.

[53] A. Bodin, S. Concaro, M. Brittberg, P. Gatenholm, Bacterial cellulose as a potential meniscus implant, Journal of Tissue Engineering and Regenerative Medicine, 6 (2007) 406-408.

[54] E. Pena, B Calvo, M.A. Martinez, D. Palanca, M Doblare, Finite element analysis of the effect of meniscal tears and meniscectomies on human knee biomechanics, Clinical Biomechanics (Bristol, Avon), 20 (2005) 498-507.

[55] H.C. Martínez, C. Brackmann, A Eneider, P Gateholm, Mechanical stimulation of fibroblasts in micro-channelled bacterial cellulose scaffolds enhances production of oriented collagen fibres, Journal of Biomedical Materials Research Part A, 100 (2012) 948–957.

[56] B. Kelly, W. Robertson, H. Potter, X.H. Deng, A. Turner, S. Lyman, R. Warren, S. Rodeo, Hydrogel meniscal replacement in the sheep knee: preliminary evaluation of chondroprotective effects, American Journal of Sports Medicine, 35 (2007) 43-52

[57] M. Kobayashi, A study of polyvinyl alcohol-hydrogel (PVA-H) artificial meniscus in vivo, Bio-Medical Materials and Engineering, 14 (2004) 505 – 515.

[58] M. Kobayashi, J. Toguchida, M. Oka, Preliminary study of polyvinyl alcohol-hydrogel (PVA-H) artificial meniscus, Biomaterials, 24 (2003), 639-647.

[59] M. Sarem, F. Moztarzadeh, M. Mozafari, V.P. Shastri, Optimisation strategies on the structural modeling of gelatin/chitosan scaffolds to mimic human meniscus tissue. Materials science & Engineering C: Materials for Biological Applications, 33 (2013) 4777-4785.

[60] K. Ishida, R. Kuroda, M. Miwa, Y. Tabata, A. Hokugo, T. Kawamoto, K. Sasaki, M. Doita, M. Kurosaka, The regenerative effects of platelet-rich plasma on meniscal cells in vitro and its in vivo application with biodegradable gelatin hydrogel, Tissue Engineering, 13 (2007) 1103–1112.

[61] J.P. Hommen, G.R. Applegate, W.D. Pizzo, Meniscus allograft transplantation: 10-year results of cryopreserved allografts, Arthroscopy, 23 (2007) 388-393.

[62] F. Noyes, S.D. Barber-Westin, Meniscus transplantation: indications, techniques, clinical outcomes, Instructional Course Lectures, 54 (2005) 341– 353.

[63] D. Maier, K. Braeun, E. Steinhauser, P. Ueblacker, M.Oberst, P. Kreuz, N. Roos, V. Martinek, A. Imhoff, In vitro analysis of an allogenic scaffold for tissue-engineered meniscus replacement, Journal of Orthopedic Research, 25 (2007) 1598–1608.

[64] A. Abdelgaied, M. Stanley, M. Galfe, H. Berry, E. Ingham, J. Fisher, Comparison of the biomechanical tensile and compressive properties of decellularised and natural porcine meniscus, Journal of Biomechanics, 48 (2015) 1389-1396.

[65] H. Pereira, A. Frias, J. Oliveira, J. Espregueira-Mendes, R. Reis, Tissue Engineering and Regenerative Medicine Strategies in Meniscus Lesions. : Systematic Review. Arthroscopy, The Journal of Arthroscopic and Related Surgery, 27 (2011) 1706-1719.

[66] G. H. Sandmann, S. Eichhorn, S. Vogt, C. Adamczyk, S. Aryee, M. Hoberg, S. Milz, A. B. Imhoff, T. Tischer, Generation and characterization of a human acellular

meniscus scaffold for tissue engineering, Journal of Biomedical Materials Research Part A, 91A (2009) 567–574.

[67] T. Stapleton, J. Ingram, J. Fisher, E. Ingham, Investigation of the regenerative capacity of an acellular porcine medial meniscus for tissue engineering applications, Tissue Engineering Part A, 17 (2011) 231-242.

[68] A. Azhim, T. Ono, Y. Fukui, Y. Morimoto, K. Furukawa, T. Ushida, Preparation of decellularised meniscal scaffolds using sonication treatment for tissue engineering. Proceedings of the 35th Annual International Conference of the IEEE Engineering in Medicine and Biology Society (EMBC' 13), IEEE, Osala, Japan, July (2013) 6953-6956.

[69] K. Stabile, D. Odom, T. Smith, C. Northam, P. Whitlock, B. Smith, M. Van Dyke, C. Ferguson, An acellular, allograft derived meniscus scaffold in an ovine model, Arthroscopy, 26 (2010) 936-948.

[70] E.L. Mulder, G. Hannink, M. Giele, N. Verdonschot, P. Buma, Proliferation of meniscal fibro chondrocytes cultured on a new polyurethane scaffold is stimulated by TGF-β. Journal of Biomaterials Applications, 27 (2013) 617-26.

[71] Y. Moriguchi, K. Tateishi, W. Ando, K. Shimomura, Y. Yonetani, Y. Tanaka, K. Kita, D..Hart, A. Gobbi, K. Shino, H. Yoshikawa, N. Nakamura, Repair of meniscal lesions using a scaffold-free tissue-engineered construct derived from allogenic synovial MSCs in a miniature swine model, Biomaterials, 34 (2013) 2185-2193.

[72] G. Zur, E. Linder-Ganz , J. Elsner, J. Shani, O. Brenner, G. Agar, E.B. Hershman , S.P. Arnoczky , F. Guilak , A. Shterling, Chondroprotective effects of a polycarbonate-urethane meniscal implant: Histopathological results in a sheep model. Knee Surgery, Sports Traumatology, Arthroscopy, 19 (2011) 255-263.

[73] T. Toyonaga, N. Uezaki, H. Chikama, Substitute meniscus of Teflon-net for the knee joint of dogs, Clinical Orthopaedics and Related Research, 179 (1983) 291–297.

[74] K.R. Stone, Meniscus replacement, Clinical Sports Medicine, 15 (1996) 557–571.

[75] J.H. DeGroot, Polyurethane Scaffolds for Meniscal Tissue Regeneration, Medical Device Technology, 6 (2005) 18-20.

[76] W. Zhu, K.Y. Chern, V.C. Mow, Anisotropic viscoelastic shear properties of bovine meniscus, Clinical Orthopaedics and Related Research, 306 (1994) 34–45.

[77] K. Messner, Meniscal substitution with a Teflon-periosteal composite graft: a rabbit experiment, Biomaterials, 15 (1994) 223–230.

[78] K. Messner, J. Gillquist, Prosthetic replacement of the rabbit medial meniscus. Journal of Biomedical Materials Research, 27 (1993) 1165–1173.

[79] M. Sweigart, C.F. Zhu, D.M. Burt, P. DeHoll, C. Agrawal, T. Clayton, K. Athanasiou, Intraspecies and Interspecies Comparison of the Compressive Properties of the Medial Meniscus, Annals of Biomedical Engineering, 32 (2004) 1569–1579.

[80] C. Moran, D. Withers, P. Kurweil, P. Verdonk, Clinical Application of Scaffolds for Partial Meniscus Replacement: Review Article, Sports Med Arthroscope Rev, 23 (2015) 944-955.

[81] W. Rodkey, K. DeHaven, W. Montgomery, C. Baker, C. Beck, S. Hormel, J Steadman, B. Cole, K. Briggs, Comparison of the Collagen Meniscus Implant with partial meniscectomy- a prospective randomized trial, The Journal of Bone and Joint Surgery, American Volume, 90 (2008) 1413-1426.

[82] R. Papalia, F. Franceschi, L. Balzani, S. D'Adamio, N. Maffulli, V. Denaro, Scaffolds for partial meniscal replacement: an updated systematic review, British Medical Bulletin, 107 (2013) 19-40.

[83] RepRap RAMPS. 26 March 2014 http://reprap.org/wiki/RAMPS_1.4

[84] Silicone Elastomers 2013 Proceedings. 10-12 June, 2013-Munich

Germany.

[85] Silicone-chemisty-www.dowcorning.com/content/publishedlit/51- 960A_

[86] L. Lewis, J. Stein, Y. Gao, R. Colborn, Platinum Metals Review, 41 (1997) 66-75.

[87] Silicone Rubbers Products https://www.wacker.com/cms/en/products/product_groups/silicone_rubbers_1/vernetzung_1.jsp.

[88] D. Eyre, R.V. Noot, B. Ellis, The rheology of silicone rubber impression materials, Journal of Dentistry, 17 (1989) 171-176.

[89] D.B. Guan, Z.Y. Cai, X.C. Liu, B. Lou, Y.L. Dou, D.H. Xu, W.G. Yao, Rheological Study on the Cure Kinetics of Two-component Addition Cured Silicone Rubber, Chinese Journal of Polymer Science, 34 (2016) 1290-1300.

[90] M.J. Owen, Why Silicones Behave Funny, Chemtech, 11 (1981) 288.

[91] Silicone Medical Application. https://www.simtec-silicone.com/liquidsilicone-rubber-for-medical-applications/ .

[92] https://www.sciencedirect.com/topics/materials-science/injectionmolding.

[93] T.J. Hinton, A. Hudson, K. Pusch, A. Lee, A.W. Feinberg, 3D Printing PDMS Elastomer in a Hydrophilic Support Bath via Freeform Reversible Embedding, ACS Biomaterials Science and Engineering, 2 (2016) 1781−1786.

[94] D.S. Kim, B.L. Tai, Hydrostatic support-free fabrication of threedimensional soft structures, Journal of Manufacturing Processes, 24 (2016) 391‑396.

[95] C.K. Chua, K.F. Leong, 3D Printing and Additive Manufacturing: Principles and Applications, 4th edition, World Scientific Publishing Co. Pte. Ltd. Singapore 2014.

[96] https://www.germanreprap.com/printer/L280EN.aspx

[97] RAMP KITS WIRING- Mendelcraft. 25March 2014. http://www.mendelcraft.com/Instructions/Step10.pdf.

[98] Lahey, F. H. (1946). Comments made following the speech “Results from using Vitallium tubes in biliary surgery,” read by Pearse, HE before the American Surgical Association, Hot Springs, VA, Annals of Surgery, 124 (1946) 1927.

[99] G. Clark, Cochlear implants: fundamentals and applications. 2006 Springer-Verlag, New York, Inc.

[100] J. Braga-Silva, The use of silicone tubing in the late repair of the median and ulnar nerves in the forearm, Journal of Hand Surgery, 24B (1999) 703- 706.

[101] FDA update on the safety of silicone gel-filled breast implants, June 2011, Center for Devices and Radiological Health U.S. Food and Drug Administration.

[102] R. Rohrich, D. Wan, Working toward a Solution: The Unanswered Questions about Silicone Gel Breast Implants, Annals of Internal Medicine, 164 (2016) 201-202.

[103] E. Balk, A. Earley, E. A. Avendano, G. Raman, Long-Term Health Outcomes in Women with Silicone Gel Breast Implants: A Systematic Review, Annals of Internal Medicine, 164 (2016) 164-175.

[104] N. Singh, G. Picha, B. Hardas, A. Schumacher, D. Murphy, Five-Year Safety Data for More than 55,000 Subjects following Breast Implantation: Comparison of Rare Adverse Event Rates with Silicone Implants versus National Norms and Saline Implants, Plastic and Reconstructive Surgery, 140 (2017) 666-679.

[105] B.Y. Li, T. Webster, Orthopedic Biomaterial, Advances and Applications, Springer Nature 2017, ISBN 978-3-319-73663-1. [106] C. Boe, E. Wagner, M. Rizzo, Long-term outcomes of silicone metacarpophalangeal arthroplasty: a longitudinal analysis of 325 cases, Journal of Hand Surgery (European Volume), 43 (2018) 1076-1082.

[107] K. Chung, S. Kotsis, H. Kim, A Prospective Outcomes Study of Swanson Metacarpophalangeal Joint Arthroplasty for the Rheumatoid Hand, 29 (2004) 626-65.

[108] Mazas F. B. (1973). GUEPAR total knee prosthesis, Clinical Orthopaedics and Related Research, 94 (1973) 211.

[109] M. Harmand, F. Briquet, In vitro comparative evaluation under static conditions of the hemocompatibility of four types of tubing for cardiopulmonary bypass. Biomaterials, 20 (1999) 1561-1571.

[110] W.L. Robb, Thin silicone membranes - their permeation properties and some applications, Annals of the New York Academy of Sciences, 146 (1968) 119-137.

[111] https://www.meddeviceonline.com/doc/silicon-a-material-with-hugepotential-for-lab-on-chips-0001.

[112] K. Zinoviev, L. Carrascosa, J. Sánchez del Río, B. Sepúlveda, C. Domínguez, and L. Lechuga, Silicon Photonic Biosensors for Lab-on-a-Chip Applications, Advances in Optical Technologies, (volume 2008), Article ID 383927, doi:10.1155/2008/383927.

[113] S. Dhanekar, S. Jain, Biosensors & Bioelectronics, 41 (2013) 54-64

[114] T. Takahashi, J. Kaschta, H. Munstedt, Melt rheology and structure of silicone resins, Rheologica Acta, 40 (2001), 490-298.

[115] M. Romano, F. Cuomo, N. Massarotti, A. Mauro, M.Salahudeen, C. Costagliola, L. Ambrosone, Temperature Effect on Rheological Behavior of Silicone Oils. A Model for the Viscous Heating, The Journal of Physical Chemistry, B, 121 (2017) 7048−7054.

[116] J. Stieghorst, T. Doll, Rheological behavior of PDMS silicone rubber for 3D printing of medical implants, Additive Manufacturing, 24 (2018) 217- 223.

[117] S. Patel, S. Malone, C. Cohen, J. Gillmor, R. Colby, Elastic Modulus and equilibrium swelling of poly (dimethylsiloxane) networks, Macromolecules, 25 (1992) 5241-5251.

[118] M. Romano, F. Cuomo, N. Massarotti¶, A. Mauro, M. Salahudeen, C. Costagliola, L. Ambrosone, Temperature Effect on Rheological Behavior of Silicone Oils. A Model for the Viscous Heating,The Journal of Physical Chemistry B, 121（2017）7048−7054.

[119] H.P. Zhang, M. Krenceski, B. Ganter, Rheology characterization of UV curable silicone elastomers, Rubber World, August 2014.

[120] N. El Kissi, J.M. Piau, P. Attané, G. Turrel, Shear Rheometry of Polydimethylsiloxanes. Master curves and testing of Gleissle and Yamamoto relations, Rheologica Acta, 32 (1993) 293.

[121] Daniel T.N. Chen,1 Qi Wen,2 Paul A. Janmey,2 John C. Crocker,3 and Arjun G. Yodh, Rheology of Soft Materials, Annu. Rev. Condens. Matter Phys. 2010. 1:301–22.

[122] Li, Y.H., Luis, E., 3D Printing of Medical Models from CT-MRI Images, Partridge Publications, Singapore, 2016.

[123] ASTM Standard Test Methods for Vulcanized Rubber and Thermoplastic Elastomers—Tension Designation: D412 – 16.

[124] ASTM Standard Test Methods for Rubber Properties in Compression Designation: D575 – 91. Test Method A.

[125] I.D. Johnston, D. McCluskey, C. Tan, M. Tracey, Mechanical characterization of bulk Sylgard 184 for microfluidics and microengineering, Journal of Micromechanics and Microengineering. 24 (2014) 035017, 1-7.

[126] G.Z.Voyiadjis,P.I. Kattan, On the theory of Elastic Undamageable Materials. Journal of Engineering Materials and Technology. April 2013. DOI 10.1135/1-4023770.

[127] G. Zagar, P. R. Onck, Erik van der Giessen, Two Fundamental Mechanisms Govern the Stiffening of Cross-linked Networks. Biophysical Journal, 108 (2015) 1470–1479.

[128] W.S. Lee, K.S. Yeo, A. Andriyana, Y. G Shee, F. R. Mahamd Adikan, Effect of cyclic compression and curing agent concentration on the stabilization of mechanical properties of PDMS elastomer, Materials & Design, 96 (2016) 470-475.

[129] T. V. Vorburger, H.-G. Rhee, T. B. Renegar, J.-F. Song, A. Zheng. Comparison of optical and stylus methods for measurement of surface texture, The International Journal of Advanced Manufacturing Technology, 33 (2007) 110-118.

[130] M. Campeau, A. Lortie, P. Tremblay, M. Béliveau, D. Dubé, È. Langelier, L. Rouleau, Effect of manufacturing and experimental conditions on the mechanical and surface properties of silicone elastomer scaffolds used in endothelial mechanobiological studies, Biomedical Engineering Online 16 (2017) 90.

[131] V. Heinrichs, S. Dieluweit, J. Stellbrink, W. Pyckhout-Hintzen, N. Richter, R. Merkel, Chemically defined, ultrasoft PDMS elastomers with selectable elasticity for mechanobiology, PLOS ONE, 13 (2018) e0195180.

[132] W.J. Li, J. Zhou, Y.Y. Xu, Study of the in vitro cytotoxicity testing of medical devices, Biomedical Reports, 3 (2015), 617-620.

[133] A. Barabadi, Reliability model selection and validation using Weibull probability plot–A case study, Electric Power Systems Research, 101 (2013) 96–101.

[134] C. Bortolotto, E. Eshja, C. Peroni, M. Orlandi, N. Bizzotto, Poggi P, 3D Printing of CT Dataset: Validation of an Open Source and Consumer- Available Workflow, Journal of Digital Imaging, 29 (2016) 14–21.

[135] G. Polyzois, P. Lagouvardos, S. Zinelis, M. Frangou, Peel testing of bond between PDMS prosthetic elastomers and cpTi: A Weibull analysis approach. International Journal of Adhesion & Adhesives, 30 (2010) 500–504.

[136] C. Woo, H. Park, W. Kim, The Effect of Maximum Strain on Fatigue Life Prediction for Natural Rubber Material. World Academy of Science, Engineering and

Technology, International Journal of Mechanical and Mechatronics Engineering, 7 (2013) 621-626.

[137] B. Gong, Y.P. Tu, Y.Y. Zhou, R.H. Li, F.Z. Zhang, Z. Xu, D. Liang, Moisture absorption characteristics of silicone rubber and its effect on dielectric properties, 2013 Annual Report Conference on Electrical Insulation and Dielectric Phenomena, 20-23 October 2013

[138] A. Barabadi, Reliability and spare part provision considering operational environment, International Journal of Performability Engineering, 8 (2012) 497–506.

[139] V. Le Saux, Y. Marco, S. Calloch, C. Doudard, P. Charrier, Evaluation of the Fatigue Lifetime of Elastomers Based on a Heat Build-up Protocol and Microtomography Measurements, International Journal of Fatigue, Elsevier, 32 (2010) 1582-1590.

[140] G.D. Goh, Y.L. Yap, H.K.J. Tan, S.L. Sing, G.L. Goh, W.Y. Yeong, Process-structure-properties in Polymer Additive Manufacturing via Material Extrusion: A review. Critical Reviews in Solid State and Materials Sciences. 2018. (under review)

[141] G.L. Goh, S. Agarwala, G.D. Goh, H.K.J. Tan, L. Zhao, T.K. Chuah, Additively manufactured multi-material free-form structure with printed electronics. The International Journal of Advanced Manufacturing Technology, 94 (2018) 1309-16.

[142] J. Gopi, G. Nando, Preparation and characterization of nanohydroxyapatite-based nanocomposites derived from immiscible blends of thermoplastic polyurethane and polydimethylsiloxane rubber, Journal of Thermoplastic Composite Materials, 30 (2015) 465-489.

[143] Y.Y.C Choong, S. Maleksaeedi, H.Eng, J.Wei, P.C. Su, 4D Printing of high performance shape memory polymer using stereolithography, Materials & Design, 126 (2017) 219-225.

[144] M. Campeau, A. Lortie, P. Tremblay, M. Béliveau, D. Dubé, È. Langelier, L. Rouleau, Effect of manufacturing and experimental conditions on the mechanical and surface properties of silicone elastomer scaffolds used in endothelial mechanobiological studies, Biomedical Engineering Online 16 (2017) 90.

[145] V. Heinrichs, S. Dieluweit, J. Stellbrink, W. Pyckhout-Hintzen, N. Richter, R. Merkel, Chemically defined, ultrasoft PDMS elastomers with selectable elasticity for mechanobiology, PLOS ONE, 13 (2018) e0195180.

[146] W.J. Li, J. Zhou, Y.Y. Xu, Study of the in vitro cytotoxicity testing of medical devices, Biomedical Reports, 3 (2015), 617-620. [147] A. Barabadi, Reliability model selection and validation using Weibull probability plot–A case study, Electric Power Systems Research, 101 (2013) 96‑101.

[148] Yan SH, Ou-Yang HK, Shan YL Tensile biomechanical characteristics of human meniscus. Emerging Materials Research S (1) (2015) 44-49.

[149] J.M.Peloquin, M.H. Santare, D.M.Elliot. Advances in Quantification of Meniscus Tensile Mechanics Including Nonlinearity, Yield and Failure. J Biomech Eng,138 (2016) 0210021-02100213.

Appendix A: Eco50 Rheology Graphs

nSill45 temp eco50

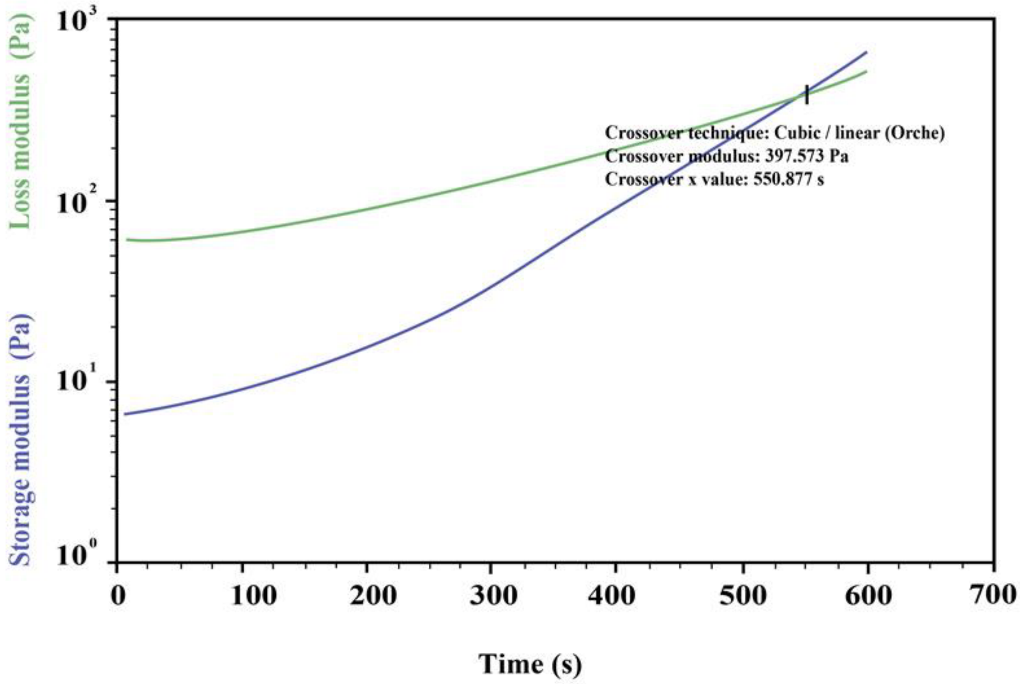

nSill50 new temp eco50

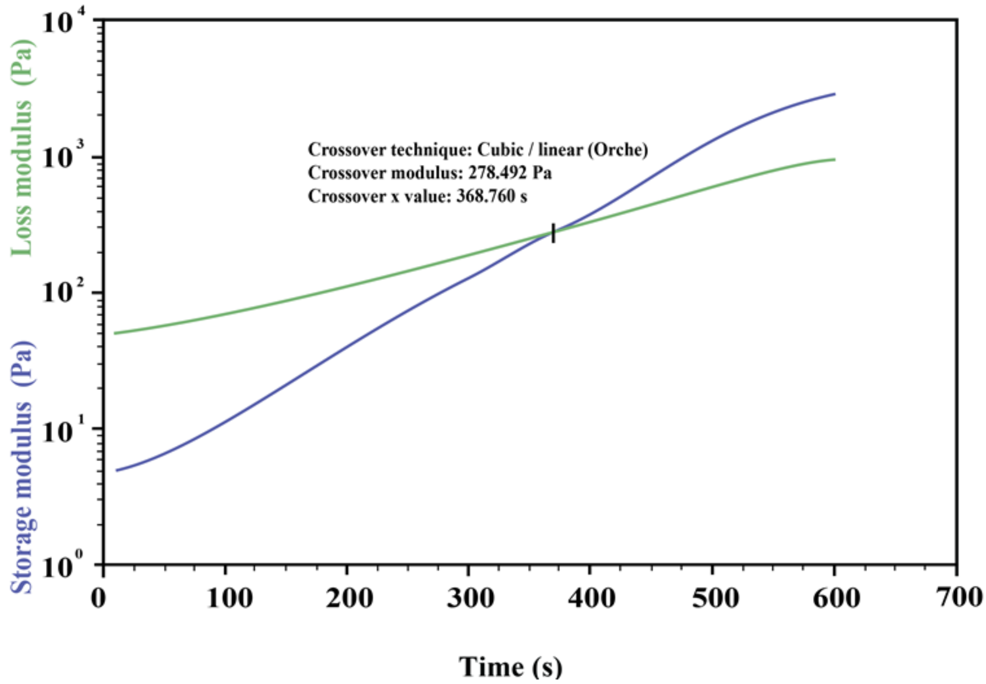

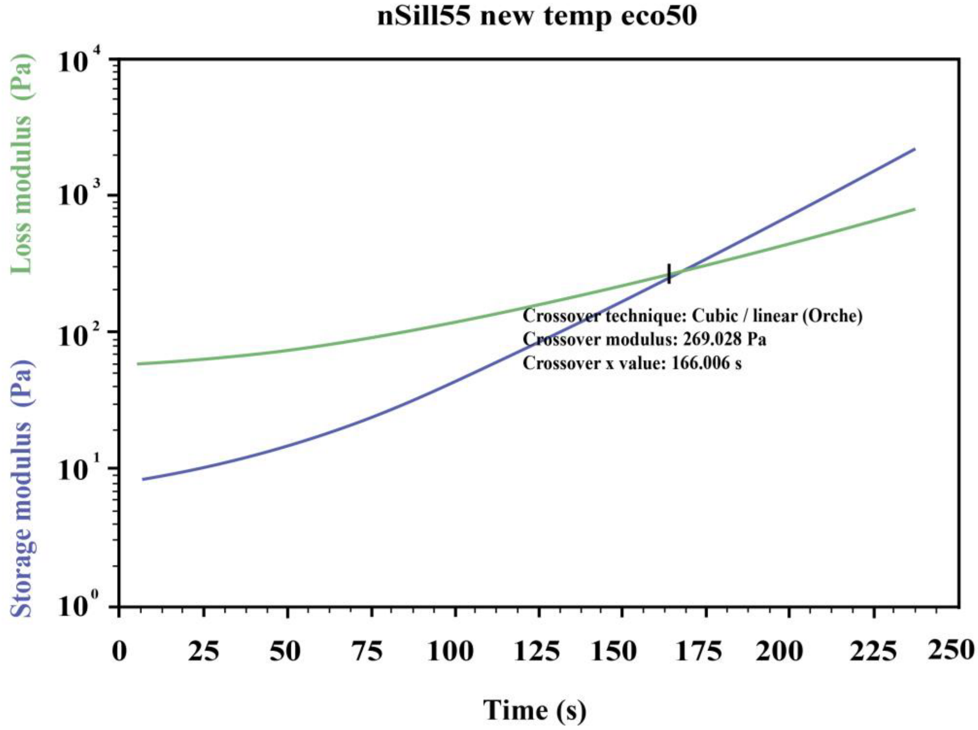
nSill55 new temp eco50
Loss modulus (Pa)
Storage modulus (Pa)
Crossover technique: Cubic / linear (Orche)
Crossover modulus: 269.028 Pa
Crossover x value: 166.006 s
Time (s)

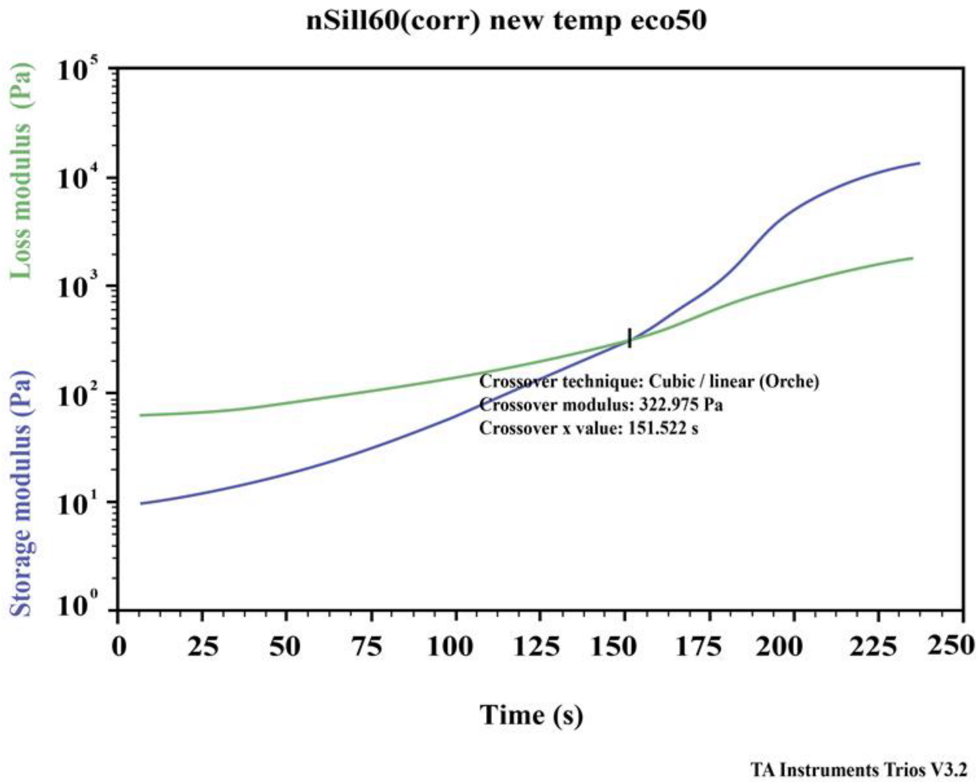
nSill60(corr) new temp eco50
Loss modulus (Pa)
Storage modulus (Pa)
Crossover technique: Cubic / linear (Orche)
Crossover modulus: 322.975 Pa
Crossover x value: 151.522 s
Time (s)
TA Instruments Trios V3.2

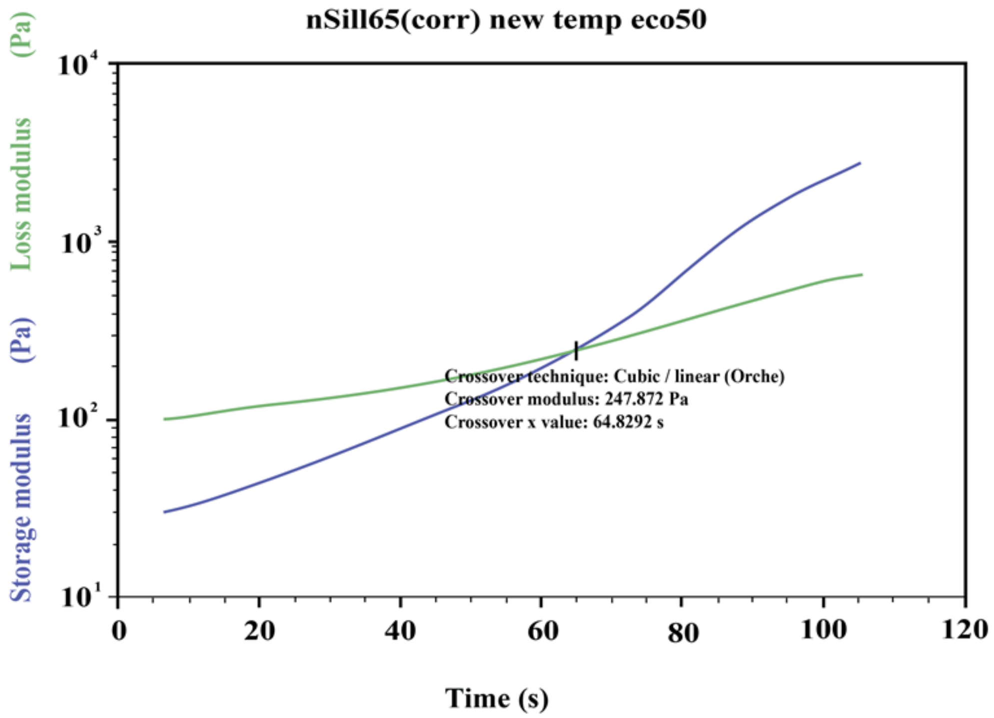
nSill65(corr) new temp eco50
Storage modulus (Pa)
Loss modulus (Pa)
Crossover technique: Cubic / linear (Orche)
Crossover modulus: 247.872 Pa
Crossover x value: 64.8292 s
Time (s)

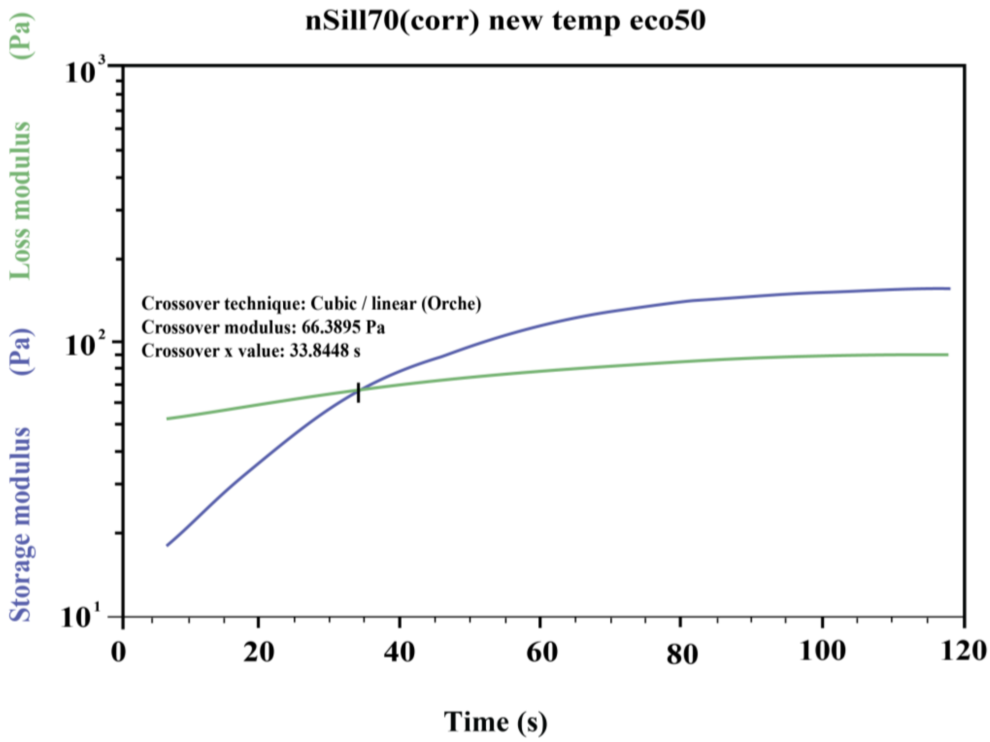
nSill70(corr) new temp eco50
Storage modulus (Pa)
Loss modulus (Pa)
Crossover technique: Cubic / linear (Orche)
Crossover modulus: 66.3895 Pa
Crossover x value: 33.8448 s
Time (s)

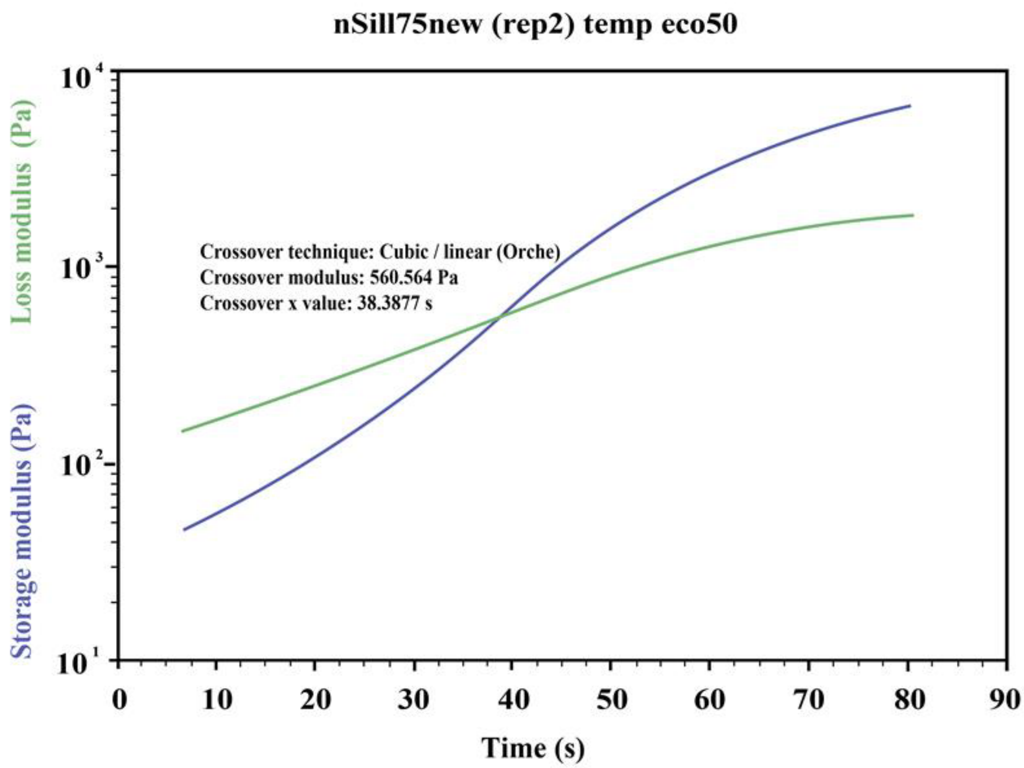
nSill75new (rep2) temp eco50
Crossover technique: Cubic / linear (Orche)
Crossover modulus: 560.564 Pa
Crossover x value: 38.3877 s
Loss modulus (Pa)
Storage modulus (Pa)
Time (s)

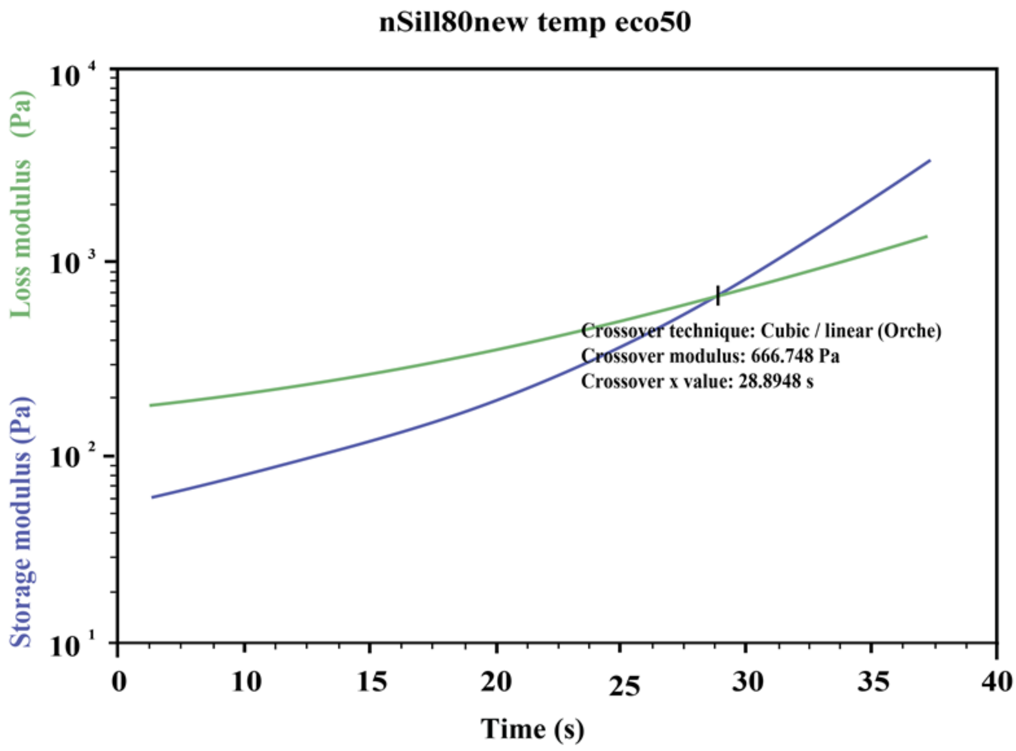
nSill80new temp eco50
Crossover technique: Cubic / linear (Orche)
Crossover modulus: 666.748 Pa
Crossover x value: 28.8948 s
Loss modulus (Pa)
Storage modulus (Pa)
Time (s)

Ecoflex 50 Oscillation Stress vs Oscillation Strain Rate

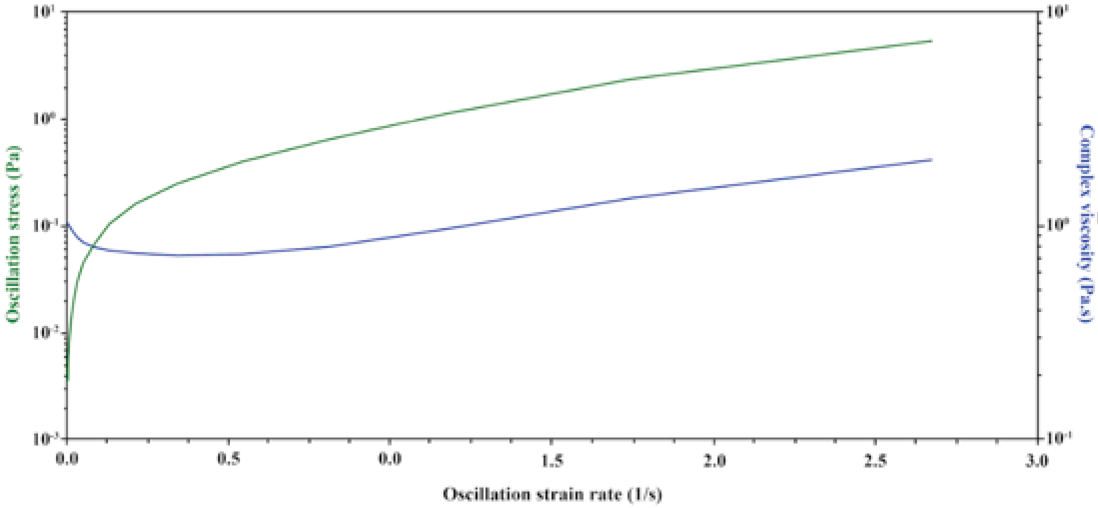

Fig 1. Ecoflex 50 40 □C stress vs strain

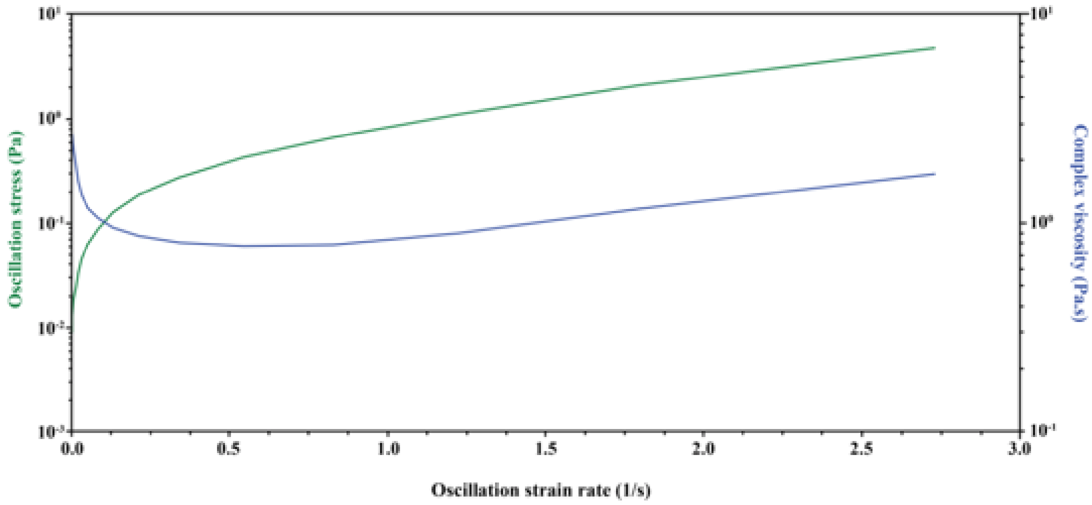

Fig 2, Ecoflex 50 50 □C stress vs strain

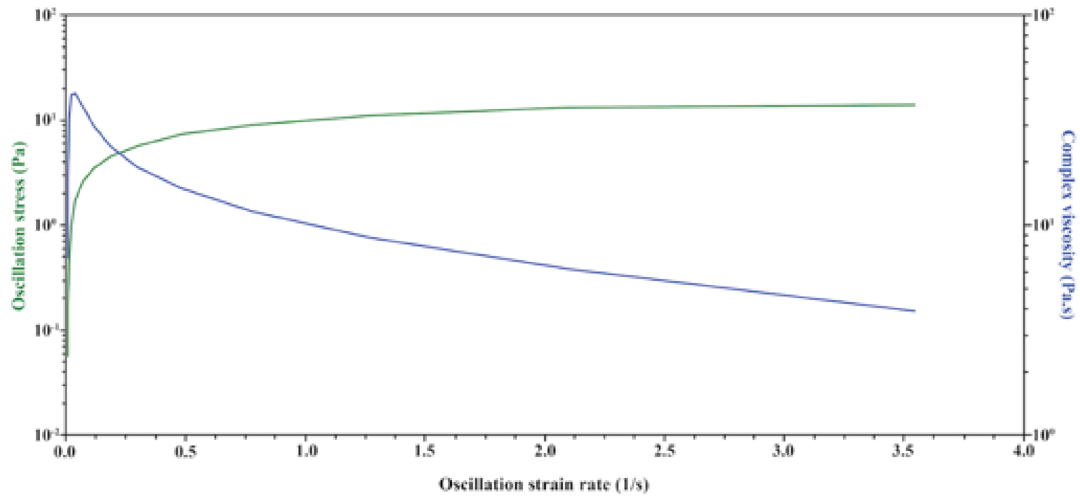

Fig 3, Ecoflex 50 60 □C stress vs strain

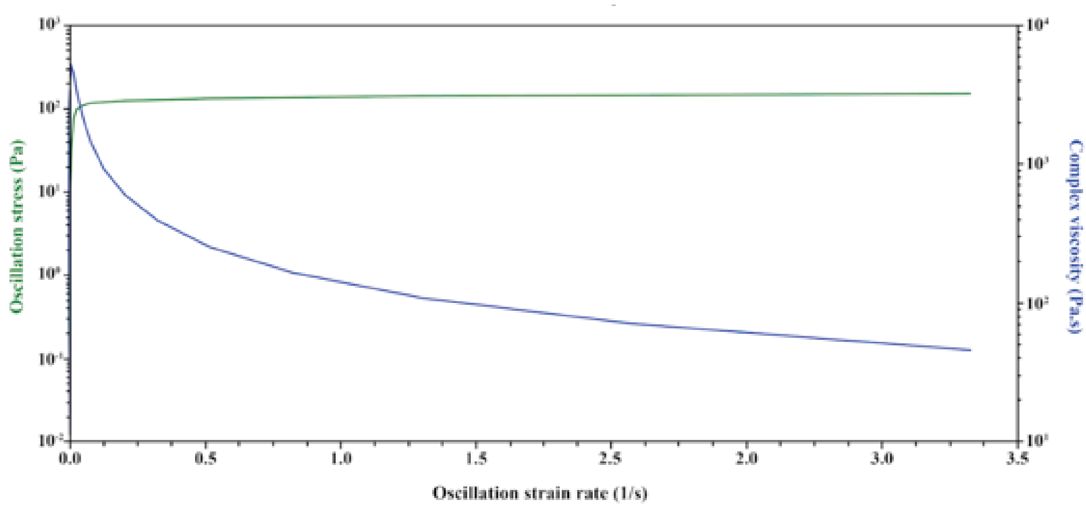

Fig 4, Ecoflex 50 70 □C stress vs strain

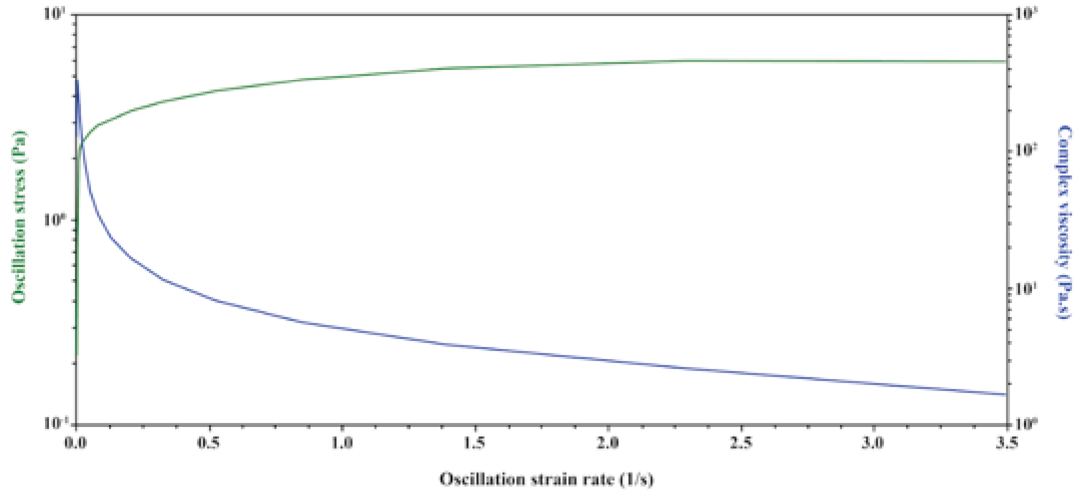

Fig 5, Ecoflex 50 80 □C stress vs strain

Ecoflex 50 Oscillation Modulus vs Oscillation Stress

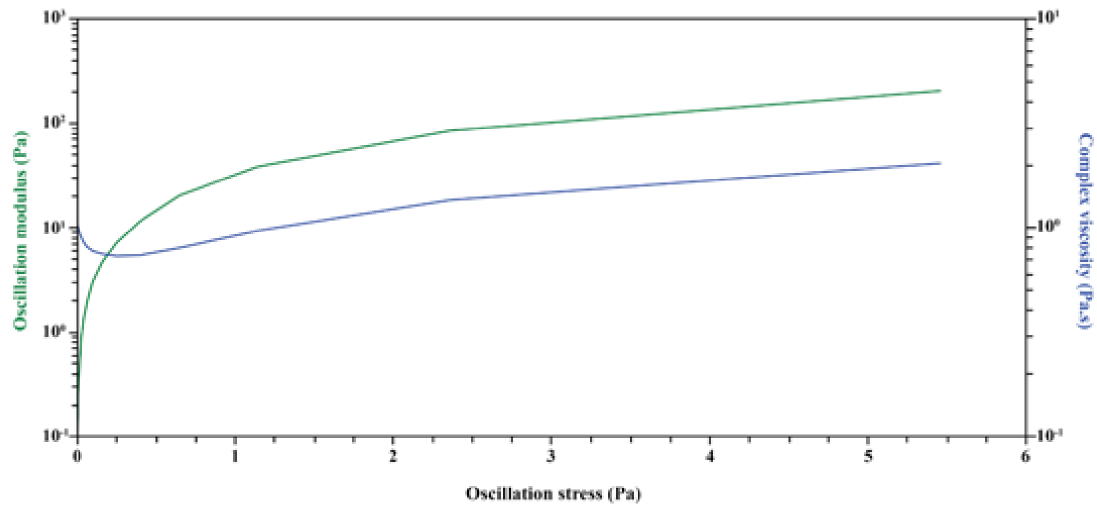

Fig 6. Ecoflex 50 40 □C modulus vs stress

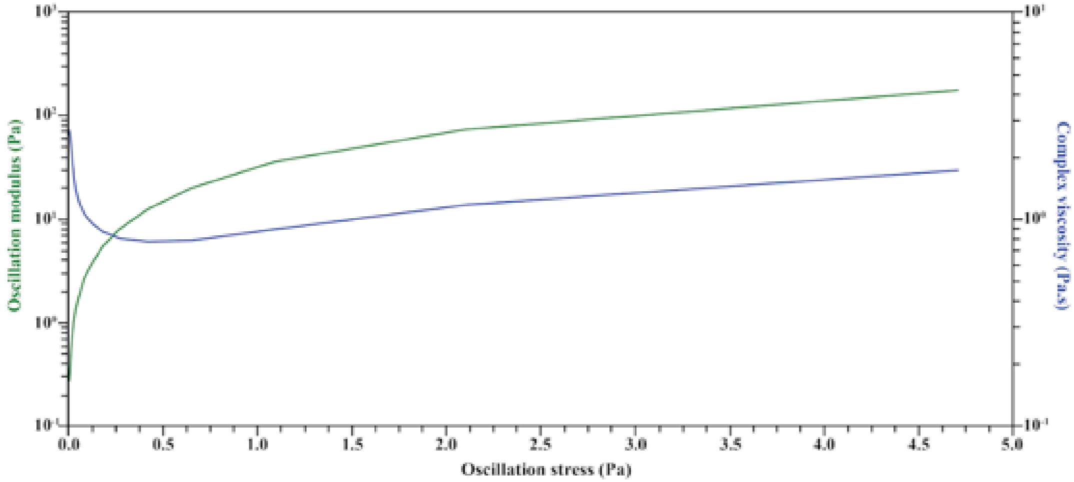

Fig 7. Ecoflex 50 50 □C modulus vs stress

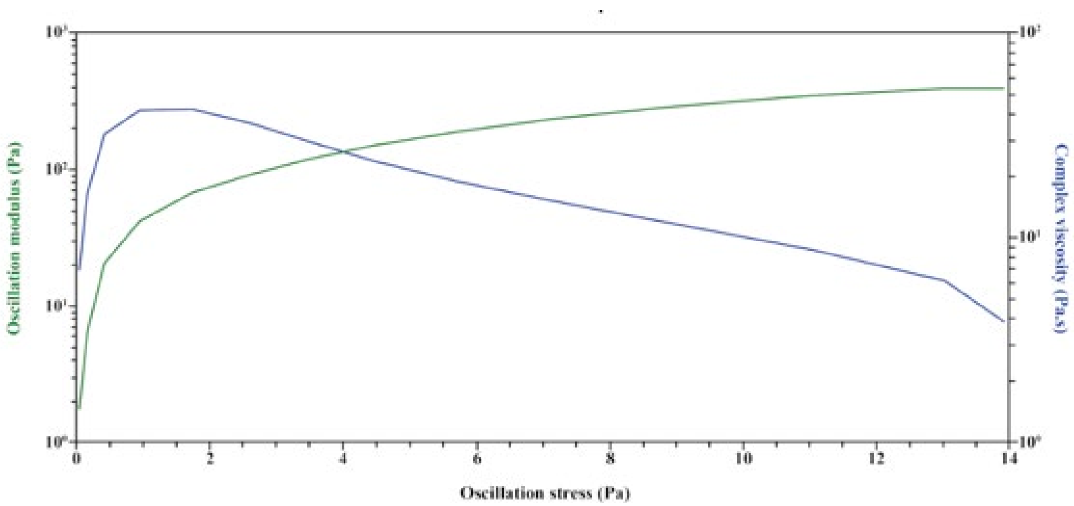

Fig 8. Ecoflex 50 60 □C modulus vs stress

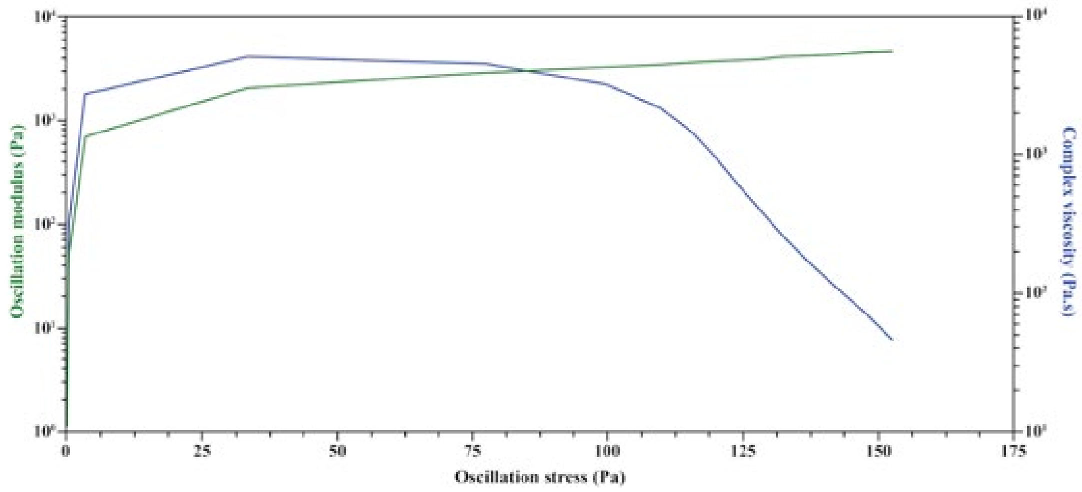

Fig 9 . Ecoflex 50 70 □C modulus vs stress

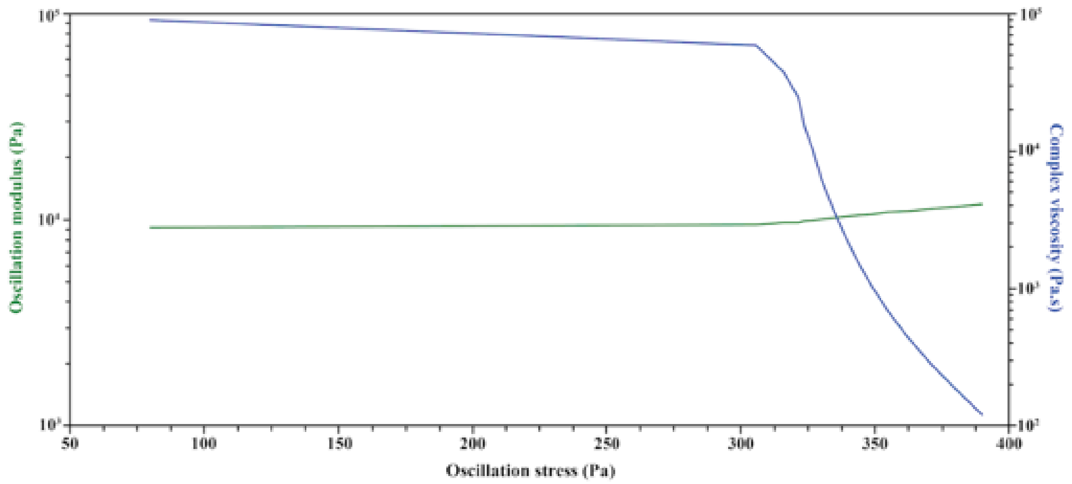

Fig 10 Ecoflex 50 80 □C modulus vs stress

Ecoflex 30 Oscillation Stress vs Oscillation Strain Rate

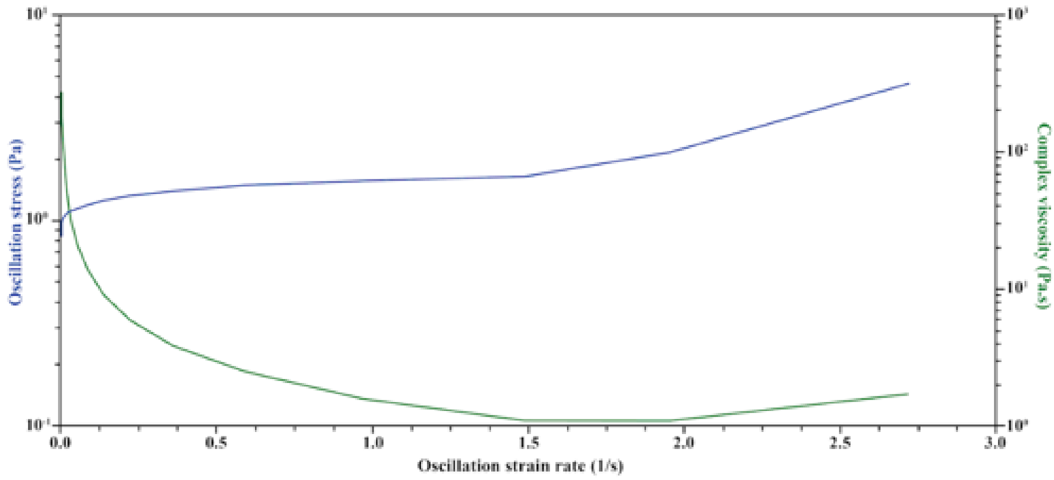

Fig 11 Ecoflex 30 30 □C stress vs strain

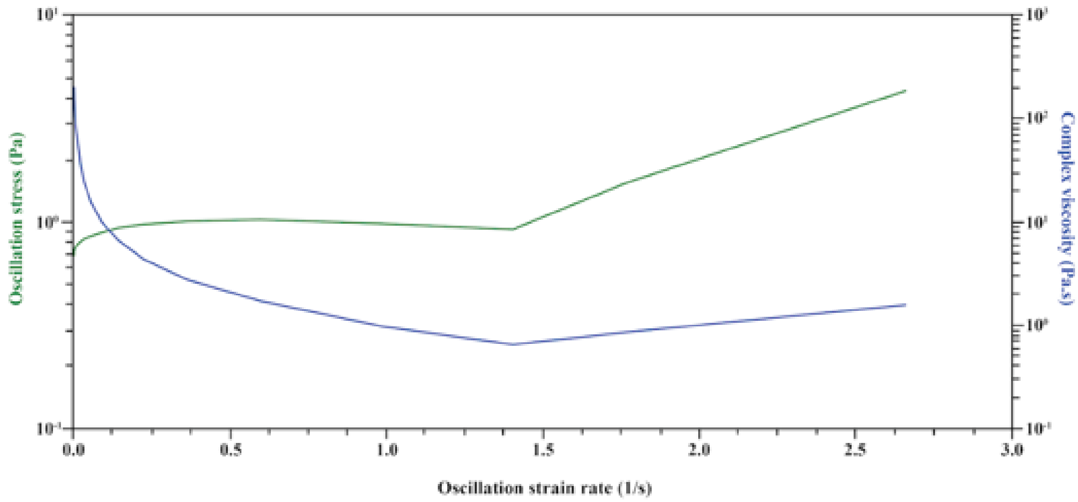

Fig 12 Ecoflex 30 40 □C stress vs strain

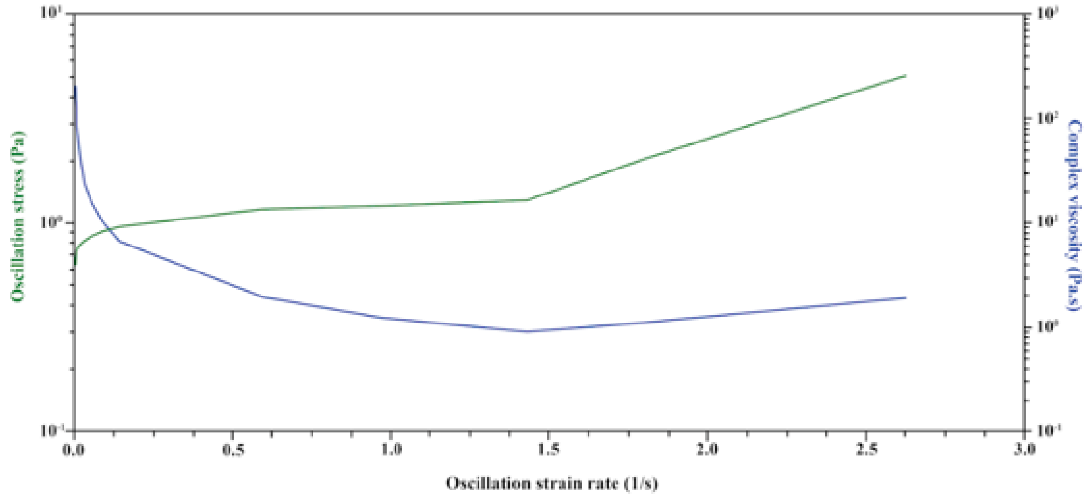

Fig 13 Ecoflex 30 50 □C stress vs strain

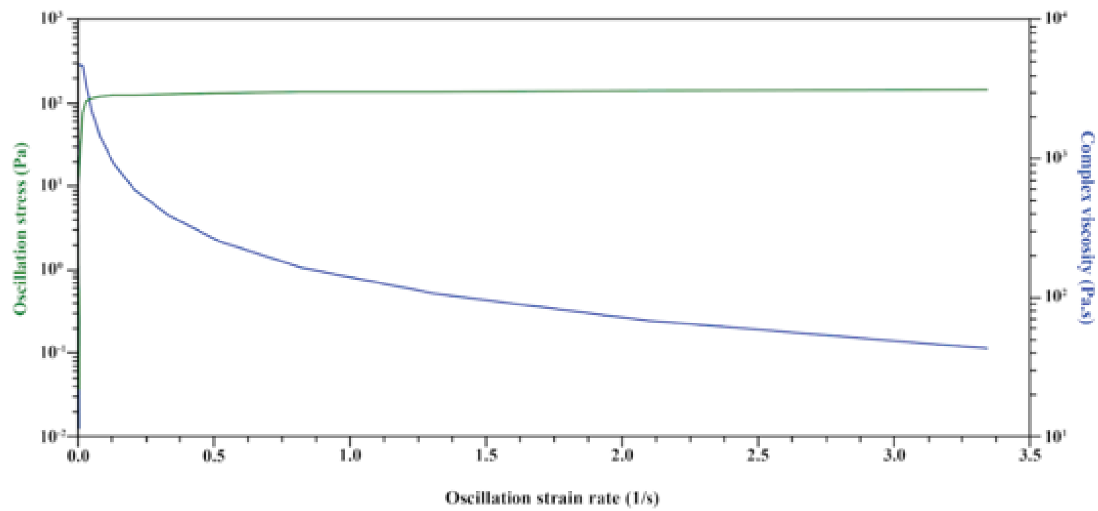

Fig 14 Ecoflex 30 60 □C stress vs strain

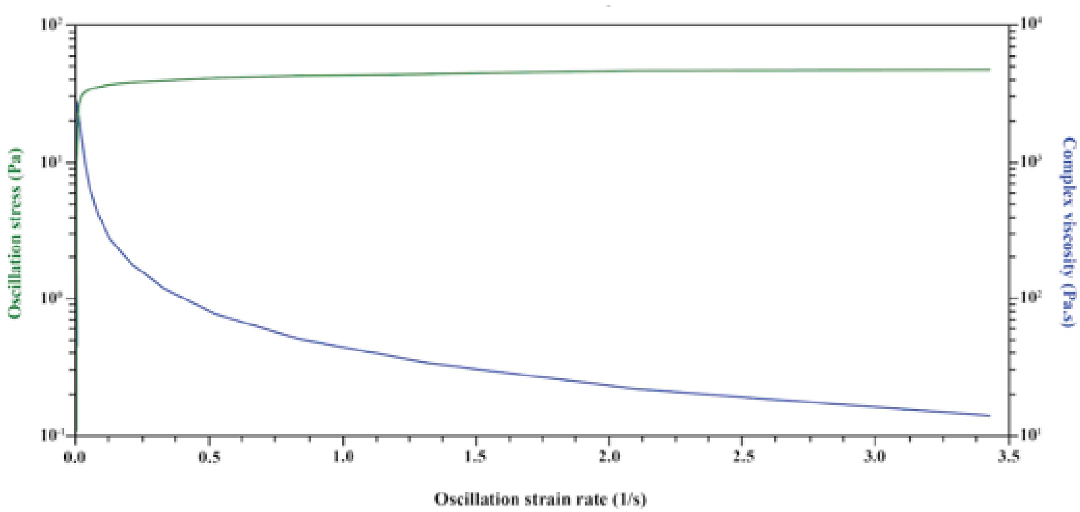

Fig 15 Ecoflex 30 70 □C stress vs strain

Ecoflex 30 Oscillation Modulus vs Oscillation Stress

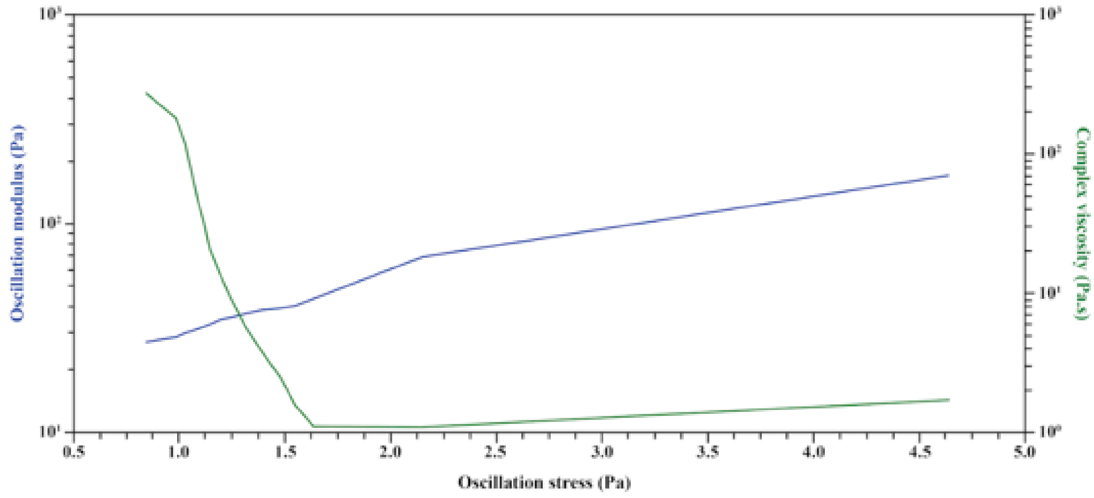

Fig 16 Ecoflex 30 30 □C modulus vs stress

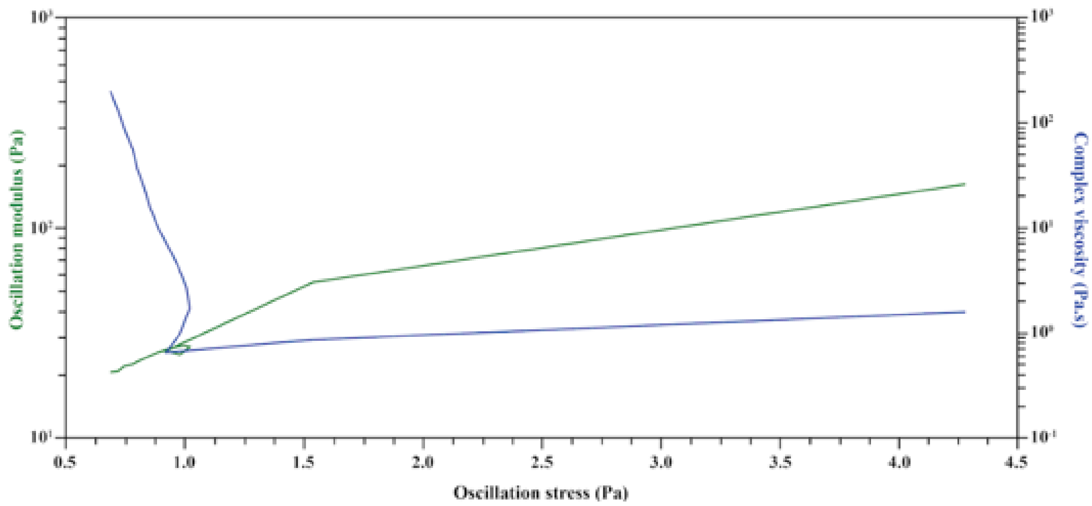

Fig 17 Ecoflex 30 40 □C modulus vs stress

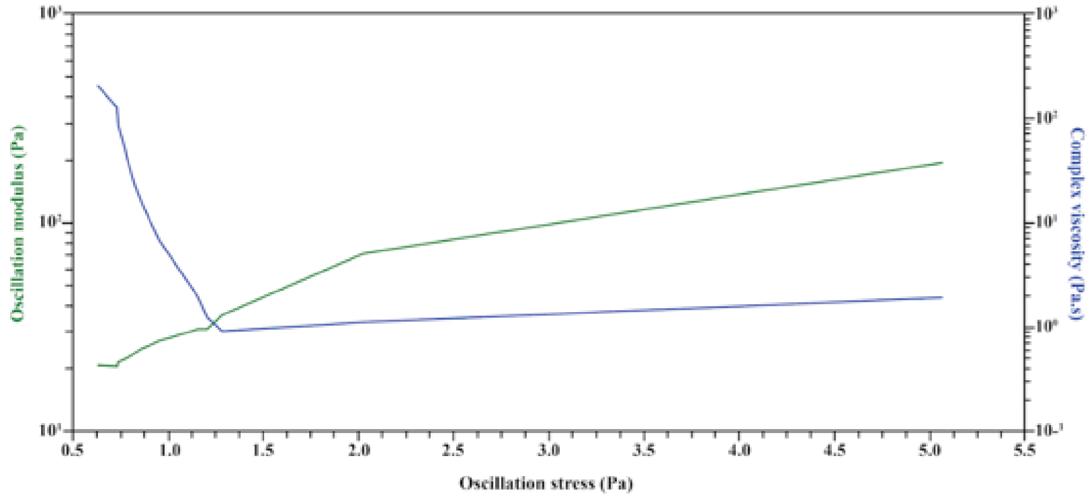

Fig 18 Ecoflex 30 50 □C modulus vs stress

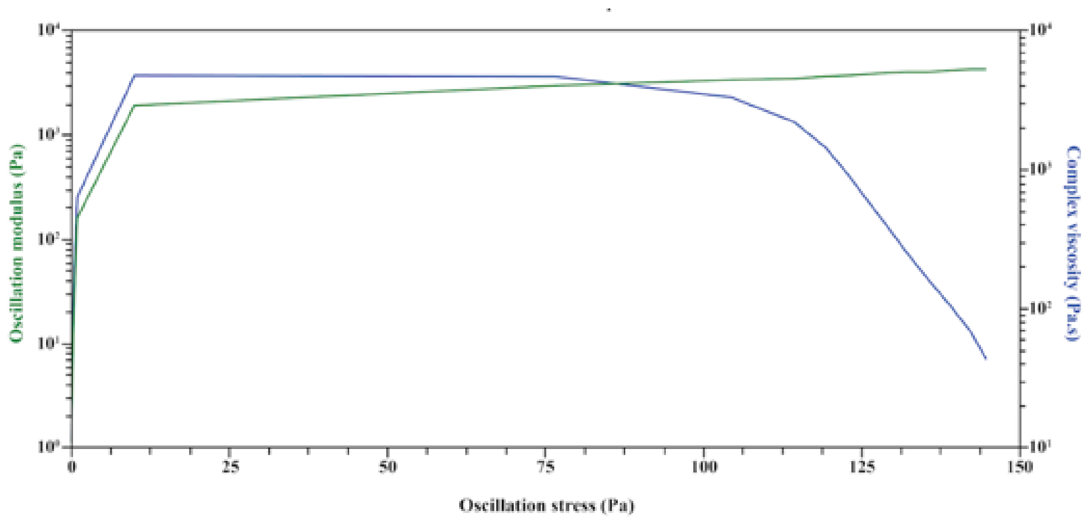

Fig 19 Ecoflex 30 60 □C modulus vs stress

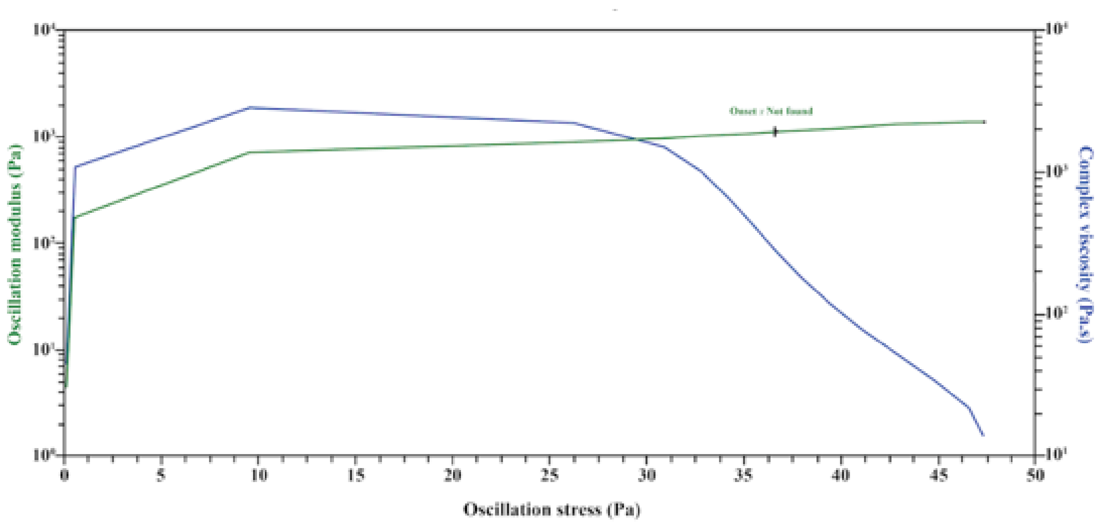

Fig 20 Ecoflex 30 70 □C modulus vs stress

Appendix B: Printer Specifications of L280s and Silicone 3D Printer

Parameters	Rep-Rep L280 series	Silicone 3D Printer
Build platform *	280mm x 280mm x200mm	200mm x 200mm x 100mm
Print speed	10 -150 mm/s	10 – 50 mm/s
Travel Speed	10 -300 mm/s	10 – 80 mm/s
Position Accuracy * (X/Y)	+/- 0.1mm/s	+/- 0.1mm/s
Layer Height (min)	0.22 - 0.9mm	0.4 – 0.7 mm
Material	EVOLV3D LC3335 Liquid Silicon Rubber LSR	Ecoflex 30 / 50 LSR
Nozzle Options	0.23 / 0.4 / 0.8 mm	0.5 / 0.6
Print Bed Temperature	110 deg C	100-110 deg C
Option	Maintenance Contract, Material Pails	
File Transfer	USB, Stand-alone printing with touch display, ethernet	USB, Stand-alone printing with touch display, ethernet

Parameters	Rep-Rep L280 series	Silicone 3D Printer
Software	Simplify 3D Software	Repertier-Marlin Software
Operating Voltage	230 VAC	240VAC
Ambient Temperature	15-26 deg C	19 -25 deg C
Weight	120 kg (without material removal system)	15 kg
Technology	Liquid Additive Manufacturing (LAM)	Liquid Additive Manufacturing (LAM)

Appendix C: Optimisation of key printing parameters using DOE and ANOVA

The 3^3 Design of Experiments and Anova results as shown:

ND	NT	BT	ND	NT	BT	NDx NT	NDxBT	NTxBT	NDxNTxBT	C Length avg	cwidth avg	c height avg	l width avg	l thickness avg
22	40	70	1	-1	-1	-1	-1	1	1	12.39	12.95	2.55	0.93	0.75
21	40	70	0	-1	-1	0	0	1	0	12.33	12.73	2.55	1.52	0.588
20	40	70	-1	-1	-1	1	1	1	-1	12.09	12.24	3.04	2.84	0.592
22	40	90	1	-1	0	-1	0	0	0	12.01	12	3.05	2.32	0.61
21	40	90	0	-1	0	0	0	0	0	14.08	14.6	4.65	1.54	0.62
20	40	90	-1	-1	0	1	0	0	0	12.3	12.56	4.6	1.11	0.56
22	40	110	1	-1	1	-1	1	-1	-1	11.06	10.64	3.88	1.48	0.56
21	40	110	0	-1	1	0	0	-1	0	11.35	10.6	3.51	2.71	1.37
20	40	110	-1	-1	1	1	-1	-1	1	14.47	14.09	6.52	1.6	0.89
22	50	70	1	0	-1	0	-1	0	-1	14.15	12.19	3.14	1.07	0.6
21	50	70	0	0	-1	0	0	0	0	12.93	13.43	1.92	2.1	0.73
20	50	70	-1	0	-1	0	1	0	0	13.04	12.78	3	3.4	0.79
22	50	90	1	0	0	0	0	0	0	11.67	11.67	3.21	1.67	0.71
21	50	90	0	0	0	0	0	0	0	12.46	12.33	3.53	1.39	0.89
20	50	90	-1	0	0	0	0	0	0	11.64	10.64	3.56	1.72	0.7
22	50	110	1	0	1	0	1	0	0	10.13	**10.52**	4.44	1.324	0.68
21	50	110	0	0	1	0	0	0	0	11.57	12.77	4.83	0.72	0.58
20	50	110	-1	0	1	0	-1	0	-1	11.01	11.72	6.55	1.52	0.62
22	60	70	1	1	-1	1	-1	-1	-1	14.11	13.8	2.74	0.91	0.64
21	60	70	0	1	-1	0	0	-1	0	12.31	12.63	3.34	1.66	0.82
20	60	70	-1	1	-1	-1	1	-1	1	12.21	10.75	2.76	2.35	0.74
22	60	90	1	1	0	1	0	0	0	8.83	9.8	2.44	1.22	0.6
21	60	90	0	1	0	0	0	0	0	12.16	12.78	3.97	1.77	0.67
20	60	90	-1	1	0	-1	0	0	0	12.06	12.61	4.5	1.83	0.86
22	60	110	1	1	1	1	1	1	1	12.02	11.78	1.72	2.06	1.01
21	60	110	0	1	1	0	0	1	0	12.69	13.5	4.85	2.53	1.28
20	60	110	-1	1	1	-1	-1	1	-1	12.57	12.72	7.12	1.47	1.22

Appendix D: Load vs Displacement curve for Ecoflex 30 and Ecoflex 50

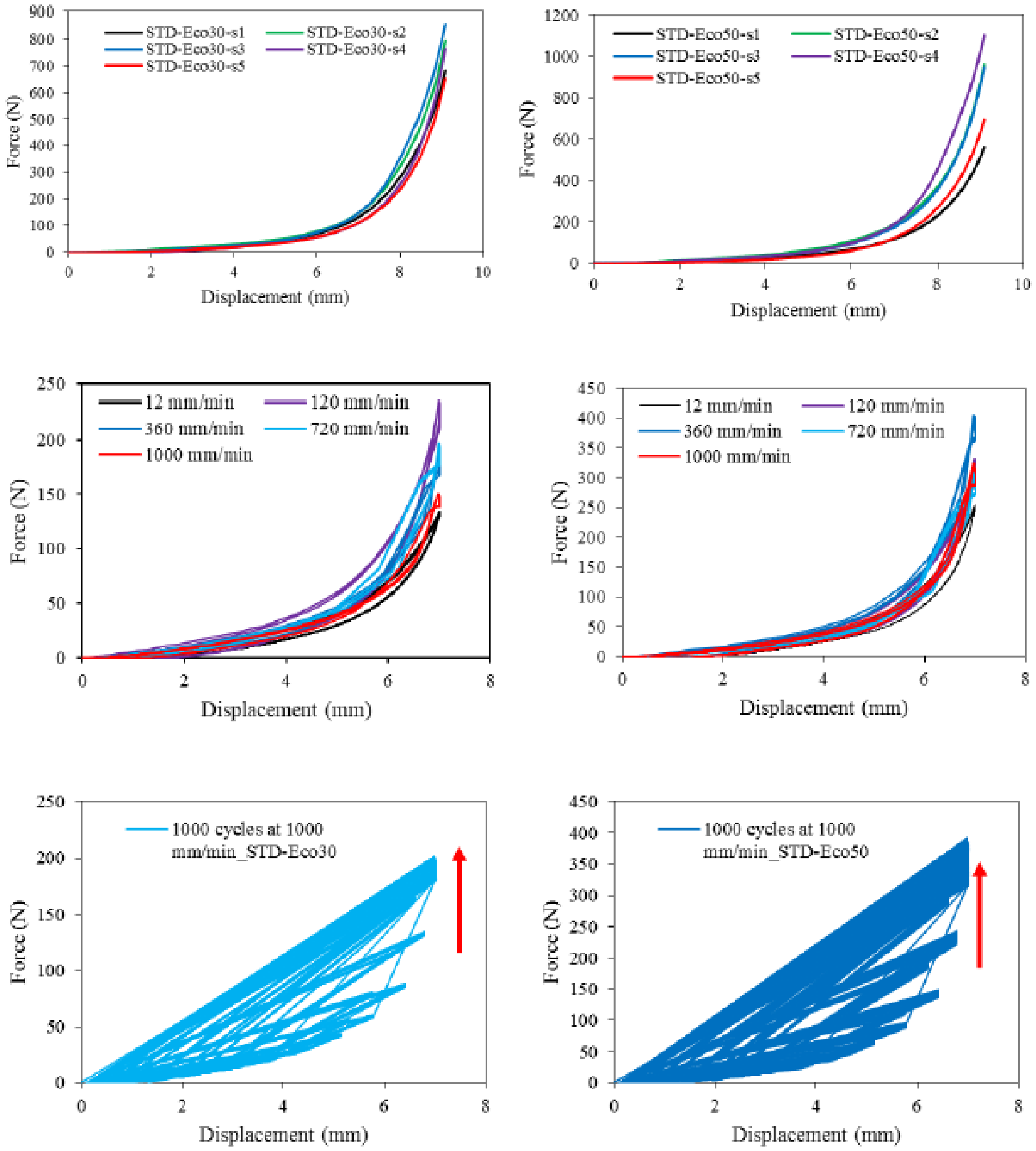

Appendix E: Optical images of silicone meniscus surface

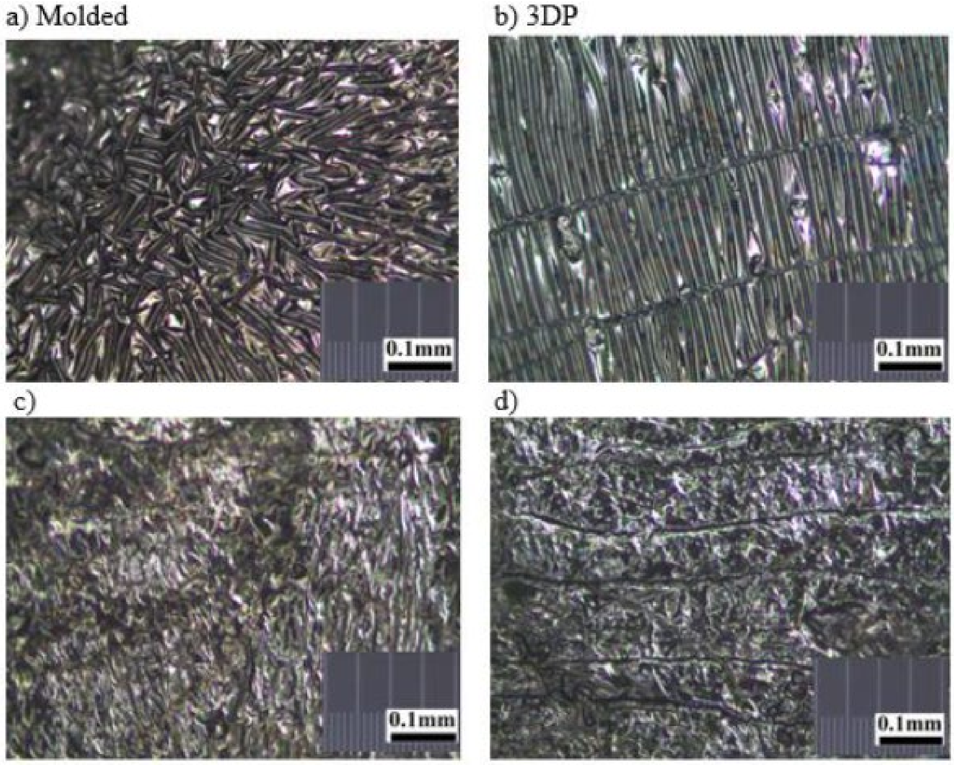

Representative stereomicroscopic images of the core surfaces of silicone meniscus implants. (a) surface of molded implant, (b) surface of 3D-printed implant, (c) cross-section of molded implant and (d) cross-section of 3D-printed implant (20× magnification).

Appendix F: XRFS spectra of (a) molded and (b) 3D printed silicone implant.

a) Molded Silicone Implant

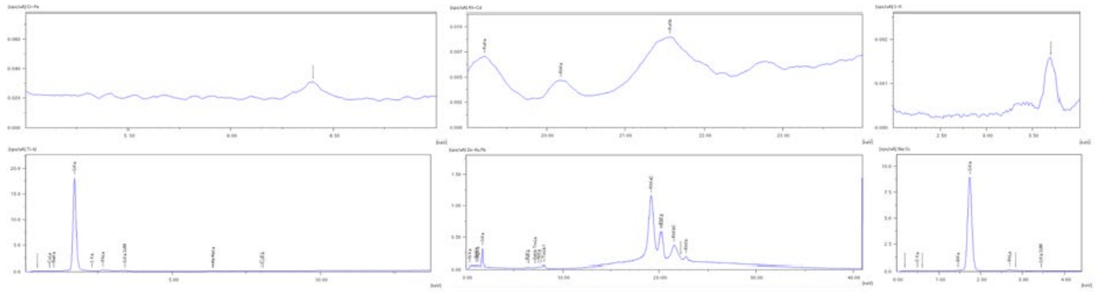

b) 3DP Silicone Implant

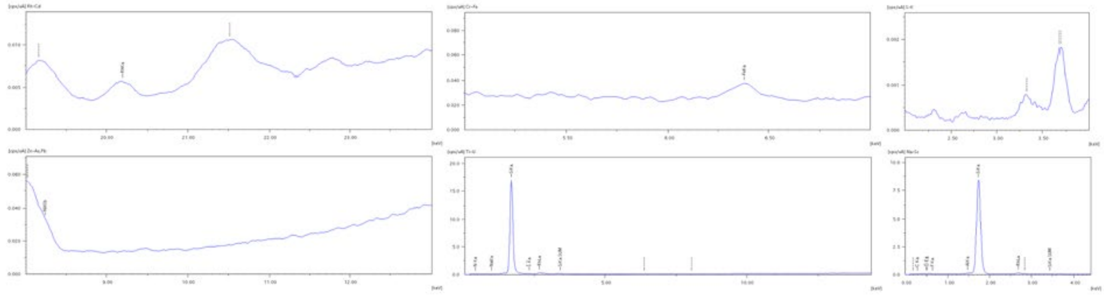

Appendix G: Combined (a) DSC, (b) TGA, and (c) DTG graphs of 3D Printed and Molded Eco30 and Eco50 samples

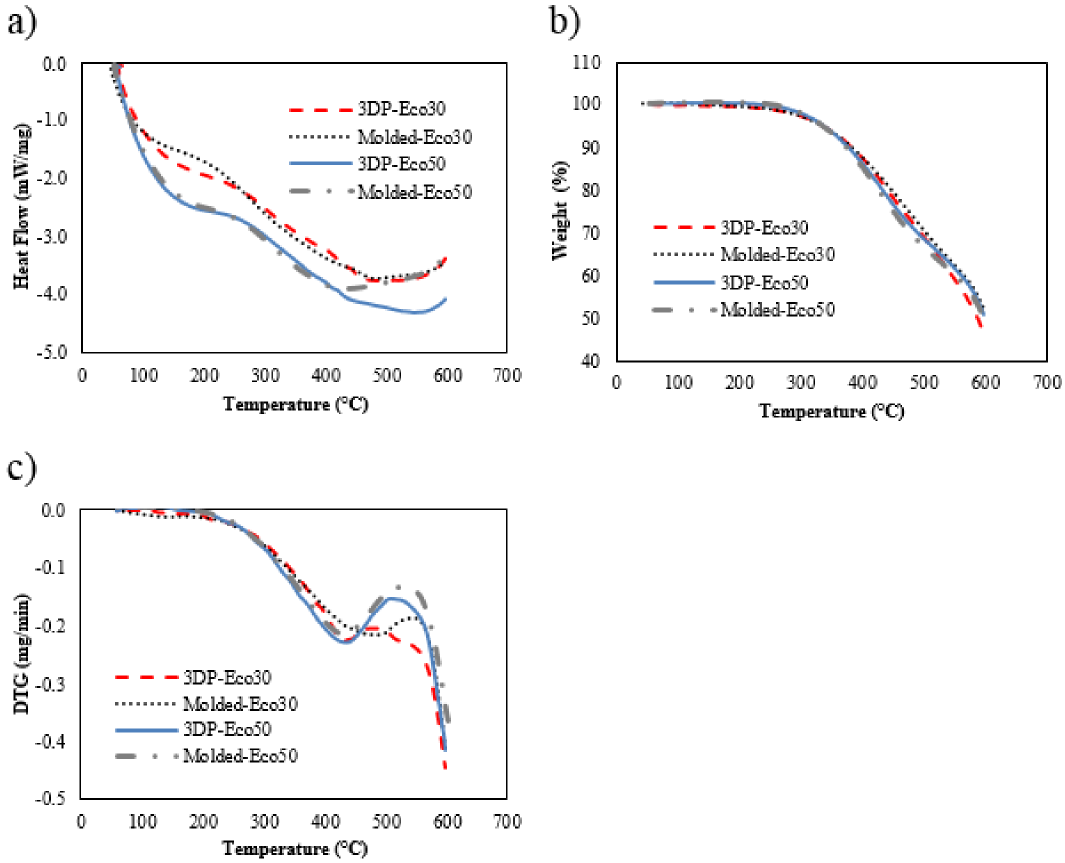

Combined (a) DSC, (b) TGA, and (c) DTG graphs of pure silicone, Si-TPU (80-20) and Si-TPU (60-40)

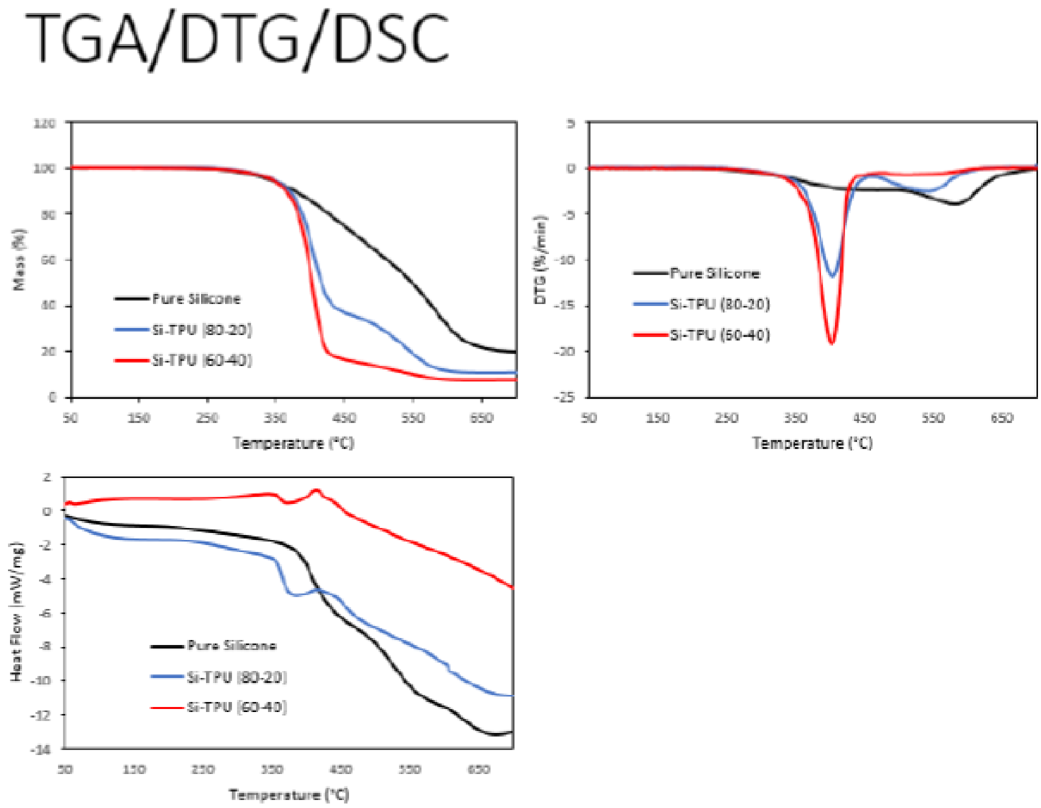

Appendix H: Overview of freeware software with segmentation tools applcable to any part of the body

Software Name	Segmentation tools	Features and comments
Seg3D	• Manual modification • Thresholding • Edge Detection • Level Sets • Connected Component filter	• Multiple Segmentation possible • Intuitive layer based interface • Editing tools available for image and segmentation • Can compute distance maps
3D Slicer	• Manual modification • Thresholding • Edge Detection • Fast marching method • Grown out method • Level tracing method • Modified filter for specific tasks	• Image Registration • Changes input data • Popular for 3D visualisation
InVersalius	• Manual modification • Thresholding	• Simple Interface • Automatic Thresholding • Popular for 3D visualisation
ITK-Snap	• Manual modification • Edge Detection	• Simple Interface • Multiple segmentations possible
Osirix	• Manual modification • Edge Detection	• Macintosh only • For visualization and image fusion • Freeware versions of Osirix MD for clinical use
Image J	• Extract mesh based on intensity isosurface using 3D viewer plug-in	• 3D image processing platform